Modélisation microscopique pour l'astrophysique Microscopic modeling for astrophysics

J. Margueron

U.F.R. SCIENTIFIQUE PARIS-SUD XI

INSTITUT DE PHYSIQUE NUCLÉAIRE D'ORSAY

HABILITATION À DIRIGER DES RECHERCHES

présentée par

Jérôme MARGUERON

pour obtenir l'Habilitation à Diriger des Recherches en sciences physiques de l'Université Paris-Sud XI

Sujet :

Modélisation microscopique pour l'astrophysique
Microscopic modeling for astrophysics

La soutenance publique est prévue le 11 mai 2012 devant la commission d'examen

M.	**Marcello Baldo**	Directeur de recherche	University of Catania	*Rapporteur*
M.	**Philippe Chomaz**	Directeur de recherche	CEA Saclay	*Examinateur*
M.	**Eric Gourgoulhon**	Directeur de recherche	Observatoire Paris-Meudon	*Rapporteur*
Mme	**Francesca Gulminelli**	Professeur	Université Caen	*Rapporteur*
M.	**Patrice Hello**	Professeur	Université Paris-Sud	*Président*
M.	**Pierre Pizzochero**	Professeur	Université de Milan	*Examinateur*

Table of contents

Chapter 1

Preamble: the needs of microscopic modeling for astrophysics

At the present time, we know that pulsars are compact stars born in the aftermath of successful core collapse supernovae explosions but the details of the explosion mechanism of supernovae are still uncertains. There is however a general agreement that the physics of neutrino transport is a key ingredient to a successful explosion: following core collapse, a hot proto-neutron star (PNS) is formed and neutrinos take away some 99% of the binding energy that is released to form a neutron star, which are the most compact stellar object after black holes. Some of the properties of neutron stars, such as masses, rotation frequencies, emission of radiations are measurable, while some other signals like gravitational wave emission is planed to be in the next years. Other properties which are not directly linked to observations, such as the internal composition or temperature, require the development of theoretical models.
Fortunately, another dense system is accessible to our experimental facilities and some of the missing information could be obtained from the study of the atomic nuclei on Earth. Some of the exotic neutron-rich nuclei produced in nuclear facilities are even located in the outer crust of neutron stars, while the inner crust is composed by drip-line nuclei immersed in a neutron gas and exhibit a neutron skin larger but similar to neutron rich nuclei. There are several questions related to nuclear physics that are interesting to be investigated in view of their importance in astrophysics. Among these questions, there are for instance the equation of state of dense matter where 2-body and 3-body correlations play a crucial role, the understanding of the dense matter phase transitions, the superfluid properties of neutron matter as well as of non-uniform matter in the crust of neutron stars, the description of nuclear clusters surrounded by a gas of light nuclei, and the impact of global properties of nuclear matter, such as the compressibility or the symmetry energy, on the properties of core collapse supernovae and neutron stars.
These questions will be addressed through this manuscript, and in this chapter, the astrophysical context and the needs for theoretical modeling are first presented.

1.1 Introduction to neutron stars and core-collapse supernova astrophysics

The history of neutron stars is of course strongly related to the discovery of the neutron, by James Chadwick in 1932, as one of the constituent of atomic nuclei with a mass almost identical to the proton one, the other nucleus constituent. It is also strongly connected with the statistical properties of Fermionic liquids proposed by Fermi in 1926, and the exclusion principle which gives rise to the Pauli pressure, and the

understanding by Fowler in 1926 that the quantal pressure in a degenerate electron gas, the Pauli pressure, can stabilize white dwarf.

All the theoretical concepts were therefore ready in the early 30s to allow Walter Baade and Fritz Zwicky to advance, *"with all reserve, the view that supernovae represent the transitions from ordinary stars into neutron stars, which in their final stages consist of extremely closely packed neutrons" (Baade and Zwicky, 1934).* The idea of compact stars is however usually attributed to Landau in February 1932 who might have discussed the implication of the discovery of the neutron in Copenhagen together with Rosenfeld and Bohr as reported by Rosenfeld in 1974 (Shapiro and Teukolsky, 1983), page 242. The intuition of Landau shall however be moderated and his exact contribution have been investigated by D. Yakovlev who discovered that Landau was not in Copenhagen in February 1932. In January 1932, before the discovery of the neutron, Landau have however written a paper *On the theory of stars* where he intuited that the density of stellar matter, might *becomes so great that atomic nuclei come close contact, forming one gigantic nucleus* (Landau, 1932). The name of neutron stars was therefore first introduced by Baade and Zwicky in 1934. This issue has been presented by D. Yakovlev in a lecture given during CompStar School "The Complex Physics of Compact Stars", Ladek Zdroj, 2008. The full lecture slides can be downloaded from the following link:
`http://www.ift.uni.wroc.pl/%7Ekarp44/talks/yakovlev.pdf`.

The link between the formation of neutron stars and white dwarf have been made by Gamow in 1939, and Chandrasekhar understood that electron capture on protons at high density (about 10^9 g cm-3) *"would cause a sudden diminution of pressure resulting in the colapse of the star to a neutron core"*. He introduced the Chandrasekhar mass limit and estimated the mass of neutron stars to be about 1.4 solar mass. In 1939, Tolman (Tolman, 1939) and at the same time Oppenheimer and Volkof (Oppenheimer and Volkoff, 1939) have proposed solutions of general relativistic hydrostatical equations and have found the existence of a maximum and limiting mass for the stable solutions for compact objects. At this time neutron stars were though to be less massive than the sun within a radius of about 10 km. After these papers, theoretical studies of neutron stars were almost inexistent since neutron stars were though to be too compact to be observed. It shall however be mentioned the precursor work by Ambartsumyan in the early 60s who investigated equation of state for dense matter including hyperons (Ambartsumyan and Saakyan, 1961). Ambartsumyan thought that the nuclei of the galaxies might be made of a very massive hyperonic stars (Ambartsumyan, 1966). However, hyperonic matter tends to soften the equation of state and therefore to keep the maximum mass of neutron stars below 2 $M_\odot$.

At the begining of the 60s, supernova remnants (SNR) were identified as sources of X-rays. In 1964, Chiu and Salpeter have suggested that the thermal emission from neutron stars could illuminate the SNR and be the source of X rays (Chiu and Salpeter, 1964). The size of the emitter in the case of the Crab SNR was however estimated to be too large to be a neutron star. In 1967, Pacini have proposed that a rapidly rotating neutron star with a huge magnetic field could instead be the source of energy observed in the crab SNR (Pacini, 1967; Pacini, 1968). In 1968, Gold have suggested a rotation powered model where the braking of the pulsar is related to the radiation of a dipole magnetic field in vacuum which is not align with the rotational axis (Gold, 1968; Gold, 1969). Equaling the observed flux from the Crab SNR to the rotational loss of energy, a huge magnetic field as large as 10^{12} G was inferred. The main features of neutrons stars related to their compactness and their huge magnetic field were therefore already envisioned before their observational discovery, but they were not predicted to be pulsars.

1.1.1 The discovery of pulsars

The existence of neutron stars remained however very conjectural until 1968 when Jocelyn Bell and her thesis advisor Anthony Hewish discovered radio pulsars (Bell Burnell, 2004), characterized by radio

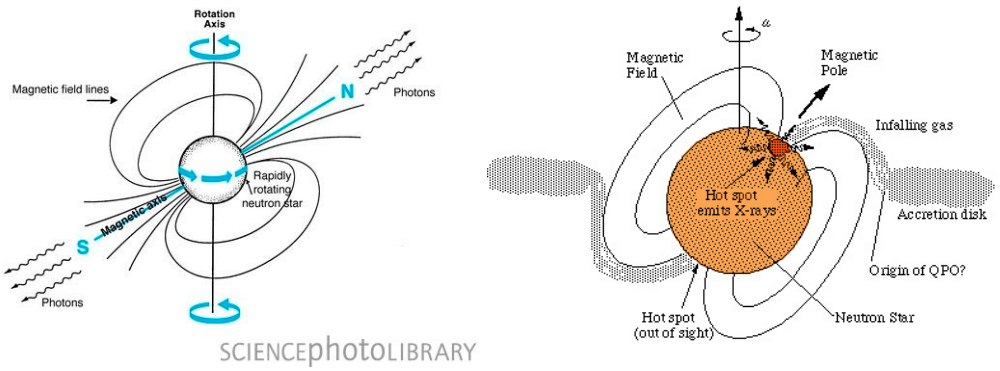

Figure 1.1: Rotating pulsar with its magnetic fields and the focussed radio beams (left), and accreting pulsar with its hot spot (right). Diagram showing the physical phenomena associated with a pulsar (rapidly-rotating neutron star). Neutron stars have powerful magnetic fields (lines at upper left and lower right) and rotate very fast (less than a second). This leads to the acceleration of charged particles by the magnetic field and the release of radiation from the poles (photons,on the left panel). The axis of rotation (blue arrows) does not coincide with the magnetic axis (blue line), and the rotation sends the two photon beams sweeping across the sky to be detected as pulses on Earth. Credit: JON LOMBERG/SCIENCE PHOTO LIBRARY.

emission with a periodicity which lies between few seconds and few tens of milliseconds (Becker and Pavlov, 2001). The vast majority of radio pulsars are isolated neutron stars because in binary systems, the accretion disk tends to screen the signal. In addition to radio emission, neutron stars are also found in interacting binary systems that emit intense X-rays. In such binaries, a neutron star closely orbits a normal optically visible star and draws gas away from it. The in-falling accreted gas is heated to millions of degrees and emits X-rays. Rapidly rotating and relatively young radio pulsars are also found in the visible spectrum (Crab pulsar, Vela pulsar). Some neutron star are also strong high-energy (greater than tens of MeV) gamma-ray sources.

The radio beam observed in 1968 from the Vela and the Crab nebula is produced by the huge magnetic field which can be deduced by the rotation powered model of Gold (Gold, 1968; Gold, 1969). Later, in 1978, a different analysis have measured a magnetic field of about 10^{12-13} G in Hercules X-1, a young high mass X-ray accreting binary, by associating a peak at about 100 keV in the hard X-ray emission spectrum to a cyclotron resonance emission process close to the hot magnetic pole. Radio pulsars can therefore be safely interpreted as spinning compact stars with an intense magnetic field misaligned with the rotation axis. Radio waves are though to be emitted by the electrons accelerated along the polar magnetic fields. Hence, the radio wave are not isotropically emitted but focussed like a beam. Rotating neutron stars can emit a pulsed signal in an analogous way as a lighthouse guiding the boats along the coast, as illustrated in Fig. 1.1.

Besides, the strongest known magnetic fields of the present universe have been found in neutron stars where surface magnetic fields are of the order of 10^{12} G. In few young neutron stars, called magnetars, much more intense magnetic fields have been observed and may exceed 10^{15-16} G. The usual dynamo effect is here unable to produce such intense magnetic fields. A possible phase transition to strongly spin polarized matter could be responsible, but this is still a speculation in dense matter. From time to time, probably due to the twist of its magnetic field, magnetars emit a giant flare like to one which has reached the Earth on December, 27, 2004 and has interrupted all radio broadcast during few seconds (Lazzati, 2005).

Measurements of masses and radii of neutron stars still represent an observational challenge (Lattimer

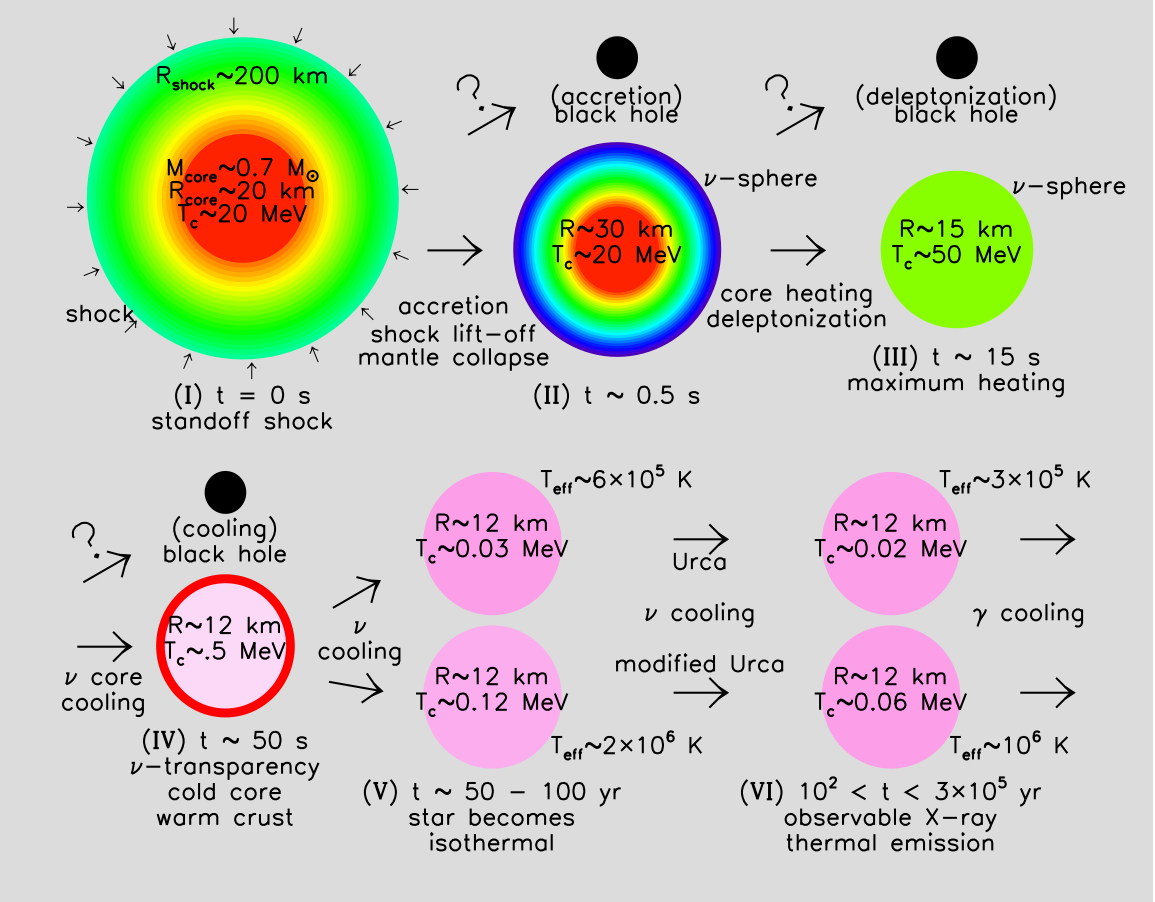

Figure 1.2: The main stages of evolution of a neutron star, from (Prakash et al., 1997). Shading indicates approximate relative temperatures.

and Prakash, 2007). The most accurate measurements of masses are obtained in binaries of neutron stars applying Kepler laws. Observed values give typically masses around 1.4 solar mass. However, a recent measurement of 1.97 ± 0.04 $M_\odot$ (Demorest et al., 2010) have brough new constraints on the dense matter equation of state (Lattimer and Prakash, 2010). The time derivative of the rotation velocity associated to the luminosity provide an estimate of the moment of inertia which, combined with the value of the mass, give a measure of the radius. This leads to a typical radius of a tenth of kilometers. These measurements cannot reach the accuracy required to disentangle the models of neutron stars. Other methods are then proposed, like the one based on black body radiations but it has been found that neutron stars may have a non-uniformly distributed surface temperature. This complicates the interpretation of the black body emission.

About 1800 neutron stars has been identified so far and, as shown, they participate to a large variety of observed systems which are characterized by their electromagnetic emission going from visible spectrum to gamma rays. The Fermi-LAT telescope, launched in 2008, has increased our knowledge on the gamma-emission of neutron stars and have shed a new light on the emission processes.

1.1.2 The birth of neutron stars

The evolution of a PNS proceeds through several distinct stages (Burrows and Lattimer, 1986; Bethe, 1990) and with various outcomes (Prakash et al., 1997), as shown schematically in Fig. 1.2. Immediately following core bounce and the passage of a shock through the PNSs outer mantle, the star contains an unshocked, low entropy core of mass $\simeq 0.7$ $M_\odot$ in which neutrinos are trapped (stage I in the figure). The core is surrounded by a low density, high entropy ($5 < s < 10$) mantle that is both accreting matter from the outer iron core falling through the shock and also rapidly losing energy due to electron captures and thermal neutrino emission. The mantle extends up to the shock, which is temporarily stalled about 200 km from the center prior to an eventual explosion.

After a few seconds (stage II), accretion becomes less important if the supernova is successful and the shock has ejected the stellar envelope. Extensive neutrino losses and deleptonization will have led to a loss of lepton pressure and the collapse of the mantle. If enough accretion has occurred, however, the star's mass could increase beyond the maximum mass capable of being supported by the hot, lepton-rich matter. If this occurs, the remnant collapses to form a black hole and its neutrino emission is believed to quickly cease (Burrows, 1988).

Neutrino diffusion deleptonizes the core on time scales of 10–15 s (stage III). Diffusion time scales are proportional to $R^2(c\lambda_\nu)^{-1}$, where R is the star's radius and λ_ν is the effective neutrino mean free path. This generic relation illustrates how both the EOS and the composition influence evolutionary time scales. The diffusion of high-energy (200–300 MeV) ν's from the core to the surface where they escape as low-energy (10–20 MeV) ν's generates heat (a process akin to joule heating) through neutrino-matter interactions. The core's entropy approximately doubles, producing temperatures in the range of 30–60 MeV during this time, even as neutrinos continue to be prodigiously emitted from the star's effective surface, or neutrinosphere.

Strange matter, in the form of hyperons, a Bose condensate, or quark matter, suppressed when neutrinos are trapped, could appear at the end of the deleptonization. Its appearance would lead to a decrease in the maximum mass that the internal pressure of matter is capable of supporting against gravity, implying metastability of the neutron star and another chance for black hole formation (Prakash et al., 1997). This would occur if the PNSs mass, which must be less than the maximum mass of hot, lepton-rich matter (or else a black hole would already have formed), is greater than the maximum mass of hot, lepton-poor matter. However, if strangeness does not appear, the maximum mass instead increases during deleptonization and the appearance of a black hole would be unlikely unless accretion in this stage remains significant.

The PNS is now lepton-poor, but it is still hot. While the star has vanishing net neutrino number, thermally produced neutrino pairs of all flavors dominate the emission. The average neutrino energy slowly decreases, and the neutrino mean free path increases. After approximately 50 seconds (stage IV), $\lambda \simeq R$, and the star finally becomes transparent to neutrinos. The neutrino luminosity rapidly decreases beyond this time. Since the threshold density for the appearance of strange matter decreases with decreasing temperature, a delayed collapse to a black hole is still possible during this epoch.

Following the onset of neutrino transparency, the core continues to cool by neutrino emission, but the star's crust remains warm and cools less quickly. The crust serves as an insulating blanket which prevents the star from coming to complete thermal equilibrium and keeps the surface relatively warm ($T \approx 3 \times 10^6$ K) for up to 100 years (stage V). The temperature of the surface after the interior of the star becomes isothermal (stage VI) is determined by the rate of neutrino emission in the star's core and the composition of the surface.

At this stage, the neutron star is born.

There is mainly no energy production in neutron stars. The conversion of protons into neutrons necessitate energy, neutrinos and anti-neutrinos mainly produced by beta decay and inverse beta decay continue to carry out the energy of the core and cool down the temperature. This is called the URCA process, by

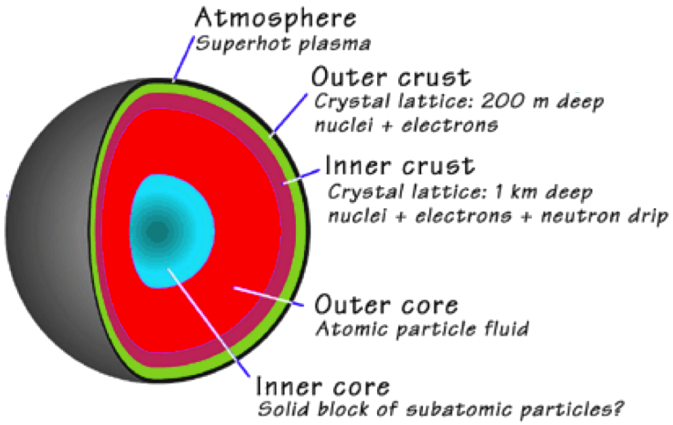

Figure 1.3: The basic structure of a neutron star.

reference to the name of a casino existing in the mid 50s in Rio di Janeiro, known by the promoter of this process, G. Gamow. According to him, the efficiency of this casino in spoiling the money of the gamblers was comparable to the URCA process in cooling down the star. Latter on, it was discovered that URCA process is strongly suppressed by energy and momentum conservation unless a minimum amount of proton, around 11% of the baryonic density, is present (Lattimer et al., 1991). This minimal amount is strongly correlated with the symmetry energy. Relativistic models, having large values of symmetry energy satisfy this criterion close to saturation density while most of non-relativistic models, with a lower value of the symmetry energy, do not (Li et al., 2008a). Anyhow, the URCA process is too efficient to explain the slowing down of the surface temperature with time which is observed for a dozen of stars: neutron stars are visible by thermal emission during a few millions of years. Several improvements has been proposed: superfluidity leading to the presence of a neutron gap may quenches cooling from the URCA process. A modified URCA process is also considered where adding an additional nucleon as a spectator of the process allows momentum and energy conservation. Other neutrino emission processes are also considered like neutrino bremsstrahlung, pair breaking emission ...

1.1.3 Anatomy of a neutron star

A few hours after birth, a neutron star has cooled down below 10^9 K, a solid crust will be formed in the external layers. The crust of neutron stars contains only a few percent of the NS mass, but plays a crucial role in NS evolution (cooling, accretion, bursts) and dynamics (glitches, non-axial deformations).

As illustrated in Fig. 1.3, cold catalyzed neutron stars are quasi-spherical objects composed of 6 major regions: the inner and outer cores ($\approx$ 99% of the mass) where nuclear matter is homogeneous and which are usually sufficient to understand the main properties of neutron stars; the inner and outer crust (1-2 km width) composed of inhomogeneous nuclear matter (nuclei or nuclear clusters) which screens the core from observations (even from neutrinos), the envelope (few meters) which influences the transport and the release of thermal energy from the surface, and finally the atmosphere (few centimeters) which plays an important role in shaping the emergent photon spectrum.

At the surface defined by the interface between the outer crust and the envelope, ^{56}Fe atoms are arranged as in a solid. Going towards the interior, the atoms are ionized and in the outer part of the crust one can find nuclei with numbers of nucleons up to A=200 arranged in a Coulomb lattice in the presence of an electron gas. Due to electron capture processes, these nuclei become richer in neutrons with increasing density

(10^9 to 10^{11} g/cm^3). The early modelization of neutron star crusts has been proposed in the 1970's in the pionering works of Baym et al. (Baym et al., 1971) and Negele and Vautherin (Negele and Vautherin, 1973); the two analysis have been performed, respectively, within a semiclassical Thomas-Fermi and a microscopic Hartree-Fock framework. To briefly summarize, an outer and an inner part can be distinguished in the crust of a neutron star. In the outer crust exotic nuclei form a Coulomb lattice in the presence of an electron gas. More deeply in the interior of the crust, density increases and nuclei are more and more neutron-rich up to the drip point $\rho \sim 4 \cdot 10^{11}$ g/cm^3. Neutrons start to leak out of nuclei at densities above the neutron drip density, the equivalent of the neutron drip line in a stellar environment (finite pressure, beta-equilibrium). Beyond the neutrin drip density, nuclei are located at the sites of a crystal immersed in a super-fluid of neutrons and relativistic leptons. The lattice can be describe by its elementary constituents, the Wigner-Seitz (WS) cells, each of them containing the most probable nuclear cluster, the neutron and the electron gases. These WS structures can be regarded as a bridge between a finite nucleus and an infinite nuclear gas.

There are still many questions that are related to the properties of the surface and the crust of neutron stars. For instance, the electromagnetic spectrum is determined by the temperature at the base of the envelope and by how photons diffuse through the atmosphere. Realistic spectra for the thermal emission of NSs that can be confronted with X-ray observations of isolated NSs requires the modeling of crust and surface matter in strong magnetic fields which is still an open question. Furthermore, the structure above 10^{11} g/cm^3 is still uncertain. Are nuclei ordered in a nearly perfect crystal lattice with only one nuclide present or is the structure heterogeneous? The answer is of crucial importance for the electrical conductivity of the crust (important for the magnetic field evolution) and its heat conductivity (crucial for the relation between the surface and the core temperature).

For densities higher than 10^{13} g/cm^3, the nuclear clusters are close enough to begin a dissolution process and deformed structures appear. It is commonly called the pasta phases because matter self-organizes itself in noodle shapes like lasagna, spaghetti or the swiss cheese. At this stage, the proton fraction has decreased down to 0.1. This process results in the formation of homogeneous nuclear matter. It should be noted that the high proportion of neutrons is due to the loss of neutrinos during the first phase of the explosion (deleptonisation). The NS core contains more than 95% of the stellar mass and its central density may exceed 10^{15} g/cm^3. Its structure is determined by the poorly known EOS beyond saturation density of atomic nuclei (hereafter noted $\rho_0 = 2.6\ 10^{14}$ g/cm^3. This part of the EOS can be strongly influenced by the onset of new degrees of freedom, such as the apparition of the strange-quark, in either deconfined matter (quark-gluon plasma) or in hyperonic matter. The role of the interaction, and in particular the three-body forces involving hyperons, on the maximum mass of neutron stars with hyperonic cores requires still to be clarifyied. Other exotic particles such as Bose condensates (pions or kaons) may also become abundant.

In laboratory experiments with relativistic heavy-ion collisions (e.g. with the LHC at CERN Geneva and RHIC at BNL Brookhaven) one is able to probe only the high-temperature domain of the QCD phase diagram under conditions of strong non-equilibrium. The high-densities and high-temperature region is known to be reached only in the early Universe and during the first minute of life of neutron stars. The high-density and low-temperature region of the phase boundary, where the most interesting correlation- and condensation phenomena are anticipated, is expected to occur only in the interiors of neutron stars. However, these objects should really be considered compact stars since most likely their central region consists rather of exotic phases of matter (e.g. hyperons), boson condensates (pions, kaons, H-matter) or deconfined quark matter (u, d, s quarks), see Fig. 1.4. Strange quark matter has even been discussed to be more stable than Fe, the most stable nucleus, which would lead to compact stars composed largely of pure quark matter. Any progress in the interpretation or prediction of characteristic phenomena of the compact star evolution is tightly related to our knowledge of the properties of high-density matter which have to be predicted using techniques of nuclear many-body theory and finite-density (and temperature) field theory.

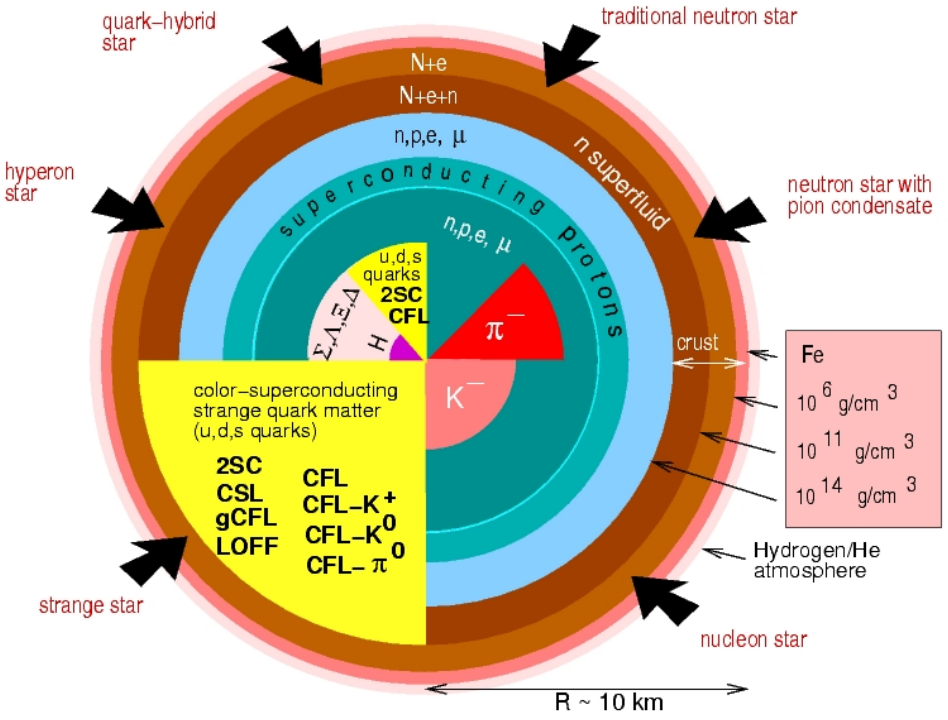

Figure 1.4: Neutron star compositions predicted by various theories (Weber et al. 2006).

1.1.4 Status of core-collapse hydrodynamical simulations

Since the first numerical simulations of core-collapse supernovae in the 1960s (Colgate and White, 1966; Arnett, 1968a; Arnett, 1968b), enormous progress has been made on both the hydrodynamics and the microphysics aspects of core-collapse supernovae. The effects of hydrodynamical instabilities, rotation, convection, and General Relativity have been analyzed and implemented in modern simulations. Several steps forward have also been made from the microphysical point of view, mainly concerning the nuclear equation of state and the knowledge of neutrino properties. Despite these improvements, a unified consensus on the supernova explosion scenario is still to be achieved. Different groups have been working in order to introduce more realistic physics. On the one hand, a detailed treatment of neutrino physics has been implemented in spherically symmetric models both in Newtonian gravity (Rampp and Janka, 2000) and in General Relativity (GR) (Liebendörfer et al., 2001). On the other hand, multi-dimensional codes have been developed with different approximation schemes for neutrino transport. New algorithms based either on implicit, adaptive grid solvers for hydrodynamics with the Boltzmann equation for neutrino transport (Liebendörfer et al., 2004), or explicit, conservative schemes with a Riemann-solver for hydrodynamics coupled with an implicit solver for the neutrino equations (such as the variable Eddington factor (Rampp and Janka, 2002) and the “ray-by-ray-plus” method (Müller et al., 2010) were employed. Moreover, a significant effort has been made in order to implement a set of nuclear reactions other than the ones treated by Bruenn (Bruenn, 1985). All state-of-the-art simulations of core-collapse supernova, however, performed in Newtonian gravity (Rampp and Janka, 2000; Thompson et al., 2003), in Newtonian gravity with relativistic corrections in the Newtonian potential (Buras et al., 2003; Buras et al., 2006a), in full GR (Mezzacappa et al., 2001; Liebendörfer et al., 2001; Liebendörfer et al., 2004; Liebendörfer et al., 2005), and with different equations of state (Janka et al., 2005; Sumiyoshi et al., 2005), agree with the results obtained in the 1980s and 1990s (Myra and Bludman, 1989; Swesty et al., 1994). Namely, the prompt shock is not able

to drive a supernova explosion, except in the case of small iron cores (Baron and Cooperstein, 1990) or very soft equations of state (Baron et al., 1987). Even in the case of the delayed mechanism, spherically symmetric simulations, as well as 2- and 3-dimensional models with convection (Janka and Müller, 1996; Burrows et al., 1995; Buras et al., 2006a) give a similar outcome: no successful explosion can be obtained for progenitors more massive than 10 $M_{\odot}$.

More recently, it has been stressed that success in the numerical simulations might be attained by taking into account hydrodynamical instabilities, like Standing Accretion Shock Instability (SASI), which would act during shock stagnation, helping the neutrino energy deposition and the shock revival (Foglizzo, 2002; Blondin et al., 2003; Foglizzo et al., 2007). Indeed, in the simulations performed by the Garching group, the onset of a SASI-aided explosion was obtained for a 11.2 $M_{\odot}$ and a 15 $M_{\odot}$ progenitor (Buras et al., 2006b; Marek and Janka, 2009), producing an explosion energy of $\sim 10^{51}$ erg. Some different mechanisms, such as magneto-hydrodynamical effects (Burrows et al., 2007) or acoustic power associated with the accreting proto-neutron star (Burrows et al., 2006) have also been proposed. Very recently, the dependence on spatial dimension of the neutrino heating mechanism in core-collapse supernova has been investigated (Nordhaus et al., 2010). The authors claimed that the tendency of the models to explode increases monotonically with the dimension of the simulation, but these results were not confirmed by a different study (Hanke et al., 2011).

The key ingredient of the explosion mechanism is therefore not yet well understood. It might be that there is no key ingredient but important contributions from both a better description of the hydrodynamical modeling, the neutrino transport and the microphysics.

1.2 Compact stars and supernovae: a play-ground for microphysics modeling

Neutron stars provide a unique and fascinating stage where the evolution from finite nuclei to infinite systems can be analyzed (Glendenning, 2000; Lattimer and Prakash, 2004). We are thus experiencing the blooming of astronuclear physics, an exciting research area in which the physics of compact stars plays a fundamental role. While a part of this physics relies on theories that are well tested in terrestrial laboratories, a good part of it is basically unknown in the regimes found in compact stars. Unveiling this picture is a task made challenging by the multidisciplinary character of the problem, which requires expertise from historically independent disciplines, such as nuclear and particle physics, astrophysics, gravitational and computational physics. In this section, we briefly discuss microphysics modeling for neutron stars and supernovae.

1.2.1 The equation of state of dense stellar matter

Typical equations of state (EoS) are represented in Fig. 1.5 in symmetric and neutron matter. These EoS have been separated into *stiff* (left) and *soft* (right) depending on the slope of the symmetric energy coefficient L (Loan et al., 2011). The difference in the symmetry part of E/A lead to very different behaviors of the energy of pure neutron matter given by the stiff and soft groups of interactions.

From the calculation of the energy per particle $E/A(n_b)$ function of the baryonic density n_b, such as those shown in Fig. 1.5, one can deduce the EoS: the pressure $P(\epsilon)$ as a function of the energy density ϵ where the rest mass energy is included (in non-relativistic approach: $\epsilon = n_b + E/V/c^2$). The pressure profile $P(r)$, where r is the radius of the neutron star, is deduced from the well-known Tolman-Oppenheimer-

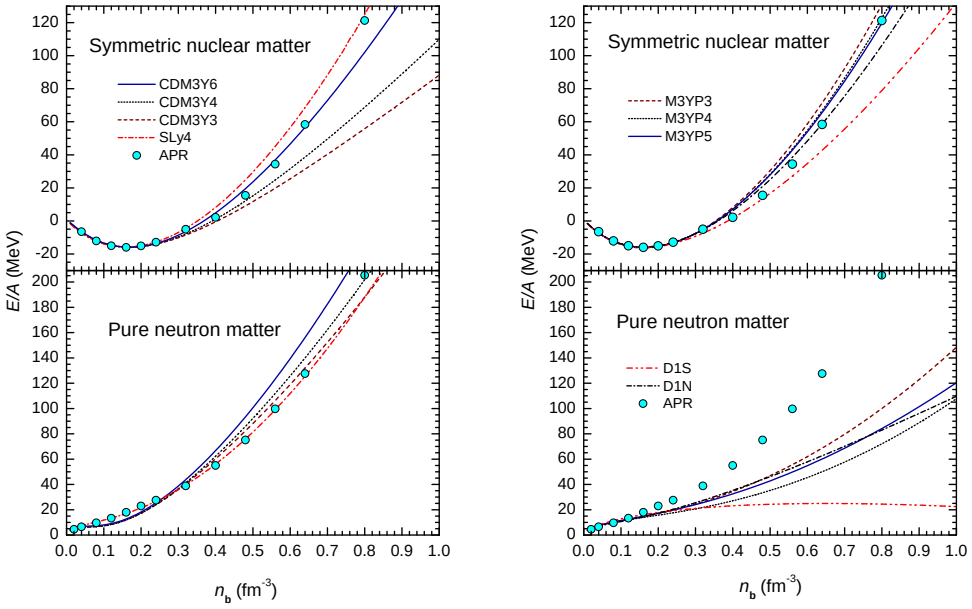

Figure 1.5: Energy per particle E/A of the symmetric and pure neutron matter calculated in the HF approximation using the in-medium nucleon-nucleon interactions that give *stiff* (left) and *soft* (right) behavior of the symmetry energy (Loan et al., 2011). Circles are results of the ab-initio calculation APR (Akmal et al., 1998).

Volkov (TOV) equilibrium equations (Glendenning, 2000),

$$\begin{aligned} \frac{dP(r)}{dr} &= -G\frac{m(r)\epsilon(P)}{r^2}\left(1+\frac{P(r)}{\epsilon(P)c^2}\right)\left(1+\frac{4\pi P(r)r^3}{m(r)c^2}\right)\left(1-\frac{2Gm(r)}{rc^2}\right)^{-1}, \\ \frac{dm(r)}{dr} &= 4\pi r^2\epsilon(P), \end{aligned} \tag{1.1}$$

where G is the universal gravitational constant and m is the gravitational mass enclosed within the sphere of radius r. The TOV equations (1.1) are supplemented with the following equation determining the number of baryons a inside this sphere (Douchin and Haensel, 2001)

$$\frac{da(r)}{dr} = 4\pi r^2 n_{\rm b}\left(1-\frac{2Gm(r)}{rc^2}\right)^{-1/2}. \tag{1.2}$$

Fixing the central density of the neutron star $n_{\rm c}$ as an external parameter, Eqs. (1.1) and (1.2) are integrated from the neutron star center, with the boundary conditions at $r = 0$: $\epsilon(0) = \epsilon_{\rm c} = \epsilon(n_b = n_{\rm c})$, $P(0) = P_{\rm c} = P(\epsilon_{\rm c})$, $m(0) = 0$, and $a(0) = 0$. The stellar surface at $r = R$ is determined from the boundary condition $P(R) = 0$. The total gravitational mass and total number of baryons are then determined as $M = m(R)$, $A = a(R)$, respectively. As a result, with different inputs for the nuclear matter pressure, the corresponding solutions of the TOV equations give different neutron star models in terms of *one-parameter* ($n_{\rm c}$) families (Douchin and Haensel, 2001) that can be labeled by the central pressure $P_{\rm c}$ or equivalently by the central density $n_{\rm c}$ of the neutron star.

Thus, at each central density we can uniquely determine the corresponding gravitational mass M and radius R, and the behavior of M versus R is often used to compare with the measured masses and radii of neutron stars. Results obtained with different EoS are plotted in Fig. 1.6. The recently measured masses and radii for the binaries 4U 1608-248, EXO 1745 -248, and 4U 1820-30 (Özel et al., 2010) are plotted in

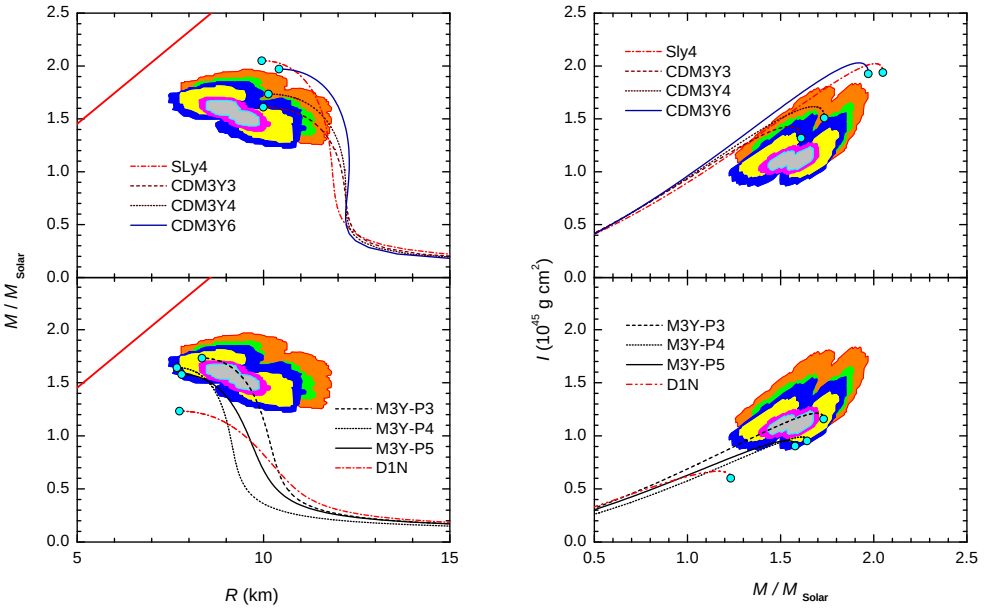

Figure 1.6: Neutron star gravitational mass versus its radius (left) and moment of inertia versus the mass (right) obtained with the EoS given by the stiff-type (upper panel) and soft-type (lower panel) in-medium nucleon nucleon interactions (Loan et al., 2011), in comparison with the empirical data (shaded contours) of the recent astronomical observation of neutron stars (Ozel et al., 2010). Circles are values calculated at the corresponding maximum central densities. Thick solid (red) line (left panels) is the limit allowed by the General Relativity (Glendenning, 2000).

Fig. 1.6 as the shaded contours. One can see that all mass-radius curves lie well below the limit allowed by the General Relativity (Glendenning, 2000) and go through or very closely nearby the empirical contours spanned by the data, excepting the curve given by D1N version of the Gogny interaction that lies well below the data. The maximum gravitational masses $M_{\rm G}$ given by the EoS under study are plotted in Fig. 1.6 as solid circles and they agree more or less with the recent data. While all the stiff-type interactions give the corresponding radius $R_{\rm G}$ quite close to the empirical range around 10 km, the $M_{\rm G}$ values given by the Sly4 and CDM3Y6 interactions are slightly higher than the observed masses, close to about twice the solar mass ($M_{\odot}$). We note, however, that the matter in the present study has been assumed to consist only of baryons, electrons and muons. At high baryon densities ($n_{\rm b} \gtrsim 3n_0$) the hyperons are expected to appear, and the maximum NS mass becomes then smaller (Lattimer and Prakash, 2004; Glendenning, 2000; Zdunik et al., 2004).

The equation of state relies indeed on the composition of dense matter in the star for which very scarce informations are available: where are localized the phase transitions between matter composed of neutrons, protons and electrons, and more massive hadrons such has hyperons? There is a global consensus that nuclear matter will convert to quark matter, but at which density? Does mesons (pions, kaons) condensation occur? Can phase transition in dense matter be observed in rotating neutron stars (Zdunik et al., 2007; Zdunik et al., 2008)? Several equations of state based on different assumptions on the matter constituents are represented in Fig. 1.7, where mainly two groups explore different path in the $M - R$ diagram: the one base on hadronic matter (black lines) and the group of quark matter (green lines) (Lattimer and Prakash, 2001).

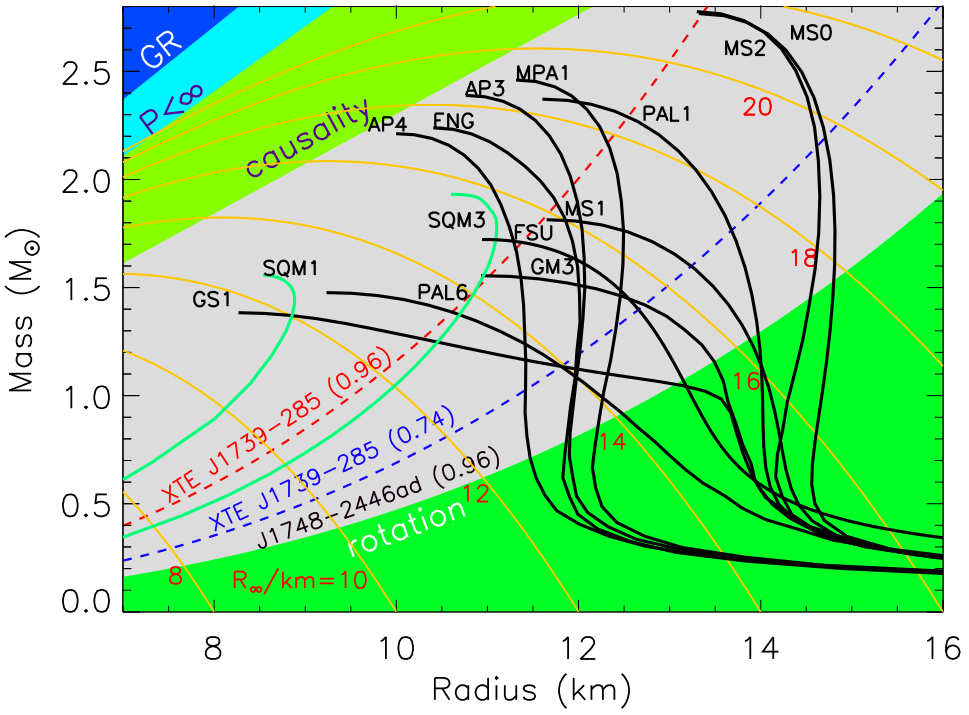

Figure 1.7: Mass-radius diagram. The three generic classes of equation of state are depicted with observational constraints. Mass-radius trajectories for typical EOS (see Lattimer 2001 for notation) are shown as black curves. Green curves (SQM1, SQM3) are self-bound quark stars. Orange lines are contours of radiation radius, $R_\infty = R/\sqrt{1-2GM/Rc^2}$. The dark blue region is excluded by the GR constraint $R > 2GM/c^2$, the light blue region is excluded by the finite pressure constraint $R > (9/4)GM/c^2$, and the green region is excluded by causality, $R > 2.9GM/c^2$. The light green region shows the region $R > R_{max}$ excluded by the 716 Hz pulsar J1748-2446ad (Hessels 2006). The upper red dashed curve is the corresponding rotational limit for the 1122 Hz X-ray source XTE J1739-285 (Kaaret 2007); the lower blue dashed curve is the rogorous causal limit using the coefficient 0.74 ms.

1.2.2 Gravitational waves: a new window into compact stars

Eagerly anticipated for over 30 years, a number of major European (GEO600 and VIRGO) and other (LIGO, TAMA) gravitational-wave observatories are now for the first time actually taking data (Abadie et al., 2010; Abadie et al., 2012). This is placing enormous pressure on the community to both study realistic sources of gravitational waves (Gourgoulhon and Haensel, 2003), and predict the signals they will produce in the detectors (Bonazzola and Gourgoulhon, 1999). Together, these gravitational wave observatories are expected to create a completely new window on the universe, providing information that is either difficult or impossible to obtain by traditional (electromagnetic waves, neutrinos) observations.

It is important to underline that a major interest in observing gravitational waves from compact stars comes from the possibility of learning more about the behavior of matter at very high densities (Marek et al., 2009), In particular, it is of great interest from the point of view of nuclear physics to understand how non-symmetric nuclear matter behaves and to constrain models for nucleon-nucleon interactions in dense matter which are at present rather poorly constrained by laboratory data. By analyzing oscillation

modes of compact stars and the gravitational waves which they produce, it is hoped to constrain these interaction models much more closely (Gourgoulhon, 2010). The study of gravitational waves produced by compact star oscillations as well by compact star merging can also give evidence for the conditions under which exotic particles and possible phase transitions may appear (Zdunik et al., 2000; Bejger et al., 2005). Obtaining evidence for the threshold density at which hyperons appear, or a QCD phase transition occurs would contribute greatly to improving understanding of nuclear interaction.

1.2.3 The life of neutron stars

With time neutron stars evolve and new phenomenons occur, such as cooling and Glitches. In the following we report on some of those phenomenons which are directly related to the properties of nuclear matter and in particular to pairing in neutron stars.

Neutron stars are fast rotating stellar objects and we know, from Earth laboratory experiments on helium 4 for instance, that a rotating super-fluid produces vortices. In the case of finite nuclei, surface effects forbid the formation of vortices (Migdal, 1959). In other words the rotational energy needed is too high and nuclei vaporize at lower energies. In the case of neutron stars, gravitational pressure maintains the nucleons together and vortices can be formed in the core as well as in the inner crust. Those vortices link together two layers of the star (core and crust) and impose a rigid rotation. As the neutron star release energy, the vortex must be destroyed from time to time and this is the possible origin of observed giant glitches (Pines and Alpar, 1985; Link, 1999). A giant glitch is a brutal variation of the rotation period of the star. One possible scenario which explains the existence of the glitches is that the neutron fluid forms vortices which can pin on the nuclear clusters in the crust (Donati and Pizzochero, 2004; Donati and Pizzochero, 2006). The unpinning would generate the angular momentum transfer from the core to the crust which is at the origin of the glitches. The pinning force depends on the neutron pairing gap in the crust (Pizzochero et al., 1997).

Cooling and giant glitches require accurate modelization of the pairing gap in the crust of neutron stars made of non-homogeneous matter. Most of the actual models are based on the Wigner-Seitz approximation (Negele and Vautherin, 1973). This allows straightforward application of the Hartree-Fock BCS or Hartree-Fock-Bogoliubov models built for the description of atomic nuclei. It has recently been shown that those models are valid if the density of states around the Fermi surface is averaged over few 100 keV by temperature effects or energy exchanged during reaction processes (Chamel et al., 2007). For temperature below few 100 keV, it is necessary to improve the modelization of the continuum states. For that, based on the ideas developed in condensed matter, first band theory type approaches have been built and represent certainly the new generation of models (Carter et al., 2005; Chamel, 2005; Chamel, 2006). It should be noted that the specific heat in the crust is also important in cooling modeling (Broglia et al., 1994; Pizzochero et al., 2002). It depends on the excitation spectrum which is different in the super-fluid phase than in the normal phase (Margueron and Sandulescu, 2012). Nevertheless, experimental probes of the pairing gap in nuclei are necessary but still very difficult. With respect to the importance of such knowledge, nuclear physics investigations should be pushed in this direction.

1.2.4 Core-collapse supernovae and microscopic modeling

Despite the crucial role played by hydrodynamics, however, the correct treatment of how microphysics comes into play in the models is one of the major challenges for compact stars (and specifically core-collapse supernovae) physics.

In particular, weak processes act in a crucial way throughout the collapse and the proto-neutron star formation. Electron capture on free protons and on exotic nuclei controls the neutronisation phase during

collapse, until the formation of an almost deleptonised central compact object, the neutron star. Neutrinos, produced thermally and in such weak processes, escape freely from the star in the first phase of collapse. The rising density increases their diffusion timescale and, for densities $\gtrsim 10^{12}$ g cm^{-3}, neutrinos become trapped, driving the system towards β equilibrium. After bounce, neutrinos are still trapped and diffuse outwards. Few hundreds of seconds after bounce, they carry out the energy gained in the collapse, contributing to the shock wave revival. We refer to the review by Bethe (Bethe, 1990) for a complete discussion of these phenomena and their relevance to supernova explosions.

Among the processes mediated by weak interaction, the electron capture is the main one acting during the infall phase. It determines the lepton fraction evolution and, as a consequence, the mass of the inner core. Indeed, at the onset of the collapse, the mass of the core is roughly the Chandrasekhar mass associated to the initial lepton fraction (i.e. the electron fraction at the beginning of the collapse) (Shapiro and Teukolsky, 1983): $M_i \approx M_{Ch}(Y_{l,i}) \sim 5.83 Y_{l,i}^2$. As the collapse proceeds, and before bounce, the density and the velocity profiles of the core obey a self-similar solution, and the mass of the homologous inner core can be determined from the value of the Chandrasekhar mass associated to the final (equilibrium) lepton fraction (Goldreich and Weber, 1980): $M_{hc} \approx M_{Ch}(Y_{l,f}) \sim 5.83 Y_{l,f}^2$. Therefore, a larger lepton fraction after trapping corresponds to a larger homologous core. The importance of the weak interaction rates and their effects in the supernova collapse dynamics have been demonstrated by different numerical simulations. In the pre-supernova stage, remarkable changes in the central electron fraction and entropy were noticed when using the shell model Monte Carlo rates (Langanke and Martinez-Pinedo, 2000) instead of the Fuller et al. (Fuller et al., 1980; Fuller, 1982; Fuller et al., 1982; Fuller et al., 1985) ones (Heger et al., 2001). Namely, the new rates result in higher (of about $0.01 - 0.015$) central values of the electron fraction at the onset of core-collapse, which in turn increases the Chandrasekhar mass, in lower (larger) core entropies for stars with $M \lesssim 20 M_\odot$ ($M \gtrsim 20 M_\odot$), and generally smaller iron core masses (the reduction was by about $0.05 M_\odot$ for progenitors with $M < 20 M_\odot$). In the collapse phase, the more recent rates calculated in the so-called hybrid model proposed by Langanke et al. (2001) have been included in the supernova simulations performed by the Oak Ridge and Garching collaboration and compared with the previous results employing the rates derived in Ref. (Bruenn, 1985). The outcome of the simulations has shown significant changes in the collapse trajectories and neutrino spectra (Hix et al., 2003; Janka et al., 2007; Langanke et al., 2003). Indeed, an increase of the electron capture in the denser regions and a reduced electron capture in the outer regions have been observed for the new rates, leading to a shift of the position of the shock formation inwards of about 16% in the core mass and to a 10% smaller velocity across the shock. Moreover, the parameter study of Ref. (Hix et al., 2005) shows that each increase of the rate of capture by a factor 10 corresponds roughly to the same decrease ($\sim 0.1 M_\odot$) of the mass of the homologous core.

1.3 Nuclei: a laboratory for neutron stars

Traditionally, the link between neutron stars and bulk nuclei properties is made via the *nuclear matter* concept: an ideal infinite system equally composed of interacting neutrons and protons where Coulomb interaction has been switched off. For instance, the central density of heavy nuclei is very close to the equilibrium density of nuclear matter, called the saturation density ρ_0. Moreover, the *nuclear matter* concept can be extended to isospin asymmetries. Asymmetric nuclear matter model is then rather similar to the nuclear matter found in neutron stars.

On the experimental side, investigations on the atomic nuclei properties, related for instance to the measurement of the giant monopole resonance or to the symmetry energy, allow to probe the equation of state around the saturation density. Heavy ion collisions, hot giant resonances, exotic nuclei properties,

hypernuclei, attempt to explore more extreme regions of the phase diagram. However the improvement of EoS at lower and higher densities than the saturation density ρ_0 and for strong isospin asymmetries is still required (Fig. 1.7). In the latter case, the density dependence of the symmetry energy is a crucial information to get the EoS in asymmetric matter. The symmetry energy therefore plays a central role in determining the structure and the evolution (cooling) of the stars. The future facilities producing exotic nuclei will allow to test this isospin dependency for values of the asymmetry parameter, $I = (N - Z)/(N + Z)$, larger than 0.2. This asymmetry is smaller than the asymmetry in neutron star, but may provide at least additional constraints for the theoretical models.

Recently, more direct relations between neutron rich nuclei and neutron star matter have been proposed (Brown, 2000; Typel and Baur, 2001; Steiner et al., 2005; Sagawa et al., 2007b; Xu et al., 2009; Warda et al., 2009; Centelles et al., 2009; Vidaña et al., 2009). For instance, the neutron skin thickness nuclei has been linked to the pressure of pure neutron matter at sub-nuclear densities and consequently to the neutron star radius (Brown, 2000; Typel and Baur, 2001; Steiner et al., 2005). Indeed, the pressure is related to the derivative of the symmetry energy and the neutron skin thickness of nuclei is an observable that yields some information about low-density neutron-rich matter and, in particular, about the density dependence of the symmetry energy (Steiner et al., 2005; Centelles et al., 2009; Vidaña et al., 2009). In neutron stars, this question is essential: the density dependence of the symmetry energy determines the proton fraction and the threshold density at which direct URCA process occurs, as discussed in previous section. Moreover, it governs the threshold densities of other particles such as hyperons, pions, kaons, quark, etc., which trigger phase transitions and cooling processes. Correlation analysis should however be performed with caution since the question of model independence is crucial.

In a recent analysis, we have shown that the correlation between the pressure on the edge of neutron stars and the slope of the symmetry energy was questionable (Ducoin et al., 2010) and we have shown that the correlation that exist is multidimensional (Ducoin et al., 2011). More details are presented in section 6.3. This example illustrates that articulations can be drawn in which nuclear physics experiments could bring useful constraints. The perspectives offered by the next-generation of radioactive beam facilities are in this sense very attractive. Identifying the experimental methods and choosing the relevant observables for the future exotic beam facilities is a strong challenge and requires an important interplay between experimental and theoretical fields. In this manuscript, we give different examples illustrating the links between nuclei and the astrophysics of dense matter. In chapter 6, close relations between neutron star physics and properties of nuclei are presented.

1.4 The menu set

In this habilitation, I decided to select the part of my activities in theoretical nuclear physics that mainly concerns astrophysics and the properties of dense matter. Several contributions are left apart, such as the modeling of breakup-up mechanisms with halo nuclei since the relation of this studies with compact stars is not direct (Margueron et al., 2002a; Margueron et al., 2003a; Margueron et al., 2004a; Margueron and Chomaz, 2005), as well as my studies of response functions in dense matter and neutrino mean free path since it was a continuation of the work I have performed during my PhD thesis (Margueron et al., 2003b; Margueron et al., 2003c; Boek et al., 2005; Margueron et al., 2005; Margueron et al., 2006). This manuscript does not contain my studies relating the unstable RPA modes to the cluster properties at sub-saturation densities and the link with heavy-ion collision within the spinodal decomposition (Margueron and Chomaz, 2003; Chomaz, 2003; Margueron et al., 2004b; Baran and Margueron, 2006; Ducoin et al., 2008). It is a poor way, I agree, to keep the size of this document moderate. In this review of my research activities, I have however selected a number of topics which are gathered together in the following chapters.

In chapter 2, I present various analysis and extensions of present models for the nuclear interaction. The spin channel of the Skyrme interaction is complemented by a new term which correct the ferromagnetic instability in dense matter. It is shown that the new term have very moderated effects in odd nuclei, and therefore does not modify the ground states of nuclei where most of the phenomenological interactions are adjusted. It is however shown that the excited collective states can be changed by the new term and its effect in the propagation of neutrino in core collapse supernovae is evaluated. Then, I present some analysis of the low-momentum interaction $V_{\rm lowk}$ with respect to its separability. Such an interaction can be incorporated in a Skyrme-like model where the finite range terms of the original Skyrme interaction are replaced by the $V_{\rm lowk}$ matrix elements. Application in nuclei of the separable form is shown to provide a good comparison to the observed masses and radii. Finally, the low-density properties of an ab-initio calculation, the Dirac-Brueckner-Hartree-Fock approach, are analyzed. It is shown a systematic deviation between the ab-initio approach and the mean field models at low density attributed to the strong two-body correlations that are not present in usual mean field models.

In chapter 3, a recent improvement of the pairing interaction in dense medium is presented. The new pairing interaction is obtained with the constraint to reproduce the feature of more microscopic calculations in symmetric and neutron matter. Properties of the Cooper pair obtained with such interaction is studied and the analysis is performed within the BCS/BEC crossover. The relations between the pairing interaction and finite nuclei are explored, both from the effect of pairing on empirical quantities such as the incompressibility modulus or the symmetry energy, or in reaction mechanism such a two-neutron pair transfer.

In chapter 4, the concept of in-medium effective mass in discussed and the effect of the temperature dependence of the effective mass on the dynamics of core collapse supernova is presented. Since a non-negligible effect has been found, we propose a more microscopic model based on energy density functional with surface-peaked effective mass, temperature dependent, that could be employed in the calculation of the EoS for supernovae.

In chapter 5, recent calculations for the crust of cold catalyzed neutron stars including state-of-the-art model to describe pairing in non-uniform matter are presented as well as the impact of the new calculations in the thermal relaxation of neutron stars.

Finally, in chapter 6, close relations between nuclear physics experiments and neutron stars are shown. The continuum coupling in superfluid nuclear systems close to the drip-line is analyzed and is shown to be very important for the superfluid properties of overflowing Wigner-Seitz cells in the crust of neutron stars. In a second part of this chapter, the relation between the symmetry energy and neutron stars is illustrated in some cases. The correlations between the pressure at the edge of neutrons stars and empirical quantities of the liquid drop model are analyzed. The effect of the symmetry energy on the stiffness of the EoS and on neutron stars properties are also analyzed.

Eventually, conclusions and outlooks for the future are presented in the final chapter of this habilitation.

Chapter 2

Modeling the in-medium nucleon-nucleon interaction

The evaluation of bulk properties of finite nuclei and nuclear matter starting from realistic models of nucleon-nucleon (NN) interaction is a major challenge in modern nuclear physics. Since the exact form of the interaction resulted from the underlying theory of the strong interaction, the QCD theory, remains unknown, one usually has deal with effective models for the nucleon-nucleon interaction. These models are however not always adapted for extrapolations towards extreme conditions in astrophysics and in this chapter, several extensions of effective models and applications in nuclei and in astrophysics are presented.

2.1 Introduction

The models employed to make predictions for the nuclear equation of state (EOS) and can roughly be divided into three classes: the ab-initio approaches, the Effective Field Theory (EFT) approaches and phenomenological density functionals.

Ab-initio approaches are based on high precision free space nucleon-nucleon interactions which fit experimental data for free nucleon-nucleon scattering up to the threshold for pion production and properties of the deuteron (Machleidt et al., 1996; Entem and Machleidt, 2003). It was done by obtaining a best fit for a large number of adjustable parameters using several thousands experimental points so that there exists several quite different potential models commonly used. A general feature of such realistic interactions is strong short-range and tensor components, which cannot be handled within the standard perturbation theory. There have been suggested different approaches in order to overcome this problem: variational calculations (Pandharipande and Wiringa, 1979; Akmal et al., 1998), Bethe-Brueckner-Goldstone expansion (Jaminon and Mahaux, 1989; Baldo, 1999; Zuo et al., 2002; Baldo et al., 2007) or relativistic Dirac-Brueckner-Hartree-Fock (DBHF) (ter Haar and Malfliet, 1987; Brockmann and Machleidt, 1990; De Jong and Lenske, 1998; Gross-Boelting et al., 1999; Fuchs, 2004; Van Dalen et al., 2004), correlated basis functions (Feenberg, 1969), Quantum Monte Carlo (Wiringa et al., 2000; Carlson et al., 2003), Diffusion Monte Carlo (Fabrocini et al., 2005), Self-Consistent Green's function theory (see, e.g., Ref. (Dickhoff and Barbieri, 2004; Dickhoff and Van Neck, 2005)). Non-relativistic ab-initio calculations do not meet the empirical region of saturation, but align on the Coester line, whereas relativistic calculations do a better job. This deficiency can be solved by the explicit inclusion of three-body forces where the relativistic approach accounts already effectively for part of these contributions. For a more detailed discussion see e.g. Ref. (Baldo et al., 2007). These methods were successfully applied to describe bulk properties of nuclear matter (Gögelein

et al., 2009), pairing gap of nucleons (Fabrocini et al., 2008), weak response and shear viscosity of nuclear matter (Benhar and Farina, 2009).

The Effective Field Theory (EFT) approaches are based on a perturbative expansion of the nucleon-nucleon interaction within power counting schemes (see (Machleidt and Entem, 2011) and refs. inside). These approaches lead to a more systematic expansion of the EOS in powers of density, respectively the Fermi momentum k_F. The EFT approaches can be based on density functional theory (Serot and Walecka, 1997b; Furnstahl, 2004) or e.g. on chiral perturbation theory (Lutz et al., 2000; Finelli et al., 2003; Finelli et al., 2004). The advantage of EFT is the small number of free parameters and a correspondingly higher predictive power. However, when high precision fits are intended, the EFT functionals are based on approximately the same number of model parameters as phenomenological density functionals.

However ab-initio or EFT approaches remain very complex to be applied directly to a description of finite nuclei, as well as inhomogeneous nuclear matter which exists in the inner crust of neutron stars. Alternatively, they have been combined either to phenomenological approaches through a local density approximation (Baldo et al., 2004a), or as an input for a density functional approach (Baldo et al., 2008). In these approaches, adjustable parameters need however to be determined. Besides the interactions derived from the ab-initio and the EFT approach, various phenomenological models have been developed, such as the Skyrme contact interaction (Skyrme, 1959; Reinhard et al., 2004) or the Gogny finite range interaction (Farine and Schuck, 1999; Bender et al., 2003), or Relativistic Mean Field (RMF) models (Serot and Walecka, 1986). The phenomenological models are adjusted to describe the experimental data for the ground states of finite nuclei and the empirical saturation point of symmetric nuclear matter. A simple parameterization of such phenomenological forces through the local single-particle densities allows a simple solution of the Hartree-Fock (HF) equations (Vautherin and Brink, 1972). Finally, these models have been successfully used for predictions of equations of state (EoS) of nuclear matter and description of pasta phase within the Wigner-Seitz (WS) cell approximation (Negele and Vautherin, 1973). In neutron stars, these models are extrapolated far from the condition where it has been adjusted and might in some cases become unstable (Margueron et al., 2002b). The instabilities of these models could however be corrected such as it reproduces the features of a G-matrix in nuclear matter (Margueron and Sagawa, 2009). An extension of the Skyrme interaction is therefore presented in section 2.2.

A new semi-empirical interaction is based on low-momentum interaction $V_{\text{low-k}}$ and allows us to perform Hartree-Fock calculations similarly to the phenomenological forces (Montani et al., 2004; Van Dalen et al., 2009). The basic idea of $V_{\text{low-k}}$ is to separate the predictions for correlations at low momenta, which are constrained by the NN scattering matrix below the pion threshold, from the high-momentum components, which may strongly depend on the underlying model of realistic NN interaction. By introducing a cutoff Λ in momentum space, one separates the Hilbert space into a low-momentum and a high-momentum part. The renormalization technique (see, e.g., (Bogner et al., 2001; Lee and Suzuki, 1980; Okubo, 1954; Bogner et al., 2007; Suzuki, 1982)) determines an effective Hamiltonian, which must be diagonalized within the model space (below the cutoff). With the cutoff in the range of Λ = 2 fm^{-1} $V_{\text{low-k}}$ becomes model independent, , i.e., is independent on the underlying realistic interaction $\hat{v}_{12}$, and reproduces the deuteron binding energy, low-energy phase shifts, and half-on-shell T matrix with the same accuracy as the initial realistic interaction as, e.g., the CD-Bonn (Machleidt et al., 1996) or Argonne V18 (Wiringa et al., 1995) potentials. This model independence demonstrates that the low-momentum physics does not depend on details of the high-momentum dynamics. In spite of its obvious advantages $V_{\text{low-k}}$ potential still remains a quite complicated object. In section 2.3 it is shown that $V_{\text{low-k}}$ potential can be simply represented by a low rank separable interaction that facilitate its use in the HF models for nuclei.

How does nuclear matter properties change when the density decreases from saturation densities ? In this low density regime, what is the role of the isospin asymmetry ? Indeed, the nuclear density functional

below saturation density has not been much studied while it has an importance for several topics concerning atomic nuclei surface properties, the equation of state of the core of neutron stars and for the dynamical description of heavy ion collision, both at intermediate and relativistic energies. Recently, several attempts have tried to establish a relation between the low density equation of state and the nuclear properties like surface behavior and pairing properties (Baldo et al., 2004b; Sedrakian et al., 2006; Sedrakian et al., 2003; Gögelein and Müther, 2007), neutron radii (Brown, 2000) or the spinodal instability (Baran and Margueron, 2006). Those works are based on phenomenological density functionals or fits of ab-initio calculations but without considering the very low properties of the equation of state. In dilute nuclear matter, effects of two-body correlations are important and induce clustering phenomena like the formation of deuteron, tritium, helium and alpha particle (Horowitz and Schwenk, 2006a; Tohsaki et al., 2001; Beyer et al., 2000). In the section 2.4, a comparison of different ab-initio and phenomenological approaches below saturation density is performed and the systematic deviations between these approaches is analyzed.

2.2 Spin and spin-isospin channels of the Skyrme interaction

Due to its very simple functional form, the standard Skyrme interaction is not suited for being extrapolated in astrophysical situation such as neutron stars. Various modifications and extensions of the Skyrme interaction have been proposed for different reasons, such as the description of asymmetric matter (see the discussion in Ref. (Chabanat et al., 1997) and references therein), the effective mass splitting and the high density behavior of the equation of state (Lesinski et al., 2006), or the improvement of the level density around the Fermi energy (see Refs. (Waroquier et al., 1983; Liu et al., 1991b; Liu et al., 1991a; Farine et al., 2001) and references therein). The last point will be further discussed in the chapter 4 in connexion also to the needs for core-collapse supernovae.

A recent extensive study of the symmetry energy deduced from Skyrme interactions (Rikovska Stone et al., 2003) has confirmed that the symmetry energy becomes negative beyond the saturation density of nuclear matter for many of these interactions. This is related to the instability of the mean field with respect to the isospin density fluctuation $\delta\rho_t$ where $\rho_t = \rho_n - \rho_p$. Depending on the parameters of the interaction, instabilities can occurs in different channels, at various densities and at different isospins. It has been shown that there is a limited interval of densities between ρ_0 and $3\rho_0$ for which the mean field is stable in symmetric matter and also in neutron matter (Margueron et al., 2002b). The stability of the ground state toward small fluctuations can be studied within the HF+RPA framework. The fluctuations around the mean field are induced by the particle-hole interaction,

$$V_{\rm ph} = \frac{1}{N_0}\sum_\ell (F_\ell + F'_\ell \tau_1\cdot\tau_2 + G_\ell \sigma_1\cdot\sigma_2 + G'_\ell(\tau_1\cdot\tau_2)(\sigma_1\cdot\sigma_2))P_l(\cos\theta)\ , \tag{2.1}$$

in terms of the dimensionless Landau parameters F_ℓ, F'_ℓ, G_ℓ, G'_ℓ and Legendre Polynomials $P_l(\cos\theta)$. $N_0 = gm^*k_F/(2\pi^2\hbar^2)$ is the density of state around the Fermi energy and g is the degeneracy. The matter is stable unless one of these parameters of multipolarity ℓ becomes lower than $-2\ell-1$.

Recently, the ferromagnetic instability has regained interest (Haensel and Bonazzola, 1996; Bhattacharya and Soni, 2007) due to the observation of extremely high magnetic fields ($\sim 10^{15-16}$ G) in compact stars (Thompson and Duncan, 1995) and also of giant flares observed recently on 27 December 2004 (Lazzati, 2005). In Fig. 2.1 is shown the region of ferromagnetic instability predicted by various Skyrme interactions for different proton fractions. The curves delimitate the region of spin-stable matter (on the left of the curve) from that of spin-unstable matter (on the right). The onset densities at which the ferromagnetic instability occurs is rather low, going from almost ρ_0 for some interactions up to $3-4\rho_0$ for other interactions. Since the onset density is of the order of the densities in the core of neutron stars, the ferromagnetic instability predicted by Skyrme interactions could give a sound basis to the the observed

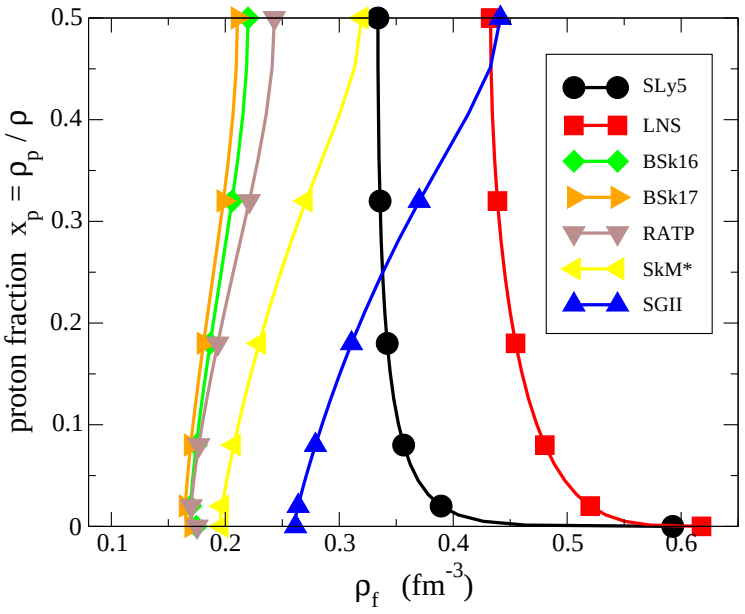

Figure 2.1: Ferromagnetic phase diagram for various effective Skyrme interactions. The horizontal axis shows the critical density $\rho_{\rm f}$ at which the asymmetric matter becomes unstable, while the vertical axis shows the proton fraction $x_p = \rho_p/\rho$. The matter is spin symmetric for smaller density than $\rho_{\rm f}$, while it becomes ferromagnetic for larger density than $\rho_{\rm f}$. See the text for details.

strong magnetic field (Haensel and Bonazzola, 1996). However, according to microscopic calculations with realistic interactions such as diffusion Monte-Carlo (Fantoni et al., 2001) or Brueckner Hartree-Fock calculations (Polls et al., 2002; Vidaña and Bombaci, 2002; Bombaci et al., 2006), there is no ferromagnetic instability up to substantially high densities. The onset of the ferromagnetic instability beyond a few times ρ_0 represents therefore a serious limitation of the Skyrme interaction (Chamel and Goriely, 2010).

In this section, we discuss an extension of the Skyrme interaction that prevent the onset of the spin instability in symmetric and neutron matter. It was shown that within the standard Skyrme interaction, the removal of the spin instability by fixing the appropriate parameters makes symmetric matter unstable at high density (Waroquier et al., 1979b; Waroquier et al., 1979a). Before our work, there were no satisfactory improvement of the Skyrme interaction which prevent the matter to fall into spin instabilities. The main purpose of our work is to improve the spin dependent parts of Skyrme interactions keeping its simplicity and good properties for ground state properties. In this way, we will be able to extend the field of possible applications of Skyrme interactions for spin dependent excitations not only in finite nuclei but also infinite nuclei within the self-consistent theoretical model.

2.2.1 Additional terms in the spin channels

From the analysis of the density dependence of the Landau parameters, it is clear that the standard Skyrme interactions are not repulsive enough in the spin channel, and most probably also in the isospin channel at higher density than the saturation density (Margueron et al., 2009). The repulsion shall come from the effect of the three body force (Zuo et al., 2003) or higher, which are mimic by the density dependent terms in the nuclear interaction (Negele and Vautherin, 1972). The most important contribution comes from the scalar-density and it is the only density which has been considered so far (Vautherin and Brink, 1972). However, spin, isospin and spin-isospin density dependent terms shall also be considered from the density

matrix expansion (Negele and Vautherin, 1972). The density matrix could indeed be decomposed as,

$$\begin{aligned}\rho(ij) &= \frac{1}{4}\rho_0(ij)\delta_{\sigma_i\sigma_j}\delta_{\tau_i\tau_j} + \frac{1}{4}\rho_1(ij)\delta_{\sigma_i\sigma_j}\langle\tau_i|\tau|\tau_j\rangle + \frac{1}{4}s_0(ij)\langle\sigma_i|\sigma|\sigma_j\rangle\delta_{\tau_i\tau_j} \\ &\quad + \frac{1}{4}s_1(ij)\langle\sigma_i|\sigma|\sigma_j\rangle\langle\tau_i|\tau|\tau_j\rangle, \end{aligned} \tag{2.2}$$

where σ and τ are the Pauli matrices for the spin and isospin.

Here, we study the impact of the new density dependent terms such as the spin and spin-isospin densities. As described in Ref. (Margueron et al., 2009), the new spin-density dependent terms added to the conventional Skyrme force are of the following form:

$$V^{\rm s,st}(\mathbf{r}_1,\mathbf{r}_2) = \frac{1}{6}t_3^s(1+x_3^sP_\sigma)[\rho_s(\mathbf{R})]^{\gamma_s}\delta(\mathbf{r}) + \frac{1}{6}t_3^{st}(1+x_3^{st}P_\sigma)[\rho_{st}(\mathbf{R})]^{\gamma_{st}}\delta(\mathbf{r}) \tag{2.3}$$

where $P_\sigma = (1+\sigma_1\cdot\sigma_2)/2$ is the spin-exchange operator, $\mathbf{r} = \mathbf{r}_1 - \mathbf{r}_2$ and $\mathbf{R} = (\mathbf{r}_1+\mathbf{r}_2)/2$. In Eq. (2.3), we have introduced the spin-density $\rho_s \equiv \rho_\uparrow - \rho_\downarrow$ and the spin-isospin-density $\rho_{st} \equiv \rho_{n\uparrow} - \rho_{n\downarrow} - \rho_{p\uparrow} + \rho_{p\downarrow}$. Spin symmetry is satisfied if the power of the density-dependent terms γ_s and γ_{st} is even.

The new density energy $\mathcal{H}(r)$ is now expressed as $\mathcal{H}(r) = \mathcal{H}^{std}(r) + \mathcal{H}_3^{s+st}(r)$, where $\mathcal{H}^{std}(r)$ is the standard Skyrme density energy and $\mathcal{H}_3^{s+st}(r)$ is the additional term induced by (2.3).

In the following, we express $\mathcal{H}_3^{s+st}(r) = \mathcal{H}_3^{s}(r) + \mathcal{H}_3^{st}(r)$ in different notations. In the notation of Ref. (Chabanat et al., 1997), we have

$$\mathcal{H}_3^s = \frac{t_3^s}{12}\rho_s^{\gamma_s}\Big[(1+\frac{x_3^s}{2})\rho^2 + \frac{x_3^s}{2}\rho_s^2 - (x_3^s+\frac{1}{2})(\rho_n^2+\rho_p^2) - \frac{1}{2}(\rho_{sn}^2+\rho_{sp}^2)\Big], \tag{2.4}$$

$$\mathcal{H}_3^{st} = \frac{t_3^{st}}{12}\rho_{st}^{\gamma_{st}}\Big[(1+\frac{x_3^{st}}{2})\rho^2 + \frac{x_3^{st}}{2}\rho_s^2 - (x_3^{st}+\frac{1}{2})(\rho_n^2+\rho_p^2) - \frac{1}{2}(\rho_{sn}^2+\rho_{sp}^2)\Big], \tag{2.5}$$

with $\rho_{sn} = \rho_{n\uparrow} - \rho_{n\downarrow}$ and $\rho_{sp} = \rho_{p\uparrow} - \rho_{p\downarrow}$.

In the DFT notations (Bender et al., 2003), we have

$$\mathcal{H}_3^{s+st} = \sum_{T\neq T'=0}^{1}\left(C_T^{s\rho}s_T^2\rho_T^2 + C_T^{ss}s_T^4 + C_{TT'}^{s\rho}s_T^2\rho_{T'}^2 + C_{TT'}^{ss}s_T^2s_{T'}^2\right), \tag{2.6}$$

with the parameters: $C_0^{s\rho} = t_3^s/16$, $C_1^{s\rho} = -t_3^{st}(2x_3^{st}+1)/48$, $C_0^{ss} = t_3^s(2x_3^s-1)/48$, $C_1^{ss} = -t_3^{st}/48$, $C_{01}^{s\rho} = -t_3^s(2x_3^s+1)/48$, $C_{10}^{s\rho} = t_3^{st}/48$, $C_{01}^{ss} = -t_3^s/48$, $C_{10}^{ss} = -t_3^{st}(2x_3^{st}11)/48$.

The additional term $\mathcal{H}_3^{s+st}$ contribute to the time-even mean field

$$U_q^{\rm s,st} = \frac{t_3^s}{12}\rho_s^{\gamma_s}\Big[(2+x_3^s)\rho - (1+2x_3^s)\rho_q\Big] + \frac{t_3^{st}}{12}\rho_{st}^{\gamma_{st}}\Big[(2+x_3^{st})\rho - (1+2x_3^{st})\rho_q\Big]. \tag{2.7}$$

while in the following the time-odd component of the mean field in neglected. While $\gamma_s = \gamma_{st} = 2$ is imposed by spin symmetry, the additional parameters t_3^s, x_3^s, t_3^{st} and x_3^{st} in Eq. (2.3) have to be determined.

We have investigated two methods to adjust the parameters. The first one is the more natural one and consists in performing a large scale adjustment on the mass and radii of even and odd nuclei, in the spirit of the Brussels-Montréal group adjustement (Margueron and Sagawa, 2009). The strategy of the mass fit is described in Ref. (Goriely et al., 2009; Chamel et al., 2008; Margueron and Sagawa, 2009). The second method is based on the remark that the contribution to the mean field (2.7) is zero in even-even nuclei. Since most of the Skyrme interactions are adjusted on (few) even-even nuclei, it is thus possible to add for these interactions the new terms (2.3) in a perturbative manner. The new parameters are therefore adjusted to reproduce the Landau parameters extracted from a G-matrix calculation in uniform matter (Margueron et al., 2009).

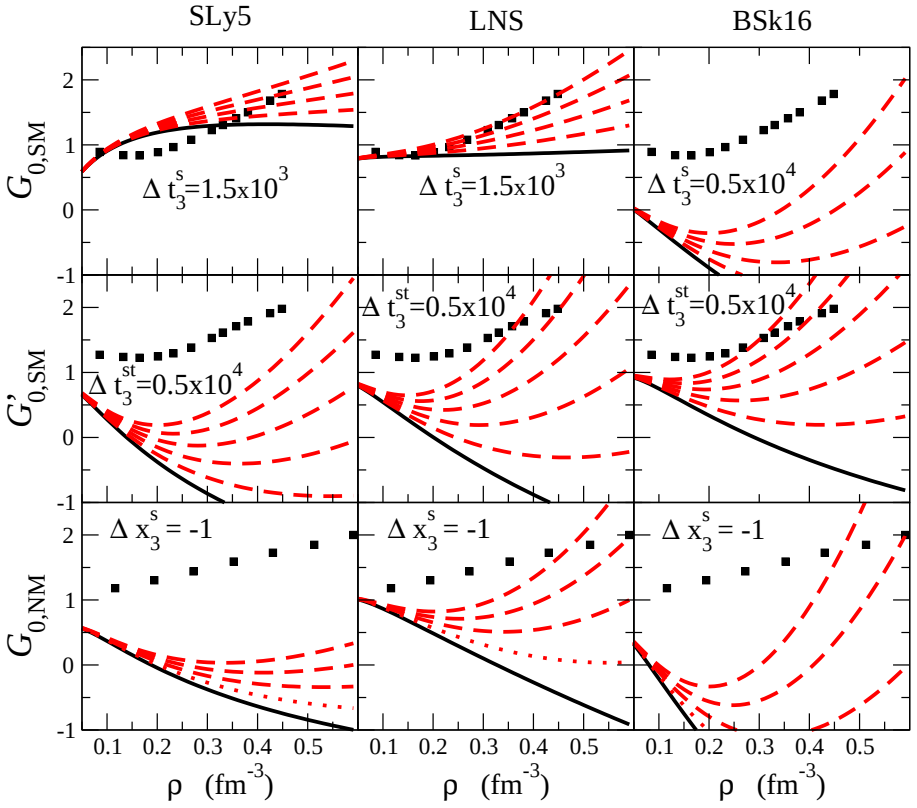

Figure 2.2: Landau parameters for spin and spin-isospin channels G_0 and G'_0 in symmetric nuclear matter and neutron matter. The solid curves are the original ones, while the filled squares are obtained by the Brueckner HF calculations using 2BF+3BF (Zuo et al., 2003). The dashed curves correspond to different values of the parameters t_3^s, t_3^{st} and x_3^s. The parameters are changed from bottom to top multiplying integers (1,2,3,-) by the mesh size given in each window. The Landau parameter $G_{0,\mathrm{NM}}$ is calculated with the optimal value for t_3^s in Tab.2 of Ref. (Margueron and Sagawa, 2009), which reproduces best the Brueckner HF $G_{0,\mathrm{SM}}$ values. The thin dotted lines in the bottom panels correspond to the results with x_3^s=0.

We show in Fig. 2.2 the contributions of the new terms for the Landau parameters G_0 and G'_0 in symmetric matter and for G_0 in neutron matter added to the three effective interactions SLy5, LNS and BSk16. The dashed lines correspond to different values of the new parameters t_3^s, t_3^{st} and x_3^s with the step indicated in each graph. The expression for the Landau parameters are given in Ref. (Margueron and Sagawa, 2009). It is confirmed that for the values of the parameters taken in Fig. 2.2 the new terms are repulsive enough to remove the spin instabilities. There are however still differences between the corrected Landau parameters and the ones given by the G-matrix. Notice that the LNS interaction, fitted originally to the equation of state deduced from the G-matrix, gives the best fitted Landau parameters among the three interactions. Finally, it could be noticed that the corrected Landau parameters G'_0 are increased by about +0.3 which makes it closer to the empirical value. The empirical value is indeed estimated to be 1.3$\pm$0.2 from Wood-Saxon single-particle states plus one-pion and rho meson models (see for instance Tab.I of Ref. (Osterfeld, 1992) and references therein and also Ref. (Suzuki and Sakai, 1999)) and $\sim$0.6 from self-consistent Skyrme mean-field models (Fracasso and Colò, 2007) (see Ref. (Margueron and Sagawa, 2009) for a more detailed discussion).

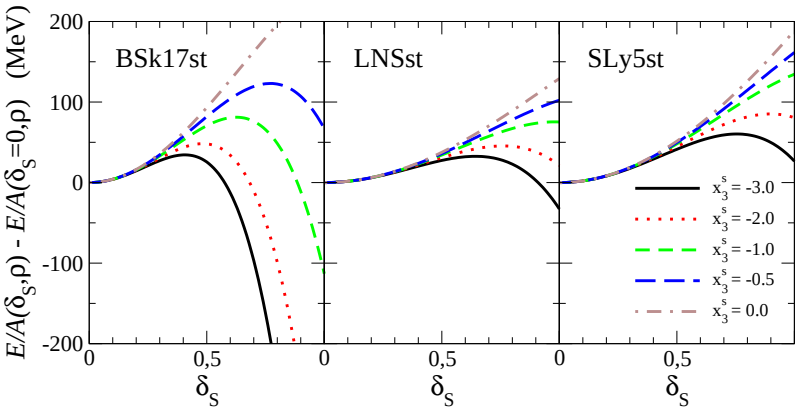

Figure 2.3: Difference between the binding energies $E/A(\delta_S, \rho) - E/A(\delta_S = 0, \rho)$ in symmetric matter for BSk17st, LNSst and SLy5st Skyrme interactions as a function of the spin polarizations and for $\rho = 0.6$ fm^{-3}. A different value from 0.0 to -3.0 for the parameter x_3^s is adopted for each line.

2.2.2 Ground state of infinite nuclear matter

As shown in Fig. 2.2, with the new terms, the Landau parameters G_0 and G_0' remains larger than -1 at all densities for SLy5st, LNSst and the BSk17st forces (Margueron and Sagawa, 2009). However, it has not been checked that the absolute ground state is really that of non-polarized matter. It shall indeed be checked that a lower minimum does not exist for matter with a non-zero polarizability. To do so, we compare in the following the energy for different spin-polarizations with that for non-polarized matter. This is done in the following for both symmetric nuclear matter and neutron matter

Symmetric matter

In Fig. 2.3 is represented the binding energies difference $E/A(\delta_S, \rho) - E/A(\delta_S = 0, \rho)$ as a function of the polarization $\delta_S = (\rho_\uparrow - \rho_\downarrow)/\rho$ for the three modified Skyrme interactions BSk17st, LNSst and SLy5st. We have fixed the density to a large value $\rho = 0.6$ fm^{-3}, the highest value where the nuclear Skyrme interaction is applied, and we have changed the values of the parameter x_3^s as indicated in the legend of Fig. 2.3. For values of the parameter x_3^s=-3 the ground state of nuclear matter is fully polarized ($\delta_S = 1$) for the interactions BSk17st and LNSst. Increasing the value of the parameter x_3^s from -3 to 0, the binding energy of fully polarized matter is going up in Fig. 2.3. There is then a critical value above which non-polarized matter is the ground-state of nuclear matter. As expected, the energy of non-polarized matter is convex around $\delta_S = 0$, but there is a change of convexity for large values of $\delta_S \sim 0.8$. We have indeed observed a large influence of the parameter x_3^s on the binding energy of fully polarized matter.

One could obtain an estimate of this critical value by analyzing the contribution of the new spin-density terms (2.3) in spin-polarized symmetric matter. It reads

$$\mathcal{H}_3^s(sym.) = \frac{t_3^s}{16}\rho^2\rho_s^{\gamma_s}\left[1 + \frac{2x_3^s - 1}{3}\delta_S^2\right], \tag{2.8}$$

and $\mathcal{H}_3^{st}(sym.) = 0$ since $\rho_{st} = 0$. The term (2.8) is zero for the spin-symmetric matter with $\rho_s = 0$ and is always positive for $\delta_S = 1$ if one chooses $x_3^s > -1$. It is thus clear that one necessary condition for the spin-symmetric matter to be the absolute ground state at all densities is $x_3^s > -1$. This is the case for the adopted value of $x_3^s = -0.5$ for BSk17st. Nevertheless, as shown in Fig. 2.3 for instance for SLy5st, the stability of spin-symmetric matter could be obtained even if $x_3^s < -1$ at the density ρ=0.6 fm^{-3}. The reason for the robustment of the SLy5st interaction is given in the next subsection (Neutron matter).

We remind that from the analysis of the Landau parameters the stability around spin-symmetric matter requires that $x_3^s < 1$ (see Eq. (11) of Ref. (Margueron et al., 2009)). As a conclusion, one could adjust the parameter x_3^s inside the range $-1 \lesssim x_3^s < 1$.

Neutron matter

The case of pure neutron matter is somehow very peculiar. The correction due to the spin-density dependent terms reads

$$\mathcal{H}_3^s(neut.) = \frac{t_3^s}{24}\rho^2\rho_s^{\gamma_s}(1-x_3^s)\Big[1-\delta_S^2\Big]. \tag{2.9}$$

It is then clear that the correction is zero for $\delta_S = 0$ and also for $\delta_S = 1$. This property is related to the anti-symmetrization of the interacting nucleons. Indeed, in fully polarized neutron matter, the quantum numbers for spin and isospin are $S = 1$ and $T = 1$ while the new spin-density dependent interaction (2.3) act in the $L = 0$ channel. The new spin-density dependent interaction (2.3) have thus no effect at all in the purely spin-polarized neutron matter. Only odd L terms in the interaction could play a role in the fully polarized neutron matter. This property has in fact been used in the Ref. (Kutschera and Wójcik, 1994) to provide a necessary condition to remove the spin instabilities and lead to the condition $-5/4 < x_2 < -1$. This condition has been used in the fitting procedure of SLy5 (Chabanat et al., 1998a) and it explains the robustness of the spin-symmetric ground state for this interaction. However if more flexibility in the Skyrme parameters is necessary, it might be interesting to introduce an interaction of the following form

$$t_5^s(1+x_5^sP_\sigma)\ \mathbf{k}'\rho_s(\mathbf{R})\cdot\delta(\mathbf{r})\mathbf{k}\ . \tag{2.10}$$

This $\ell = 1$ term will not contribute to spin-symmetric matter and could be adjusted to fit the energy of fully polarized matter obtained from more microscopic calculations. For simplicity, we have however not introduced this term in our new spin-dependent interaction.

2.2.3 Ground state of odd-nuclei: the weak effect of the new spin-terms using the one-spin polarized approximation (OSPA)

The new interaction (2.3) could only change the properties of odd nuclei in their ground states and the collective spin-excitations for all nuclei. In this subsection, we mainly study the effects of the new spin-terms on the ground state of odd nuclei. The effects on the RPA dynamical response function are analyzed in subsection 2.2.4.

To provide an approximate maximal estimate of the effects while keeping our model simple, we introduce the one-spin polarized approximation (OSPA) to treat odd nuclei. In this approximation, we use the equal filling approximation, so that the time-reversal symmetry is not broken, but with an additional ansatz. As within this scheme the spin-densities would be by definition equal to zero, when constructing the spin-densities with the wave function of the odd nucleon, we assume that the spin-up state is completely filled while the spin-down state is empty between the two possible spin orientations (or, equivalently, the opposite). We call this procedure for the construction of spin-densities the *one-spin polarized approximation* (OSPA). The OSPA gives an upper value of the contribution of the new terms. According to the OSPA, we define the densities $\rho_s(r)$ and $\rho_{st}(r)$ in odd nuclei as

$$\rho_s(r) = \frac{1}{4\pi r^2}\sum_i \varphi_i^2(r)m_s(i)\ , \tag{2.11}$$

$$\rho_{st}(r) = \frac{1}{4\pi r^2}\sum_i \varphi_i^2(r)m_s(i)m_t(i), \tag{2.12}$$

Nucleus	$E_{\rm TOT}$ (MeV)	$E_{\rm MF}$ (MeV)	$E_{\rm so}$ (MeV)	$E_{\rm Coul}$ (MeV)	$E_{\rm kin}$ (MeV)	s.p. energy (MeV)
^{42}Ca	-362.591	-1111.434	-9.173	72.023	685.993	-9.66
^{41}Ca	-352.942	-1081.395	-5.259	72.116	661.596	-9.64
^{41}Ca with (2.3)	-352.918	-1081.359	-5.259	72.115	661.584	-9.64
ΔE	0.024	0.036	0.000	-0.001	-0.012	
^{50}Ca	-429.654	-1326.381	-33.958	70.905	859.779	-5.84
^{49}Ca	-423.876	-1305.865	-33.639	71.105	844.523	-5.70
^{49}Ca with (2.3)	-423.825	-1305.754	-33.634	71.102	844.461	-5.70
ΔE	0.051	0.111	0.005	-0.003	-0.062	

Table 2.1: Total energy, mean field, spin-orbit, Coulomb and kinetic contributions to the total energy (third column) and single-particle energy of the neutron state $1f_{7/2}$ for $^{41-42}$Ca and $2p_{3/2}$ for $^{49-50}$Ca calculated, for the nearest even nuclei and for the odd nuclei, without/with the spin-dependent terms (2.3) in the mean field. ΔE is the difference of energy with and without the spin-dependent terms (2.3).

Nucleus	$E^{\rm odd}_{\rm TOT}$ (MeV)	$E^{\rm odd}_{0}$ (MeV)	$E^{\rm odd}_{\rm eff+fin+sg}$ (MeV)	$E^{\rm odd}_{3}$ (MeV)
^{41}Ca	0.329	0.196	-0.007	0.140
^{49}Ca	0.151	0.187	-0.176	0.140

Table 2.2: Total and separate contributions to the energy from the time-odd (spin symmetry breaking) terms of the SLy5 Skyrme interaction (Bender 2003).

where $m_s(i)$ and $m_t(i)$ are the spin and isospin z-component for each single nucleon having the wave function $\varphi_i(r)$. The last occupied state fully contributes to the spin-density. It is then clear that the OSPA corresponds to maximizing the spin-density and its effects.

Note that if the time-reversal symmetry is not broken (in the filling approximation, for instance) both spin-up and spin-down states must be degenerate and the densities ρ_s and ρ_{st} are zero. Since in this work we aim at an approximate and maximal estimate and not at a precise prediction of the effects, we use the HF method with the OSPA to treat odd nuclei.

We have made several calculations for the ground-state energies that are summarized in Tables 2.1 and 2.2. The partial contributions to the ground-state energy are written $E_{\rm MF} \equiv \int d^3r\ (\mathcal{H}_0 + \mathcal{H}_3 + \mathcal{H}_{\rm eff} + \mathcal{H}_{\rm fin} + \mathcal{H}_{\rm sg})$, $E_{\rm so} \equiv \int d^3r\ \mathcal{H}_{\rm so}$, $E_{\rm Coul} \equiv \int d^3r\ \mathcal{H}_{\rm Coul}$ and $E_{\rm kin} \equiv \int d^3r\ \mathcal{H}_{\rm kin}$, using the notations of Ref. (Chabanat et al., 1998a; Chabanat et al., 1998b). In Table 2.1 the total energy, the mean field, the spin-orbit, the Coulomb and the kinetic contributions to the total energy and the single-particle energy (for the neutron states $1f_{7/2}$ or $2p_{3/2}$) are provided for the odd nuclei ^{41}Ca and ^{49}Ca and for the nearest even-even nuclei ^{42}Ca and ^{50}Ca. The calculation for the odd nuclei are performed either with or without the spin-density dependent interaction (2.3). The difference between the total energy, and its contributions, without and with the corrections ΔE is shown to be less than 50 keV in both odd nuclei ^{41}Ca and ^{49}Ca. It is interesting to notice that the kinetic energy contributes to reduce the impact of the spin-dependent interaction (2.3). The spin-orbit and the Coulomb energies are very weakly affected by the new spin-density terms.

In Table 2.2 the total and separate contributions coming from the time-odd terms of the Skyrme interaction are provided, in the case of the odd nuclei ^{41}Ca and ^{49}Ca: these contributions are calculated perturbatively within the OSPA. These terms are classified according to the standard notations and labeled

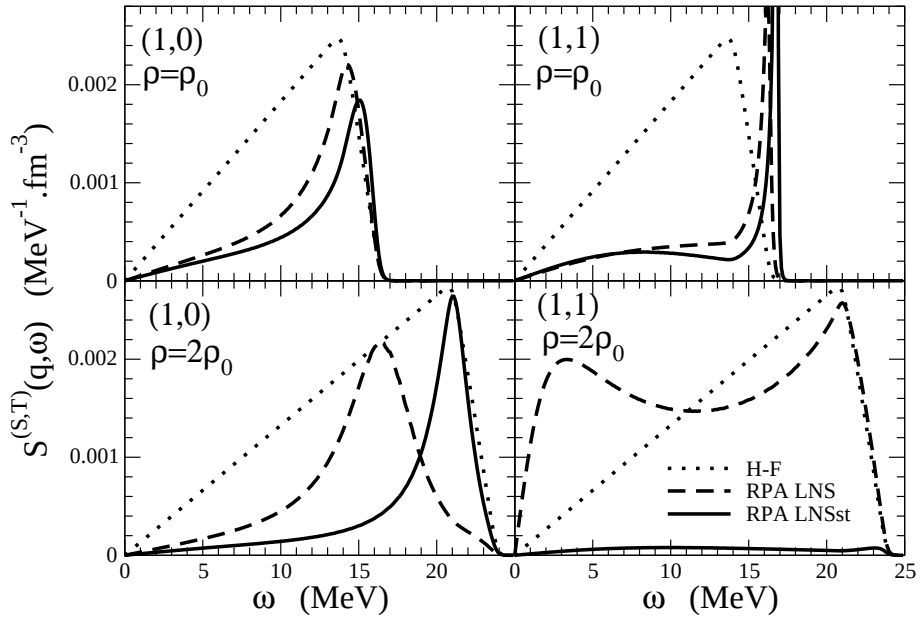

Figure 2.4: RPA response functions $S^{(S,T)}(q,\omega)$ for q=0.22 fm^{-1} with the temperature T=0 MeV calculated with LNS and LNSst interactions. Top panels are calculated for $(S,T)=(1,0)$ and $(1,1)$ with $\rho=\rho_0$ and bottom panels are for the same channels with $\rho=2\rho_0$.

as $E_0^{\rm odd}$, $E_{\rm eff+fin+sg}^{\rm odd}$ and $E_3^{\rm odd}$ which are the contributions from the central, the momentum dependent and the density dependent terms, respectively. The corrections $E_0^{\rm odd}$ and $E_3^{\rm odd}$ give a dominant and repulsive contribution which increases the total energy while the correction $E_{\rm eff+fin+sg}^{\rm odd}$ is smaller and attractive. The total correction remains quite small, that is, of the order of 0.15-0.3 MeV for both nuclei. Note that the sign of these corrections could change from one Skyrme interaction to another, but such corrections in Table 2.2 remain larger than $\Delta E_{\rm TOT}$ in Table 2.1.

Eventually, from the quantitative comparison shown in Tables 2.1 and 2.2, we can infer, as expected, that the new spin-density dependent terms (2.3) modify the ground state energies of odd nuclei much smaller than those coming from the time-odd terms of the standard Skyrme interaction. Since the time-odd terms of the standard Skyrme interaction are weakly constrained, and therefore neglected in most of the calculations, we can safely conclude that the new spin interaction (2.3) have a very weak effect in odd nuclei.

2.2.4 Excited states in nuclear matter and spin modes

The new spin interaction (2.3) is design such that it does not impact the ground state of even-even nuclei in the HF framework. In the previous subsection, it has moreover been shown that the new spin interaction weakly modify the ground state of odd nuclei. There remarks are not much surprising since the new spin interaction have been introduced mainly to modify the Landau parameters in spin-unpolarized matter. It is then expected that the new spin interaction have an impact on the RPA response function of nuclei and nuclear matter. We therefore study the RPA response function in this section.

Since the Landau parameters G_0' at saturation density is increased by about 0.3 with the new spin interaction, see for instance Fig. 2.2, it is expected that the new spin interaction modify the response function of collective spin modes already at saturation density ρ_0. The increased of the Landau parameters may have significant influence on spin and spin-isospin excitations such as Gamow-Teller states.

In the following, we calculate the RPA response function in nuclear matter from the following expres-

sion, which is valid also at finite temperature T,

$$S^{(S,T)}(q,\omega,T) = -\frac{1}{\pi}\frac{1}{1-e^{-\omega/T}}\mathrm{Im}\chi^{(S,T)}(q,\omega,T) \tag{2.13}$$

where $\chi^{(S,T)}(q,\omega,T)$ is the susceptibility, or polarizability, obtained as the solution of the Bethe-Salpeter equation (Fetter and Walecka, 1971; Garcia-Recio et al., 1992). In Fig. (2.4), we show the response functions in the spin channels ($S=1$) at $T=0$ MeV and at densities $\rho=\rho_0$ and $\rho=2\rho_0$ calculated by the LNS (Cao et al., 2006b) and LNSst (Margueron and Sagawa, 2009) interactions. The HF solution (dotted line) is compared with the RPA using the original LNS Skyrme interaction (dashed line) and also with the RPA including the new terms in LNSst (solid line). According to the semi-classical Steinwedel-Jensen model (Ring and Schuck, 1980) the optimal transfered momentum to compare with nuclei shall be approximatively given by $q=\pi/2R$ where R is the radius of the nuclei. For ^{208}Pb, one thus obtain q=0.22 fm^{-1}.

For $\rho=\rho_0$ in Fig. (2.4), the effect of the new terms is to move the collective mode to slightly higher energies by 0.5-1 MeV. For $\rho=2\rho_0$, the $(S=1,T=1)$ Gamow-Teller channel is not far from being unstable from the original Skyrme interaction and the low energy collective mode is being formed. By the new term t_3^{st}, the low energy mode is suppressed and the strength is reduced substantially at $\omega>0$. A reduction of the strength at low energy is also observed for the $(S=1,T=0)$ channel. This effect shall be seen in the calculation of microscopic processes such as the neutrino cross section.

2.2.5 Application to the neutrino mean free path in dense medium

Neutrinos play a crucial role in physics of supernova explosions (Bethe, 1990) and in the early evolution of their compact stellar remnants (Burrows and Lattimer, 1986; Janka and Müller, 1995; Reddy et al., 1998). To clarify the effect coming from the new spin interaction (2.3), we consider the case of pure neutron matter. The scattering of neutrinos on neutrons is then mediated by the neutral current of the electroweak interaction. In the non-relativistic limit, the mean free path of a neutrino with initial energy E_ν is given by (Iwamoto and Pethick, 1982)

$$\lambda^{-1}(\mathrm{E}_\nu,T) = \frac{G_F^2}{16\pi^2}\int d\mathbf{k}_3\left(c_V^2(1+\cos\theta)\,S^{(S=0)}(q,\omega,T)+c_A^2(3-\cos\theta)\,S^{(S=1)}(q,\omega,T)\right), \tag{2.14}$$

where G_F is the Fermi constant, c_V (c_A) is the vector (axial) coupling constant, $k_1=(E_\nu,\mathbf{k}_1)$ and k_3 are the initial and final neutrino four-momenta, while $q=k_1-k_3$ is the transferred four-momentum, and $\cos\theta=\hat{\mathbf{k}}_1\cdot\hat{\mathbf{k}}_3$. In the following, we impose the average energy $E_\nu=3T$ in MeV (Reddy et al., 1998). In Eq. (2.14), the contribution of the response function $S^{(S)}(q,\omega,T)$ is clearly identified. It describes the response of neutron matter to excitations induced by neutrinos, and contain the relevant information on the medium. The vector (axial) part of the neutral current gives rise to density (spin-density) fluctuations, corresponding to the spin $S=0$ ($S=1$) channel.

The neutrino mean free path is shown in Fig. 2.5 as a function of the baryonic density and for different temperatures (T=1, 10, 20 MeV). The neutrino mean free path calculated with the original LNS Skyrme interaction (dashed line) is strongly reduced at high density as a consequence of the onset of the spin instabilities (Hernandez et al., 1999; Margueron, 2001). The inclusion of the new density dependent interaction (2.3) in LNSst removes the spin instability and reduces the response function as shown in Fig. 2.4. As a consequence, the mean free path is increased and the matter is more transparent to neutrino as the density increases. This result is similar to a previous calculation of neutrino mean free path deduced directly from a microscopic G-matrix (Margueron et al., 2003b). It illustrates the important contribution of the spin channel to the neutrino mean free path at high density. It is also clear from Fig. 2.5 that the effects of the correlations are not washed out by the temperature in the range going up to $T=20$ MeV.

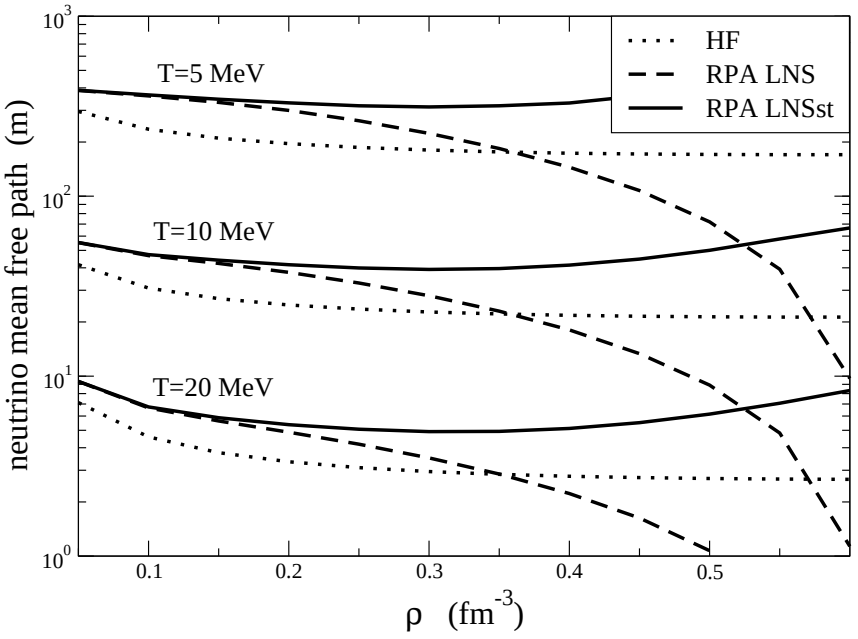

Figure 2.5: Neutrino mean free path in neutron matter for different temperatures T=1, 10 and 20 MeV. The neutrino energy is set to be $E_\nu = 3T$. The mean free path is calculated with the LNS Skyrme interaction by the HF mean field approximation (dotted line), including the RPA correlations with the original LNS interaction (dashed line) and RPA with the modified spin channel in LNSst (thick line).

2.2.6 Final remarks

The occurrence of the spin instability beyond the saturation density is a common feature shared by different effective mean-field approaches such as Skyrme HF (Margueron et al., 2002b), Gogny HF (Margueron, 2001) or relativistic HF (Niembro et al., 2001). The analysis of the spin component of the Skyrme interaction as well as its extensions might thus guide us to a wider understanding of the spin channel in general for nuclear interaction. We have analyzed the effect in nuclei and in nuclear matter of a new density dependent interaction (2.3) correcting the Skyrme interaction and shown that on top of stabilizing unpolarized nuclear matter for a range of densities where Skyrme model can be reasonably applied, this new interaction modify the RPA response function by slightly pushing up the spin modes in nuclear matter at saturation. The effect is however larger at twice saturation density and has a large influence on the neutrino mean free path in proto-neutron stars, as illustrated in section 2.2.5.

The momentum dependence of the p-h interaction have recently been analyzed with respect to the stability of the mean field. It could be related to the finite-size fluctuations of the mean-field. It has indeed been observed that the instability of some Skyrme interactions in doing HF iteration in finite nuclei can be related to these finite-size instabilities, assuming that the range of momenta explored during the iterations is going from 0 to $2k_F$ (Lesinski et al., 2006). The finite-size instabilities have been found to be a very drastic criterium in adjusting Skyrme interactions, and extensions (K; Bennaceur, private communication).

There are many more reasons for looking at the spin channel. For instance for its competition with pairing correlations in the odd-even-mass staggering (Duguet et al., 2001a; Duguet et al., 2001b), for rotating superdeformed nuclei (Dobaczewski and Dudek, 1995), for a better description of GT response, and for all applications in astrophysics such as for instance predictions of β-decay half-lives of very neutron rich nuclei produced during the *r*-process nucleosynthesis (Borzov, 2006), reliable calculation of neutron star crust properties such as ground-states and collective motion (Grasso et al., 2008), for $0\nu-$ and 2ν double

beta decay processes, and for URCA fast cooling.

I have therefore different projects in the future to investigate the other application of the new spin interaction (2.3). There is a collaboration with Karim Bennaceur, Jacques Meyer, and Paul-Henry Heenen to look at hightly-rotating nuclei, supported by the *Comité de Financement Théorie IN2P3*, and another collaboration with Ivan Borzov, Alexei Severyukhin, Nguyen Van Giai and Victor Voronov to study β-decay half-lives of very neutron rich nuclei within the PICS-RFBR 2011-13 Program between Dubna and IPN, Orsay. Pierre Morfouace, the PhD student of Serge Francho, is also investigating the effect of the new spin term, the tensor interaction and the effect of pairing in the position of the drip-line for O, F, and other semi-magic nuclei.

The extension of the so-called t_3 density-dependent term in the Skyrme interaction that not only include the isoscalar density, but also the spin and spin-isospin density is quite natural and provided new degrees of freedom. These degrees of freedom keep almost unchanged the ground-state of even and odd nuclei, while it changes the collective modes at saturation density, and beyond. In isospin asymmetric matter, the additional inclusion of a new density dependent term based on the isospin-density can also provide new degrees of freedom and changes the density dependence of the symmetry energy. While in the present Skyrme functional, an iso-stiff EoS at low density, as it is favored by heavy-ion collisions (Chen et al., 2007), implies that the EoS is iso-soft at high density, the inclusion of new degrees of freedom in the isospin asymmetric matter mediated by an explicit isovector-density dependent term of the t_3 kind could definitively help in changing this feature. It would indeed be interesting to explore new functionals that are iso-stiff at low density as well as at high density.

2.3 Separable form of the $V_{\text{low-k}}$ nuclear interaction

As discussed in the introduction, a new semi-empirical interaction based on the low-momentum interaction $V_{\text{low-k}}$ have been proposed to perform Hartree-Fock calculations (Montani et al., 2004; Van Dalen et al., 2009). The advantage of this new interaction is that it contains the important properties of the realistic nucleon-nucleon interaction at low energy, including the spin-orbit and the tensor interactions, and the number of additional parameters to fit is limited (3-5 compared to 9 for Skyrme interactions). The inclusion of $V_{\text{low-k}}$ brings an ab-initio modeling of the finite-range terms, called t_1, t_2 in *Skyrme-words*.

In spite of its obvious advantages $V_{\text{low-k}}$ potential still remains a quite complicated object. On the one hand, it is nonlocal and therefore is represented as a matrix element in momentum space for each partial wave channel. This nonlocality increases the computational time in Hartree-Fock iterations, and prevents the use of $V_{\text{low-k}}$ if the number of nucleons is too large, such as in the Wigner-Seitz cells present in the crust of neutron stars for instance (Negele and Vautherin, 1973). On the other hand, the renormalization technique used to produce $V_{\text{low-k}}$ seems not to be trivial. The resulting interaction is given as a matrix table which is not an easy-to-use form and prevents this potential to be popular. A possible way out is to find a separable representation of $V_{\text{low-k}}$, since it significantly simplifies many-body calculation (Baldo and Ferreira, 1988; Tian et al., 2009). Moreover recent calculations of triton binding energies demonstrate the $V_{\text{low-k}}$ can be very good approximated by a low-rank separable force for low values of the cutoff Λ (Kamada, 2006). We investigate the separability of $V_{\text{low-k}}$ by using the diagonalization of the matrix in momentum space for each partial wave channel. It allows us to find a low rank separable form of $V_{\text{low-k}}$, which can be used in HF calculations of nuclear matter as well as finite nuclei.

2.3.1 Separability analysis by diagonalization

Originally $V_{\text{low-k}}$ is nonlocal and defined in terms of matrix elements in a basis of NN states labeled by relative momentum for pairs of nucleons. Thus for each partial wave channel there exists a matrix, which

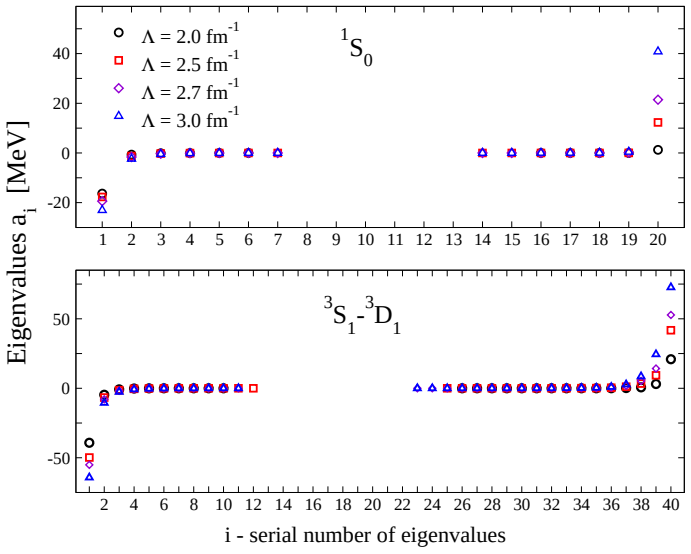

Figure 2.6: Top: Nonzero eigenvalues a_i of ${}^1S_0$ channel. Bottom: Nonzero eigenvalues a_i of ${}^3S_1$-${}^3D_1$ channel.

represents $V_{\text{low-k}}(k,k')$ on a mesh of N discretized relative momenta k and k' in the range $0 \leq k,k' \leq \Lambda$. Since this matrix is real and symmetric with respect to k,k' one can diagonalize it, so that, it can be written as a sum of N real eigenvalues multiplied with the respective eigenvectors

$$V_{\text{low-k}}(k,k') = \sum_{i=1}^{N} a_i f_i^*(k) f_i(k'), \tag{2.15}$$

where N is the number of mesh-points and the dimension of $V_{\text{low-k}}$ matrix. In the following we will omit the symbol of complex conjugation because all eigenvectors are real. The eigenvectors $f_i(k)$ satisfy the orthogonality relation

$$\frac{2}{\pi}\int_0^{\Lambda} dk k^2 f_i(k) f_j(k) = \delta_{ij}. \tag{2.16}$$

The last equality (2.15) is nothing else but the general definition of a separable potential of the rank N. If the rank of the separable potential equals the dimension of the matrix $V_{\text{low-k}}(k,k')$ the whole information is exactly restored from the eigenvalues a_i and eigenvectors f_i. As we will see later, some of eigenvalues a_i can be zero or negligibly small so that one can reduce the rank of separable interaction taking into account only the n eigenvalues with largest absolute values. It leads to a new approximated separable interaction $V^{[n]}_{\text{low-k}}(k,k')$

$$V_{\text{low-k}}(k,k') \simeq V^{[n]}_{\text{low-k}}(k,k') = \sum_{i=1}^{n} a_i f_i(k) f_i(k'), \qquad (n \leq N). \tag{2.17}$$

The low-rank separable representation of NN interaction leads to significant simplifications in many-body calculations.

The nonzero eigenvalues a_i obtained from diagonalization of 20×20 matrix of $V_{\text{low-k}}(k,k')$ in ${}^1S_0$ channel are shown on the top of Fig.2.6 for different values of the cut-off parameter Λ. At the value of the cutoff parameter $\Lambda = 2$ fm^{-1} the diagonalization procedure yields only 11 nonzero eigenvalues, other words, $V_{\text{low-k}}$ interaction in ${}^1S_0$ channel is a separable interaction of the $11th$ rank. The nonzero eigenvalues are essentially independent on N, the dimension of the matrix representing $V_{\text{low-k}}$. Going further one can notice, that many of the nonzero eigenvalues are nevertheless very small, and only some of them, e.g.,

at $i = 1, 2, 20$ carry the main part of the information about the interaction model. This gives rise to a substantial lowering of the rank of separable potential, as it was shown in Eq.(2.17). With the increase of the cutoff Λ the absolute values of the eigenvalues increase as well and as a consequence the rank n of the separable form $V^{[n]}_{\text{low-k}}$ defined in (2.17) has to be increased to achieve a reasonable accuracy. Increasing Λ more information about the short-range components of the underlying bare interaction is included, which requires a larger rank in the separable representation of the interaction. This is in line with the findings of Bogner et al. who explored the finite-rank expansion of the low momentum interaction by means of a Weinberg eigenvalue analysis (Bogner et al., 2006).

In case of the coupled channels, like $^3S_1$-$^3D_1$ channel, the dimension N of the $V_{\text{low-k}}$ matrix is twice as large if one keeps the number of mesh-points in each channel the same as for the uncoupled partial waves. It turns out that also the number of nonzero eigenvalues increases as shown in the lower panel of Fig.2.6. It is obvious that the rank of the separable potential should be higher than for $^1S_0$ channel. It is a general feature that coupled channels require higher rank separable interaction than the uncoupled ones (Haidenbauer and Plessas, 1984). Also one observes pairs of positive and negative eigenvalues which have about the same absolute value. This symmetry between positive and negative eigenvalues play a crucial role in the convergence of the separable form $V^{[n]}_{\text{low-k}}$ to the initial $V_{\text{low-k}}$ with increase of rank.

At Λ = 2 fm^{-1} one observes a fast convergence to zero deviation already at the rank $n = 2$. The growth of the cutoff monotonically increases the rank of the separable potential. At Λ = 3 fm^{-1} one may expect a good accuracy starting from $n = 5$. The analysis carried in Ref. (Grygorov et al., 2010) indicates that $V^{[2,3]}_{\text{low-k}}$ is an accurate low-rank separable representation of $V_{\text{low-k}}$ interaction. However, in order to make it accessible to other users, it should be parameterized in a simple form. Here we suggest the fitting function for all $f_i(k)$ in all channels

$$f_i(k) = \alpha_i + (\beta_i \exp(\gamma_i k^{\delta_i}) + \mu_i) \sin(k\sigma_i + \lambda_i), \tag{2.18}$$

We summarized all parameters of the separable fitted form in Ref. (Grygorov et al., 2010).

2.3.2 Application to nuclei

The $V_{\text{low-k}}$ Hartree-Fock calculations demonstrate a monotonic increase of the binding energy of symmetric nuclear matter as a function of the nucleon density, thus it cannot reproduce the empirical saturation point (Boek et al., 2006; Kuckei et al., 2003). In order to achieve the saturation in nuclear matter one has to add three-body interaction terms or a density-dependent two-nucleon interaction. Therefore we support the low-momentum interaction by a simple contact interaction, which have been chosen following the notation of the Skyrme interaction (Skyrme, 1959; Vautherin and Brink, 1972; Chabanat et al., 1997)

$$\Delta\nu = \Delta\nu_0 + \Delta\nu_3, \tag{2.19}$$

with

$$\Delta\nu_0 = \frac{1}{4} t_0 \left[(2 + x_0)\rho^2 - (2x_0 + 1)(\rho_n^2 + \rho_p^2)\right] \tag{2.20}$$

and

$$\Delta\nu_3 = \frac{1}{24} t_3 \rho^\alpha \left[(2 + x_3)\rho^2 - (2x_3 + 1)(\rho_n^2 + \rho_p^2)\right], \tag{2.21}$$

where ρ_p and ρ_n are the local densities of nucleons while the total matter density is denoted as $\rho = \rho_p + \rho_n$. The values of α and x_0 were fixed at $\alpha = 0.5$, $x_0 = 0.0$, while t_0, t_3, x_3 were fitted in such a way that HF calculations using $V_{\text{low-k}}$ or $V^{[2,3]}_{\text{fit}}$ plus the contact term (2.19) reproduces both the empirical saturation point of the symmetric nuclear matter and the symmetry energy at saturation density. Following (Van Dalen et al., 2009) the contact interaction produced for $V_{\text{low-k}}$ will be labeled by CT, and the respective interaction model $V_{\text{low-k}}$+CT. For the fitted potential $V^{[2,3]}_{\text{fit}}$ we suggest two possible parameterizations: CT1 and CT2.

Interaction	ρ_0 [fm^{-3}]	E/A(ρ_0) [MeV]	K [MeV]
$V_{\text{low-k}}$+CT	0.16	-16.0	258
$V_{\text{fit}}^{[2,3]}$+CT1	0.16	-16.1	241.9
$V_{\text{fit}}^{[2,3]}$+CT2	0.156	-16.0	240.5

Table 2.3: Bulk properties of symmetric nuclear matter derived from $V_{\text{low-k}}$ and its separable representation. They are supplemented by the respective contact interaction.

Interaction	^{16}O	^{40}Ca	^{48}Ca	^{60}Ca	^{208}Pb
	E/A [MeV]				
$V_{\text{low-k}}$+CT	-7.91	-8.57	-8.42	-7.75	-7.76
$V_{\text{fit}}^{[2,3]}$+CT1	-7.79	-8.56	-8.35	-7.78	-7.76
$V_{\text{fit}}^{[2,3]}$+CT2	-7.84	-8.58	-8.37	-7.79	-7.76
Experiment	-7.98	-8.55	-8.67	–	-7.87
	r_{ch} [fm]				
$V_{\text{low-k}}$+CT	2.79	3.50	3.54	3.68	5.51
$V_{\text{fit}}^{[2,3]}$+CT1	2.81	3.51	3.55	3.68	5.52
$V_{\text{fit}}^{[2,3]}$+CT2	2.82	3.53	3.58	3.71	5.56
Experiment	2.74	3.48	3.47	–	5.50

Table 2.4: The binding energy per nucleon and rms charge radii of finite nuclei. Experimental data taken from Refs. (Brown 1998) and (Fricke 1995).

The properties of nuclear matter is shown in Table 2.3. This value for the compressibility modulus is also in agreement with that of the Skyrme interaction which reproduce correctly the breathing mode in nuclei (giant isoscalar resonance) (Shlomo et al., 2006).

2.3.3 Final remarks

It is interesting to notice that the accuracy obtained with our semi-empirical models for the comparison to binding energies and radii of representative nuclei, cf Table 2.4 is comparable to that of the widely used Skyrme interactions, such as SLy4 for instance, while the number of free parameters is only 3 (t_0, t_3, x_3) or 5 if one needs to vary also x_0 and α. The number of empirical data needed to adjust the interaction is therefore reduced compared to empirical nuclear interactions and the interaction model we propose contains interesting features of the complex bare potential such as for instance the tensor matrix elements. Studies of $T = 0$ and $T = 1$ pairing channels as well as the properties of exotic nuclei will be addressed in future applications of our model.

There is a project within the LIA-Vietnam (PhD program) which aims at performing an HFB calculation with finite-range interactions such as Gogny, DD-M3Y, and the model presented here. This model will be used to be applied to the calculations of Wigner-Seitz cells in the crust of neutrons stars as discuss in chapter 5.

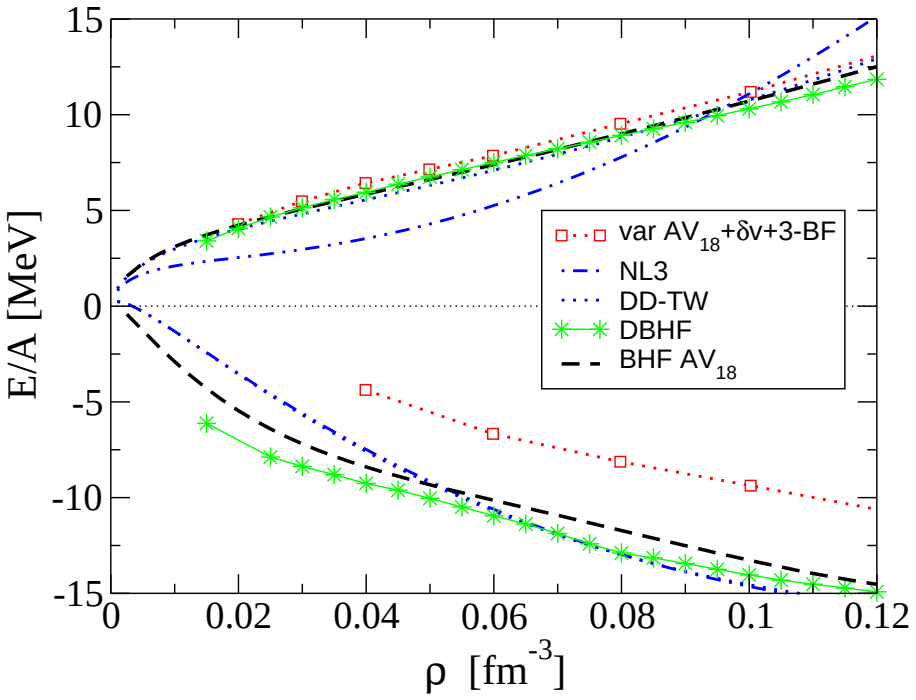

Figure 2.7: (Color online) Comparison of several equation of state with the DBHF results. The DBHF calculation are represented by the stars, the variational by the empty squares, the non-relativistic Brueckner results by the dashed line and two different relativistic mean field parametrisations: NL3 (dashed-dotted line) and DD-TW (dotted line).

2.4 Low-density properties of the uniform matter equation of state

In this section we are going to consider densities which are low with respect to saturation density, but still large compared to typical values where the onset of few-body clustering occurs. The onset density for deuteron clustering in nuclear matter is for instance estimated to be one tenth of saturation density (Baldo et al., 1995). Typically, we are considering densities between about one tenth to one half of the saturation density. It is the region which is however not expected to be formed of uniform matter but of the so-called deformed pasta phases (Ravenhall et al., 1983; Lassaut et al., 1987). It is however interesting to extrapolate the many-body approaches well-suited to describe uniform matter at and beyond saturation density and to compare their predictions at low density where only the two-body correlations are expected to dominate over the three-body one's. For instance, some properties of dilute clusterized matter can be inferred from that of uniform matter, either by studying Bose-Einstein Condensation from BCS approach (Baldo et al., 1995; Matsuo, 2006; Margueron et al., 2007a; Jin et al., 2010), or by analyzing the RPA unstable modes (Müller and Serot, 1995; Baran et al., 2001; Margueron and Chomaz, 2003; Chomaz et al., 2004; Margueron et al., 2007b; Ducoin et al., 2008). For neutron matter this is a known fact and has e.g. also been investigated in the - hypothetical - unitary limit $ak_F \to \infty$ where a is the nn scattering length. In this limit many-body calculations (BHF, variational and GFMC) lead to a different low density behavior than RMF theory, see discussion in Ref. (Carlson et al., 2003). In this low density region, microscopic calculations based on the relativistic Dirac-Brueckner-Hartree-Fock (DBHF) approach (ter Haar and Malfliet, 1987; Fuchs, 2004; Gross-Boelting et al., 1999; Van Dalen et al., 2004; Van Dalen et al., 2005) are expected to be quite accurate, and they will be, therefore, the starting point of our analysis.

In Fig. (2.7) are compared the energy per particle for the low density regime of symmetric nuclear matter

(below zero) and pure neutron matter (above zero) predicted from microscopic many-body approaches as well as two typical phenomenological relativistic mean field models. From the microscopic side these are the DBHF results (Van Dalen et al., 2004) which will be further analyzed, non-relativistic Brueckner (BHF) calculations (Baldo et al., 2004b) and variational calculations (Akmal et al., 1998). The variational and BHF calculations are based on the AV_{18} Argonne potential. The variational calculations include in addition phenomenological 3-body-forces (Urbana IX) and relativistic boost corrections which both do, however, not play an important role in the low density regime. The phenomenological models are the well established NL3 (Lalazissis et al., 1997) relativistic mean field (RMF) parametrisation and the DD-TW RMF model (Typel and Wolter, 1999). The latter is a phenomenological version of density dependent RMF theory using density dependent meson-nucleon couplings (Fuchs et al., 1995) which allows for a larger freedom in the adjustment of the EOS. Both approaches fit finite nuclei properties with high accuracy.

The first what becomes evident from Fig. (2.7) is the remarkable agreement of the microscopic approaches (DBHF, BHF, variational) concerning the pure neutron matter EOS. This indicates that both, the interaction and the many-body schemes are well controlled in the nn sector at low densities. The reason is on the one hand-side the large nn scattering length and on the other side the lack of clustering phenomena (d, α etc) which make the treatment of neutron matter at subnuclear densities less model dependent. In this context it is worth noticing that the microscopic calculations (BHF/DBHF, variational) are consistent with the low density limit of 'exact' Quantum-Monte-Carlo calculations for neutron matter (Carlson et al., 2003) and with the result of the renormalization group V_{lowk} approach (Bogner et al., 2003).

The situation seems to be different for symmetric nuclear matter. The Brueckner calculations show significantly more binding than the variational calculations of Ref. (Akmal et al., 1998). On the other hand, the DBHF and BHF results are very close and exhibit the same low density behavior: in contrast to RMF theory and also to Ref. (Akmal et al., 1998) one can observe a non-linear convergence to zero when the density decreases. This fact is associated to the deuteron channel and can possibly be interpreted as a manifestation of the onset of the super-fluid phase. In this context it is interesting to note that a recent study of low density nuclear matter (Horowitz and Schwenk, 2006b; Horowitz and Schwenk, 2006a), based on a virial expansion which includes protons, neutrons and α-particle degrees of freedom, revealed a low density EOS which is in qualitative agreement with the DBHF predictions. In the virial approach the binding energy goes smoothly to zero for neutron matter while the energy per particle E/A minus the (free) kinetic energy in symmetric matter remains practically constant at a value around -8 MeV down to extremely low densities ($\rho_B \simeq 0.0002\ \mathrm{fm}^{-3}$) before it rapidly drops to zero (Fig. 15 in Ref. (Horowitz and Schwenk, 2006a)). Subtracting from the DBHF result the kinetic energy of a non-relativistic Fermi gas $3k_F^2/10M$ yields at $k_F = 0.5\ \mathrm{fm}^{-1}$ ($\rho_B = 0.0084\ \mathrm{fm}^{-3}$) a values of -8.4 MeV which coincides remarkably well with the virial low density limit.

2.4.1 Low-density expansion of the non-linear relativistic mean field EOS

To understand the low-density behavior of the mean field approaches, we expand in this section the equation of state obtained from the RMF approach in power of the baryonic density.

A Lagrangian density of interacting many-particle system consisting of nucleons, isoscalar (scalar σ, vector ω), and isovector (scalar δ, vector ρ) mesons is the starting point of the relativistic mean field (RMF) theory,

$$\begin{aligned}\mathcal{L} &= \bar{\psi}[i\gamma_\mu\partial^\mu - (M - g_\sigma\sigma - g_\delta\vec{\tau}\cdot\vec{\delta}) - g_\omega\gamma_\mu\omega^\mu - g_\rho\gamma^\mu\vec{\tau}\cdot\vec{\rho}_\mu]\psi \\ &\quad + \frac{1}{2}(\partial_\mu\sigma\partial^\mu\sigma - m_\sigma^2\sigma^2) - U(\sigma) + \frac{1}{2}m_\omega^2\omega_\mu\omega^\mu + \frac{1}{2}m_\rho^2\vec{\rho}_\mu\cdot\vec{\rho}^\mu \\ &\quad + \frac{1}{2}(\partial_\mu\vec{\delta}\cdot\partial^\mu\vec{\delta} - m_\delta^2\vec{\delta}^2) - \frac{1}{4}F_{\mu\nu}F^{\mu\nu} - \frac{1}{4}\vec{G}_{\mu\nu}\vec{G}^{\mu\nu},\end{aligned} \tag{2.22}$$

where σ is the σ-meson field, ω_μ is the ω-meson field, $\vec{\rho}_\mu$ is ρ meson field, $\vec{\delta}$ is the isovector scalar field of the δ-meson. $F_{\mu\nu} \equiv \partial_\mu\omega_\nu - \partial_\nu\omega_\mu$, $\vec{G}_{\mu\nu} \equiv \partial_\mu\vec{\rho}_\nu - \partial_\nu\vec{\rho}_\mu$, and the $U(\sigma)$ is a nonlinear potential of σ meson : $U(\sigma) = \frac{1}{3}a\sigma^3 + \frac{1}{4}b\sigma^4$. Dynamical equations deduced at the mean field approximation as well as all the standard definitions are presented in Ref. (Margueron et al., 2007b). Hereafter, we introduce the coupling constants $f_i = g_\rho/m_i$ for i=σ, δ, ω and ρ, and the non-linear constant $f_\sigma^{nl} = a(f_\sigma/m_\sigma)^3$. In the following the energy density ϵ is expanded up to the power 4 in proton and neutron densities.

For the linear version of the RMF model, i.e. without a nonlinear σ-meson potential $U(\sigma)$ such an expansion can be found in (Serot and Walecka, 1997a). In our work presented in Ref. (Margueron et al., 2007b), we have extended this expansion to the non-linear case and to the isospin sector, i.e. to $\rho_p \neq \rho_n$ (the isovector mesons ρ and δ are included). Notice however, that in the present form, only the non-linear term with the coupling constant a is included because the one with the coupling constant b contributes to higher terms in the density expansion.

The scalar field is the solution of the following self-consistent equation

$$g_\sigma\sigma = f_\sigma^2\rho_s - \frac{a}{g_\sigma m_\sigma^2}(g_\sigma\sigma)^2 - \frac{b}{(m_\sigma g_\sigma)^2}(g_\sigma\sigma)^3 \ . \tag{2.23}$$

Let's call σ_0 the solution of the linear self-consistent equation, $g_\sigma\sigma_0 = f_\sigma^2\rho_s$, and suppose that $\sigma_1/\sigma_0 \ll 1$ (we will verify this hypothesis after-while). Taking into account only first order corrections up to the power 9 in k_{Fi}, Eq. (2.23) reduces to (Margueron et al., 2007b),

$$g_\sigma\sigma \quad = \quad f_\sigma^2\rho_s - \frac{af_\sigma^4}{g_\sigma m_\sigma^2}\rho_s^2 + o(k_{Fi}^9). \tag{2.24}$$

The first term on the r.h.s. of Eq. (2.24) is the solution of the linear self-consistent equation, while the second term is induced by non-linear corrections.

The low-density expansion of the scalar density ρ_{si} is then required. It yields

$$\begin{aligned}\rho_{si} \quad = \quad & \rho_i - \frac{3}{10M_i^{*2}}\left(\frac{6\pi^2}{\gamma}\right)^{2/3}\rho_i^{5/3} + \frac{9}{56M_i^{*4}}\left(\frac{6\pi^2}{\gamma}\right)^{4/3}\rho_i^{7/3} - \frac{15}{144M_i^{*6}}\left(\frac{6\pi^2}{\gamma}\right)^{2}\rho_i^{3} \\ & + \frac{105}{1408M_i^{*8}}\left(\frac{6\pi^2}{\gamma}\right)^{8/3}\rho_i^{11/3} + o(\rho_i^4) \ ,\end{aligned} \tag{2.25}$$

where γ is the degeneracy of the system. Note that this expansion is also a relativistic expansion in the parameter k_{Fi}/M_i^*.

Now, we evaluate the full density functional,

$$\epsilon \quad = \quad \epsilon_{kin} + \frac{1}{2}f_\sigma^2\rho_s^2 - \frac{2}{3}f_\sigma^{nl}\rho_s^2 + \frac{1}{2}f_\omega^2\rho_B^2 + \frac{1}{2}f_\rho^2\rho_3^2 + \frac{1}{2}f_\delta^2\rho_{s3}^2 + o(\rho^4) \tag{2.26}$$

where ϵ_{kin} is the kinetic term. The density functional is decomposed into several terms:

$$\epsilon(\rho_n,\rho_p) = M\rho_B + \epsilon_{FG}(\rho_n,\rho_p) + \epsilon_L(\rho_n,\rho_p) + \epsilon_{NL}(\rho_n,\rho_p) + o(\rho^4) \ , \tag{2.27}$$

where the term ϵ_{FG} is the contribution of the free Fermi gas without the rest mass, the term ϵ_L is generated by the interactions and the Dirac mass and the term ϵ_{NL} is the correction coming from the non-linear σ coupling. The explicit form of those terms are given in Ref. (Margueron et al., 2007b) where they are classified according to the power in Fermi momentum.

The convergence of this series expansion is very fast in symmetric nuclear matter (SNM) and pure neutron matter (PNM) using the set of coupling constants, set A NL$\rho\delta$, obtained by Liu et al. (Liu et al., 2005). The convergence is essentially due to the shorting in power of k_F/M which comes with our expansion (Margueron et al., 2007b). The terms with power counting larger that 4 in the density expansion are negligible, even for the higher densities explored (about 0.3 fm^{-3}).

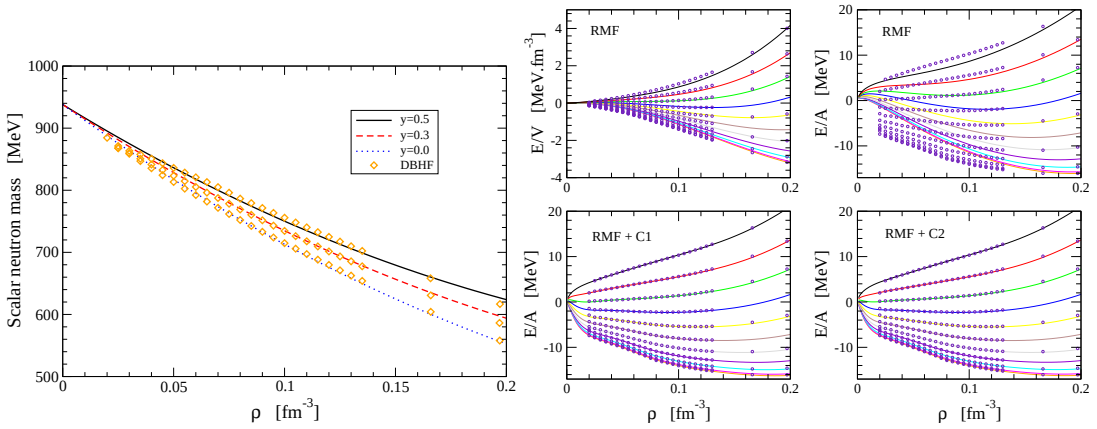

Figure 2.8: (Left) Comparison between the best RMF adjustment and the scalar mass calculated with DBHF approach. The asymmetry parameter $y = \rho_p/\rho_B$, ranges from 0.5 to 0. It clearly shows a linear ($f_\sigma^2\rho_B$) and a quadratic ($f_\sigma^{nl}\rho_B^2$) behavior in the baryonic density. The isospin asymmetry is also well reproduced by the linear term $f_\delta^2\rho_3$ in the asymmetry density ρ_3. (Right) Comparison of the DBHF results (circles points) and the low density functionals in asymmetric nuclear matter. On the top panels are shown the energy density and the binding energy for the parameters RMF, while on the bottom panels are shown the binding energies for the corrected functionals RMF+C1 and RMF+C2.

2.4.2 Analysis of the low-density properties of the DBHF approach

In this section, we compare the result of the DBHF calculation (Dirac mass, energy density and binding energies) in the density region between 0.01 and 0.2 fm^{-3} and the best fit of the low density RMF functional defined in Eqs. (2.25)-(2.27). The DBHF calculation includes 23 calculated points between ρ_B=0.02 and 0.13 fm^{-3}, plus two densities, ρ_B=0.1658 fm^{-3} and ρ_B=0.197 fm^{-3}, for $y = \rho_p/\rho_B$=0 to 0.5 with a step=0.05.

In contrast to DBHF theory, which shows a non-linear convergence to zero in the binding energy, RMF theory converges smoothly. We show in Fig. 2.8 (right panel) a comparison between the DBHF calculation and the low density functional RMF for the density of energy, E/V, and the binding energy, E/A. The low density effects are reduced on the energy density plot compared to the effects on the binding energy. In fact, as $E/V = \rho_B E/A$, the low density behavior of the binding energy is strongly reduced by the factor ρ_B in the energy density. Therefore, we adjust the mean field functional on the energy density obtained from the DBHF calculation in asymmetric nuclear matter, where the low density effects are weaker. We also force the functional to reproduce exactly the DBHF calculations at $\rho_B = 0.197$ fm^{-3} in symmetric nuclear matter and pure neutron matter. This constraint ensure that the symmetry energy at saturation density is well reproduced. Comparing the DBHF points with the RMF function on Fig. 2.8 (right panel) we conclude that the DBHF calculations at low density have a completely different behavior compared to standard mean field prediction.

In our work (Margueron et al., 2007b) we have performed a fit of the difference between the DBHF equation of state and the low density RMF functional. Thus we add two new functions $g^S(\rho_B)$ and $g^N(\rho_B)$ to the energy density so that

$$\epsilon_{\rm DBHF}(\rho_n,\rho_p) = \epsilon_{\rm RMF}(\rho_n,\rho_p) + (1-\beta^2)g^S(\rho_B) + \beta^2 g^N(\rho_B)\ , \tag{2.28}$$

where $\beta = (\rho_n - \rho_p)/\rho_B$. The additional terms $g^S(\rho_B)$ and $g^N(\rho_B)$ are respectively adjusted in symmetric nuclear matter and pure neutron matter. The isospin degree of freedom is factorized with a quadratic function which respects the nuclear isospin symmetry. This approximation is often performed (see for

fits	$B_0[MeV]$	$\rho_0[fm^{-3}]$	$K_0[MeV]$	$a_s^1[MeV]$	$a_s^2[MeV]$
RMF	-16.08	0.1933	365	35.8	37.7
RMF+C1	-16.27	0.1857	251	35.1	36.9
RMF+C2	-16.24	0.1856	242	35.1	36.9
DBHF	-16.15	0.1814	230	34.4	-

Table 2.5: Properties of the functionals. The symmetry energy has been obtain in two different ways: assuming a quadratic dependence of the equation of state between symmetric and pure neutron matter (a_s^1), or performing numerical derivation of the binding energy around symmetric nuclear matter (a_s^2). A systematic difference is observed but is less than 5%.

instance (Baldo et al., 2004b)) but in our case, it is also justified afterwards by comparing the new functionals RMF+C1 and RMF+C2 to the DBHF binding energies at low densities (Fig. (2.8), right panels). The functional correction is unknown, but it is clear that this correction should be small around saturation density, and should converge to zero at very small densities. Explicit form for these corrections are given in Ref. (Margueron et al., 2007b). As shown in Fig. 2.8, these two functionals reproduce the DBHF calculations at the same level of accuracy.

The table 2.5 give the properties of the functionals RMF, RMF+C1 and RMF+C2 around saturation density: the binding energy B_0, the saturation density ρ_0, the incompressibility K_0 and the symmetry energies a_s^1 and a_s^2. The properties of the DBHF calculation are also indicated. The properties of the low density RMF functional differ significantly from the DBHF results. Indeed, the saturation density and the compression modulus are higher than the DBHF results. It is a consequence of the low value of the parameters f_σ^{nl}, as expected. This parameter could not be changed, as it is already adjusted to the quadratic density dependence of the scalar mass, However, the saturation properties of the corrected functionals RMF+C1 and RMF+C2 are very close to the DBHF calculation. Then, in our framework, the reduction of the incompressibility modulus is induced by the low density physics. This is a very different understanding from the standard one which relies on non-linear corrections at high densities. We have also calculated the symmetry energy in two different manner: either assuming a quadratic dependence in the asymmetry parameter β (a_s^1), or as we have a functional, by performing the second derivative around symmetric nuclear matter (a_s^2). The latest calculation is the exact one. We note a systematic underestimation by about 1-2 MeV of the symmetry energy assuming a quadratic behavior. This is a small error with respect to the difference in energy between symmetric nuclear matter and pure neutron matter.

In this context it is worth to mention that RMF fits to finite nuclei require relatively high compression moduli $K \sim 300$ MeV (Lalazissis et al., 1997; Ring, 1996). Equations of state with a stiff high density behavior stand, however, in contrast to the information extracted from heavy ion reactions (Sturm et al., 2001; Fuchs et al., 2001). The pure RMF fits to the DBHF EOS, i.e. discarding the low density correction term, provide equations of state which are stiff, however, not due to their high density behavior but do to the low density part. The compression moduli of the pure RMF contributions without correction term are K=365 MeV in contrast to the soft DBHF EOS with K=230 MeV. If one assumes that the correction terms contain effectively contributions from the deuteron and/or reflect the precursor of a superfluid low density state which leads to additional binding in infinite matter, but plays no substantial role in finite nuclei, this could explain the discrepancy between the EOS obtained from RMF fits to finite nuclei and that predicted by DBHF or the a low density virial expansion (Horowitz and Schwenk, 2006b).

2.4.3 Final remarks

Since, one of the open problems in nuclear structure is how to predict properties of finite nuclei from the knowledge of a bare nucleonnucleon interaction of the meson-exchange type, a promising starting point consists in Dirac-Brueckner-Hartree-Fock (DBHF) calculations using realistic nucleon nucleon interactions like the Bonn potentials, which are able to reproduce satisfactorily the properties of symmetric nuclear matter without the need for three-body forces, as is necessary in non-relativistic BHF calculations (Van Giai et al., 2010). However, the DBHF formalism is still too complicated to be used directly for finite nuclei and a possible route is to define effective Lagrangians with density-dependent nucleonmeson coupling vertices (Fuchs et al., 1995; Typel and Wolter, 1999), which can be used in the relativistic Hartree (or relativistic mean field (RMF)) or preferably in the relativistic HartreeFock (RHF) approach (Long et al., 2004; Long et al., 2006; Long et al., 2007). The matching between the density-dependent RMF or RHF is however usually believed to be done at or around saturation density (Van Giai et al., 2010; Van Dalen and Müther, 2011).

Completely consistent calculations in this scheme still have to be performed, but it would also be interesting to extrapolate the matching of the density dependence of the effective Lagrangians down to one tenth of saturation density where large deviations between ordinary mean fields and DBHF are expected. The impact of the low density regime on the description of nuclei, by fitting new density dependences of the effective Lagrangian, is a project that was initiate by Elisabeth Massot during her Post-doc at Orsay (2009-2011). She is continuing part-time and results are expected soon.

2.5 Conclusions and outlooks

In this chapter, we have discussed some improvements of the in-medium nuclear interaction such as the correction in the spin channel of the Skyrme interaction, a model partially based on the low momentum interaction V_{lowk}, and the deviation at low-density between usual mean-field models and the G-matrix. A general and unified model for the in medium nuclear interaction is still not known while a large amount of efforts are developed to improve the present models.

The large amount of data continuously accumulated in all branches of nuclear physics, such as the ground state properties of exotic nuclei, the collective excitations in nuclei, but also the informations obtained by the heavy-ion collisions at various energies offers a wide range of phenomenons where nuclear modeling can be tested. The additional inclusion of the properties of dense matter existing in the core of neutron stars gives even tighter constraints to the nuclear models. In this chapter, we have illustrated the needs for further developments in the nuclear interaction given by the constraints related to unstable spin modes as well as deviations at low-density between usual mean-field models and BHF or DBHF approaches. The recent developments establishing links between nucleon-nucleon interaction and the underlying QCD symmetries through the Effective Field Theory, as well as the universal properties of the nucleon-nucleon bare potential at low energy deduced from a renormalisation group approach can potentially renew the models for the low-energy nuclear interaction. In view of that, we have analyzed in this chapter a new model partially based on where the finite-range terms of the Skyrme interaction are replaced by the finite range $V_{\mathrm{low\,k}}$ interaction (Van Dalen et al., 2009). An interesting question is indeed related to the application at finite-density of the methods proposed in EFT. What are the relation between the low-energy QCD symmetries of the bare interaction with the medium corrections induced at finite density? In other words, does the low-energy QCD symmetries still give important constraints to the nuclear interaction in a dense medium? These questions has started to emerge and might irrigate the future developments in nuclear interaction modeling.

Chapter 3

Superfluid properties of dense medium

Studies on pairing effects in both nuclear matter and finite nuclei have shown intensified interests in the recent years. On one hand, various theoretical calculations of pairing gaps in pure neutron matter strongly disagree each other, which induce a large uncertainty on the superfluid properties of neutron stars and it observable realization, such as the crust thermal relaxation and the Giant glitches. On the other hand, large scale calculations for the ground state of finite nuclei using various pairing interactions fail to give strong constrains on the nature of the pairing density functional (PDF), such as its localization close to the surface of nuclei. This may indicate the needs for another approach, using additional constrains: should the PDF be extended, including new degrees of freedom to be sensible to the isospin degree of freedom for instance, and are there additional relevant observables to constrain the PDF? In this section, we will address these timely questions in order to better understand the pairing properties of both nuclei and neutron stars.

3.1 Introduction

In this chapter, we study the pairing properties in uniform matter and in spherical nuclei based on the Hartree-Fock-Bogoliubov (HFB) model (Ring and Schuck, 1980) choosing a Skyrme interaction for the particle-hole channel. Since the HFB model for spherical nuclei will be described in the chapter 5, we briefly review the HFB equations in uniform matter.

Pairing in uniform nuclear matter is evaluated with the BCS ansatz (Bardeen et al., 1957; De Gennes, 1989; Ring and Schuck, 1980) :

$$|BCS\rangle = \prod_{k>0}(u_k + v_k \hat{a}^\dagger_{k\uparrow}\hat{a}^\dagger_{-k\downarrow})|-\rangle \ , \tag{3.1}$$

where u_k and v_k represent the BCS variational parameters and $\hat{a}^\dagger_{k\uparrow}$ are creation operators of a particle with momentum k and spin $\uparrow$ on top of the vacuum $|-\rangle$ (Bardeen et al., 1957; De Gennes, 1989; Ring and Schuck, 1980). The BCS equations are deduced from the minimization of the energy with respect to the variational parameters u_k and v_k. For a contact interaction (3.7), the equation for the pairing gap Δ_τ, where τ=n or p, takes the following simple form at zero temperature,

$$\Delta_\tau = -\frac{v_0}{2} g[\rho_n, \rho_p] \frac{1}{(2\pi)^3} \int d^3k \frac{\Delta_\tau}{E_\tau(k)} \theta(k) \ , \tag{3.2}$$

where $\theta(k)$ is the cut-off function that can be introduced to regulate some interactions such as, for instance contact pairing interaction used hereafter, $E_\tau(k) = \sqrt{(\epsilon_\tau(k) - \nu_\tau)^2 + \Delta_\tau^2}$ is the neutron quasi-particle energy, $\epsilon_\tau(k) = \hbar^2 k^2 / 2m^*_\tau$ is the neutron single particle kinetic energy with the effective mass m^*_τ. The concept of effective mass is discussed in chapter 4. We define the effective neutron chemical potential

$\nu_\tau = \mu_\tau - U_\tau$, where the neutron mean field potential U_τ is subtracted from the neutron chemical potential μ_τ. The effective neutron chemical potential ν_τ gives the neutron density,

$$\rho_\tau = \frac{2}{V}\sum_k n_\tau(k) \tag{3.3}$$

where V is the volume and $n_\tau(k)$ is the occupation probability defined as

$$n_\tau(k) = \frac{1}{2}\left[1 - \frac{\epsilon_\tau(k) - \nu_\tau}{E_\tau(k)}\right] . \tag{3.4}$$

Finally, the nucleon Fermi momentum $k_{F\tau}$ is defined as $\rho_\tau \equiv k_{F\tau}^3/3\pi^2$. At zero temperature and without pairing correlation, $k_{F\tau}$ represents the momentum of the last occupied state for the nucleon τ.

The nuclear energy density $\epsilon(\rho, I)$, function of the total density ρ and of the asymmetry parameter $I = (\rho_n - \rho_p)/\rho$, is the sum of the Skyrme part, $\epsilon_{\rm Skyrme}$, that includes the kinetic energy (Bender et al., 2003), plus the pairing energy density,

$$\epsilon = \epsilon_{\rm Skyrme} + \epsilon_{\rm pair}. \tag{3.5}$$

Here, see for instance Eq. (37.53) of (Fetter and Walecka, 1971),

$$\epsilon_{\rm pair} = -\frac{1}{4}(N_n\Delta_n^2 + N_p\Delta_p^2) , \tag{3.6}$$

where N_τ is the density of states, given by $N_\tau = m_\tau^* k_{F\tau}/\pi^2\hbar^2$, with $\tau = n, p$.

After many years of study, there is still no unambiguous universal Pairing Density Functional (PDF) ranging on the whole nuclear chart, and current efforts are aiming in that direction. The problem may be due to the method used to constrain it, namely comparing the pairing gap with odd-even mass differences, or evaluating the separation energies along a given isotopic chain (Bender et al., 2003; Khan et al., 2009). It therefore may be useful to consider a more general context, such as to improve the form of the present pairing interactions or to change the description of pairing and introduce the bare interaction in the proper channel, and also to find additional observables that could constrain the pairing interaction in the different part of the nuclei for instance.

The pairing functional studies may thus enter in a new era, renewing the method to design the PDF:

- i) using an isospin dependence of the PDF ;
- ii) using the nuclear matter and neutron stars observables as an additional constrain for the PDF ;
- iii) looking for additional observables in nuclei than the odd-even mass staggering to constrain the PDF.

Point i) has been investigated in Ref. (Margueron et al., 2007a; Margueron et al., 2008) and will be commented in section 3.2. Motivated by the isospin dependence of the experimental odd-even mass difference (Vogel et al., 1984; Yamagami et al., 2009), it is expected that introducing the isospin degree of freedom in the PDF might unify the PDF in the neutron and proton channels. Point ii) is quite an ambitious task since the link between the PDF and the astrophysical observables might not be direct, but related to the complexity of the description of the neutrons stars. It will be discussed in the chapter 5. In this section 3.3 the properties of the Cooper pairs in uniform matter for various densities and isospin asymmetries are analyzed with respect to the BCS-BEC crossover. In the case of point iii) an obvious observable are pairing vibrations, measured through two-particle transfer(Broglia et al., 1973; von Oertzen and Vitturi, 2001). However in the 70-80's the transition has never been calculated fully microscopically. The first

microscopic calculations has been performed only recently (Khan et al., 2004), and several calculations followed (Matsuo et al., 2005; Avez and Simenel, 2008), showing the renewed interest for such studies.

The question of the behavior of the incompressibility modulus K_∞ with respect to the pairing gap is also raised since it seems clear from nuclear data that the finite nucleus incompressibility K_A decreases with increasing pairing gap (Khan et al., 2009). This apparent decrease of incompressibility in superfluid nuclei raises the question of a possible similar effect in infinite nuclear matter: until now, the nuclear matter incompressibility is evaluated by neglecting the pairing part of the functional. We report in this chapter the investigations that we have performed in this direction.

3.2 Density-dependent contact pairing interactions

The derivation of the pairing interaction on a non-empirical microscopic basis is being performed nowadays and pairing gaps have actually been obtained from low-momentum interactions V_{low-k} (Hebeler et al., 2009). However, in most of the available mean-field-based models, a more phenomenological attitude is still usually adopted also because the agreement between the theoretical V_{low-k}-gaps and the experimental values does not improve significantly with respect to what is obtained with empirical interactions. It is worth mentioning that in phenomenological interactions not only the bare interaction but also higher-order terms are taken into account in an effective way (Duguet, 2004). While in the Gogny case almost the same interaction is employed in both particle-hole and particle-particle channels, in Skyrme-mean-field-based models the pairing interaction which is used in the particle-particle channel is usually different from the interaction used in the mean-field channel (Garrido et al., 1999). This prevents the problems related to double counting in the particle-particle channel.

One of the current choices for the pairing interaction v_{nn} is a zero-range interaction acting on the singlet $^1\mathrm{S}_0$ channel,

$$\langle k|v_{nn}|k'\rangle = \frac{1-P_\sigma}{2} v_0\, g[\rho_n,\rho_p]\, \theta(k,k')\ , \tag{3.7}$$

where the cut-off function $\theta(k,k')$ is introduced to remove the ultra-violet divergence in the particle-particle channel (induced by the contact form of the interaction). A simple regularization could be done by introducing a cut-off momentum k_c. That is, $\theta(k,k') = 1$ if $k,k' < k_c$ and 0 otherwise. In finite systems, a cut-off energy e_c is usually introduced instead of a cut-off momentum k_c. The relation between the cut-off energy and the cut-off momentum may depend on the physical problem, and it is known that the pairing strength v_0 depends strongly on the cut-off.

The spatial structure of neutron Cooper pair in low density nuclear matter has been studied using both finite range interactions like Gogny or G3RS and density dependent contact interactions properly adjusted to mimic the pairing gap obtained with the former interactions (Matsuo, 2006). It was found that the contact interactions provide almost equivalent results compared to the finite range ones for many properties of the Cooper pair wave functions. It is thus reasonable to investigate the evolution of the Cooper pair wave function with respect to the density and the isospin asymmetry using contact interactions adjusted to realistic interactions.

The density-dependent functional $g[\rho_n,\rho_p]$ is often depending only on the isoscalar density $\rho = \rho_n + \rho_p$ but extensions of this form to include also a dependence on the isovector density $\rho_1 = \rho_n - \rho_p$ have been recently proposed (Margueron et al., 2007c; Yamagami et al., 2009). In the following, we review different approximations of the density-dependent function $g[\rho_n,\rho_p]$.

	η=0.35	η=0.65	η=1.00
SLy5 (Chabanat et al., 1998a; Chabanat et al., 1998b)	-285	-390	-670
Sk255 (Agrawal et al., 2003)	-265	-390	-600
Sk272 (Agrawal et al., 2003)	-265	-390	-600
LNS (Cao et al., 2006b)	-250	-390	-670

Table 3.1: Strength v_0 (in MeV·fm^3) of the pairing interactions obtained in the case of various Skyrme functionals. The parameter α in (3.8) is set to $\alpha = 1$. The values of v_0 are adjusted, for each η, to obtain similar S_{2n} in Tin isotopes (Khan et al., 2009) The energy cutoff for the pairing window is taken to be 60 MeV.

3.2.1 Isoscalar density-dependent pairing interaction

In its standard form (isoscalar form), the density dependent term $g[\rho_n, \rho_p]$ is expressed as

$$g[\rho_n, \rho_p] = 1 - \eta \left(\frac{\rho}{\rho_0} \right)^{\alpha}, \tag{3.8}$$

where $\rho = \rho_n + \rho_p$. If η=0, the pairing interaction is qualified as being of volume kind, while if η=1, the pairing interaction is said to be of surface kind since the pairing interaction is quenched in the bulk part of nuclei.

The parameters appearing in the expression of the pairing interaction (3.8) are fitted on nuclear properties following different criteria. One of these criteria consists in using the experimental odd-even mass staggering as a constraint and this choice has been extensively analyzed (Dobaczewski et al., 1984; Goriely et al., 2007; Dobaczewski et al., 2001; Duguet et al., 2001a; Duguet et al., 2001b). ^{120}Sn is often considered as an archetype of superfluid nucleus where the pairing interaction is empirically adjusted and employed for intermediate and heavy nuclei. The pairing interaction has however to be readjusted for lighter nuclei. Another empirical criteria is to use the two-neutron separation energy, $S_{2n}(N) = E(N) - E(N-2)$, where $E(N)$ is the total energy of a nucleus with N neutrons (Bender et al., 2003; Khan et al., 2009). An example of parameters is given in Table 3.1. These empirical recipes to adjust the pairing interaction give however very similar results. The pairing interaction shall moreover be readjusted through the nuclear chart. The PDF obtained in such a way is therefore not universal.

A global adjustment of the pairing interaction through the nuclear chart have been performed assuming either a surface kind pairing form or a mixed type (Bertsch et al., 2009). A slight improvement of the gobal rms between the experimental masses and the predicted one's have been found with the mixed form of the isoscalar pairing interaction. However, the improvement is quite moderated. More recently, a real improvement have been obtained using an additional isoscalar density dependence in the PDF. This is reviewed in the following.

3.2.2 Non-empirical isoscalar and isovector densities-dependent pairing interaction

Recently, we have introduced a more general types of pairing interactions and the novelty is a dependence on the ratio of neutron to proton composition of the considered system (Margueron et al., 2007a;

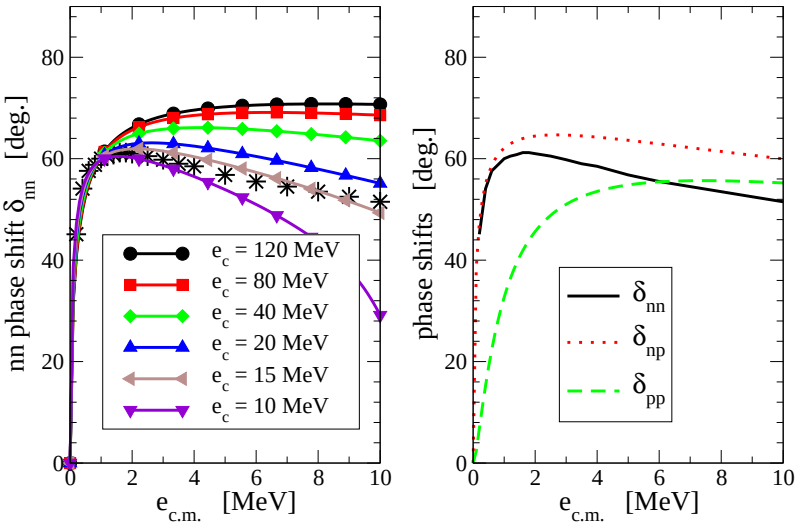

Figure 3.1: Phase shifts for s-wave nucleon-nucleon scattering as a function of the center of mass energy. In the left panel are shown nn phase shifts obtained from Argonne v_{18} potential (Esbensen et al., 1997) (stars) and the result of the best adjustment obtained with a contact interaction for a set of cut-off energies (from 10 to 120 MeV). In the right panel are shown the s-wave phase shifts for various channels: nn, np and pp. The np and pp phase shifts have been provided by the Nijmegen group (http://nn-online.org).

Margueron et al., 2008). We thus define the density dependent function $g_n[\rho_n, \rho_p]$ in Eq. (3.7) as

$$g_n[\rho_n, \rho_p] = 1 - f_s(I)\eta_s \left(\frac{\rho}{\rho_0}\right)^{\alpha_s} - f_n(I)\eta_n \left(\frac{\rho}{\rho_0}\right)^{\alpha_n}, \tag{3.9}$$

where I is the asymmetry parameter, defined as $I = (N-Z)/(N+Z)$, and ρ_0=0.16 fm^{-3} is the saturation density of symmetric nuclear matter. In Eq. (3.9), the interpolation functions $f_s(I)$ and $f_n(I)$ are not explicitly known but should satisfy the following condition $f_s(0) = f_n(1) = 1$ and $f_s(1) = f_n(0) = 0$. For simplicity we choose the linear interpolation between $I = 0$ and $I = 1$ which fixes the functions f_s and f_n as $f_s(I) = 1 - f_n(I)$ and $f_n(I) = I$. Since we proposed this model, additional microscopic calculations have been performed and can be used to help the interpolation in asymmetric matter (Zhang et al., 2010). Notice that the proton pairing interaction is simply given satisfying isospin symmetry, $g_p[\rho, I] = g_n[\rho, -I]$.

We have 5 parameters to adjust: v_0, η_s, α_s, η_n and α_n. These parameters are calibrated such that the pairing interaction reproduces the important feature of the low energy nucleon scattering and the BCS pairing gaps in symmetric and neutron matter based on the nucleon-nucleon interaction (Cao et al., 2006a). The motivation for choosing these constrains are the following: we aim at designing a pairing interaction that could describe the low-density neutron gas in the crust of neutron stars and we want at the same time to describe the pairing properties in the nuclear clusters in the crust of neutron stars and the isolated nuclei that exist or are produced on earth.

In the following, we give additional details on the procedure to constrain the pairing interaction. In Ref. (Bertsch and Esbensen, 1991), it has been proposed to deduce the free interaction parameter v_0 from the low energy phase shift of nucleon-nucleon scattering. The nn, np and pp phase shifts versus the center of mass energy are shown on the right panel of Fig. 3.1. It is clear from this figure that each of these three channels are different and the interaction parameter v_0 should depend on the channel of interest. In this work, we are interested only in the nn channel. We then express the phase shift as a function of the cut-off

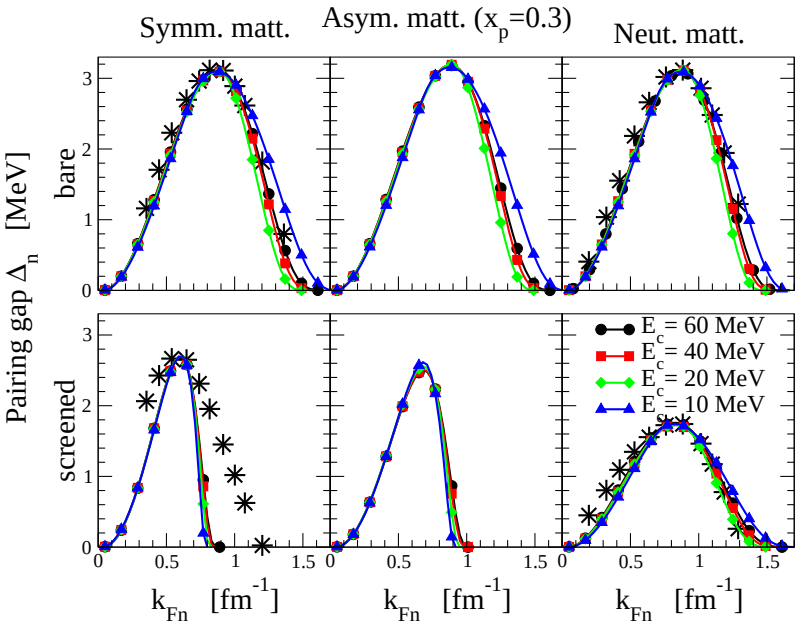

Figure 3.2: (Color online) Pairing gap in symmetric, asymmetric ($x_p = \rho_p/\rho$) and neutron matters adjusted to the "bare gap" (upper panel) or to the "screened gap" (lower panel) for various cut-off energies E_c. The pairing gap calculated from the microscopic treatment presented in Ref. (Cao 2006) is also shown as star symbols.

momentum k_c and the scattering length a_{nn} (Esbensen et al., 1997; Garrido et al., 1999):

$$k\cot\delta \;=\; -\frac{2}{\alpha\pi}\left[1+\alpha k_c+\frac{\alpha k}{2}\ln\frac{k_c-k}{k_c+k}\right]=-\frac{1}{a_{nn}}-\frac{k}{\pi}\ln\frac{k_c-k}{k_c+k} \tag{3.10}$$

where $\alpha = 2a_{nn}/(\pi - 2k_c a_{nn})$. In this way, for a given cut-off momentum k_c, the phase shift can be adjusted using the scattering length a_{nn} as a variable. Notice that the empirical value of the scattering length $a_{nn} = -18.5$ fm is large. A consequence of the large scattering length is that low-density neutron matter is very close to the unitary limit (infinite scattering length).

Fixing $e_c = \hbar^2 k_c^2/m$ and a_{nn}, one can deduce the interaction strength $v_0 = 2\pi^2\alpha\hbar^2/m$ and the effective range $r_{nn} = 4/\pi k_c$. Since the scattering length is large, one can deduce the interaction strength approximately from the relation $v_0 \approx v_0^\infty\,(1+\pi/2k_c a_{nn}+\dots)$ where $v_0^\infty = -2\pi^2\hbar^2/mk_c$ is the interacting strength in the unitary limit ($k_c a_{nn}\to\infty$).

We have chosen to adjust the density dependent function g of our interaction to the results of nuclear matter pairing gaps in Ref. (Cao et al., 2006a) since it was at this time the only calculations performed for both symmetric and neutron matters. More recent calculations of pairing gaps in asymmetric matter have now been calculated and shall be used in our framework (Zhang et al., 2010). The results of the fits are shown in Fig. 3.2. One should note that for the bare interaction, even if the pairing gap is identical in symmetric and neutron matters, the adjusted contact interaction is not necessarily isoscalar. Indeed, the transformation from the Fermi momentum, the x-axis of Fig. 3.2, to the density is different in symmetric nuclear matter, $\rho/\rho_0 = (k_{Fn}/k_{F0})^3$ (where $\rho_0 = 2/(3\pi^2)k_{F0}^3$=0.16 fm^{-3}), and in neutron matter, $\rho/\rho_0 = 0.5(k_{Fn}/k_{F0})^3$. Therefore, an interaction which depends only on the ratio ρ/ρ_0 gives different results if it is plotted as a function of k_{Fn} in symmetric and neutron matters. As the pairing gap calculated with the bare interaction (Cao et al., 2006a) is quasi-identical in symmetric and neutron matters when it is plotted versus k_{Fn}, one can then deduce the following relations between the parameters of the density dependent

term g_1 (neglecting the isospin dependence of the effective mass): $\alpha_s = \alpha_n$ and $\eta_s = \eta_n/2^{\alpha_n}$.

For the bare pairing gap and for a given cut-off energy E_c, the position and the maximum value of the gap are reproduced well by the contact interaction in Fig. 3.2. However, in the high Fermi momentum region $k_{Fn} > 1$ fm^{-1}, we can see appreciable difference between the microscopic predictions and the pairing gap obtained from the contact interactions. The best agreement is obtained for a cut-off energy $E_c = 40$ MeV. In the screened case, the dependence of the pairing gap on k_{Fn} is badly reproduced, especially for symmetric nuclear matter. This is because the maximum position of the pairing gap is shifted towards a lower neutron Fermi momentum (one third in density from that for the bare gap). Consequently, the density dependence of the function g_1 becomes stiffer in the "screened" case than in the bare case, and the gap drops faster after the maximum, as it is shown in Fig. 3.2. This may indicate that the screened interaction has a different density dependence and cannot be cast into a simple power law of the density as in Eq. (3.9). In our work (Margueron et al., 2007a) we decided to include the corrections of the screened interaction in the density dependence of the pairing gap. In doing so, we realized that pairing in nuclei is much reduced. We also realized latter that it might not be the most appropriate treatment of the polarization effects. In this manuscript, I therefore decided not to discuss much on the screening corrections to the pairing interaction. The parameters of the pairing interactions for various cut-off are given in Ref. (Margueron et al., 2007a).

Eventually, it was remarked in Ref. (Margueron et al., 2007a) that the pairing interaction that reproduce the bare BCS pairing gaps in both symmetric and neutron matter might be obtained from a simple form

$$g_n[\rho_n] = 1 - \eta \left(\frac{\rho_n}{\rho_0}\right)^{\alpha} \tag{3.11}$$

with $\alpha \approx 0.5$ and $\eta \approx 1$. The parameters of the pairing interactions for various cut-off are given in Ref. (Margueron et al., 2007a). It is in agreement with the analysis performed in (Duguet, 2004).

Let us next compare the experimental OES with the mean pairing gap calculated from the pairing field $\Delta_{\rm n}(r)$ as,

$$\Delta_{\rm n} \equiv \frac{1}{N} \int d^3r \rho_{\rm n}(r) \Delta_{\rm n}(r) \ , \tag{3.12}$$

where $N = \int d^3r \rho_{\rm n}(r)$ is the number of neutrons. In the next section, we will discuss also another formula for the mean pairing gap. The results are shown in Fig. 3.3. We remind the reader that this comparison should be taken with caution and we have removed from the comparison the OES calculated at the neutron shell closure. It is observed that the pairing gaps obtained with the interaction IS+IV Induced are systematically too small along the isotopic chains. This is the reason why the results with the interaction IS+IV Induced are close to the HF calculations in Fig. 3.3. Contrary, the results with the interaction IS+IV Bare are in good agreement with the experimental OES, including the isotopic trend for all the four isotopic chain.

3.2.3 Empirical isoscalar and isovector densities-dependent pairing interaction

Concomitantly with our work on isovector density-dependence of the pairing interaction (Margueron et al., 2007a; Margueron et al., 2008), Yamagami and collaborators have investigated a different isovector dependence and have set-up a different adjustment procedure (Yamagami et al., 2009). In their work, they defined the following density-dependent pairing functional,

$$g_\tau \left[\rho, \rho_1\right] = 1 - \eta_0 \frac{\rho\left(\boldsymbol{r}\right)}{\rho_0} - \eta_1 \tau_3 \frac{\rho_1\left(\boldsymbol{r}\right)}{\rho_0} - \eta_2 \left[\frac{\rho_1\left(\boldsymbol{r}\right)}{\rho_0}\right]^2 , \tag{3.13}$$

where $\tau_3 = 1$ for $\tau = n$ (neutron) and -1 for p (proton) and $\rho_1 = \rho_n - \rho_p$.

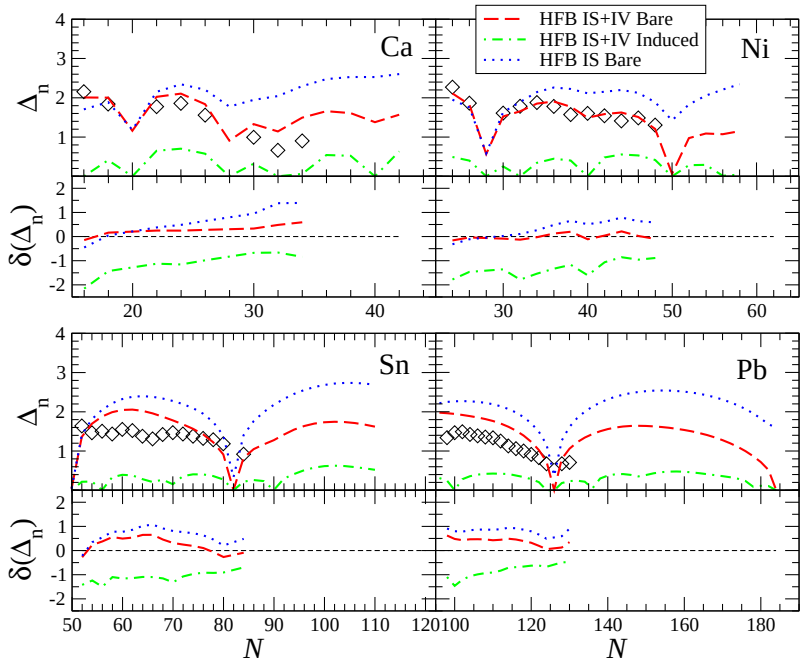

Figure 3.3: Comparison of the HFB pairing gaps $\Delta_{\rm n}$ calculated with Eq. (3.12) with the OES given by $\Delta^{(3)}$ for a series of semi-magical nuclei. The value $\delta(\Delta_{\rm n})$ is defined as $\delta(\Delta_{\rm n}) = \Delta_{\rm n}({\rm th.}) - \Delta_{\rm n}({\rm exp.})$. The solid line shows the results without pairing interaction (HF), while the dotted, short dashed, and long dashed lines are obtained with the pairing interactions IS+IV Bare, IS+IV Induced and IS Bare, respectively. For each isotopic chain, we also plot the difference $\delta({\rm B}/A) = {\rm B(th.)}/A - {\rm B(exp.)}/A$ between the theoretical and the exprimental values for the binding energy. All units are given in MeV.

In a recent work, we have extended the number of nuclei where the pairing interaction is adjusted. The original region is indicated in Fig. 3.4 are denoted as Zone 0 (Yamagami et al., 2009), while the new fit is performed for the nuclei represented in Fig. 3.4 (Zone 0, 1, 2 and 3) (Yamagami et al., 2012).

By comparing two different fitting procedures on a large number of nuclei, it is shown that the strength parameter v_0 of the pair-DF is very well constrained and that the isoscalar-density dependent parameter η_0 can be determined almost uniquely for several Skyrme forces in the particle-hole channel by adjusting to the neutron and the proton pairing gaps with the isovector-density terms. The parameter η_1 is therefore important, but its value is however less tightly constrained. It is concluded from this global adjustment through the mass table shown in Fig. 3.4 that the isovector-density helps in defining a unique pairing interaction for both neutrons and protons which respect the isospin symmetry.

The parameters of the pairing interaction are given in Ref. (Yamagami et al., 2012).

3.2.4 Final remarks

Several other modelizations and analyses of the isospin-density dependence of the pairing interaction has recently been carried on. An method to extract the pairing interaction strength from the pairing gaps in uniform matter has been proposed and used by the *Brussel group* to improve the fit of the HFB microscopic mass formula (Chamel et al., 2008; Chamel, 2010). Pairing gaps in asymmetric matter have recently been calculated (Zhang et al., 2010) and can be used to adjust the interpolation function between symmetric and neutron matter in (3.9).

Finally, a similar global study through the nuclear chart, as the one carried out in Ref. (Bertsch et al.,

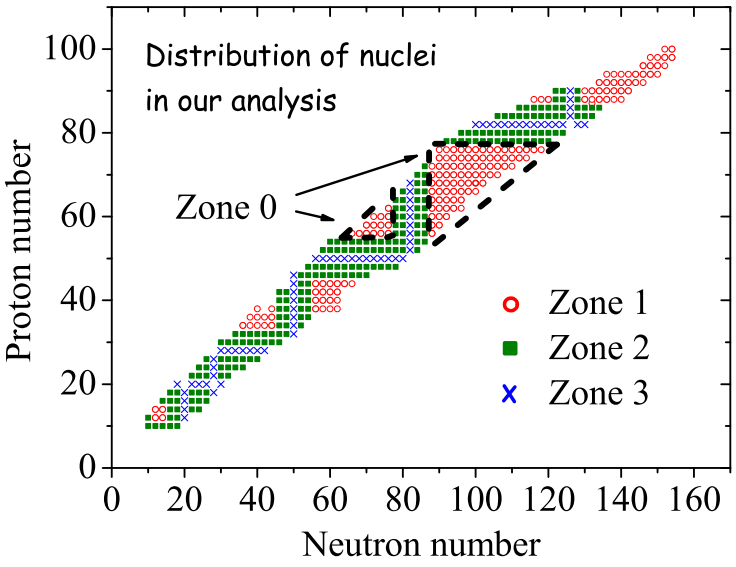

Figure 3.4: Experimental pairing gaps of even-even nuclei are grouped into Zone 1, 2, and 3. The subset of Zone 1, which we call Zone 0, is also indicated.

2009) replacing the isoscalar from (3.8) by the isovector one (3.9), has shown a major improvement of the rms deviation between the experimental masses and the predicted ones (Bertulani et al., 2009; Bertulani et al., 2012). It was mainly shown that the effect of the isovector-density dependence is the reconcile the parameters of the pairing interaction for both the neutron and the proton channel. This conclusion is also in agreement with the one that we obtained in Ref. (Yamagami et al., 2012).

The isovector-density dependence of the DFP hat was originally proposed (Margueron et al., 2007a) to reconcile the pairing models in uniform matter with that in used in the Wigner-Seitz cells in the crust of neutron stars have also provided an improvement in the calculation of the pairing correlations in finite nuclei. The agreement is of the same quality as the one obtained using $V_{low k}$ interaction in the pairing channel (Hebeler et al., 2009). It can therefore be concluded that an isovector-density dependence of the PDF have help the design of a universal PDF, and that the relation between the pairing properties of uniform matter and of nuclei can be treated on equal footing.

3.3 Properties of the Cooper pair in dilute matter

The spatial localization of two paired neutrons in low density medium which corresponds to the surface of the nucleus (Pillet et al., 2007; Pillet et al., 2010) opens the question of condensation of the cooper pairs in finite nuclei (Hagino et al., 2007; Hagino et al., 2010). The same conclusion is drawn in Ref. (Matsuo et al., 2005; Matsuo, 2006), by analyzing the di-neutron configuration in the excitation spectrum of finite nuclei, and also performing calculations in low density matter. The discussion concerning the nature of the paired wave function can be simply formulated in terms of the BCS and the BEC limits where the paired wave function is either widely expanded (BCS), or is condensed in a very narrow volume (BEC). In the following, we study the BCS-BEC crossover in dilute nuclear matter as a function of the isoscalar density ρ and the isospin asymmetry I.

$(k_{Fn}a_{nn})^{-1}$	$P(d_n)$	ξ_{rms}/d_n	Δ_n/ϵ_{Fn}	ν_n/ϵ_{Fn}	
-1	0.81	1.10	0.21	0.97	BCS boundary
0	0.99	0.36	0.69	0.60	unitarity limit
1	1.00	0.19	1.33	-0.77	BEC boundary

Table 3.2: Reference values of $(k_{Fn}a_{nn})^{-1}$, $P(d_n)$, ξ_{rms}/d_n, Δ_n/ϵ_{Fn} and ν_n/ϵ_{Fn} characterizing the BCS-BEC crossover in the regularized model for the contact interaction. The values d_n, $P(d_n)$, and $\xi_{\rm rms}$ are the average distance between neutrons $d_n = \rho_n^{-1/3}$, the probability for the partner neutrons correlated within the relative distance d_n, and the rms radius of Cooper pair, respectively. The numbers have been taken from Refs. (Engelbrecht 1997; Matsuo 2006).

3.3.1 BCS/BEC Crossover

It has been proposed to define the limit of the BCS-BEC phase transition using a regularized model for the pairing gap (Engelbrecht et al., 1997; Papenbrock and Bertsch, 1999; Matsuo, 2006). Although the BCS ansatz has been developed to describe the Cooper pair formation in the weak BCS regime (Bardeen et al., 1957), it has been shown that the BCS equations are also valid in the strong BEC condensation regime (Nozières and Schmitt-Rink, 1985; Pieri and Strinati, 2003). The BCS equations are thus adopted in this section as a useful framework to describe the intermediate BCS-BEC crossover regime at zero temperature (Engelbrecht et al., 1997). In this model, the BCS gap is combined with the relation between the interaction strength and the scattering length (3.10) which has a similar divergent behavior. The difference between those two divergent integrals gives a regularized equation,

$$\frac{m_n}{4\pi a_{nn}} = -\frac{1}{2V}\mathrm{Tr}\left(\frac{1}{E_n(k)} - \frac{1}{\epsilon_n(k)}\right) , \tag{3.14}$$

which has no divergence. The gap equation can be solved analytically for the contact interaction with a constraint of the particle number conservation. The solution of this regularized gap equation is independent of the strength of the interaction, and the gap is uniquely determined by the value of the scattering length a_{nn}. From Eq. (3.14), one can study the boundaries of the BCS-BEC phase transition with respect to the dimensionless order parameter $k_{Fn}a_{nn}$.

We give in Table 3.2 the values of several quantities which specify the BEC/BCS crossover: the probability $P(d_n)$ for the partner neutrons to be correlated within the relative distance d_n (d_n is the average distance between neutrons $d_n = \rho_n^{-1/3}$), the ratio of the rms radius to the mean neutron distance ξ_{rms}/d_n, where the rms radius is defined as $\xi_{rms} = \sqrt{\langle r^2\rangle} = \sqrt{\int dr r^4 |\Psi_{pair}(r)|^2}$, the ratio of the pairing gap to the single particle kinetic energy Δ_n/ϵ_{Fn} and also the ratio of the effective neutron chemical potential to the kinetic energy of the unpaired system at the same density ν_n/ϵ_{Fn}. As we already mentioned, these boundaries are indicative because the phase transition is smooth at the boundaries.

The order parameters listed in Table 3.2 are closely related. For instance, approximating ξ_{rms} by ξ_P, the Pippard's coherence length $\xi_P = \hbar^2 k_{Fn}/m_n^*\pi\Delta_n$, it could be shown that the ratio ξ_{rms}/d_n is proportional to ϵ_{Fn}/Δ_n. Since the strong coupling regime BEC is reached if the ratio ξ_{rms}/d_n is small, the ratio Δ_n/ϵ_{Fn} shall therefore be large in the BEC regime. The effective neutron chemical potential ν_n could be interpreted as being half of the binding energy of Cooper pairs at finite density according to the Schrödinger-like equation of a Cooper pair (Nozières and Schmitt-Rink, 1985; Margueron et al., 2007a). The sign of ν_n gives therefore an indication on the Cooper pair: a negative sign can be interpreted as a quasi-bound state close to the BEC limit, while a positive sign will indicate that the Cooper pair is weakly coupled as in the BCS limit. The scale is given by the Fermi energy of the uncorrelated system $/\epsilon_{Fn}$, the ratio ν_n/ϵ_{Fn}

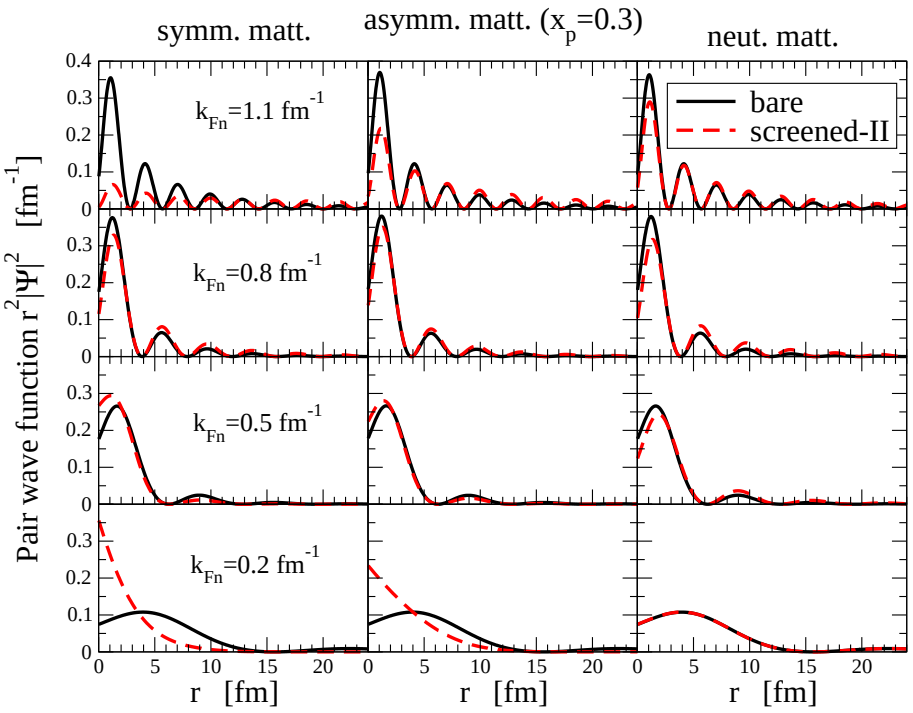

Figure 3.5: Neutron Cooper pair wave function $r^2|\Psi_{pair}(r)|^2$ as a function of the relative distance r between the pair partner at the Fermi momenta k_{Fn}=1.1, 0.8, 0.5 and 0.2 fm^{-1}.

therefore provides an order parameter of the BCS/BEC crossover.

It is expected that the correlations between two neutrons get larger as the density decreases and as a consequence, the BCS-BEC crossover occurs in the uniform matter at low density (Matsuo, 2006). The radial shape of the Cooper pair wave function changes as a function of the density and the asymmetry (Matsuo, 2006; Margueron et al., 2007a). It is deduced from the Fourier transform of $\Psi_{pair}(k) = u_k v_k = \Delta_n/2E_n(k)$ (Nozières and Schmitt-Rink, 1985). The neutron Cooper pair wave function $r^2|\Psi_{pair}(r)|^2$ is shown in Fig. 3.5 as a function of the relative distance r between the pair partners taking different Fermi momenta k_{Fn}=1.1, 0.8, 0.5 and 0.2 fm^{-1}, which correspond respectively to the densities: ρ_n/ρ_0=0.3, 0.1, 0.03 and 0.002. Calculations in symmetric, asymmetric and neutron matters are shown in the left, middle and right panels, respectively. In Fig. 3.5, we observe that the spatial extension and the profile of the Cooper pair varies strongly with the density. A large extension is found close to the saturation density at k_{Fn}=1.1 fm^{-1}. The profile of the wave function behaves as an oscillation convoluted by a decreasing exponent and casts into the well known limit $\sim K_0(r/\pi\xi_P)\sin(k_F r)/k_F r$ (Bardeen et al., 1957). This indicates that the Cooper pair is in the weak coupling BCS regime. At lower densities, the Cooper pair shrinks and the oscillation disappears. The wave function resembles now the strong coupling limit (BEC) $\sim \exp(-\sqrt{4m/\hbar^2\,|\mu|}r)/r$ (Pieri and Strinati, 2003). This is an indication that a possible BCS-BEC crossover may occur in uniform matter.

In Ref. (Margueron et al., 2007a) we studied the different order parameters given in Table 3.2 for the boundaries of the BCS-BEC crossover. Here I show only one illustrative example by looking at the rms radius of a Cooper pair ξ_{rms} in Fig. 3.6, as a function of the neutron Fermi momentum k_{Fn}. The order parameter ξ_{rms}/d_n is shown on the bottom part of Fig. 3.6. The rms radius of the Cooper pair is less than 5 fm in the region $k_{Fn} \sim (0.4 - 0.9)$ fm^{-1} ($\rho_n/\rho_0 \sim 0.01 - 0.15$) in the three panels for the bare interaction. The screened-II interaction gives different effects in symmetric and asymmetric matters: it

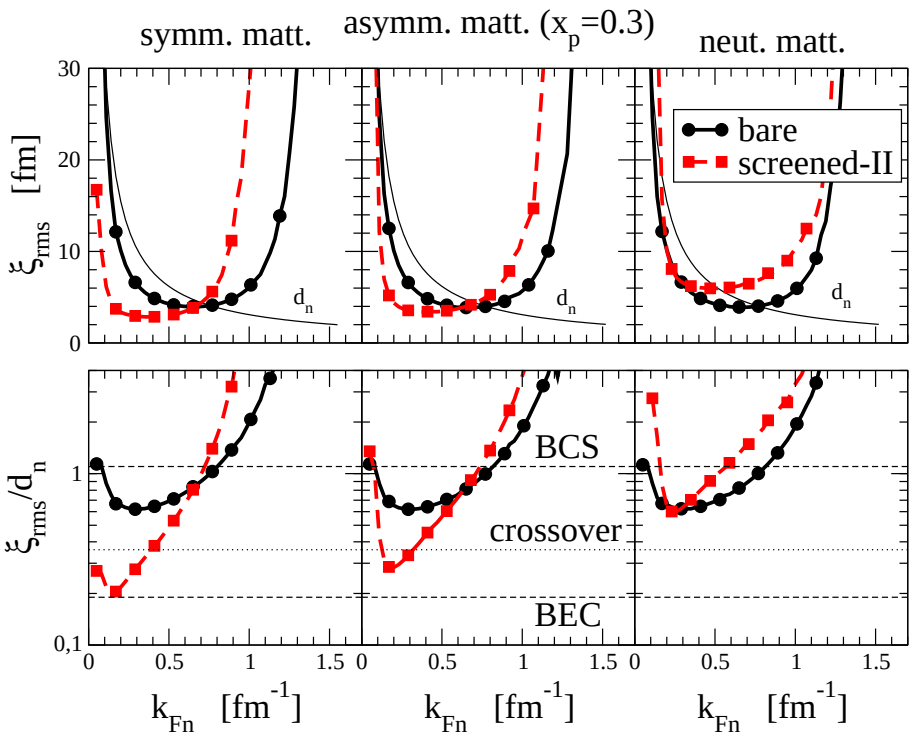

Figure 3.6: (Color online) Top panels: Comparison between the rms radius ξ_{rms} of the neutron pair and the average inter-neutron distance $d_n = \rho_n^{-1/3}$ (thin line) as a function of the neutron Fermi momentum k_{Fn} in symmetric (left panel), asymmetric (central panel) and neutron matters (right panel). Bottom panels: The order parameter ξ_{rms}/d_n as a function of k_{Fn}. The boundaries of the BCS-BEC crossover are represented by the two dashed lines, while the unitary limit is shown by the dotted line. The two pairing interactions are used for the calculations.

increases the rms radius for the neutron matter, while the rms radius stays small around 4 fm even at very low density at $k_{Fn} \sim 0.15$ fm^{-1} ($\rho_n/\rho_0 \sim 0.0007$) in symmetric matter. For the bare interaction, the size of the Cooper pair becomes smaller than d_n for the Fermi momentum $k_{Fn} < 0.8$ fm^{-1} ($\rho_n/\rho_0 \sim 0.1$) in general. There are substantial differences for symmetric and asymmetric matter in the case of the screened-II interaction. The crossover region becomes smaller for the neutron matter, while the crossover region increases in the cases of asymmetric ($x_p = 0.3$) and symmetric matter. Especially, the correlations becomes strong in symmetric matter and the Cooper pair reaches almost the BEC boundary at $k_{Fn} \sim 0.2$ fm^{-1} ($\rho_n/\rho_0 \sim 0.002$). Notice that the two-neutrons system is known experimentally to have a virtual state in the zero density limit. We have shown that this virtual state could lead to a strongly correlated BEC state at low density in symmetric nuclear matter according to the screened-II interaction.

3.3.2 Final remarks

The properties of the Cooper pairs in dilute nuclear matter has been investigated by use of the concept of BCS/BEC crossover. Going from saturation density ρ_0 down to $\rho_0/100$, it was shown the system goes from the BCS limit of extended and weakly coupled Cooper pairs towards the region of the BCS/BEC crossover, where is located the unitary limit. It indicates that the pairing correlations are stronger in dilute matter compared to saturation density where are located isolated nuclei.

Moreover, in the case of the screened interaction, the Cooper pairs are getting very close together at

densities of the order of $\rho_0/1000$ ($k_F \sim 0.1$ fm^{-1}) in symmetric matter. Such a system might be realized in the crust of neutron stars where nuclear clusters are embedded in a superfluid neutron gas. The neutron gas overlapping the nuclear cluster resemble the uniform matter close to symmetry. In this space region of the crust, the neutron gas might be strongly correlated and form a BEC state. The properties of the superfluid neutron flowing through the lattice made of nuclear cluster might be modified by the formation of *almost di-neutron* pairs around the nuclear clusters. The effects of the BEC condensation close to symmetric matter shall be further investigated within models of flowing neutrons such as the ones presented in Refs. (Chamel, 2005; Chamel, 2006; Di Gallo et al., 2011). However, close to symmetric matter, another condensate made of neutrons and protons, the deuteron, is expected to be formed below saturation density (Baldo et al., 1995). This condensate is so attractive that it destroys the nn and pp condensates. It is therefore difficult to clearly anticipate the effect of the formation of a strongly coupled BEC nn condensate in the crust of neutron stars.

3.4 Effects of superfluidity on the incompressibility and on the symmetry energy

The nuclear incompressibility and the symmetry energy are closely related to the isoscalar Giant Monopole Resonance (GMR) (Blaizot, 1980; Colò et al., 2004) and to the isovector Giant Dipole Resonance (GDR) (Trippa et al., 2008), respectively. These collective modes are observed in nuclei. The question of the effect of pairing correlations on the centroid energy of the GMR has been first addressed in Ref. (Civitarese et al., 1991), and it has recently known a renewed interest (Li et al., 2008b; Khan et al., 2009). In both the Sn and Pb isotopic chains, a specific increase of the GMR energy, associated with the corresponding finite nucleus incompressibility K_A, has been predicted for the doubly magic ^{132}Sn and ^{208}Pb nuclei (Khan et al., 2009; Khan, 2009). A part of this apparent stiffness of doubly magic nuclei may be related to pairing effects which in fact decrease the GMR energy in open-shell nuclei. However, this study has been undertaken only with a pure surface pairing interaction. It is therefore relevant to analyze more systematically this effect using various pairing functionals, and quantitatively estimate the effects of the pairing functional on the collective modes.

The density dependence of the symmetry energy is one of the most debated issues in nuclear physics at present. In fact, this has relevant implications (i) for nuclear structure, since it has an important effect on the size of the neutron root-mean-square (r.m.s.) radius in neutron-rich nuclei, (ii) for nuclear reactions, e.g., in intermediate energy heavy ion collisions where the isospin distribution of the reaction products is dictated by the density dependence of the symmetry energy, and obviously (iii) for the description of neutron stars. Review papers have been devoted to this topic (Steiner et al., 2005; Li et al., 2008a). Empirical information on the symmetry energy can be obtained from various sources, none of them being so far conclusive by itself. No measurement of the neutron skin is available which is accurate enough to constrain the symmetry energy. The properties of the isovector GDR, of the low-lying electric dipole excitations, and of the charge-exchange spin-dipole strength have been suggested as constraints (see e.g. (Klimkiewicz et al., 2007)). In addition, different model analysis of heavy-ion collisions have been proposed as a test of the main trend of the symmetry energy at densities below saturation. However, in none of these studies, to our knowledge, the problem of the pairing effects on the symmetry energy has been addressed.

In this work, the effects of the pairing correlations on the incompressibility and on the symmetry energy are studied consistently in symmetric nuclear matter and in finite nuclei. The effects coming from the correlation energy associated with the pairing force are included. An isoscalar pairing interaction of the form (3.8) is chosen in this section. More details are given in Ref. (Khan et al., 2010).

Fig. 3.7 displays the pressure $P(\rho)$, the incompressibility $K(\rho)$, and the symmetry energy $S(\rho)$ without

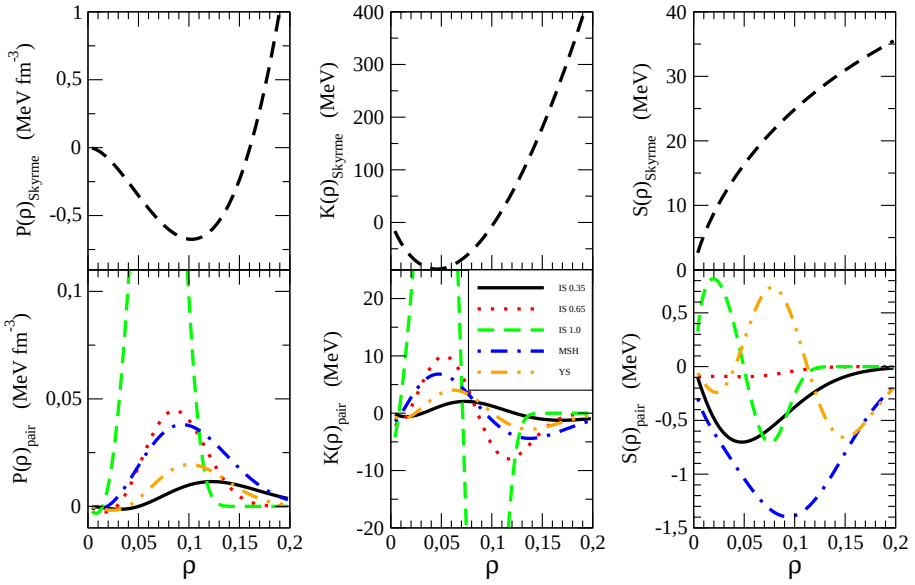

Figure 3.7: (Color online) Pressure, incompressibility, and symmetry energy without pairing (top panels), and the contributions of various pairing interactions to these quantities (bottom panels). The HF energy ϵ_{Skyrme} is calculated using the SLy5 interaction. For details, see the caption to Fig. 1 and the text.

pairing (top panels), and the contribution of pairing to these quantities (bottom panels), using the SLy5 Skyrme interaction. This contribution is calculated with the same equations, but considering only the pairing term of the energy density in Eq. (3.5). Close to the saturation density, the contribution from pairing is very small. In the case of the incompressibility K_∞, pairing can still produce a few % effect (for instance K_∞ is changed from 230.2 MeV to 223.9 MeV in the case of the MSH pairing interaction in table 3.3). The MSH, YS, IS 0.35 pairing interactions modify the incompressibility by 3 to 6 MeV, that is, by about 2%. It should be noted that at the saturation density, the contribution to the slope parameters of the symmetry energy, L, and $K_{\rm sym}$, of the interactions MSH and YS is larger than that of the other IS forces. The effects on L can be about 15% while $K_{\rm sym}$ can be modified in an important way. This is related to the dependence of these pairing interaction on the isovector density.

However at lower densities, the pairing effects become appreciably larger as seen in Fig. 3.7. In the case of the pure surface pairing, there are important contributions to the pressure, incompressibility and symmetry energy: these quantities can be strongly affected by pairing, which can lead to variations up to about a factor 2. Other pairing interactions also provide significant corrections to the pressure and the incompressibility, typically, around 10%. In the case of the symmetry energy, below $\rho \approx 0.1$ fm^{-3}, the IS+IV pairing interactions (MSH and YS) predict an opposite and positive contribution compared to the negative contributions of IS pairing interactions. It should be noted that the pairing contribution to these quantities is generally larger at densities below saturation.

It is expected that the above pairing effects at low densities may also affect finite nuclei. In the case of incompressibility, we can define a finite nucleus value K_A and expect that this value is affected by the pairing more than K_∞, due to the presence of a lower density region, i.e. the nuclear surface. The general expressions in uniform matter can be related with the observables in finite nuclei within the local density approximation (LDA). The aim is to estimate the role of pairing in the incompressibility and symmetry energy of finite nuclei in a simple and transparent way. The validity of the LDA will be estimated by comparing the predicted nuclei incompressibility with the one obtained by a microscopic approach.

Pairing	ρ_0 [fm^{-3}]	E/A(ρ_0) [MeV]	K_∞ [MeV]	J [MeV]	L [MeV]	$K_{\rm sym}$ [MeV]
no pairing	0.1604	-15.999	230.2	32.03	48.25	-112.3
IS η=0.35	0.1601	-15.998	227.3	31.93	48.49	-129.7
IS η=0.65	0.1603	-15.998	228.1	32.02	48.30	-113.7
IS η=1.00	0.1604	-15.999	230.1	32.03	48.25	-112.3
MSH	0.1599	-15.998	223.9	31.33	55.77	-139.7
YS	0.1602	-15.998	227.0	31.39	52.04	13.2

Table 3.3: Properties of nuclear matter for various pairing interactions. The SLy5 Skyrme force is used for the mean field.

In Ref. (Khan et al., 2010), we have obtained

$$K_A^{\rm LDA} = \frac{\rho_0}{A}\int d^3r\; K_{\rm Nucl}(r) \tag{3.15}$$

with

$$K_{\rm Nucl}(r) = \frac{\rho_0}{\rho}\; K(\rho(r)). \tag{3.16}$$

For small values of the density ($\rho \lesssim 0.6\rho_0$, that is r $\gtrsim$ 5 fm in ^{120}Sn), the incompressibility is found to be negative: this is due to the spinodal instability in nuclear matter which is not present in finite systems (Margueron and Chomaz, 2003). For this reason, the integral (3.15) is limited to the region where $K_A^{\rm LDA}(r)$ is positive. In this way, the spurious component due to the spinodal instability is removed.

Introducing the quantity

$$S_A(r) = \frac{1}{2\rho_0}\frac{\partial^2\epsilon}{\partial\delta^2}\bigg|_{\delta=0} = \frac{\rho}{\rho_0}S(\rho(r)), \tag{3.17}$$

the symmetry energy in nuclei reads

$$S_A^{\rm LDA} = \frac{\rho_0}{A}\int d^3r\; S_A(r). \tag{3.18}$$

We first perform a self-consistent HF calculation which provides the neutron and proton densities in ^{120}Sn. From these densities we deduce the radial distributions of mean field part and pairing part of $\epsilon(r)$ given in Eq. (3.5), $K_A^{\rm LDA}(r)$ and $S_A^{\rm LDA}(r)$. We obtain, in the SLy5 case, $B_A = -13.5$ MeV, $K_{\rm Nucl}$=119.8 MeV, and S_A=25.7 MeV without the contribution due to the pairing correlations and the Coulomb contribution has not been included. The value for $K_A^{\rm LDA}$ should be compared with that of 141 MeV obtained by the constrained HFB (CHFB) (Khan et al., 2010) (which includes the Coulomb interaction estimated to be of the order of 20 MeV in ^{120}Sn (Sagawa et al., 2007a; Sagawa et al., 2008)). The good agreement between the LDA and the CHFB results ensures that LDA provides a sound framework to relate the nuclear matter incompressibility and the finite nucleus one.

The contributions of pairing correlations to the binding energy, the bulk modulus and the symmetry energy are shown in Tab. 3.4 for the various pairing interactions considered. The contribution of the surface-type pairing (IS η=1.0) reduces K_A by about 5%, whereas, for the IS mixed-type (η=0.35 or 0.65) and the IS+IV (MSH and YS) pairing interactions, the effect on K_A is predicted to be smaller. In Table 3.4, it is also observed that pairing effects affect the binding energy by few percents, up to 5% for the surface-type

Pairing	$B_{\rm pair}$ [MeV]	$K_{\rm pair}$ [MeV]	$S_{\rm pair}$ [MeV]
IS η=0.35	-0.03	-0.5	-0.25
IS η=0.65	-0.11	-3.9	-0.03
IS η=1.00	-0.64	-6.0	-0.03
MSH	-0.13	-3.2	-0.93
YS	-0.05	-1.9	-0.24

Table 3.4: Contributions of pairing correlations to the binding energy, the incompressibility and the symmetry energy in ^{120}Sn. The mean field is calculated by using SLy5 interaction

pairing interaction. For the symmetry energy, pairing effects are negligible, being below 1% except the IS+IV pairing (MSH).

In finite nuclei, we use the sum rule approach in order to calculate the centroid energy of the isoscalar GMR. It is known that the finite nucleus incompressibility K_A is related to that centroid energy by means of the relation

$$E_{\rm ISGMR} = \sqrt{\frac{\hbar^2 K_A}{m\langle r^2\rangle}}, \tag{3.19}$$

where m is the nucleon mass and $\langle r^2\rangle$ denotes the ground-state expectation value of the square radius. In a microscopic approach, for the so-called scaling K_A, we calculate the energy as

$$E_{\rm ISGMR} = \sqrt{\frac{m_1}{m_{-1}}}. \tag{3.20}$$

where the $k-th$ energy weighted sum rule is defined as $m_k = \sum_i E_i^k |\langle i|\hat{Q}|0\rangle|^2$, with the RPA excitation energy E_i and the isoscalar monopole transition operator, $\hat{Q} = \sum_{i=1}^{A} r_i^2$. The m_1 moment is evaluated by the double commutator using the Thouless theorem (Thouless, 1961):

$$m_1 = \frac{2\hbar^2}{A}\langle r^2\rangle. \tag{3.21}$$

Concerning the evaluation of the m_{-1} moment, the CHFB approach is used. It should be noted that the extension of the constrained HF method (Bohigas et al., 1979; Colò et al., 2004) to the CHFB case has been recently demonstrated in Ref. (Khan, 2009) and employed also in (Khan et al., 2009). The CHFB Hamiltonian is built by adding the constraint associated with the IS monopole operator, namely

$$\hat{H}_{constr.} = \hat{H} + \lambda\hat{Q}, \tag{3.22}$$

and the m_{-1} moment is obtained from the derivative of the expectation value of the monopole operator on the CHFB solution $|\lambda\rangle$,

$$m_{-1} = -\frac{1}{2}\left[\frac{\partial}{\partial\lambda}\langle\lambda|\hat{Q}|\lambda\rangle\right]_{\lambda=0}. \tag{3.23}$$

It should be stressed that both K_A and K_∞ are here evaluated consistently in a microscopic model. As expected, K_A is clearly correlated with K_∞. To find out the pairing effects, we study the case of the open-shell nuclei ^{114}Sn and ^{120}Sn in Fig.3.8 for the four Skyrme interactions LNS, SLy5, Sk255 and Sk272. These four interactions span a large range of incompressibilities and have been fitted by using

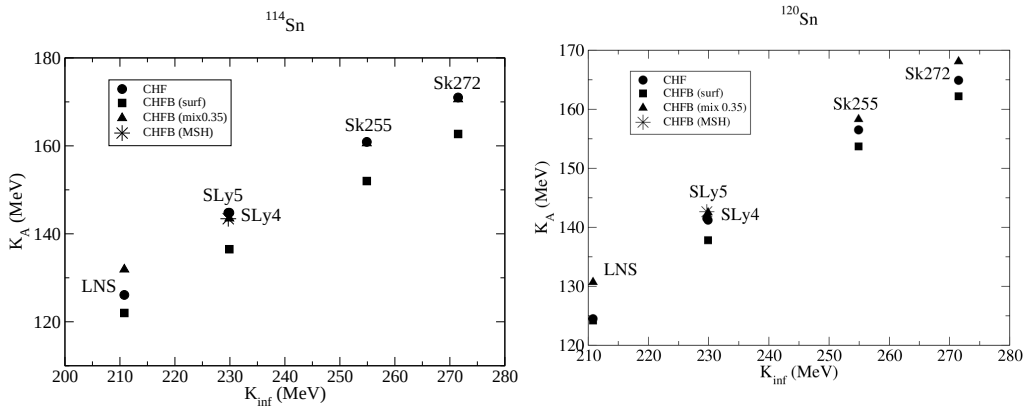

Figure 3.8: K_∞ versus K_A for ^{114}Sn (left) and ^{120}Sn (right) obtained by the CHF and the CHFB method with surface-type and mixed-type pairing interactions for several Skyrme interactions.

different physics inputs: the neutron matter EOS from realistic forces in the case of SLy5, Brückner-HF calculations in nuclear matter in the case of LNS, and the empirical properties of symmetric uniform matter plus a few binding energies and charge radii of selected nuclei (the same which had been used to fit some relativistic functionals like NL3) in the case of Sk255 and Sk272. In this sense, these interactions provide representative samples of the Skyrme functionals. Are shown: (i) the CHF result, without pairing, (ii) the CHFB result using the surface-type pairing interaction, and (iii) the CHFB result using the mixed-type (η=0.35) pairing interaction. In the case of SLy5, the IS+IV MSH pairing interaction is also used. The surface-type interaction decreases the finite nucleus incompressibility K_A by about 10% in ^{114}Sn and 5% in ^{120}Sn whereas the mixed-type pairing interaction has a negligible effect on K_A. Conversely, it should be reminded that the mixed pairing interaction has some effect on K_∞ whereas the pure surface pairing interaction has a negligible effect on K_∞, as seen on Fig. 3.8. In the case of LNS, the reduction of K_A is smaller for the surface pairing, and an increase of K_A is even observed for the mixed pairing case. In the SLy5 case, predictions using the IS+IV MSH pairing interactions show no variation of K_A but affects K_∞.

To study how these conclusions in ^{114}Sn are sensitive to the nuclear shell structure, the results for ^{120}Sn are also displayed in the right panel of Fig. 3.8, where pairing effects are expected to be smaller than in ^{114}Sn due to the subshell closure. In this case the reduction of K_A due to the surface-type pairing effect drops to 5%. For the mixed pairing interaction a small increase of K_A is observed. This feature is again more pronounced in the LNS case. In the SLy5 case, predictions using the IS+IV MSH pairing interactions show no variation of K_A but affects K_∞. It should be noted that similar trends are observed with the LDA predictions (See Table 3.4). Also, they are consistent with previous studies (Li et al., 2008b; Khan, 2009). To further study shell effects, the same calculations have been performed on ^{126}Sn, and a similar pattern than Fig. 3.8 is found, showing that the present results a rather independent from shell effects in open shell nuclei.

Evidently, the pairing effects tend to decrease the finite nucleus incompressibility K_A in the surface pairing case, whereas K_∞ is decreased in the mixed pairing case. Hence the question of constraining the pairing interaction through precise (typical resolution of few hundreds of keV) GMR measurement is raised. The systematic softness of open-shell Sn and Cd isotopes measured recently (Li et al., 2007; Li et al., 2010) through the energy of the GMR might be the sign of a surface pairing interaction at work (Khan, 2009).

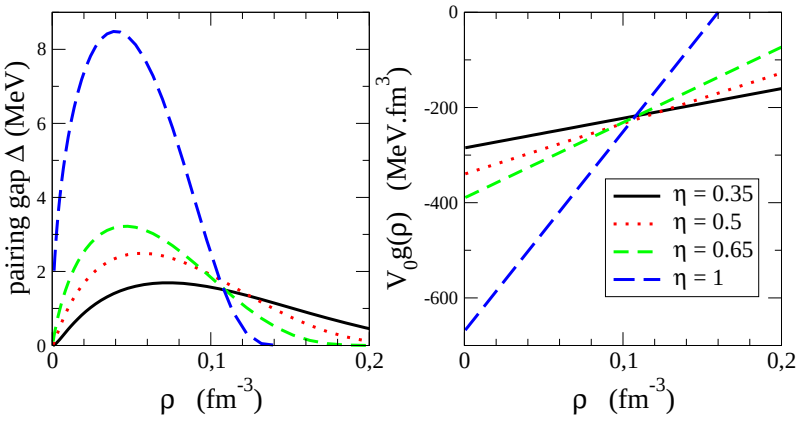

Figure 3.9: Pairing gap and pairing strength versus the density of uniform matter for different pairing interactions.

3.5 Constraining the pairing interaction with pairing vibrations

Let us introduce this section with Fig. 3.9 where is shown the pairing gap (left) and the interaction strength $V_0 g(\rho)$ (right) in symmetric matter and for the different isoscalar density-dependent pairing interactions (3.8). These pairing interaction has been adjusted to reproduce the two-neutron separation energy S_{2n} in Sn isotopes and for different values of the parameter η ranging from 0.35 to 1. In this section, we shall restrict to the PDF without isospin dependence and the parameters of these interactions are given in table 3.1 (Khan et al., 2009). It is observed from Fig. 3.9 that these different interactions leads to very different pairing gaps at low density, going from 2 to more than 8 MeV, while around saturation density, there is a density (ρ=0.11 fm^{-3}) at which the pairing gap and pairing strength suprizingly coincide for the four pairing interactions. Assuming a LDA this density correspond to a radius of about 5 fm in Tin isotopes ^{124}Sn and ^{136}Sn, and is localized at the surface of these nuclei.

From Fig. 3.9, two conclusions can be drawn: i) the two-neutron separation energy used to adjust the parameters of the pairing interaction is an observable which provides, on the average, a strong constrain on the pairing gap localized at the surface of the nuclei, and ii) to better constrain the value of the parameter η one shall find another observable sensible to the pairing strength at low density (large radius). Indeed, in the very external part of the nuclei the pairing strength is very different from one interaction to another. The pure surface pairing interaction predict a pairing gap as high as 8 MeV at low density while the various mixed pairing interaction are grouped below 3 MeV.

As stated above, it may be useful to consider an additional observable than the separation energy, in order to constrain the PDF. There are only few observables which could be relevant to constrain pairing effects. Among them, the first 2^+ state is know to depend on the properties of the pairing interaction (Khan et al., 2002; Khan et al., 2009). However, this mode might not bring a very different constrain than the average odd-even mass staggering. In our study, we shall prefer observable that are more sensible to the pairing properties at the surface of nuclei (von Oertzen and Vitturi, 2001). Pairing vibrations in heavy nuclei may be more adequate observable since they are known to be sensitive to the surface nature of the pairing interaction (Broglia et al., 1973). They can be probed for instance with two neutron transfer in nuclei close to shell closure. We refer to (von Oertzen and Vitturi, 2001; Broglia et al., 1973) for details on pairing vibrations. Basically, these modes corresponds to the (collective) filling of subshells, in transition from an A to A+2 nuclei. In order to extract the pairing properties around the surface of nuclei, one might use pair-transfer reaction mechanisms, like (α, ^{6}He) which is very surface peaked, coupled to microscopic

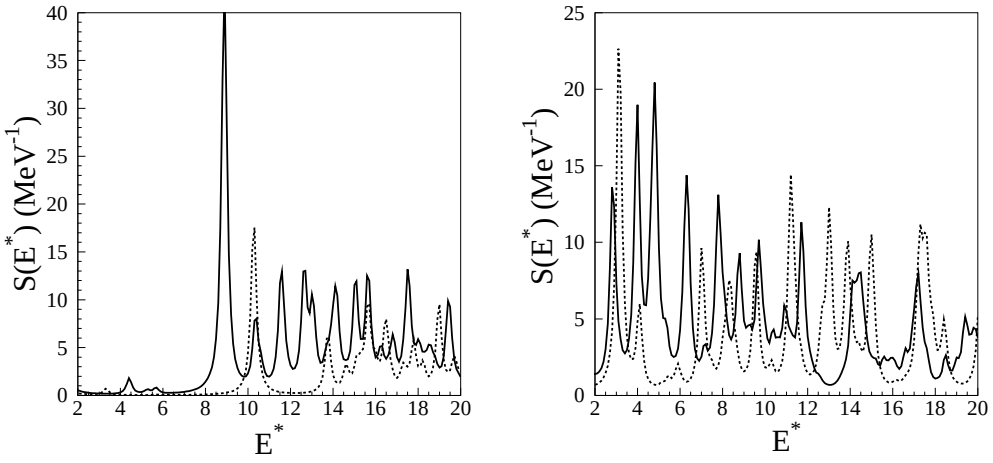

Figure 3.10: QRPA response function for ^{124}Sn in the two neutrons 0^+ addition mode. The pure surface mode is in solid line. In dashed line is a mixed surface/volume x=0.5 mode

calculation of pairing vibration.

In the following, we study the properties of pairing vibrations obtained from the various mixed and surface type pairing interactions in Fig. 3.9, and calculate the QRPA response for ^{124}Sn and ^{136}Sn nuclei that are spherical nuclei where pairing vibrations are likely to occur (von Oertzen and Vitturi, 2001). Moreover, one os these nuclei is stable and the second has a large neutron excess and can be named as being *exotic*. The neutron skins is therefore thicker for ^{136}Sn compared to ^{124}Sn. Surface effects in an isospin asymmetric environment and low-density pairing features are thus expected to be typically more important in ^{136}Sn. With the next-generation facilities, it is expected that beams of very neutron-rich tin isotopes such as ^{134,136}Sn will be produced with sufficiently high intensity for performing two-nucleon transfer experiments. Owing to this, we shall compare the pair-transfer reactions ^{124}Sn$(p,t)^{122}$Sn as well as ^{136}Sn$(p,t)^{134}$Sn involving a more neutron-rich nucleus (E_p ranging from 15 to 35 MeV). In the pair-transfer reaction, we use the form factor that are consistently extracted from the QRPA calculation.

3.5.1 Quasiparticle Random-Phase Approximation (QRPA)

The HFB solutions are used in the quasiparticle random-phase approximation (QRPA) scheme to evaluate self-consistently the excitation modes associated to the pair-transfer reactions. Since we analyze here two-neutron transfer, we focus on the neutron HFB quasiparticle states that are used to construct the elementary configurations of the excited modes. Details on the QRPA model are given in Ref. (Khan et al., 2009) and in Refs. therein.

Figs. 3.10 show the QRPA response for ^{124}Sn and ^{136}Sn, with a pure surface interaction and a mixed one. As expected the residual interaction plays a similar role in all the cases, gathering strength and shifting it to lower energy. In the case of ^{124}Sn, a peak around 9 MeV is the strongest for the surface PDF, to be compared with the one around 10 MeV for the other interactions. Hence it is expected that the pairing vibration transition strength should be larger in the case of a pure surface force. However it is known that is is difficult to describe accurately the magnitude of these transitions, especially for absolute cross section calculations (Igarashi et al., 1991): one-step or sequential two-step process, triton wave function, zero-range or finite-range DWBA. It is therefore necessary to rely on the angular distribution, calculated from the form factor, related to the pairing transition density.

3.5.2 Two-neutron transfer reaction

In order to show that the observables associated to pairing vibrations can indeed guide us toward a deeper comprehension of this specific aspect of the pairing interaction, cross sections have to be evaluated. The analysis is pursued here in this direction. The idea is to perform a calculation of cross sections where the form factor of the transition is evaluated microscopically. The self-consistent microscopic QRPA results are used as structure inputs for the reaction calculation.

Cross sections for (p, t) two-neutron transfer reactions are calculated in the one-step zero-range distorted-wave Born approximation for the tin isotopes ^{124}Sn and ^{136}Sn and for incident proton energies from 15 to 35 MeV. The cross sections in the DWBA are calculated using the Distorted Waves University of Colorado Kunz 4 (DWUCK4) code (P. D. Kunz, University of Colorado, unpublished). Microscopic quasiparticle random-phase approximation form factors are provided for the reaction calculation and phenomenological optical potentials are used in both the entrance and the exit channels. For recent reviews on the main advances achieved in multinucleon transfer reactions at energies close to the Coulomb barrier see Refs. (Szilner et al., 2007; Corradi et al., 2009).

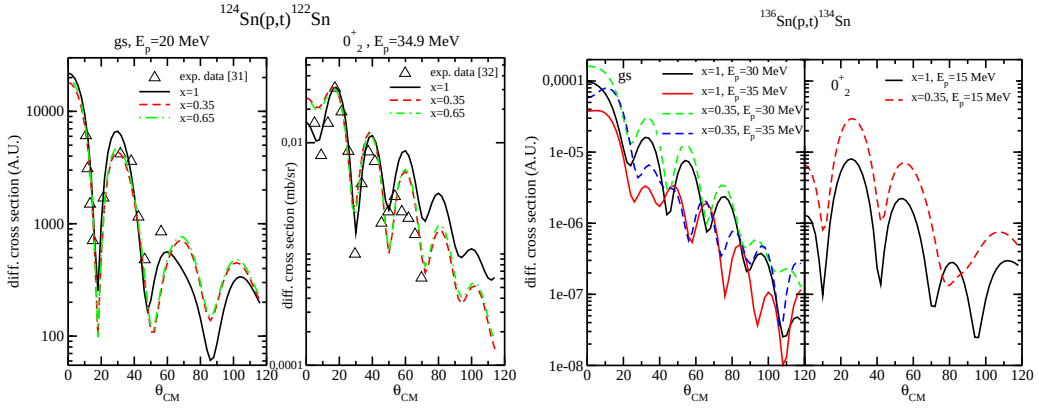

Figure 3.11: Left: Comparison between the calculated and the experimental cross sections for the transition to the ground state of the final nucleus. The reaction is ^{124}Sn$(p, t)^{122}$Sn and the incident proton energy is equal 20 MeV. Right: Comparison between the calculated and the experimental cross sections for the transition to the first excited 0^+ state of the final nucleus. The reaction is ^{124}Sn$(p, t)^{122}$Sn and the incident proton energy is equal 35 MeV.

In this work, we are interested in the transitions to the first 0^+_1 state, which is the ground state (gs) of the $A - 2$ nucleus, and to the first 0^+ excited state (0^+_2) of the final $A - 2$ nucleus. We thus consider the first two peaks of the QRPA response functions and calculate the corresponding transition densities. The transition densities for the ^{124}Sn$(p, t)^{122}$Sn and ^{136}Sn$(p, t)^{134}$Sn reactions are shown in Fig. 3.11: first panel on the left refers to the gs transition for ^{124}Sn$(p, t)^{122}$Sn, the second panel refers to the 0^+_2 transition for the same reaction. The two other panels correspond to the same but for ^{136}Sn$(p, t)^{134}$Sn reaction. In general, one observes that the two form factors associated to the two mixed interactions are quite similar one to the other and different from the form factor corresponding to $x = 1$, especially in the right panels (0^+_2 transitions). For ^{136}Sn$(p, t)^{134}$Sn reaction, one observes in both panels that the profiles of the cross sections corresponding to $x = 1$ and $x = 0.35$ differ at large angles ($\Theta_{CM} > 70$ degrees). We are aware that measurements are more difficult at large angles because the corresponding cross sections are very low. Nevertheless, this result indicates that very neutron-rich Sn isotopes may be interesting cases to analyze.

On the basis of this first indication, we continue our investigation for ^{136}Sn and we show in Fig. 3.12 the ratios of the cross sections associated to the gs and to the 0^+_2 transitions at different proton energies.

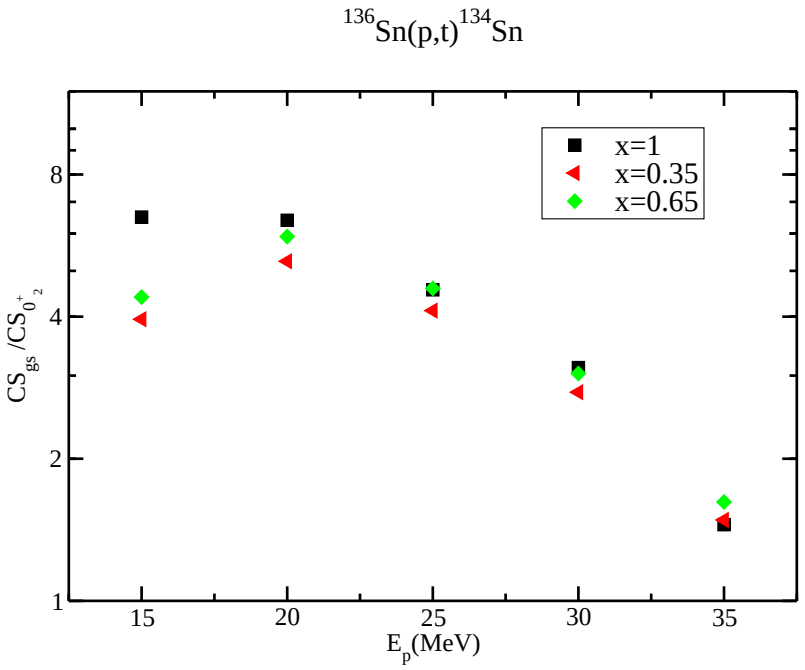

Figure 3.12: Ratios of the cross sections associated to the gs and to the 0_2^+ transitions at different proton energies for the reaction ^{136}Sn$(p,t)^{134}$Sn.

Even if absolute cross sections cannot be calculated within the present reaction model, the ratios of the cross sections related to the gs and the 0_2^+ transitions are meaningful quantities to analyze. These ratios are proportional to the ratios of the transition probabilities associated to the two transitions and that the proportionality factor is the same independently of the pairing interaction. The comparison of the ratios obtained with different pairing interactions can thus provide interesting predictions about the sensibility of the cross sections to the choice of the pairing interaction. It can be seen that differences exist among the three sets of results and they are more important at the lowest energy of 15 MeV, that represents the case where the reaction takes place mostly in the surface region of the nucleus. Hence, we suggest very neutron-rich Sn isotopes and proton energies around 15 MeV as favorable cases for future (p,t) or (t,p) pair-transfer experiments that can provide a deeper insight into the surface/volume character of the pairing interaction. Performing (t,p) reaction measurements in inverse kinematics is quite more challenging than (p,t), but such reactions would allow one to populate different states of Sn isotopes that may also represent very favorable cases for pairing studies.

3.5.3 Final remarks

We have evaluated (p,t) two-neutron transfer-reaction cross sections in the zero-range DWBA approximation for the two cases ^{124}Sn$(p,t)^{122}$Sn and ^{136}Sn$(p,t)^{134}$Sn. As a conclusion, we indicate (p,t) two-neutron transfer reactions with very neutron-rich Sn isotopes and at proton energies around 15 MeV as good experimental cases where the surface/volume mixing of the pairing interaction may be probed. This is a first indication.

While in our theoretical work the evaluation of the form factors is based on self-consistent and completely microscopic structure calculations, some limitations of the present reaction calculations have to be mentioned. A first limitation is the inability of such calculations to reproduce measured absolute cross sections (Franey et al., 1978): we thus compare in this work only angular profiles and in particular the location

of the diffraction minima. Furthermore, it has to be noticed that in one-step DWBA calculations inelastic excitations in the reaction channels and two-step processes corresponding to sequential particle transfers are missing (Franey et al., 1978). The relative importance of these processes is still quite an open question. Owing to these limitations, we consider the results presented in this work as a first qualitative indication and not a precise prediction about the sensitivity of the cross sections to the surface/volume character of the pairing interaction. More precise reaction calculations should certainly be performed to get absolute cross sections; more accurate predictions could be obtained by taking into account more complex processes like two-step excitations which are so far neglected in the present calculations whereas they are included in more sophisticated reaction codes (Potel et al., 2010).

3.6 Conclusions and outlooks

In this chapter, a new density dependent pairing interaction has been proposed with the motivation to establish a relation between the pairing properties in nuclear matter and that in nuclei. The crust of neutron stars described within the Wigner-Seitz approximation, cf chapter 5, can also be described extending the models used for nuclei. The isospin-density dependence in the PDF have improved the rms deviation between the experimental masses and the one obtained from the HFB approach. An universal PDF for neutrons and protons is now available.

The odd-even mass staggering imposes a tight constraint on the pairing interaction for a density which correspond to the average density in nuclei, at about 0.11 fm^{-3}. In order to explore experimentally the density dependence of the pairing interaction, it is interesting to investigate the role of other nuclear processes that are mainly sensible to the surface of nuclei for instance. The surface of nuclei are indeed interesting for the fact that the density is reduced compared to the average density in nuclei, and that in exotic nuclei where an extended neutron skin is formed, that the pairing correlations in mostly neutron rich dilute nuclear matter can be probed. Vibrational modes have been investigated in this chapter as a possible process which are sensible to the pairing correlations at the surface of nuclei. We have reported the expected effect of different density dependence of the PDF. However the model that we used have limitation that shall be overcome for more quantitative predictions such as absolute values of cross sections for transition processes.

In this chapter, we have however given a sound basis for the pairing interaction which will be used in the crust of neutron stars in chapter 5. In the future, finite range pairing interaction shall also be investigated and models for nuclei and for Wigner-Seitz cells shall be developed. A project to develop mean field approaches using finite range nuclear interaction in both WS cells and nuclei has already started together with a PhD thesis in *cotutelle* with Khoa in Hanoi.

Chapter 4

The in-medium effective mass

Particles in a medium are different from that in vacuum. Due to the large correlations among particles, it is not given that the constituent elements well identified as particles in vacuum still exists in dense medium. In the Landau theory of Fermi liquids, the concept of quasi-particles has been introduced to replace that of particles and these particles are viewed as excitations of the medium. The concept of quasi-particles therefore implicitly contains more than that of particles, since not only the quasi-particles could be off-mass shell, but it can also be fragmented and have fractional occupation numbers. The group velocity of quasi-particles can also vary from that of the particles in vacuum. One usually introduce the effective mass to describe the effect of the medium on the velocity. The modification of the medium on the effective mass reveals a modification of the group velocity of the quasi-particles. In nuclear matter, since the effective mass tends to be lower than that of the particles in vacuum, the group velocity is larger in the medium compared to the velocity of particles in vacuum. In this chapter, we are interested in the temperature dependence of the effective mass, and its effects on the initial stages of the massive stars core-collapse.

4.1 Introduction

The most general form of the single-particle wave equation reads, see for instance (Mahaux et al., 1985),

$$i\frac{\partial}{\partial t}\psi(\mathbf{r},t) = -\frac{1}{2m}\nabla^2\psi(\mathbf{r},t) + \int d\mathbf{r}'dt'\mathcal{M}(\mathbf{r},\mathbf{r}',t-t'), \tag{4.1}$$

where $\mathcal{M}(\mathbf{r},\mathbf{r}',t-t')$ represent the most general form of the mean-field.

In case of a stationary state, one has $\psi(\mathbf{r},t) = \psi_\omega(\mathbf{r})\exp -i\omega t$, and in uniform system, $\mathcal{M}$ only depends upon $|\mathbf{r}-\mathbf{r}'|$ and ω, while $\psi_\omega(\mathbf{r})$ is a plane wave $\psi_\omega(\mathbf{r}) = \exp i\mathbf{k}\cdot\mathbf{r}$. The wave equation (4.1) reduces to an energy-momentum relation, namely

$$\omega = \frac{k^2}{2m} + \mathcal{M}(\mathbf{k},\omega). \tag{4.2}$$

The dependence of $\mathcal{M}(\mathbf{k},\omega)$ upon $\mathbf{k}$ reflects the non-locality of the single-particle field in space, while its dependence upon ω corresponds to its non-locality in time. The non-locality in space is familiar because it is already encountered in the Hartree-Fock approximation. Anti-symmetrization leads to the Fock term, which is non-local. Non-locality in time is less familiar because most theoretical analyses are based on stationary states rather than on the time evolution of wave packets. Inside a uniform medium, the physical velocity of the wave packet associated with the nucleon is the group velocity,

$$v_g = \frac{1}{\hbar}\frac{d\omega}{dk}. \tag{4.3}$$

Since in free space, the velocity of a nucleon with momentum $\hbar k$ is given by $v = \hbar k/m$, the group velocity (4.3) yields to the definition of an effective mass m^*,

$$v_g = \frac{\hbar k}{m^*}. \tag{4.4}$$

In most of the cases, we have $m^* < m$, which leads to the conclusion that in general one has $v_g > v$. The velocity of a nucleon in the nuclear medium is larger that in free space. This is somewhat surprising. One could have expected the group velocity to be smaller, since the nucleon has to cut its way through the medium.

The effective mass is a powerful concept used to characterize the quasiparticle properties of a particle inside a strongly interacting medium as the nucleus, or nuclear matter. From Eqs. 4.3 and 4.4, the in-medium effective mass is defined as,

$$\frac{\hbar^2 k}{m^*} \equiv \frac{d\omega}{dk}. \tag{4.5}$$

Injecting the energy-momentum relation (4.2) into (4.5), the effective mass decompose as a product of a so-called *k-mass* and ω-*mass* as (Migdal, 1967),

$$\frac{m^*}{m} = \frac{m_k}{m} \cdot \frac{m_\omega}{m}, \tag{4.6}$$

where the *k-mass* reads,

$$\frac{m_k}{m} = \left[1 + \frac{m}{\hbar^2 k}\frac{\partial \mathcal{M}}{\partial k}\right]^{-1}, \tag{4.7}$$

and the ω-*mass* is defined as

$$\frac{m_\omega}{m} = \left[1 - \frac{\partial \mathcal{M}}{\partial \omega}\right]. \tag{4.8}$$

The *k-mass* comes from the spatial non-locality, or momentum dependence, of the mean field and is a by-product of the Hartree-Fock approximation, while the ω-*mass*, being related to the time non-locality of the mean field, indicates to which extend the exact wave function is in a single particle state. The ω-*mass* can indeed be related to the inverse of the spectroscopic factor. The deviation of the ω-*mass* from 1 reveals the fragmentation of the state.

Another interested feature of the mass operator $\mathcal{M}$ lies inside its imaginary component which is related to the width of the particles. It can be shown that the width of the HF mean field picture, which is based on time-independent single particle states, get generally close to the physical picture for quasi-particles that are close to the Fermi energy. The Landau theory of Fermi liquids is generally justified as a theory that describe the excitations around the Fermi energy in terms of quasi-particles. As long as these quasi-particles are on-shell and weakly fragmented, that is close enough to the Fermi energy, the usual mean field picture is expected to be "correct".

Already in the 1960s, G.E. Brown *et al.* suggested that the effective mass m^*/m should be close to 1 around the Fermi energy in order to reproduce the experimental level density from a mean field approach (Brown and Gunn, 1963). The HF mean field models such as those based on Skyrme (Skyrme, 1956), Gogny (Gogny, 1975) and M3Y interactions (Nakada, 2003) or on the relativistic approaches like RMF (Serot, 1992) or RHF (Long et al., 2006), have however an effective mass around 0.6-0.8. This value for the effective mass is expected from the analysis of the optical potential. By comparing the energy dependent term of the real optical potential in the energy range 10-30 MeV, which is used in phenomenological analyses of nucleon scattering data, to the equivalent local potential from the Skyrme interaction, it was deduced that the effective mass m^*/m is approximatively $m^*/m \approx 0.75 \pm 0.03$ (Dover and Van Giai, 1972). The damping of the effective mass was also found by Perey who used phenomenological local and non-local potential giving the same phase shifts (Perey and Buck, 1962; Ma and Wambach, 1983). The static mean field theory fails in reproducing the observed level density around the Fermi energy.

The solution of this problem has been found by recognizing that the mean field is not static, but highly dynamic (Bertsch and Kuo, 1968). Among the modes associated with the fluctuations of this field one finds vibrations of the nuclear surface (Bernard and Van Giai, 1979; Brown et al., 1979; Bortignon and Dasso, 1987). The coupling of the fermions to the phonons describing these modes leads to self-energy corrections which are non-local in time, since the phonons propagate in the nuclear medium with finite velocity. The non-locality can be absorbed in terms of an effective mass, the so-called ω-*mass*. In the particle-vibration coupling model it is found that the dynamical correlations lead to an increase of the effective mass at the surface of nuclei, going from approximatively 0.7 in the bulk part of nuclei up to about 1 at the surface (Van Giai and Van Thieu, 1983). In nuclear matter, the effective mass is also found to be increased close to the Fermi energy. This increased is also induced by the dynamical correlations which impact the ω-*mass* (Mahaux et al., 1985; Mahaux and Sartor, 1992).

The increase of the level density around the Fermi energy due to the increase of the effective mass shall have an impact on the low-energy properties around the Fermi energy such as pairing correlations (Dean and Hjorth-Jensen, 2003; Yoshida and Sagawa, 2008), collective modes (Harakeh and Van der Woude, 2001) as well as on temperature-related properties such as the entropy, the critical temperature, the specific heat (Chamel et al., 2009a). In nuclear astrophysics, a good description of the density of states around the Fermi energy turned out to be relevant also for the energetics of core-collapse supernovae (Donati et al., 1994; Fantina, 2010).

During the supernova core-collapse, the temperature of the dense medium can rise up to few MeV before the melting of the nuclear clusters. The energy of low-lying collective vibrations, related to the ω-*mass*, is of the order of 1-3 MeV, while the rigidity of the mean field, related to the *k-mass*, is controlled by the energy difference between major shells $\hbar\omega_0 = 41A^{-1/3}$ MeV, which is ≈ 8 MeV for medium heavy nuclei. Consequently, the question of the temperature dependence of the ω-*mass* is equivalent to the temperature dependence of the ω-*mass*, at least within a range of temperature under discussion (few MeV). It was found that the ω-*mass* decreases appreciably in the temperature interval 0-1 MeV (Donati et al., 1994). This decrease is indeed related to the damping width of collective modes.

In section 4.2, the effect of the temperature dependence of the effective mass on the supernovae core-collapse is studied. The temperature dependence has consequences, among other things, on the level-density parameter and on the symmetry energy, which in turns affect the neutronization process in collapsing stars. It is found that the temperature dependence of the effective mass reduces the neutronization and the final lepton fraction is getting systematically slightly larger.

In section 4.3, an energy-density functional based on a modification of the Skyrme functional is proposed to mimic a surface peaked effective mass.

4.2 Temperature dependence of the in-medium effective mass

Investigations of the temperature dependence of the effective mass in nuclei have been made by different authors (Bortignon and Dasso, 1987; Hasse and Schuck, 1986; Donati et al., 1994). In the Ref. (Bortignon and Dasso, 1987) an analysis was carried out for the nucleus ^{208}Pb in the RPA framework showing a decrease of the ω-*mass* with the temperature in the range 0-4 MeV. In the Ref. (Hasse and Schuck, 1986) the radial profile of the effective mass at different temperature was used in order to obtain the level density parameter a/A as a function of the temperature. A reduction has been found for $T > 4$ MeV. In Ref. (Donati et al., 1994), the temperature dependence of the nucleon effective mass has been calculated for the nuclei ^{98}Mo, ^{64}Zn and ^{64}Ni, of astrophysical interest, where the particle-vibration coupling was calculated in the QRPA framework base on an empirical Wood-Saxon potential. It was found that the ω-*mass* decreases appreciably in the temperature interval 0-1 MeV.

4.2.1 A simple model

For applications to the supernova core-collapse, it was proposed to fit the temperature dependence of the ω-*mass* by the simple expression (Donati et al., 1994),

$$\frac{m_\omega(T)}{m} = 1 + \left(\frac{m_\omega(T=0)}{m} - 1\right) \exp\left(-T/T_0\right), \tag{4.9}$$

where T_0 is obtained from the fit and found to be $T_0 \approx 2$ MeV. In semi-infinite nuclear matter, it was found that $T_0 \approx 1.1$ MeV (Giovanardi et al., 1996).

The effective mass is an important quantity which impacts several parts of the equation of state, such as the symmetry energy, the thermal energy and the chemical potential. The temperature dependence of the effective mass is therefore expected to modify these quantities. In the following, we review how the temperature dependence of the effective mass is incorporated in the equation of state.

In analogy to the results of the Fermi gas model and assuming that only the kinetic part of the symmetry energy $E_{\rm sym}(A,Z,T)$ depends on the effective mass, it was argued that the temperature dependence of $E_{\rm sym}(A,Z,T)$ can be fitted by the following analytical expression

$$E_{\rm sym}(A,Z,T) = J_0(T)\left(1 - 2\frac{Z}{A}\right)^2, \tag{4.10}$$

where the symmetry coefficient $J_0(T)$ is parameterized as,

$$J_0(T) = J_0(T=0) + \frac{\hbar^2 k_F^2}{6m}\left(\frac{m}{m^*(T)} - \frac{m}{m^*(T=0)}\right). \tag{4.11}$$

In Eq. (4.11), the effective mass is given by the product of the *k-mass* and the ω-*mass* as given in Eq. (4.6), and the only temperature dependence is given by the ω-*mass* parameterized as in Eq. (4.9). The *k-mass* is indeed fixed to be temperature-independent but it has a dependence on the density and the isospin asymmetry. This dependence can be taken as in the Skyrme model, or as given by Eq. (3.6) in Ref. (Bethe et al., 1983), but for simplicity, we decide here to fix $m_k/m = 0.76$ (Fantina, 2010). Introducing the fit (4.9) in the symmetry energy (4.11), an increase of $E_{\rm sym}(A,Z,T)$ of $\approx 8\%$ is found in the interval $T = 0-1$ MeV.

The temperature dependence of the symmetry energy was also explored in the Shell Model Monte Carlo (SMMC) approach (Dean et al., 2002). The symmetry energy was deduced from isobaric pairs with masses A in the range $A = 56 - 66$. Upon averaging over various pairs, a variation of the symmetry energy of $\approx 6\%$ is found in the interval $T = 0.33-1.23$ MeV, in reasonable agreement with the QRPA results (Donati et al., 1994).

The nuclear thermal energy (per baryon) stored in excited states reads ((Bethe et al., 1983)):

$$E_{\rm th} = \frac{\pi^2}{4}\frac{(k_B T)^2}{\epsilon_F}\frac{m^*(T)}{m}, \tag{4.12}$$

where k_B is the Boltzmann constant and $\epsilon_F \simeq 40$ MeV is the nuclear kinetic Fermi energy ((Bethe et al., 1983)). The thermal energy also represents the thermal average of the excitation energy over the density of states.

The symmetry energy enters in the bulk nuclear energy and, as a consequence, in the neutron chemical potential, μ_n, and in the neutron-proton energy difference, $\hat{\mu} = \mu_n - \mu_p$, as

$$\hat{\mu} = \frac{4}{(1-2x)}E_{\rm sym}(A,Z,T) - W_{\rm surf}(A,x)\left(\frac{1}{x} + \frac{2}{x}\frac{1-2x}{1-x}\right), \tag{4.13}$$

where $x := Z/A$ and $W_{\rm surf}(A,x) = 290x^2(1-x)^2A^{-1/3}$ is the surface energy ((Bethe et al., 1983)). These quantities appear in the expressions for the free particle abundancies, in the Q-value of the electron

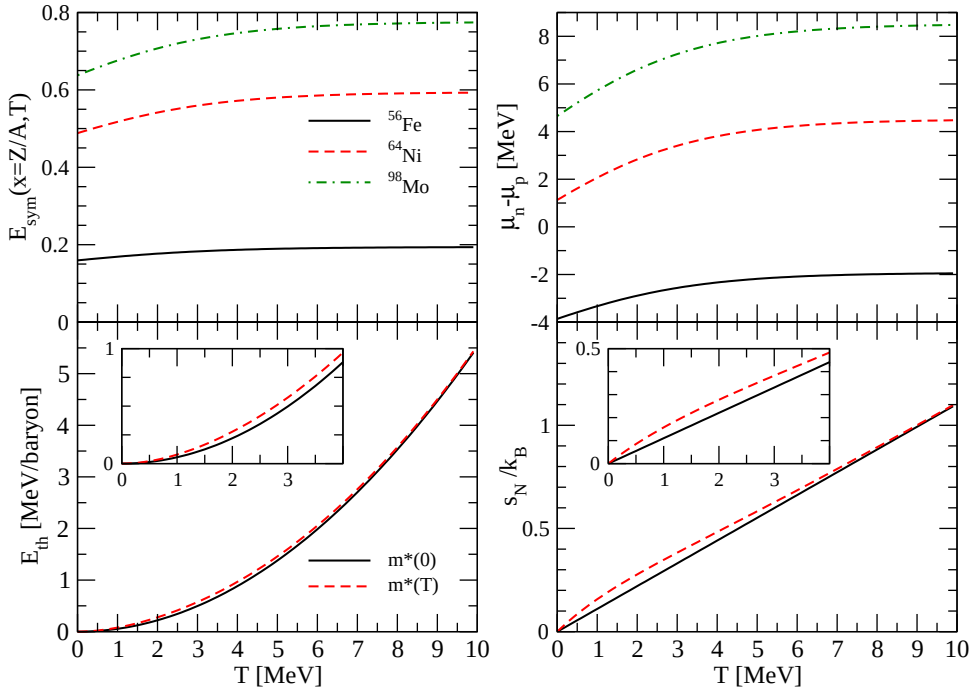

Figure 4.1: Upper panels: nuclear symmetry energy and neutron-proton energy difference $\hat{\mu}$ as a function of temperature, for the nuclei $^{56}_{26}$Fe, $^{64}_{28}$Ni, $^{98}_{42}$Mo. Lower panels: nuclear thermal excitation energy and corresponding entropy (see text for details).

capture reaction (see Eq.(4.17)), and in the nuclear entropy ((Bethe et al., 1983)):

$$s_N = 2\frac{E_{\rm th}}{k_B T} = \frac{\pi^2}{2}\frac{k_B T}{\epsilon_F}\frac{m^*(T)}{m} \,. \tag{4.14}$$

The temperature dependence of the in-medium nucleon mass and of the nuclear symmetry energy affects both the EoS of the system, and the electron capture rates on nuclei. In particular, the increase of the nuclear symmetry energy, $E_{\rm sym}$, yields an increase of the neutron-proton energy difference $\hat{\mu}$. This is shown in Fig. 4.1 (upper panels) where $E_{\rm sym}(A,Z,T)$, Eq. (4.10), and $\hat{\mu}$, Eq. (4.13), are plotted as a function of temperature for three selected nuclei of astrophysical interest: $^{56}_{26}$Fe, $^{64}_{28}$Ni and $^{98}_{42}$Mo (the past two are among those studied in Paper (Donati et al., 1994)). We notice that most of the increase of $E_{\rm sym}(A,Z,T)$ is located in the temperature interval $0-4$ MeV, which is the relevant one for the collapse phase. In the same temperature range, $\hat{\mu}$ increases by about a factor 2. One therefore expects that the increase of $E_{\rm sym}$ with T would inhibit the electron capture on nuclei, resulting in a larger electron fraction during the deleptonisation phase. This theoretical prediction was indeed confirmed by the one-zone collapse simulations performed in Refs. (Donati et al., 1994; Fantina et al., 2009). The lower panels of Fig. 4.1 display the impact of the temperature dependence of $m^*(T)$ on the nuclear thermal energy and the corresponding entropy. The solid (dashed) lines represent the case where $m^* = m^*(0)$ ($m^* = m^*(T)$) in Eqs. (4.12) and (4.14). Since these two quantities are plotted per baryon, there is no dependence on the mass number of the nucleus. Also in this case, the main effect due to the temperature dependence of the in-medium nucleon mass lies in the range $T = 0 - 4$ MeV (shown by the insets). At 2 MeV, the difference between $E_{\rm th}(m^*(0))$ and $E_{\rm th}(m^*(T))$ and between $s_N(m^*(0))$ and $s_N(m^*(T))$ is of about 26%, while at 4 MeV, this difference decreases to about 9%.

4.2.2 Application to core-collapse supernovae

We now analyze the influence of the temperature dependence of the in-medium nucleon mass on a one-dimensional core-collapse simulation. To do this, we run simulations employing the BBAL EoS (Bethe et al., 1979) matched to the Suraud EoS (Suraud, 1985), with corrections to the symmetry and thermal energies given by Eqs. (4.11) and (4.12).

Electron capture is treated using the prescription given by Bruenn (Bruenn, 1985), where the expressions of the neutrino emissivity $j(\omega)$ and the absorption mean free path $\lambda^{(a)}(\omega)$ for electron capture rates on nuclei read,

$$j(\omega) = \frac{G_F^2}{(\hbar c)^4\pi} n_b \frac{X_h}{A}\, g_A^2\, \frac{2}{7} N_{\rm p}(Z) N_{\rm h}(N) f_e(\omega+Q')\,(\omega+Q')^2 \left[1-\frac{(m_e c^2)^2}{(\omega+Q')^2}\right]^{1/2} \quad (4.15)$$

$$\frac{1}{\lambda^{(a)}(\omega)} = \frac{G_F^2}{(\hbar c)^4\pi} n_b \frac{X_h}{A}\, e^{(\hat{\mu}-Q')/k_B T}\, g_A^2\, \frac{2}{7} N_{\rm p}(Z) N_{\rm h}(N)[1-f_e(\omega+Q')]\,(\omega+Q')^2 \times \left[1-\frac{(m_e c^2)^2}{(\omega+Q')^2}\right]^{1/2}, \quad (4.16)$$

where G_F is the Fermi coupling constant, $n_b X_h/A$ in Eq. (4.15) is the number density of the parent nucleus species, $n_b X_h e^{(\hat{\mu}-Q')/k_B T}/A$ in Eq. (4.16) the number density of excited $(Z-1, A)$ nuclei, $g_A = 1.23$ is the axial coupling constant, f_e is the Fermi distribution, m_e the electron mass, and the Q-value of the capture reaction reads,

$$Q' = (m^*_{Z-1,A} - m_{Z,A})c^2 = (m_{Z-1,A} - m_{Z,A})c^2 + \Delta_{\rm N} \approx \hat{\mu} + \Delta_{\rm N}. \quad (4.17)$$

Notice that since the neutron and proton chemical potentials do not include the rest mass, the neutron-proton mass difference has to be explicitly included in computing the Q-value, Eq. (4.17). In Eq. (4.17) the excitation energy of the nuclear Gamow-Teller (GT) resonance, $\Delta_{\rm N}$, is set to 3 MeV ((Bethe et al., 1979; Bruenn, 1985)).

In Eqs. (4.15) and (4.16), the product $\frac{2}{7} N_{\rm p} N_{\rm h}$ represents an estimate of the typical GT matrix element $|M_{\rm GT}|^2$ for the capture on nuclei, where

$$N_{\rm p}(Z) = \begin{cases} 0 & Z \le 20 \\ Z-20 & 20 < Z \le 28 \\ 8 & Z > 28 \end{cases}, \quad (4.18)$$

and

$$N_{\rm h}(N) = \begin{cases} 6 & N \le 34 \\ 40-N & 34 < N \le 40 \\ 0 & N > 40 \end{cases}. \quad (4.19)$$

This parameterization is fixed to reproduce the zero-order shell model results ((Fuller, 1982; Bruenn, 1985)).

In order to explore the sensitivity of the model to uncertainties in the nuclear electron capture rates, we have performed a parameter study, each time varying the strength of the electron capture on nuclei. We then change by hand the product $N_{\rm p} N_{\rm h}$ in Eqs. (4.18) and (4.19). The same procedure has been adopted e.g. in the paper by Hix et al. (Hix et al., 2005).

We now analyze the influence of the temperature dependence of the in-medium nucleon mass on the simulation for core-collapse supernovae. The simulations are carried out with a Newtonian, spherically symmetric (1D) code ((Blottiau, 1989)). The hydrodynamics and neutrino transport are coupled and solved by an implicit finite-differencing scheme written in Lagrangian coordinates. The core is divided into 40 zones, and the envelope into 60 zones, giving a total number of $N_{\rm zone} = 100$. This grid spacing might raise

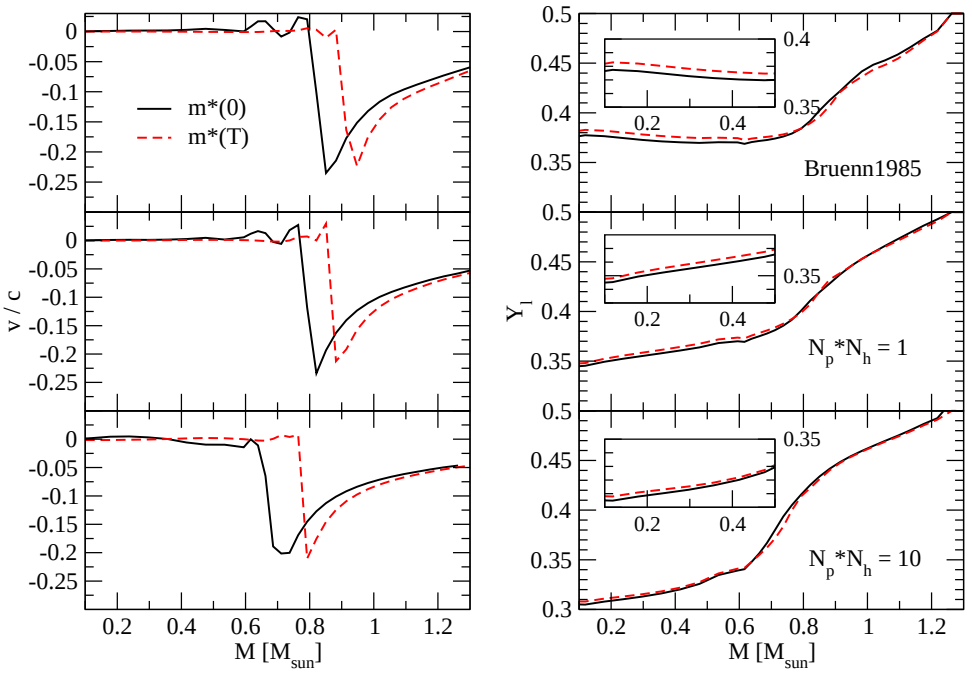

Figure 4.2: Velocity (left panels), and lepton fraction (right panels) profiles as a function of the enclosed mass at bounce (see text for details).

some questions about the precision of the spatial grid. However, this spacing is sufficient to correctly reproduce the dynamical features we are interested in (collapse and shock formation) in a short computational time (few tens of hours), and allows a more precise neutrino energy resolution. The shock is treated in the shock tracking fashion; the prescription for the artificial viscosity is similar to the one given by Noh (Noh, 1978). Unlike the latter, we set the artificial viscosity to a non-zero value only when the divergence (and not the gradient as in the paper by (Noh, 1978)) of the velocity field is negative, a condition which ensures that the matter is in the compression phase. The system of conservation equations to be solved for each mass shell (i.e. mass, momentum and energy conservation, plus the electron number evolution equation). Details are given in Refs. (Fantina, 2010; Fantina et al., 2012), we also refer to Ref. (Mihalas, 1999) textbook for a complete treatment of the radiation hydrodynamics.

A parameter study of the effect of the temperature dependence of $m^*(T)$ is represented in Fig. 4.2, where the velocity and the lepton fraction profiles are shown at bounce for different strengths of electron capture rates on nuclei (from top to bottom panels): the *standard* Bruenn prescription (Bruenn, 1985) with the product $N_{\rm p}N_{\rm h}$ given by Eqs. (4.18) and (4.19), or fixing the product $N_{\rm p}N_{\rm h}$ equal to 1 and 10. This choice is indeed consistent with the present theoretical large uncertainties of the capture rates. For each set of parameterization of the electron capture, we run the code twice: either with $m^*(T)$ or with $m^*(0)$, i.e. taking or not into account the temperature dependence of the in-medium nucleon mass. We observe in all cases the same *systematic* behavior: the deleptonization process is slightly slown down when the temperature dependence of the nucleon effective mass is considered, and the shock wave formation is shifted outwards. It shall also be noticed that the uncertainties on the electron fraction represented by the different prescriptions in Fig. 4.2 have a large impact on the position of the shock wave at bounce. Quantitatively, in it estimated to be of the order of about 0.15 $M_\odot$. However, the modification due to the temperature dependence of the effective mass is to shift outwards the position of the shock wave at bounce by about 0.1 $M_\odot$ whatever the prescription for the electron capture rates. In the insets in the right panels

Capture rates	$\rho_{\rm c,b}$ [10^{14} g cm^{-3}]	$M_{\rm b}$ [$M_\odot$]	$Y_{l,{\rm b}}$
Bruenn 1985, $m^*(0)$	2.83	0.82	0.372
Bruenn 1985, $m^*(T)$	2.61	0.90 (0.08)	0.377 (0.005)
$N_{\rm p}N_{\rm h} = 1$, $m^*(0)$	2.79	0.79	0.345
$N_{\rm p}N_{\rm h} = 1$, $m^*(T)$	2.57	0.87 (0.08)	0.348 (0.003)
$N_{\rm p}N_{\rm h} = 10$, $m^*(0)$	2.67	0.67	0.308
$N_{\rm p}N_{\rm h} = 10$, $m^*(T)$	2.49	0.77 (0.1)	0.311 (0.003)

Table 4.1: Central density, enclosed mass, central lepton fraction at bounce, for different strengths of the electron capture on nuclei, and for $m^* = m^*(0)$ or $m^* = m^*(T)$. The values in parentheses are the differences due to the thermal effect under study in the enclosed mass and lepton fraction at bounce.

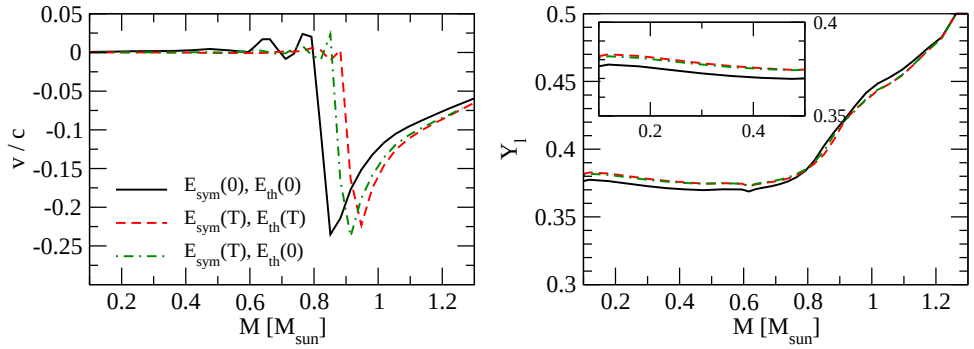

Figure 4.3: Velocity (left panel), and lepton fraction (right panel) profiles as a function of the enclosed mass at bounce (see text for details). The capture rates are the "standard" ones by (Bruenn 1985).

of Fig. 4.2 focused views of the lepton fraction in the central region are shown. The modification of the lepton fraction induced by the temperature dependence of the effective mass is indeed quite limited while the effect on the position of the shock wave is stronger. In the following, a deeper analysis is the effect of the temperature dependence of the effective mass is therefore performed.

In Table 4.1 the maximum central density, together with the enclosed mass and central lepton fraction at shock formation, are listed. In the third and fourth column, in parentheses, the "thermal" variation $\delta_{\rm T}$ due to the temperature dependence of the nucleon effective mass in nuclei is given: $\delta_{\rm T}M_{\rm b} := M_{\rm b}|_T - M_{\rm b}|_0$ (for the enclosed mass), and $\delta_{\rm T}Y_{l,{\rm b}} := Y_{l,{\rm b}}|_T - Y_{l,{\rm b}}|_0$ (for the lepton fraction). We notice that the "thermal" variations of the lepton fraction (last column in Table 4.1) are in good agreement with the results obtained in Ref. (Fantina et al., 2009). Despite the small values of $\delta_{\rm T}Y_l \simeq 0.003 - 0.005$, the effects on the position of the formation of the shock wave are quite large, namely $\delta_{\rm T}M_{\rm b} \simeq 0.1\ M_\odot$. This might be due to the influence of the temperature dependence of the in-medium nucleon mass on the EoS of the system rather than its influence on the electron capture rates. However, because of the non-linear relation among the T-dependent nucleon effective mass, the EoS (chemical potentials, abundances, nuclear thermal excitation energy) and the Q-value of the capture reaction, it is difficult to decouple the different contributions. Nevertheless we want to investigate this question.

To do so, we have run a simulation for the *standard* reference Bruenn capture rates, removing the contribution of the T-dependence of the nucleon effective mass from the nuclear thermal excitation energy (Eq. (4.12)). Indeed, the corresponding entropy term was known to have a non-negligible effect on the collapse trajectory (Fantina et al., 2009). To this purpose, we have set $m^*(T) = m^*(0)$ in Eq. (4.12), leaving

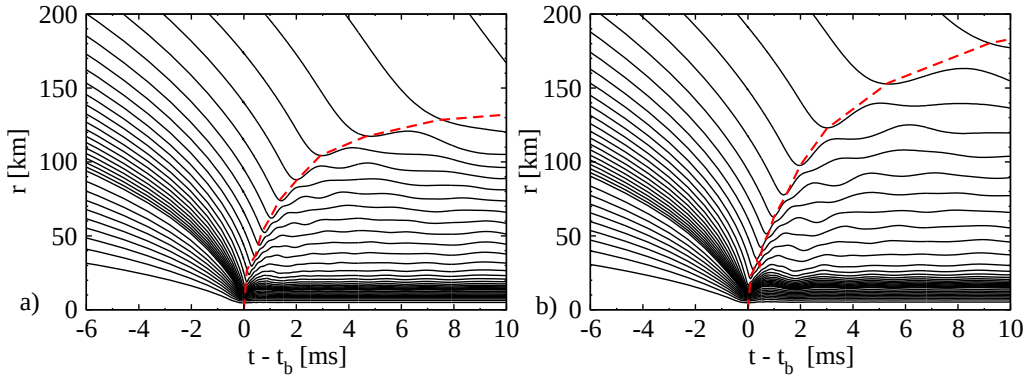

Figure 4.4: Time evolution (with respect to the time of bounce) of the trajectories of fluid elements spaced with an interval of $\sim 0.06\ M_\odot$, starting from the lowest mass shell at $0.059\ M_\odot$. In the simulations we set (a) $m^*(0)$; (b) $m^*(T)$. The capture rates on nuclei are the*standard* ones by (Bruenn 1985).

the other equations containing $m^*(T)$ unchanged. The results of the simulation are shown in Fig. 4.3. Since the expression for the Q-value is not modified, the effect of the temperature dependence of the nucleon effective mass is still acting on the capture rates. Indeed, even removing the contribution of $m^*(T)$ in the nuclear thermal excitation energy, we still observe almost the same effect on the final lepton fraction at bounce (Fig. 4.3, right panel), i.e. the deleptonisation is reduced ($\delta_{\rm T} Y_l \simeq 0.005$), as in the case where $m^*(T)$ is implemented everywhere. However, it is clear from the left panel, where the velocity profile at bounce is displayed, that the inclusion of $m^*(T)$ in the nuclear thermal excitation energy turns out to be non-negligible in the collapse dynamics. Indeed, when the temperature dependence of the in-medium nucleon mass is implemented except in the nuclear thermal excitation energy (dashed-dotted line), the shock wave is forming at $M_{\rm b} \simeq 0.87\ M_\odot$, to be compared with $M_{\rm b} \simeq 0.82\ M_\odot$ when $m^* = m^*(0)$ and with $M_{\rm b} \simeq 0.90\ M_\odot$ when $m^*(T)$ is fully implemented. In conclusion, the contribution of the temperature dependence of the nucleon effective mass in the nuclear thermal excitation energy accounts for a non-negligible fraction of the global effect.

We also notice that in the *standard* case (Fig. 4.2, upper panels), the shock is forming at $\sim 0.8\ M_\odot$, i.e. outwards with respect to the simulations carried by, e.g., Hix et al. (Hix et al., 2005). This might come from the EoS adopted (BBAL (Bethe et al., 1979) together with the Suraud EoS (Suraud, 1985)), instead of the LS (Lattimer and Swesty, 1991) one. We also stress that the neutrino-electron scattering, which is expected to move the position of the formation of the shock wave inwards of about 0.1 $M_\odot$ ((Bethe, 1990)), is not included in our simulations.

The position of the formation of the shock is undoubtedly a first crucial indication to estimate the possible fate of the shock wave. However, in order to evaluate the efficiency of the shock wave, it is important to follow the time evolution of the fluid trajectories and the propagation of the shock. In Fig. 4.4, the first few milliseconds of the time evolution of the radii of different mass shells are displayed as a function of the post-bounce time. The core is shown, together with the first shells of the envelope. Both panels show the results of the simulation where we employed the *standard* Bruenn capture rates, and the BBAL (Bethe et al., 1979) matched to the Suraud EoS (Suraud, 1985). The left (right) panel corresponds to the simulation in which we set $m^* = m^*(0)$ ($m^* = m^*(T)$). The lines indicate the trajectories of the fluid elements spaced by $\sim 0.06 M_\odot$. We notice from Fig. 4.4 the collapse of the innermost shells, followed by the bounce (at $t = t_{\rm b}$) and the formation and propagation of the shock. Fig. 4.4 also shows that the inclusion in the simulation of the temperature dependence of the in-medium nucleon mass not only shifts the position of the shock wave formation (see Fig. 4.2), but also leads to a *gain* in the position of the shock front in the first

few milliseconds after bounce. Indeed, as an example, at 2 ms after bounce, the shock front is at ~ 90 km in the case illustrated by panel a), and at ~ 100 km in panel b). At 10 ms after bounce, the shock front is at ~ 130 km in the case illustrated by panel a), and at ~ 180 km in panel b). If compared to the position of the shock stagnation usually found in 1D simulations (around 100-200 km), the *gain* found after implementing the temperature dependence of the nucleon effective mass in nuclei (about 10% after 2 ms, and about 30% after 10 ms) is not negligible.

4.2.3 Final remarks

In this section we have studied the impact of the temperature dependence of the nucleon effective mass in nuclei in a core-collapse supernova simulation by means of a one-dimensional Newtonian code with neutrino transport treated in the MGFLDA. We have implemented this temperature dependence in the BBAL EoS finding a systematic reduction of the deleptonization during the collapse phase, in agreement with the results presented in Ref. (Fantina et al., 2009). Moreover, we have evaluated the position of the formation of the shock wave. It is shifted outwards by a significative amount when the T-dependence of the in-medium nucleon mass is taken into account. We also notice that the temperature dependence of the in-medium nucleon mass has an important impact on the nuclear thermal excitation energy of the system. Furthermore, we have shown that the shock front, in the first few milliseconds after the core bounce, is located outwards of about 10 km (50 km) at 2 ms (10 ms) after bounce in the simulation where we set $m^* = m^*(T)$. Therefore, even if we do not expect dramatic changes in the outcome of the simulation, we conclude that the implementation of the temperature dependence of the nucleon effective mass has a non-negligible effect on the shock wave propagation (Fantina et al., 2012).

In the future, it would be interesting to include this effect in the GR framework, which has been shown to be physically relevant in compact star models (e.g. (Bruenn et al., 2001; Liebendörfer et al., 2001)), and into multi-dimensional simulations, which are undoubtedly required to correctly reproduce the supernova mechanism, in particular during the long-term post-bounce evolution. The inclusion of such a temperature dependence in more realistic and commonly used EoSs, such as the LS (Lattimer and Swesty, 1991) one, or more recent EoSs based on statistical distribution of nuclei, is a further point to investigate.

It shall be also noticed that other thermal effects different from the one discussed in this work might play a role in the supernova mechanism. As far as concerning the EoS, it would be worth elaborating on the impact of temperature on the cluster structure at sub-saturation density (Gulminelli and Raduta, 2012), as well as on the temperature dependence of some key quantities such as the nuclear surface energy and the curvature parameter of the nuclear symmetry energy ($K_{\rm sym}$) in asymmetric matter. The value of $K_{\rm sym}$ has been shown for instance to be relevant for the estimation of the thickness of the neutron star crust ((Vidaña et al., 2009)).

Nevertheless, this is not a straightforward task: supernova simulations rely most on tabulated EoSs and thus it is difficult to play with the different parameters. New EOS tables shall therefore be tabulated for each improvement of the microscopic model. The ESF network CompStar is producing a set of routines, *CompOSE*, for implementing in astrophysical simulations the new EoS.

Finite temperature effects have a crucial role also in the calculation of the electron capture rates (Heger et al., 2001). The spin channel of the nuclear interaction is also weakly constrained in present models, as discussed in section 2.2. The effect of the new term in the Skyrme interaction to correct the spin channel in the electron capture reaction rate shall therefore be studied. It is one of the aim of the project performed with Dubna group.

4.3 Energy Density Functional with a surface peaked effective mass

In this section, we propose to improve the simple model presented in section 4.2 within the energy density functional (EDF) framework. We propose a modification of the Skyrme Energy Density Functional in order to simulate a surface peaked effective mass in nuclei. We proceed in two steps: first, the surface peaked effective mass at zero temperature is calibrated and its effects on the density of states and on pairing is analyzed. Then, in a second step, we propose a finite-temperature correction that makes the link with the simple model presented in section 4.2 and with the microscopic calculations performed in Ref. (Donati et al., 1994).

In the following, we explore the impact of adding to the Skyrme functional an iso-scalar correction of the form (Fantina et al., 2011):

$$\mathcal{H}_0^{\rm corr}(\mathbf{r}) = C_0^{\tau(\nabla\rho)^2}\tau(\mathbf{r})\left(\nabla\rho(\mathbf{r})\right)^2 + C_0^{\rho^2(\nabla\rho)^2}\rho(\mathbf{r})^2\left(\nabla\rho(\mathbf{r})\right)^2 \ , \tag{4.20}$$

where the first term is similar to one of the proposed corrections in Ref. (Zalewski et al., 2010) and produces a surface-peaked effective mass. The second term is new and is introduced in our work to moderate the effect of the first one in the mean field. It can be viewed as being closed to the Thomas-Fermi approximation of the first term.

The effective mass is obtained from the functional derivative of the energy H and is expressed as (q runs over neutrons and protons: $q = n, p$):

$$\frac{\hbar^2}{2m_q^*(\mathbf{r})} \equiv \frac{\delta H}{\delta\tau_q} = \frac{\hbar^2}{2m} + C_q^\tau\rho_q(\mathbf{r}) + C_0^{\tau(\nabla\rho)^2}(\nabla\rho(\mathbf{r}))^2 \ , \tag{4.21}$$

where the coefficient $C_q^\tau = (C_0^\tau \pm C_1^\tau)/2$ (with $+$ for $q = n$ and $-$ for $q = p$), and the mean field reads:

$$U_q(\mathbf{r}) = U_q^{\rm Sky}(\mathbf{r}) + U^{\rm corr}(\mathbf{r}) \ , \tag{4.22}$$

where $U_q^{\rm Sky}(\mathbf{r})$ is the mean field deduced from the Skyrme interaction (Bender et al., 2003) and $U^{\rm corr}(\mathbf{r})$ is the correction term induced by Eq. (4.20) which is defined as:

$$U^{\rm corr}(\mathbf{r}) = -2C_0^{\tau(\nabla\rho)^2}\Big(\tau(\mathbf{r})\nabla^2\rho(\mathbf{r}) + \nabla\tau(\mathbf{r})\nabla\rho(\mathbf{r})\Big) - 2C_0^{\rho^2(\nabla\rho)^2}\Big(\rho(\mathbf{r})(\nabla\rho(\mathbf{r}))^2 + \rho(\mathbf{r})^2\nabla^2\rho(\mathbf{r})\Big) \ . \tag{4.23}$$

In the original work of Ma and Wambach (Ma and Wambach, 1983), the term $U^{\rm corr}(r)$ was derived directly from the Green's function with energy dependent self-energies while, in our approach, $U^{\rm corr}(r)$ is derived from the new term (4.20) in the EDF. A one-to-one correspondence between EDF and the Green's function approach is not possible. However, since the terms $U^{\rm corr}(r)$ and $U_q^{\rm eff}(r)$ compensate each other in the Green's function approach (Ma and Wambach, 1983), we want to reproduce the same behavior in the EDF. We obtain approximate compensation between $U^{\rm corr}(r)$ and $U_q^{\rm eff}(r)$ by imposing the following relation between the new coefficients:

$$C_0^{\rho^2(\nabla\rho)^2} = 12 \text{ fm } C_0^{\tau(\nabla\rho)^2} \ . \tag{4.24}$$

We have investigated the sensitivity of the results to the value of the proportionality constant and we have checked that the reasonable values lie in the range 10-20 fm, after which the compensation is no longer efficient.

Notice that a surface-peaked effective mass could also be obtained from a modified Skyrme interaction. This different approach potentially leads to an improved agreement with experimental single particle energies (Farine et al., 2001). Since the new term explored in Ref. (Farine et al., 2001) is simultaneously momentum and density dependent, the functional obtained is quite different from Eq. (4.20): the number

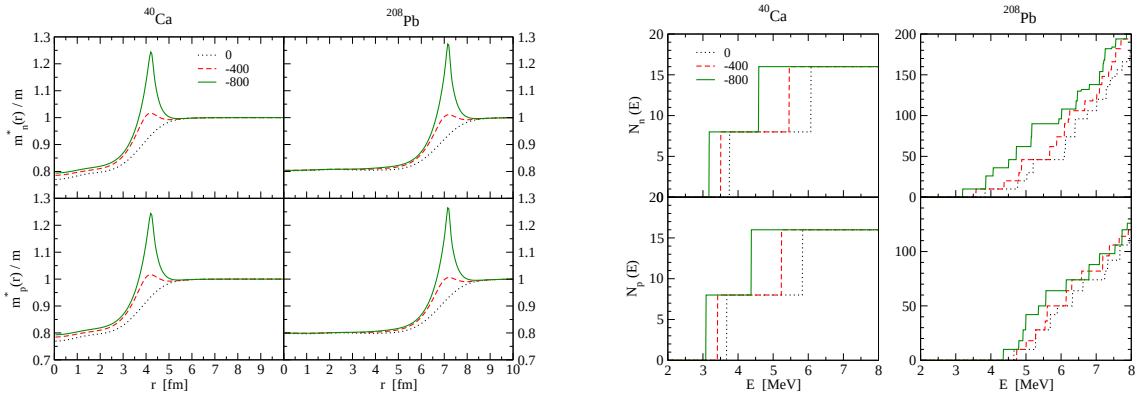

Figure 4.5: On the left panel is shown the neutron and the proton effective mass $m^*_{n,p}/m$ as a function of radial coordinate for ^{40}Ca and ^{208}Pb, with different choices for the parameter $C_0^{\tau(\nabla\rho)^2} = 0$, -400, -800 MeV fm^{10}. On the right panel is shown the number of states as a function of the excitation energy for ^{40}Ca and ^{208}Pb, and for the same values of the parameter $C_0^{\tau(\nabla\rho)^2}$.

of terms is much larger and the correction to the effective mass is a polynomial in the density. It would be interesting to carry out a more detailed comparison of these two different approaches in a future study.

In the following, we study the influence of the correction introduced by the new term $\mathcal{H}_0^{\rm corr}$ for two representative nuclei: ^{40}Ca and ^{208}Pb, using BSk14 interaction (Goriely et al., 2007), which is adjusted to a large number of nuclei (2149 in total). The effective mass in symmetric matter at saturation density is $0.8m$ and the isospin splitting of the effective mass in asymmetric matter qualitatively agrees with the expected behavior deduced from microscopic Brueckner-Hartree-Fock theory (Van Dalen et al., 2005). In the following, we study the effect of the correction term on top of BSk14 interaction without refitting the parameters. The refit is in principle necessary since the correction term impacts the masses and changes the single particle energies. In this first exploratory work, we improve the level density and discuss the effects on the pairing.

4.3.1 Mean field properties

The neutron and proton effective masses are plotted in the left panel of Fig. 4.5 for different values of the coefficient $C_0^{\tau(\nabla\rho)^2} = 0$, -400, -800 MeV fm^{10}. Notice that the case $C_0^{\tau(\nabla\rho)^2} = 0$ is that of the original Skyrme interaction BSk14. Increasing $|C_0^{\tau(\nabla\rho)^2}|$ from 0 to 800 MeV fm^{10}, we observe an increase of the effective mass m^*/m at the surface, which produces a peak for large values of $C_0^{\tau(\nabla\rho)^2}$, while at the center of the nucleus the effective masses get closer to the values obtained without the correction term. Fig. 4.5 can be compared with Fig. 1 of Ref. (Ma and Wambach, 1983). Due to the different surface-peaked functions (here $(\nabla\rho)^2$ instead of a single ∇ dependence in Ref. (Ma and Wambach, 1983)), the width of the effective mass at the surface is larger in Ref. (Ma and Wambach, 1983) than in the present work. For values of the coefficient $|C_0^{\tau(\nabla\rho)^2}|$ larger than 800 MeV fm^{10}, the potentials $U^{\rm corr}(r)$ and $U_q^{\rm eff}(r)$ (Eq. (4.23) induce large gradients of the mean field in a tiny region close to the surface of the nuclei, which in turn produce an instability in the HF iterations.

In order to evaluate the impact of the new term on the density of states, we display in the right panel of Fig. 4.5 the neutron and proton number of states as a function of the excitation energy, defined as:

$$N(E) = \int_0^E dE'\, g(E') \,, \tag{4.25}$$

where g(E) is the density of states,

$$g(E) \equiv \frac{\mathrm{d}N(E)}{\mathrm{d}E} = \sum_{\lambda_1<F,\lambda_2>F} (2j_{\lambda_2}+1)\,\delta(E-(\epsilon_{\lambda_2}-\epsilon_{\lambda_1}))\,, \tag{4.26}$$

and ϵ_{λ_1} (ϵ_{λ_2}) represent the single-particle energies below (above) the Fermi surface. The expected relation between the surface-peaked effective mass and the density of states is clearly shown in Fig. 4.5: the number of states at given excitation energy increases as the coefficient $C_0^{\tau(\nabla\rho)^2}$ goes from 0 to -800, meaning that the density of states also increases as $|C_0^{\tau(\nabla\rho)^2}|$ gets larger. Figs. 4.5 clearly illustrate the relation between the increase of the effective mass at the surface of nuclei and the increase of the density of states close to the Fermi energy.

4.3.2 Pairing properties

Most of the nuclei are superfluid and it could be shown that in the weak coupling limit of the BCS approximation, the pairing gap at the Fermi surface Δ_F and the pairing interaction v_{pair} are related in uniform matter through the relation (Lombardo, 1999):

$$\Delta_F \approx 2\epsilon_F \exp[2/(N_0 v_{pair})], \tag{4.27}$$

where ϵ_F is the Fermi energy, $N_0 = m^* k_F/(\hbar^2\pi^2)$ is the density of states at the Fermi surface. Then a small change of the effective mass m^* can result in a substantial change of the pairing gap.

In the following, we will consider ^{120}Sn because it is an excellent candidate to study pairing correlations (Bender et al., 2003): ^{120}Sn is spherical and only neutrons are participating to the S-wave Cooper-pairs. An accurate description of the pairing properties can be obtained already at the level of the spherical HF+BCS framework (Bender et al., 2003). In this section, we study qualitatively the relation between the increase of the effective mass at the surface and its consequences on the pairing properties.

We adopt a density-dependent contact interaction v_{nn} given by Eq. (3.8) where the strength v_0 of the pairing interaction is adjusted to obtain an average pairing gap equals to 1.3 MeV in ^{120}Sn. The power of the density dependence $\alpha = 1$ and we explore different values for η going from 0 (volume pairing) to 1 (surface pairing). We define a cut-off of 8 MeV complemented by a smooth Gaussian function of the following form $\exp\left(-[(E_\lambda - E_c)/a]^2\right)$ where $E_c = 8$ MeV and $a = 1$ MeV. Notice that to be compatible with HFB calculations, the cutoff is implemented on the quasiparticle energy, $E_{\lambda,q} = [(\epsilon_{\lambda,q}-\mu_q)^2 + \Delta^2_{\lambda,q}]^{1/2}$, where ϵ_λ is the HF energy, μ the chemical potential, and $\Delta_{\lambda,q}$ the average pairing gap for the state λ.

In the following, we study the influence of the correction term (4.20) on the pairing properties at $T = 0$. A realistic calculation for nuclei shall treat consistently the pairing interaction in the particle-particle channel and that in the particle-hole channel. The bare interaction in the particle-particle channel shall then be replaced by the induced one which accounts for a 50% correction (Goriely et al., 2005). It is however not our intention in the present work to investigate this question. We want, at a simpler level, to clarify the role of the correction term (4.20) on the pairing properties, and we will show that there is indeed a correlation in space between the enhancement of the effective mass and that of the probability distribution of the Cooper pairs.

In order to reproduce the value of the average gap $\tilde{\Delta}_n = 1.3$ MeV in ^{120}Sn, we have adjusted the pairing gap for three kinds of pairing interactions (volume, mixed, and surface), for the functional without the correction term (4.20). We obtain for the values (η, v_0): (0; -259 MeV fm^3), (0.5; -391 MeV fm^3), (1; -800 MeV fm^3). In Table 4.2 we report the values for the average neutron pairing gap $\tilde{\Delta}_n$, calculated as the average gap over the abnormal density,

$$\tilde{\Delta}_n \equiv \frac{1}{\tilde{N}} \int d\mathbf{r}\ \tilde{\rho}_n(\mathbf{r})\Delta_n(\mathbf{r})\,, \tag{4.28}$$

$C_0^{\tau(\nabla\rho)^2}$		η	
[MeV fm^{10}]	0	0.5	1
0	1.30	1.30	1.30
-200	1.33	1.36	1.47
-400	1.37	1.43	1.62
-600	1.42	1.52	1.79
-800	1.49	1.60	1.96

Table 4.2: Average neutron pairing gap $\tilde{\Delta}_n$ for ^{120}Sn for different values of the coefficient $C_0^{\tau(\nabla\rho)^2}$.

where $\tilde{N} = \int d\mathbf{r}\ \tilde{\rho}_n(\mathbf{r})$, and for several values of the coefficient $C_0^{\tau(\nabla\rho)^2}$. In Table 4.2, it is shown that the effect of the correction term (4.20) on the pairing gap is non-negligible. The pairing gap is increased by 200 to 700 keV as the coefficient $|C_0^{\tau(\nabla\rho)^2}|$ gets larger. An important dependence with respect to the kind of the pairing interaction (volume, mixed, surface) is also observed. The largest effect of the correction term (4.20) is obtained for the surface pairing gap. From the results presented in Table 4.2 we notice that the correction term (4.20) in the functional has an important influence on the average pairing gap.

4.3.3 Thermal corrections

The density of states around the Fermi energy shall influence the temperature-related quantities such as the entropy and the specific heat (Chamel et al., 2009b), and at the same time the density of states is also affected by the temperature in mean field models (Vinh Mau and Vautherin, 1985; Donati et al., 1994; Giovanardi et al., 1996).

We explore the effect of the new term on ^{120}Sn in the framework of HF+BCS at finite temperature, using the pairing interaction where the strength has been renormalized at $T = 0$ for each value of the coefficient $C_0^{\tau(\nabla\rho)^2}$. In Fig. 4.6 we show the neutron pairing gap as a function of temperature, for the three different kinds of pairing interactions (volume, mixed, surface). The results on the left are obtained keeping the coefficient $C_0^{\tau(\nabla\rho)^2}$ constant, while, on the right, we plot the results obtained letting $C_0^{\tau(\nabla\rho)^2}$ vary exponentially with temperature, according to the following relation:

$$C_0^{\tau(\nabla\rho)^2}(T) = C_0^{\tau(\nabla\rho)^2} \times e^{-T/T_0}\ , \tag{4.29}$$

with $T_0 = 2$ MeV. The choice of this kind of temperature dependence relies on the work by Donati *et al.* (Donati et al., 1994), where a study of the ω-mass in the framework of QRPA for temperatures up to some MeV was carried out on some neutron rich nuclei. The variation of m_ω with respect to temperature was parameterized with an exponential profile and the typical scale of the variation of m_ω with temperature was found to be around 2 MeV. Notice that in semi-infinite nuclear matter, the typical scale was found to be 1.1 MeV (Giovanardi et al., 1996). The reduction of the scale might be due to the semi-infinite model which is still far from a realistic finite nucleus case.

We observe in all cases in Fig. 4.6 the typical behavior associated to the existence of a critical temperature T_c after which pairing correlations are destroyed (Goodman, 1981). In particular, as expected, T_c is not modified by the new term for the case of constant coefficient, since we absorbed the effect of the new term through the renormalization procedure. Instead, the effect of a temperature dependent coefficient $C_0^{\tau(\nabla\rho)^2}(T)$ is to reduce the critical temperature; indeed, the chosen dependence (4.29) shifts the critical temperature of ~ 40 keV in the case of volume interaction and of ~ 60 keV in the case of surface interaction. The relation $T_c \simeq \tilde{\Delta}_n(T=0)/2$ is still verified; more precisely, the ratio $T_c/\tilde{\Delta}_n(T=0)$ is $\simeq 0.55$ (for volume interaction) and $\simeq 0.57$ (for surface interaction) for the case of T-independent $C_0^{\tau(\nabla\rho)^2}$, while

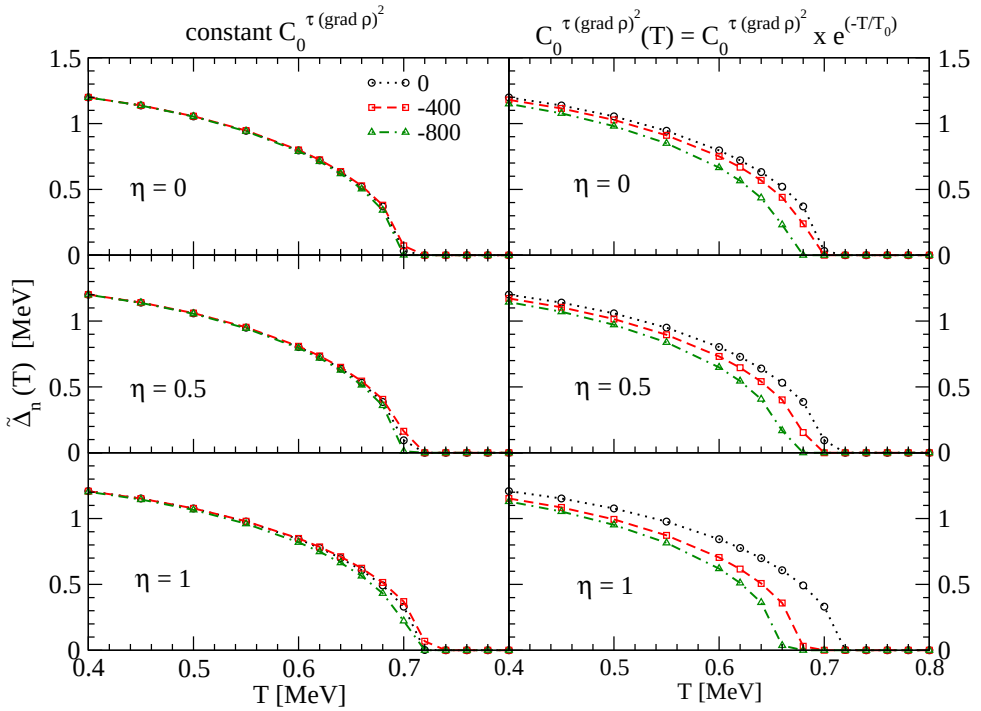

Figure 4.6: Neutron pairing gap for ^{120}Sn as a function of temperature for different values of the coefficient $C_0^{\tau(\nabla\rho)^2}$. The results on the left are obtained keeping $C_0^{\tau(\nabla\rho)^2}$ constant ($C_0^{\tau(\nabla\rho)^2}$ = 0, -400, -800 MeV fm^{10}), while the results on the right are obtained using for $C_0^{\tau(\nabla\rho)^2}$ the prescription in Eq. (4.29).

with the T-dependent prescription (4.29) it varies from $\simeq 0.55$ (for volume interaction) to $\simeq 0.51$ (for surface interaction). In conclusion, we remark that through its temperature dependence, the surface-peaked effective mass has an effect on the critical temperature, that could also be extracted experimentally (Dean and Hjorth-Jensen, 2003). This perspective motivates the application of the present work to realistic cases at finite temperature.

Finally, in Fig. 4.7 we show the total entropy and specific heat as a function of temperature for volume and surface interaction, and for three values of $C_0^{\tau(\nabla\rho)^2}$ (0, -800 MeV fm^{10}, and $C_0^{\tau(\nabla\rho)^2}(T)$ for the case -800 MeV fm^{10}). The entropy of the system is calculated as: $S_{tot} = S_n + S_p$, being:

$$S_q = -k_B \sum_\lambda \left[f_{\lambda,q} \ln(f_{\lambda,q}) + (1 - f_{\lambda,q}) \ln(1 - f_{\lambda,q}) \right] , \tag{4.30}$$

where $f_{\lambda,q}$ is the Fermi-Dirac distribution. The specific heat is then defined as:

$$C_V = T \, \frac{\partial S_{tot}}{\partial T} . \tag{4.31}$$

We observe the change of the slope in the entropy curve, which causes the discontinuity in the specific heat in correspondence of the critical temperature. In agreement with the previous results, T_c is shown to be modified by a temperature-dependent $C_0^{\tau(\nabla\rho)^2}$, the effect is stronger in the case of surface interaction, and the temperature dependent coefficient acts as to reduce T_c.

4.3.4 Final remarks

In this section we have studied the influence of the correction term (4.20) on various nuclear properties. The isoscalar correction term (4.20) has been shown to produce a surface-peaked effective mass in the

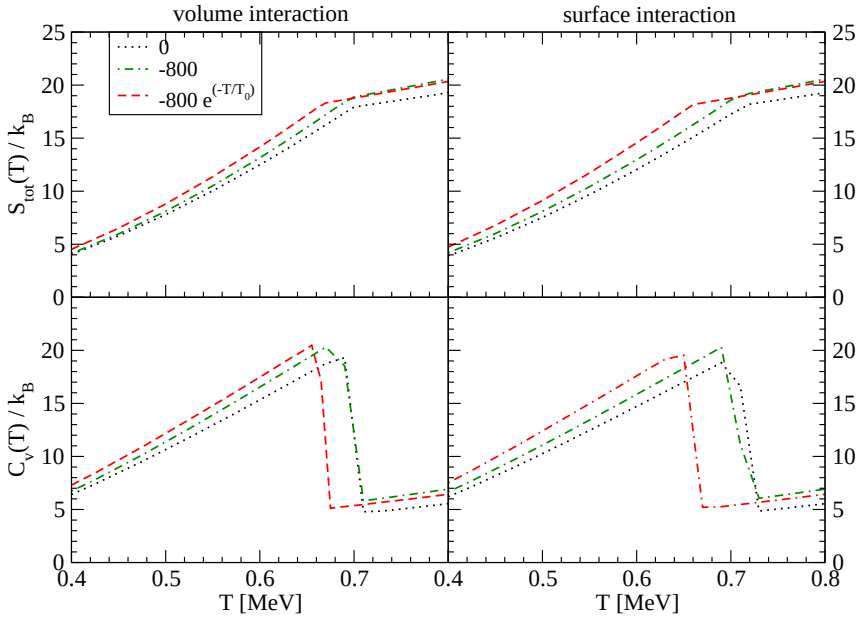

Figure 4.7: Total entropy S_{tot} and specific heat C_V (in units of the Boltzmann constant), for ^{120}Sn as a function of temperature, for $C_0^{\tau(\nabla\rho)^2} = 0$, -800 MeV fm^{10}, -800 e^{-T/T_0} MeV fm^{10}, and for volume (on the left) and surface (on the right) pairing interaction.

nuclei under study (^{40}Ca and ^{208}Pb), without modifying significantly the mean field profiles. The increase of m^*/m at the surface is up to about 1.2 - 1.3 for the maximum value of the strength of the correction we used. As the effective mass gets enhanced at the surface of nuclei, the density of states increases. Then, we have studied the impact of such a term on the neutron pairing gap in the semi-magic nucleus ^{120}Sn, within an HF+BCS framework, and it turned out that its effect is non-negligible; if the pairing interaction is not renormalized consistently with the new term, the average gap increases from 200 keV to 700 keV under variation of the strength of the correction term and depending on the volume/surface character of the interaction.

In a recent work (Baldo et al., 2010), it has been stressed that the surface enhancement of the pairing field induced by the PVC might also play a role on the size of the Cooper-pairs at the surface of nuclei. In uniform matter, the coherence length is indeed inversely proportional to the pairing gap. The surface enhancement of the pairing field could then make the Cooper-pairs smaller at the surface of nuclei. It would be interesting to investigate whether this interesting feature of the pairing correlation might be probed experimentally, for example by pair transfer reaction mechanism. This would make a connexion with the work presented in section 3.5.

Finally, we have explored some finite temperature properties in ^{120}Sn, within a HF+BCS framework at finite temperature. We observed for the neutron pairing gap that the critical temperature at which pairing correlations vanish is shifted if a T-dependence in the new coefficient is considered. As a consequence, the entropy and specific heat profiles are affected by the introduction of the new term.

In the future, we shall go on with a global refitting of all the parameters of the functional, including the new correction term (4.20). It would be very instructive to know whether both the masses and the single particle levels could be improved in such a way, and to use this new model in core-collapse simulation in a similar way as what have been shown in section 4.2.2.

4.4 Conclusions and outlooks

In this chapter, we have explored the effect of the temperature on the effective mass in nuclei on the astrophysical simulation of core-collapse supernovae. A simple model which provides a parameterization of a microscopic QRPA model performed in few nuclei was explored. Corrections of the temperature dependence of the effective mass on the EOS such as the symmetry and the thermal energies have been included within this simple model. It was found a non-negligible impact on the position of the shock wave at bounce as well as on the velocity of the shock. The effect is that including the temperature dependence of the effective mass in the simple modeling the shock wave is formed more externally and is going faster. It can therefore be stated that the temperature dependence of the effective mass definitively helps in the energetics of the shock wave. This motivates the inclusion of this effect in 3-dimensional models that still have problems to explose.

On the microphysical side, the success of the simple model proposed in section 4.2 motivate some improvements. A re-analysis of the role of the effective mass in the EoS indicates that the expected corrections shall better appear in the surface term of the liquid-drop model rather that in the bulk terms as it have been done in section 4.2. This new corrections are however less easy to include in EoS such as BBAL (Bethe et al., 1979) since the surface term of the liquid-drop model is treated in a parameterized way making the link with the liquid-drop model difficult to establish. Another extension of the simple model on the base of the energy density functional have been proposed in section 4.3. It have shown its possibility to reproduce the expected outcomes of producing a surface-peaked effective mass, and it was generalized to include the temperature dependence. In the future, it would be interesting to produce a model correctly adjusted on binding energies and radii of nuclei in their ground-state and to generate an EoS table for core-collapse simulations.

Finally, it shall be mentioned that a statistical approach partially based on the experimental density of states can also be explored and shall contain all the key ingredients to simulate the temperature dependence of the effective mass and its impacts on the EoS (Gulminelli and Raduta, 2012). In conclusions, there are different ways to extend the simple model that was used in core-collapse simulations and which will help in understanding the microscopic features presented in this section.

Chapter 5

Microscopic modeling of the crust of neutron stars

In this chapter we discuss the effects of pairing correlations on inner crust matter in the density region where nuclear clusters are supposed to coexist with non-localised neutrons. The pairing correlations are treated in the framework of the finite temperature Hartree-Fock-Bogoliubov approach and using zero range nuclear forces. After a short introduction and presentation of the formalism we discuss how the pairing correlations affect the structure of the inner crust matter, i.e., the proton to neutron ratio and the size of Wigner-Seitz cells. Then we show how the pairing correlations influence, though the specific heat of neutrons, the thermalization of the crust in the case of a rapid cooling scenario.

5.1 Introduction

Many observed neutron star phenomena are intimately related to the physics of the crust. For instance, X-ray bursts in Low-Mass X-ray Binaries are associated with thermonuclear burning in the accreting neutron star envelope (Strohmayer and Bildsten, 2006). In the subgroup of soft X-ray transients, accretion outbursts are followed by long period of quiescence during which the accretion rate is essentially zero. In some cases, the period of accretion can last long enough for the crust to be heated out of equilibrium with the core. The thermal relaxation during the quiescent state has been recently monitored for KS 1731−260 and for MXB 1659−29 after an accretion episode of 12.5 and 2.5 years respectively (Cackett et al., 2006). These observations thus provide information on the thermal properties of neutron star crusts (Rutledge et al., 2002; Shternin et al., 2007). The thermal relaxation of the crust could also be potentially observed in very young isolated neutron stars, $10 - 100$ years after their formation (Lattimer et al., 1994; Gnedin et al., 2001).

In the standard model of neutron stars (Baym et al., 1971), the crust is believed to be formed of nuclear clusters in a body centered cubic lattice stabilized by Coulomb forces and considered infinite and pure (made of only one type of nuclei at a given density). In the inner crust, at densities above $\sim 4.10^{11}$ g.cm^{-3} and below $\sim 10^{14}$ g.cm^{-3}, the "neutron drip" regime is reached and the clusters are surrounded by a neutron fluid. A formal comparison can be made with electrons in ordinary solids present on earth: part of the neutrons participate to the nuclear clusters which form the lattice (equivalent to electrons bounded to atoms) while part of the neutrons are delocalized over the whole crystal (equivalent to valence electrons). As a consequence, the band theory of solids developed in condensed matter (Kittel, 1996) can be applied to describe the crust of neutron star. But due to the highly specific numerical issues of band theory, nuclear

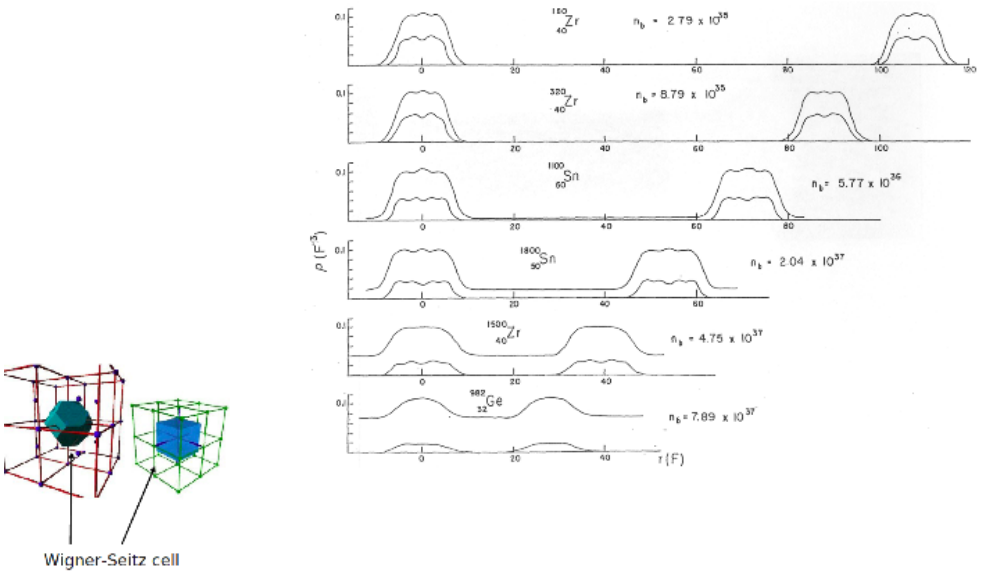

Figure 5.1: Left: representation of 2 lattices. Right: NV calculations at different densities.

physicists have preferred to use an approximation due to Wigner and Seitz (W-S) (Wigner and Seitz, 1933; Wigner and Seitz, 1934), where the crust is divided into independent and spherical cells. Since the work of Negele and Vautherin (Negele and Vautherin, 1973), the W-S approximation has been used to predict the structure of the crust, the pairing properties, the thermal effects, or the low lying energy excitation spectrum (Bonche and Vautherin, 1981; Sandulescu et al., 2004; Sandulescu, 2004; Khan et al., 2005; Vigezzi et al., 2005; Baldo et al., 2005a; Baldo et al., 2006). Only recently, band theory calculations have been carried out in order to study the hydrodynamical properties of the neutron fluid and in particular the neutron effective mass giving rise to entrainment effects (Carter et al., 2005; Chamel, 2005; Chamel, 2006), although these calculations are not yet self-consistent. While the W-S approximation is well justified below the "neutron drip" regime, its validity beyond remains to be assessed.

5.2 Microscopic quantum description of neutron star inner crust

An accurate description of the inner crust, assuming that it is a perfect crystal, should rely on the band theory of solids (Kittel, 1996). In this section, we briefly review this theory in the context of neutron star crust and discuss the W-S approximation in this framework.

5.2.1 Band theory of solids

According to the Floquet-Bloch theorem, the single particle quantum states are given by modulated plane waves

$$\varphi_{\alpha\boldsymbol{k}}(\boldsymbol{r}) = u_{\alpha\boldsymbol{k}}(\boldsymbol{r})e^{i\boldsymbol{k}\cdot\boldsymbol{r}}\,, \tag{5.1}$$

where the functions $u_{\alpha\boldsymbol{k}}(\boldsymbol{r})$ have the full periodicity of the lattice. Each single particle quantum state is thus labeled by a discrete index α and by a wave vector $\boldsymbol{k}$. The energy spectrum is therefore formed of a series of sheets or "bands" in $\boldsymbol{k}$-space.

The Bloch states (5.1) are completely determined by the knowledge of the functions $u_{\alpha\boldsymbol{k}}(\boldsymbol{r})$ inside a W-S cell of the lattice, whose shape is imposed by the symmetry of the crystal. The cell, centered around one nuclear cluster, is electrically neutral and therefore contains as many electrons as protons. The effects of the ion lattice on the electrons, which give rise to complicated band structures in ordinary terrestrial matter are negligible in the inner crust of a neutron star due to the very high densities (Pethick and Ravenhall, 1995). Nevertheless, the neutron band effects due to nuclear inhomogeneities cannot be ignored.

In the present study, we consider the outermost layers of the inner crust where pairing effects are negligible (Baldo et al., 2005b). In the Hartree-Fock approximation with Skyrme forces which we shall consider in the following, the occupied nucleon single particle wave functions are obtained by solving the self-consistent equations ($q = n, p$ for neutrons and protons respectively)

$$h_0^{(q)}\varphi_{\alpha\boldsymbol{k}}^{(q)}(\boldsymbol{r}) = \varepsilon_{\alpha\boldsymbol{k}}^{(q)}\,\varphi_{\alpha\boldsymbol{k}}^{(q)}(\boldsymbol{r}) \tag{5.2}$$

where the single particle Hamiltonian is defined by

$$h_0^{(q)} \equiv -\boldsymbol{\nabla}\cdot\frac{\hbar^2}{2m_q^{\oplus}(\boldsymbol{r})}\boldsymbol{\nabla} + U_q(\boldsymbol{r}) - \mathrm{i}\boldsymbol{W_q}(\boldsymbol{r})\cdot\boldsymbol{\nabla}\times\boldsymbol{\sigma}\,, \tag{5.3}$$

the effective masses $m_q^{\oplus}(\boldsymbol{r})$, mean fields $U_q(\boldsymbol{r})$ and spin-orbit terms $\boldsymbol{W_q}(\boldsymbol{r})$ being functionals of the single particle wave functions. These equations have to be solved inside the W-S cell with the boundary conditions imposed by the Floquet-Bloch theorem

$$\varphi_{\alpha\boldsymbol{k}}^{(q)}(\boldsymbol{r}+\boldsymbol{T}) = e^{\mathrm{i}\boldsymbol{k}\cdot\boldsymbol{T}}\varphi_{\alpha\boldsymbol{k}}^{(q)}(\boldsymbol{r})\,, \tag{5.4}$$

where $\boldsymbol{T}$ is any lattice vector. This means in particular that the wavefunction between two opposite faces of the cell has a phase shift $e^{\mathrm{i}\boldsymbol{k}\cdot\boldsymbol{T}}$ where $\boldsymbol{T}$ is the corresponding lattice vector. The single particle energies are periodic in the reciprocal lattice whose vectors $\boldsymbol{K}$ satisfy $\boldsymbol{K}\cdot\boldsymbol{T} = 2\pi n$ (where n is any integer)

$$\varepsilon_{\alpha,\boldsymbol{k}+\boldsymbol{K}}^{(q)} = \varepsilon_{\alpha\boldsymbol{k}}^{(q)}\,. \tag{5.5}$$

Consequently only the values of $\boldsymbol{k}$ inside the first Brillouin zone (*i.e.* W-S cell of the reciprocal lattice) are relevant.

Equivalently, equations (5.2) can be written directly for the $u_{\alpha\boldsymbol{k}}^{(q)}(\boldsymbol{r})$ functions in the decomposition (5.1) which leads to

$$(h_0^{(q)} + h_{\boldsymbol{k}}^{(q)})u_{\alpha\boldsymbol{k}}^{(q)}(\boldsymbol{r}) = \varepsilon_{\alpha\boldsymbol{k}}^{(q)}\,u_{\alpha\boldsymbol{k}}^{(q)}(\boldsymbol{r}) \tag{5.6}$$

where the $\boldsymbol{k}$-dependent Hamiltonian $h_{\boldsymbol{k}}^{(q)}$ is defined by

$$h_{\boldsymbol{k}}^{(q)} \equiv \frac{\hbar^2 k^2}{2m_q^{\oplus}(\boldsymbol{r})} + \boldsymbol{v_q}\cdot\hbar\boldsymbol{k}\,, \tag{5.7}$$

and the velocity operator $\boldsymbol{v_q}$ is defined by the commutator

$$\boldsymbol{v_q} \equiv \frac{1}{\mathrm{i}\hbar}[\boldsymbol{r}, h_0^{(q)}]\,. \tag{5.8}$$

The band theory takes into account all the symmetries of the system. However equations (5.2) with the boundary conditions (5.4) are numerically very complicated to solve. The approximation introduced a long time ago by Wigner and Seitz in the study of metallic sodium (Wigner and Seitz, 1933; Wigner and Seitz, 1934) has been widely applied in the context of neutron star crust.

The specific heat (per unit volume) is defined as

$$c_V(T) = \left.\frac{\partial U}{\partial T}\right|_V = T\left.\frac{\partial S}{\partial T}\right|_V\,, \tag{5.9}$$

(taking the Boltzmann's constant $k_{\rm B} = 1$) where U is the total internal energy density, S the entropy density and the partial derivatives are evaluated at constant volume V. We have found that the latter expression is numerically more convenient. The entropy density of the unbound neutrons is given by

$$S = -\sum_{\alpha} \int \frac{\mathrm{d}^3\boldsymbol{k}}{(2\pi^3)} \Big[f_{\alpha\boldsymbol{k}} \ln f_{\alpha\boldsymbol{k}} + (1 - f_{\alpha\boldsymbol{k}}) \ln(1 - f_{\alpha\boldsymbol{k}}) \Big] \tag{5.10}$$

where α is the band index, $\boldsymbol{k}$ is the Bloch wave vector and $f_{\alpha\boldsymbol{k}}$ is the Fermi-Dirac distribution. The latter depends on the temperature and the neutron chemical potential μ_n which is determined from the total density ρ_n^G of unbound neutrons by

$$\rho_n^G = \sum_{\alpha} \int \frac{\mathrm{d}^3\boldsymbol{k}}{(2\pi^3)} f_{\alpha\boldsymbol{k}} \,. \tag{5.11}$$

Note that the number of unbound neutrons per cluster is determined by the shape of the mean fields, which vary with temperature. Consequently ρ_n^G can also depend on the temperature. In particular, with increasing temperature the most loosely bound neutrons may be excited into the delocalized states.

For the range of temperatures considered here, $T \ll \varepsilon_{\rm F}$, where $\varepsilon_{\rm F}$ is the Fermi energy. The specific heat is then approximately given by (ref. (Ashcroft and Mermin, 1976), p47)

$$c_V(T) \simeq \frac{\pi^2}{3} g(\varepsilon_{\rm F}) T \,, \tag{5.12}$$

where $g(\varepsilon_{\rm F})$ is the density of states at the Fermi level. This expression is valid provided i) the density of unbound neutrons ρ_n^G and $\varepsilon_{\rm F}$ are independent of the temperature, ii) the density of states $g(\varepsilon)$ is sufficiently smooth. The density of states $g(\varepsilon_{\rm F})$ in Eq. (5.12) can be expressed as an integral over the Fermi surface $\mathcal{S}_{\rm F}$,

$$g(\varepsilon_{\rm F}) = \frac{1}{(2\pi)^3 \hbar} \sum_{\alpha} \oint_{\mathcal{S}_{\rm F}} \frac{d\mathcal{S}}{|\boldsymbol{v}_{\alpha\boldsymbol{k}}|} \,. \tag{5.13}$$

where $\boldsymbol{v}_{\alpha\boldsymbol{k}} = \hbar^{-1} \nabla_{\boldsymbol{k}} \varepsilon_{\alpha\boldsymbol{k}}$ is the group velocity of the unbound neutrons. The presence of nuclear clusters leads to the existence of resonances. As a result, the energy bands of unbound states may be locally flat in k-space thus distorting the Fermi surface (Chamel et al., 2007). The deformation can be estimated by the ratio $\xi_{\rm F}$ of the area of the deformed surface to that of the unperturbed Fermi sphere. Therefore, we have $\mathcal{S}_{\rm F} = \xi_{\rm F} 4\pi k_{\rm F}^2$, where by definition $\xi_{\rm F} = 1$ in the absence of clusters. Numerical calculations show that the nuclear lattice reduces the area of the Fermi surface by a factor of 2 in the shallowest layer (see Table II of Ref. (Chamel et al., 2009b)).

5.2.2 Wigner-Seitz approximation

The spherical W-S approximation is a computationally very efficient method with the advantage of reducing the 3D partial differential Eqs. (5.2) to ordinary differential radial equations. This approximation is twofold. First of all, the Hamiltonian $h_{\boldsymbol{k}}^{(q)}$ in equation (5.6) is neglected. Consequently the wave functions and the energies are independent of $\boldsymbol{k}$ and approximated by the solutions at $\boldsymbol{k} = 0$. Only the band index α remains. Secondly, the W-S polyhedron is replaced by a sphere of equal volume. The equations are then usually solved with the Dirichlet-Neumann mixed boundary conditions which yield a nearly constant neutron density outside the cluster.

The W-S approximation turns out to be very good if the boundary conditions play a minor role. For instance, bound states whose associated wave functions are vanishingly small outside the clusters are very well treated provided that the spatial extent of these states is smaller than the lattice spacing. This condition is fulfilled almost everywhere in the crust except in the bottom layers where the clusters nearly touch. The aim of this section is to investigate the validity of the W-S approximation for the outermost layers of the inner crust where the bound neutron states are not altered by the boundary conditions.

Let us emphasize that in the W-S approximation, the nuclear clusters are supposed to be spherical while in the full band theory, no assumption is made about their shape. For the low densities of interest in this study, the nuclear clusters can still be considered as spherical. It should mentioned that in a recent development of the W-S approximation (Magierski and Heenen, 2002), the W-S cell is replaced by a cube with strictly periodic boundary conditions. Possible deformations of the nuclear clusters are thus included but at the price of unphysical boundary conditions because the W-S cell of the body centered cubic lattice is a truncated octahedron and not a cube (the cube being the W-S cell of the simple cubic lattice). This is the reason why we still consider the spherical W-S approximation closer to the physical situation than the cubic one at low density.

5.2.3 Comparison between the band theory and the W-S approximation

The comparison between the band theory and the W-S approximation gives an estimate of the contribution (5.7) of the k-dependent Hamiltonian $h_{\boldsymbol{k}}$ and incidentally on the effects of the boundary conditions. We have considered the shallow layers of the crust at the average baryon density $\rho \sim 7 \times 10^{11}$ g/cm^3 formed of a crystal made of zirconium like clusters ($Z = 40$) with 160 neutrons (bound and unbound) per lattice site(Negele and Vautherin, 1973). In the following we shall refer to such cluster as ^{200}Zr. A small but non-zero neutron density is present at large radius generating a non-zero mean field potential. Asymptotically, this potential is equal to -0.05 MeV. All the states with energy larger than -0.05 MeV are therefore unbound or "free". We found that among the 160 neutrons per lattice site, 70 are unbound. Under such conditions, only unbound neutrons are sensitive to the boundary conditions and the nuclear clusters are spherical.

As the spin-orbit splitting is weak for most of the states we set the spin-orbit potential $\boldsymbol{W_n}(\boldsymbol{r})$ to zero. In order to study the effects of the boundary conditions, the Schrödinger equation is solved with no further iterations by imposing the Bloch boundary conditions (5.4) and using the Linearized Augmented Plane Wave method (see (Chamel, 2006) for details). The coordinate space is divided in two regions: a spherical region around the cluster plus an interstitial region. In the latter region, the wave functions are expanded on a plane wave basis in order to fulfill the Bloch boundary conditions. The lattice spacing is determined by requiring that the volume of the W-S sphere is equal to the volume of the exact W-S cell of the crystal, assumed to be a body centered cubic lattice(Baym et al., 1971).

Results and detailed discussions can be found in Ref. (Chamel et al., 2007). In summary:

- The unbound neutron densities calculated with the W-S approximation and the full band theory are quite similar.
- The single particle wave functions of unbound neutrons are qualitatively well reproduced by the W-S approximation inside the nuclear clusters. The main differences in the wavefunctions between the two calculations are found in the interstitial region due to the different boundary conditions. However this has a rather small effect on the ground state properties of the neutron gas, like the neutron density distribution.
- Single particle energy spectrum: Since in band theory, the energies depend also on the wavevector $\boldsymbol{k}$, only the energy bands along some specific symmetry directions in $\boldsymbol{k}$-space are displayed. The energy spectrum obtained with the W-S approximation is comparable to the one obtained in the band theory for the symmetry point Γ corresponding to the center $\boldsymbol{k} = 0$ of the first Brillouin zone (W-S cell of the reciprocal lattice). The correspondence is not exact and the differences come from the spherical approximation. As a result, the W-S approximation predicts less states but with larger degeneracies than the band theory at the symmetry point Γ. The figures show clearly another important difference between the band theory and the W-S approximation: in the former case the energy spectrum is continuous while in the latter case it is discrete.

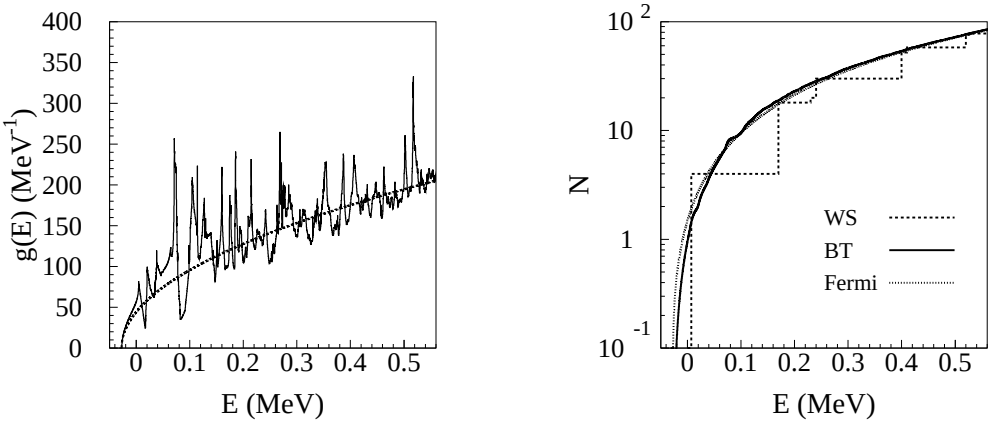

Figure 5.2: Left: level density for neutron unbound states calculated with the band theory (solid line) compared with the prediction of the free Fermi gas (dashed line). The energy resolution is of the order of keV. Right: Integrated state number calculated with the W-S approximation (WS, dashed lines), band theory (BT, solid line), and free Fermi gas (doted lines).

- The level density is represented in Fig. 5.2. As expected the figure shows that the energy spectrum in the band theory is continuous and has a complex fine structure. The spectrum exhibits a quasi band gap of about 30 keV slightly around 90 keV. This is in sharp contrast with the W-S approximation for which the energy levels are discrete and separated by about 100 keV. In other words, the W-S approximation overestimates the neutron shell effects. In contrast, in the band theory the spherical symmetry is partly broken due to the translational symmetry of the crystal lattice. The energy levels thus broaden into bands, with a low residual degeneracy (at most 6 at each $\boldsymbol{k}$ point for cubic crystals, counting the spin degeneracy (Koster, 1957)), which overlap so that the energy spectrum is continuous.

- Thermal properties: We have considered three different layers in the shallow region of the inner crust (Chamel et al., 2009b). The neutron chemical potential $\mu_n(T)$, the entropy density $S(T)$, and the neutron specific heat have been calculated for a set of temperatures between $T = 10$ keV and $T = 100$ keV. Band theory and Wigner-Seitz calculations have been found to give very close results for these quantities. From the comparison of various approximations to the neutron specific heat, we have found that the Fermi gas model reproduces very well the results of the band theory, while more sophisticated approaches like the Wigner-Seitz or the de Gennes approximations are less accurate.

- The dynamical effective mass $m_n^\star$ has been calculated for the considered layers, using the same numerical method as in Ref. (Chamel, 2005). If the unbound neutrons were free we would have found $m_n^\star/m_n = 1$. However, the dynamical effective mass is much larger than the bare neutron mass $m_n^\star/m_n > 1$ indicating that the interactions between the neutrons and the clusters are very strong. Nevertheless, this analysis in terms of the topology of the Fermi surface explains why the presence of the nuclear clusters has such a strong impact on the motion of the unbound neutrons but not on their specific heat.

In conclusion, for processes which involve transferred energies above the characteristic level spacing around the Fermi energy, the differences between the W-S approximation and the full band theory are

expected to be small. For instance, it is typically the case for neutrino response function (Margueron et al., 2004b) or thermal effects before the star cools completely down. However at lower energies, as pertaining for instance the effective neutron mass relevant for fluid dynamics (Carter et al., 2005; Chamel, 2005; Chamel, 2006), the full band theory is required. The level spacing can be roughly evaluated from the quantity $\hbar^2/2mR_{\rm cell}^2$. From the top to the bottom layers of the crust, the characteristic level spacing varies from about 100 keV to 200 keV, which corresponds to temperatures of the order of 10^9 K. Such temperatures are found in young neutron stars less than a few hundred years after their birth (Page and Reddy, 2006). The W-S approximation is therefore well suited for describing the hot dense matter (except for the high density layers where the spherical approximation may be too restrictive) in young neutron stars and in the collapsing core of massive stars during supernova explosions (Bonche and Vautherin, 1981). This discussion however does not take into account pairing effects, which are negligible in the outermost layers of the crust considered in this work but are expected to be important in denser and deeper layers (Baldo et al., 2005b). It should be noted that a recent study has shown that the pairing properties of the unbound neutrons are strongly sensitive to the choice of boundary conditions in the W-S approximation, especially in the bottom layers of the crust (Baldo et al., 2006; Baldo et al., 2007).

5.3 Superfluid properties of the crust of neutron stars

One of the important feature of neutron stars lies in their superfluid properties which is located in their entire volume from their crust to their deep inside core. They can therefore be view as a stellar superfluid object with specific observational consequences. Among them, the superfluid properties of the inner crust of neutron stars have been considered long ago in connection with post-glitch timing observations and cooling processes. The vortex flux tubes formed in rotating superfluid matter and present in the entire volume of the neutron star are indeed pinned to the crust and make the rotation of the star rigid. The loss a energy of the neutron star through electromagnetic, cosmic ray and gravitational emission imposes from times to times a release of the angular momentum trapped in the vortex flux tubes which induces as a glitch in the rotation period (Anderson and Itoh, 1975; Pines and Alpar, 1985). The cooling process is also strongly influenced by the pairing properties of Baryons. In the crust of neutron stars, it is essentially the $^1S_0$ neutron pairing which is of relevance for the thermalization process, defined as the time needed for the crust matter to equilibrate its temperature to the colder core. It occurs in the cooling of isolated neutron stars (Lattimer et al., 1994; Brown et al., 1988) or in the thermal after-burst relaxation of neutron stars from X-ray transients (Shternin et al., 2007; Brown and Cumming, 2009; Haensel et al., 2007). In this chapter, we present a microscopic approach to describe pairing properties in non-uniform neutron star matter.

Neutron matter superfluidity has been intensively studied over the last decades. Briefly summarized the issue in $^1S_0$ neutron superfluidity is that while there is almost no difference in the calculation of the BCS pairing gap calculated from various NN potential, different approaches beyond the first order BCS one's predict a large variety of pairing gaps in neutron matter (Lombardo and Schuck, 2001). Models based on diagrammatic expansion which treat polarization in both particle-particle and particle-hole channels predict a screening of the pairing gap and a reduction by a factor 2-3 compared to the BCS one. Other more global Monte-Carlo models predict pairing gaps that are closer to the original BCS one. We explore in this section the impact of these various predictions for pairing properties in non-uniform neutron star matter.

The neutron-drip line fixes a limit to the neutron-rich nuclei produced in laboratories or in supernova explosions (via rapid neutron-cupture processes). However, this limit can be overpassed in the inner crust of neutron stars since there dripped neutrons are kept together with the neutron-rich nuclei by the gravitational pressure. It is generally considered that in most of its part the inner-crust is formed of nuclei-like clusters (Baym et al., 1971; Negele and Vautherin, 1973). The inner-crust matter of non-accreting cold neutron

			DME (Negele and Vautherin, 1973)			SLy4 (Grill et al., 2011)		
N_{cell}	ρ_B [g cm^{-3}]	k_F [fm^{-1}]	N	Z	R_{WS} [fm]	N	Z	R_{WS} [fm]
1	$7.9\ 10^{13}$	1.12	1460	40	20			
2	$3.4\ 10^{13}$	0.84	1750	50	28			
3	$1.5\ 10^{13}$	0.64	1300	50	33	980	40	30.2
4	$9.6\ 10^{12}$	0.55	1050	50	36	726	30	31.6
5	$6.2\ 10^{12}$	0.48	900	50	39	538	30	33.2
6	$2.6\ 10^{12}$	0.36	460	40	42	252	22	34.6
7	$1.5\ 10^{12}$	0.30	280	40	44	158	22	36.6
8	$1.0\ 10^{12}$	0.26	210	40	46	120	24	38.6
9	$6.6\ 10^{11}$	0.23	160	40	49	80	24	39.8
10	$4.6\ 10^{11}$	0.20	140	40	54	58	24	41.4

Table 5.1: The structure of the Wigner-Seitz cells obtained from mean field calculations without pairing. Are shown the results of the density matrix expansion (DME) (Negele and Vautherin, 1973) and the Skyrme SLy4 interaction (Grill et al., 2011). ρ_B is the baryon density, $k_F = (3\pi^2 n_B)^{1/3}$ the Fermi momentum calculated as in Ref. (Baldo 2005) where n_B is the number of baryons per fm^3, N and Z are the numbers of neutrons and protons while R_{WS} is the radius of the WS cells. No results are shown for the cells 1 and 2 since a clear minimum has not been found with SLy4 interaction.

stars is indeed formed by a crystal lattice of spherical nuclear clusters immersed in a sea of low-density superfluid neutrons and ultra-relativisitic electrons. More inside the star, before nuclei dissolve completely into the liquid of the core, the nuclear matter can develop other exotic configurations as well, i.e, rods, plates, tubes, and bubbles (Pethick and Ravenhall, 1995). The thickness of the inner crust is rather small, of the order of or less than one kilometer, and its mass is only about 1% of the neutron star mass. However, despite its small size, the properties of inner crust matter, especially its superfluid properties, have important consequences for the dynamics and the thermodynamics of neutron stars, but their accurate calculation requires a proper model for non-uniform crust matter.

So far only a few microscopic calculations have been performed to describe the properties of the non-uniform crust matter. The first microscopic calculation of the inner-crust structure, still used as a benchmark in present neutron stars studies, see for instance Refs. (Page et al., 2006; Pizzochero et al., 2002; Monrozeau et al., 2007), was performed in Ref. (Negele and Vautherin, 1973). In this work the crystal lattice is divided in independent spherical cells which are treated in the Wigner-Seitz (WS) approximation. The nuclear energy component of the WS cells is estimated in this work in the framework of Hartree-Fock (HF) approximation based on Density Matrix Expansion (DME) (Negele and Vautherin, 1972). This approach was preferred at this time to the Density-Dependent Hartree-Fock theory (Negele, 1970) to reduce computational complication induced by the non-local exchange potential. The parameters of the DME theory were adjusted to reproduce the experimental binding energies of atomic nuclei and the theoretical calculation of infinite neutron matter energy available at that time. The spin-orbit interaction among protons was taken into account but neglected for the neutrons. The HF equations were solved in coordinate representation imposing mixed Dirichlet-Von Neuman boundary conditions at the border of the WS cells. Some of the properties of the Wigner-Seitz cells found in Ref. (Negele and Vautherin, 1973), determined for a set of densities, are shown in Table 5.1. The most remarkable result of this calculation is that the majority of WS cells have magic proton numbers, i.e., Z=40,50. This result indicates that in these calculations there are

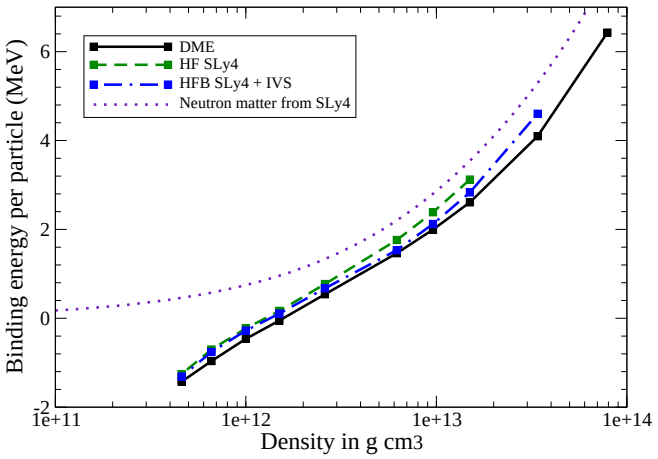

Figure 5.3: Energy per particle versus the baryon density in the inner crust of neutron stars for various models discussed in this chapter.

strong proton shell effects, as remarkable as that observed for isolated atomic nuclei. This effect is not observed in semi-classical Thomas-Fermi approaches (Douchin and Haensel, 2001), neither in models based on liquid-drop approximation (Baym et al., 1971), that does not include quantum shell effects. It could however be introduced in Thomas-Fermi approach through Strutinsky approximation (Onsi et al., 2008). More recent microscopic HF calculation which consistently takes into account the shell effects predict however a disappearance of the proton magic numbers for most of the cells (Baldo et al., 2005a; Grill et al., 2011). The calculation in Ref. (Grill et al., 2011) is made for the same densities as in the seminal work of Negele-Vautherin (Negele and Vautherin, 1973) and could therefore be directly compared in Table 5.1. With modern CPUs, the non-local exchange potential does not represent a limitation for extensive calculations and therefore, the calculation in Ref. (Grill et al., 2011) is done using Skyrme SLy4 interaction (Chabanat et al., 1998a).

A comparison of the predictions for the binding energies based on different models is shown in Fig. 5.3 for the set of densities given in Table 5.1 and for different models: DME (Negele and Vautherin, 1973), HF with Skyrme SLy4 interaction, HFB with SLy4 and IVS pairing interaction (Grill et al., 2011). For all calculations in non-uniform matter obtained with these different models, the binding energies that are obtained are well below that of the uniform neutron matter at the same density. The binding energies deduced from these models are however very close to each other despite the very different proton number Z corresponding to WS cells configurations (see Tables 5.1 and 5.2).

In this chapter, we present the most sophisticated microscopic calculations done till now based on the Hartree-Fock Bogoliubov (HFB) framework at finite temperature, and apply it for the calculation of the structure of the inner crust including superfluidity, the formation of vortices in rotating neutron stars, the calculation of the specific heat in non-uniform matter and its utilization for the calculation of the thermalization time of the crust.

5.3.1 Modeling the non-uniform crust matter

The model used to describe the superfluid properties in the crust of neutron stars is based on the finite-temperature Hartree-Fock-Bogoliubov (FTHFB) approach using density dependent contact interaction (DDCI) in the pairing channel. We first present the various pairing interactions, then the FTHFB model for non-rotating neutron stars, and finally we briefly describe the HFB equations for rotating neutron stars

and the vortex formation.

The pairing interaction should in principle be deduced from the bare NN force in the $^1S_0$ channel (Hebeler et al., 2009). We however face the needs for exploring different pairing scenarii since different calculations of pairing in neutron matter based on different models predict very different pairing gaps. A flexible interaction is therefore required. Since the density dependence contact interaction (DDCI) in the pairing channel have shown its simplicity and ability to describe pairing in nuclei and since it offers a large flexibility to mimic different pairing scenarii in uniform matter (Margueron et al., 2007a), we decided to use a pairing interaction of the type given in (3.7). In the calculations we use two different functionals for $g[\rho_n(\mathbf{r}), \rho_p(\mathbf{r})]$. The first one, called below isoscalar (IS) pairing force, depends only on the total baryonic density, $\rho_B(r) = \rho_n(r) + \rho_p(r)$. Its expression is given by Eq. (3.8). This effective pairing interaction is extensively used in nuclear structure calculations and it was also employed for describing pairing correlations in the inner crust of neutron stars (Sandulescu et al., 2004; Sandulescu, 2004; Sandulescu, 2008; Monrozeau et al., 2007). The parameters are chosen to reproduce in infinite neutron matter two possible pairing scenarii, corresponding to a maximum gap of about 3 MeV (strong pairing scenario, hereafter named ISS) and, respectively, to a maximum gap around 1 MeV (weak pairing scenario, called below ISW). These two scenarii are simulated by two values of the pairing strength, i.e., V_0={-570,-430} MeV fm^{-3}. The other parameters are taken the same for the strong and the weak pairing, i.e., α=0.45, η=0.7 and ρ_0=0.16 fm^{-3}. The energy cut-off, necessary to cure the divergence associated to the zero range of the pairing force, was introduced through the factor $e^{-(E_i-20)^2/100}$ acting for $E_i > 20$ MeV, where E_i are the HFB quasiparticle energies.

The second pairing functional, referred below as isoscalar-isovector pairing, depends explicitly on neutron and proton densities as in Eq. (3.9). This interaction is calibrated to mimic the behavior of the bare NN interaction, see section 3.2: using the relation between V_0 and the cut-off energy given in Ref. (Bertsch and Esbensen, 1991), it reproduces the low energy phase shift and the pairing functional is adjusted to mimic the BCS pairing gaps in neutron and symmetric uniform matter (Cao et al., 2006a). It is therefore applicable in different regimes: the low density neutron gas and the dense systems composed either of nuclear clusters close to $N = Z$ or of neutrons. As shown in Refs. (Margueron et al., 2008; Bertulani et al., 2009), this pairing functional describes well the two-neutron separation energies and the odd-even mass differences in semi-magic nuclei. The isotopic and isotonic behavior of the odd-even mass difference is better reproduced with an isoscalar and isovector interaction than with a simple isoscalar interaction (Margueron et al., 2008). In the present calculations for this pairing functional we have used the parameters V_0= -703.86 MeV fm^{-3}, η_s=0.7115, α_s=0.3865, η_n=0.9727, α_n=0.3906, with the same cut-off prescription as for the isoscalar pairing forces and this force is referred hereafter as IVS.

For zero range pairing forces and spherical symmetry the radial finite-temperature Hartree-Fock-Bogoliubov (FTHFB) approach (Goodman, 1981) have a similar form as the HFB equations at zero temperature, ie.,

$$\begin{pmatrix} h_{T,q}(r) - \lambda_q & \Delta_{T,q}(r) \\ \Delta_{T,q}(r) & -h_{T,q}(r) + \lambda_q \end{pmatrix} \begin{pmatrix} U_{i,q}(r) \\ V_{i,q}(r) \end{pmatrix} = E_{i,q} \begin{pmatrix} U_{i,q}(r) \\ V_{i,q}(r) \end{pmatrix} , \tag{5.14}$$

where $E_{i,q}$ is the quasiparticle energy, the fields $U_{i,q}(r)$ and $V_{i,q}(r)$ are the components of the radial FTHFB wave function and λ_q is the chemical potential of the species q. The quantity $h_{T,q}(r)$ is the thermal averaged mean field hamiltonian and $\Delta_{T,q}(r)$ is the thermal averaged pairing field defined as,

$$\Delta_{T,q}(r) = V_0 \; g_{\mathrm{Pair},q}[\rho_n(\mathbf{r}), \rho_p(\mathbf{r})] \; \kappa_{T,q}(r). \tag{5.15}$$

The pairing field $\Delta_{T,q}(r)$ depends on the pairing interaction through V_0 and $g_{\mathrm{Pair},q}[\rho_n(\mathbf{r}), \rho_p(\mathbf{r})]$ as well as on the local pairing tensor $\kappa_{T,q}(r)$ defined as,

$$\kappa_{T,q}(r) = \frac{1}{4\pi} \sum_i g_{i,q} \; U^*_{i,q}(r) V_{i,q}(r)(1 - 2f_{i,q}), \tag{5.16}$$

where $f_{i,q} = [1+\exp(E_{i,q}/T)]^{-1}$ is the Fermi distribution, T is the temperature expressed in energy units, and $g_{i,q} = 2j_{i,q}+1$ is the degeneracy of the state i with angular momentum $j_i = l_i + s_i$. The summation in the pairing tensor (5.16) is going over the whole quasiparticle spectrum, including the unbound states if they are inside the cut-off. To keep the analogy with the mean field, the pairing field is defined negative.

In a self-consistent calculation based on a Skyrme-type force, $h_{T,q}(r)$ is expressed in terms of thermal averaged densities, i.e., particle density $\rho_{T,q}(r)$, kinetic energy density $\tau_{T,q}(r)$ and spin density $J_{T,q}(r)$ (Bender et al., 2003). The thermal averaged densities mentioned above are given by (Sandulescu, 2004):

$$\rho_{T,q}(r) = \frac{1}{4\pi}\sum_i g_{i,q}\left[|V_{i,q}(r)|^2(1-f_{i,q}) + |U_{i,q}(r)|^2 f_{i,q}\right], \tag{5.17}$$

$$\begin{aligned}\tau_{T,q}(r) = \frac{1}{4\pi}\sum_i g_{i,q}\Bigg\{&\left[\left(\frac{dV_{i,q}(r)}{dr} - \frac{V_{i,q}(r)}{r}\right)^2 + \frac{l_{i,q}(l_{i,q}+1)}{r^2}V_{i,q}(r)^2\right](1-f_{i,q}) \\ &+ \left[\left(\frac{dU_{i,q}(r)}{dr} - \frac{U_{i,q}(r)}{r}\right)^2 + \frac{l_{i,q}(l_{i,q}+1)}{r^2}U_{i,q}(r)^2\right] f_{i,q}\Bigg\},\end{aligned} \tag{5.18}$$

$$\begin{aligned}J_{T,q}(r) = \frac{1}{4\pi}\sum_i g_{i,q}&\left(j_{i,q}(j_{i,q}+1) - l_{i,q}(l_{i,q}+1) - \frac{3}{4}\right) \\ &\times\left(|V_{i,q}(r)|^2(1-f_{i,q}) + |U_{i,q}(r)|^2 f_{i,q}\right),\end{aligned} \tag{5.19}$$

The summations in the equations above are over the whole quasiparticle spectrum without cut-off.

We therefore solve the FTHFB equations in the Wigner-Seitz approximation, as commonly done in inner crust studies (Negele and Vautherin, 1973; Baldo et al., 2005a), using a coordinate space representation and where the unbound states are represented by the discrete box states. To generate a constant density on the edge of the WS cell corresponding to the neutron gas, the FTHFB equations are solved by imposing Dirichlet-Von Neumann boundary conditions at the edge of the cell (Negele and Vautherin, 1973), i.e., all wave functions of even parity vanish and the derivatives of odd-parity wave functions vanish.

In practice, the self-consistent FTHFB equations (5.14) are solved by iterations, fixing at each iteration the chemical potential λ_q and the pairing field $\Delta_{T,q}(r)$, until the convergence of the single particle energies and of the pairing gap. The pairing gap $\Delta_{i,q}$ of each state i is defined as,

$$\Delta_{i,q} \equiv \frac{1}{V_{i,q}}\int d^3\mathbf{r}\ \Delta_{T,q}(r)|V_{i,q}(r)|^2, \tag{5.20}$$

where $V_{i,q} = \int d^3\mathbf{r}\ |V_{i,q}(r)|^2$ is the norm of the wave function $V_{i,q}(r)$. Since the number of particle $\int d^3r\rho_{T,q}(r)$ is fixed constant, Eq. (5.17) is first inverted to extract λ_q for fixed pairing gaps $\Delta_{i,q}$, then the kinetic and spin current densities (5.18)-(5.19) are evaluated and used at the next evaluation for defining the new mean-field hamiltonian $h_{T,q}(r)$ in Eq. (5.14). The pairing field $\Delta_{T,q}(r)$ is also recalculated (5.15) and Eqs. (5.14) are solved again.

We represent in Fig. 5.4 (left panel) the neutron and proton density profiles obtained for the crust structures given in table 5.1 for HF calculation, and the neutron and proton pairing field profiles $\Delta_{T=0}(r)$ for the crust structures given in table 5.2 for HFB calculations using SLy4 interaction and ISS for the pairing channel. In cell 4-10 the unbound neutron density profile is very shallow and therefore we increased the scale in the sub-set view graphs. As discussed in this section, a necessary condition for the validity of the WS approximation is the appearance of a well-defined plateau before the edge of the cell. From Fig. 5.4 (left panel), it can be observed that this condition is satisfied for the cells 3-10, while some small oscillations are observed in cell 2 and the plateau is not very well defined in cell 1. Going higher in densities would make this condition even more difficult to be satisfied and in some case, an inversion of densities producing bubble-like structures is observed.

From the right graphs in Fig. 5.4, it is remarked that the proton pairing field stays localized inside the nuclear cluster since a drip out of protons is not observed in our calculations. It can also be noticed that for

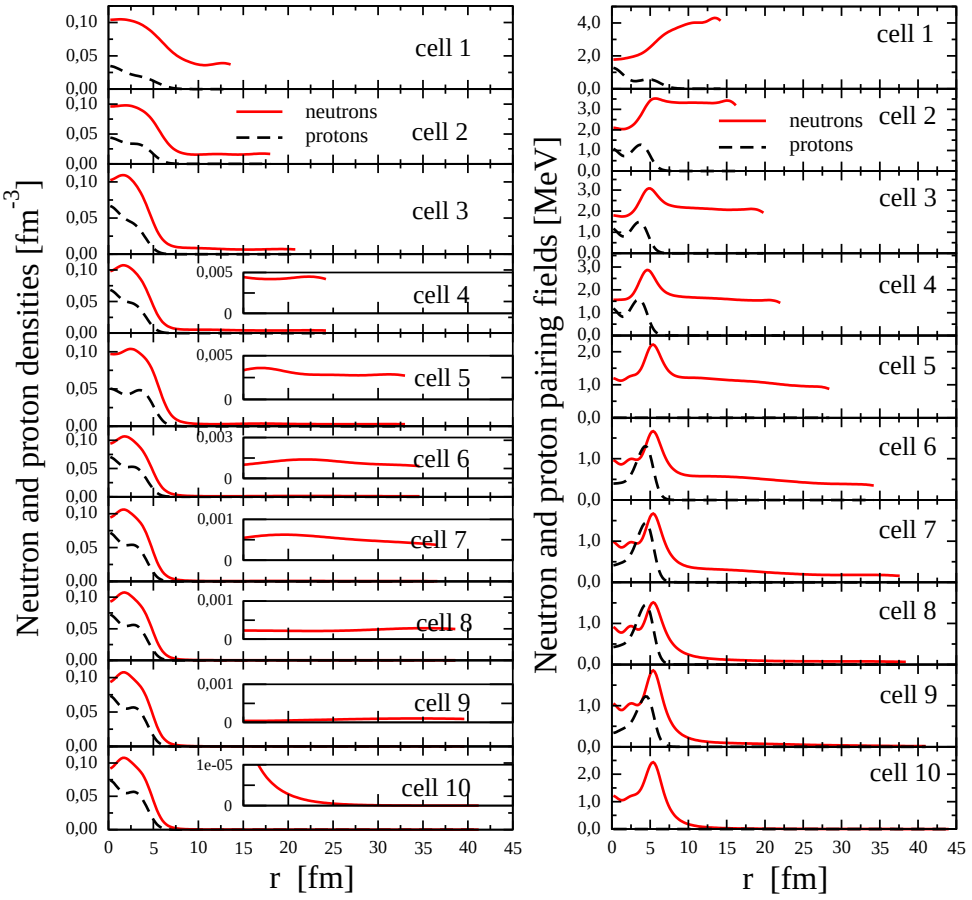

Figure 5.4: The radial profiles of densities (left) and pairing fields (right) for neutrons (full lines) and protons (dashed lines). The densities correspond to the HF calculations with SLy4 (Chabanat et al. 1998) while the pairing fields to the HFB calculations with the pairing force ISS.

the cells 5 and 10, which have proton number $Z = 20, 28$ (see Table 5.2), the proton fields are zero. This indicates that in the nuclear clusters corresponding to these cells the proton numbers $Z = 20, 28$ behave as magic numbers, as in atomic nuclei. The neutron pairing field extend well further the nuclear cluster which shows that the unbound neutrons are superfluid. The peak in the pairing field located at the surface of the clusters is related to the maximum of the pairing gap observed in uniform matter. This shows that even if the approach developed here is applied to non-uniform matter, the features of uniform matter could serve to understand qualitatively the pairing field profile.

We now analyze the effect of the temperature on the pairing properties obtained from FTHFB and applied in non-uniform matter. In Fig. 5.5 is therefore shown the evolution with the temperature of the pairing field in the WS cell number 6 defined in table 5.2. It is first noticed that for all temperatures the nuclear clusters modify significantly the profile of the pairing field. One can also see that the effect of the temperature is non-uniformly impacting the pairing field profile. Increasing the temperature, the pairs corresponding to the unbound neutrons that are closer to the Fermi energy are destroyed much before the pairs localized at the surface to the cluster and inside the clusters. They correspond indeed to pairs formed of bound states which are deep below the Fermi energy. The FTHFB is therefore able to treat differently the unbound neutron states and the bound states inside the nuclear clusters. Other calculations based on finite temperature Hartree-Fock BCS (FTHFBCS) approximation does not exhibit such a non-uniform behavior (Chamel

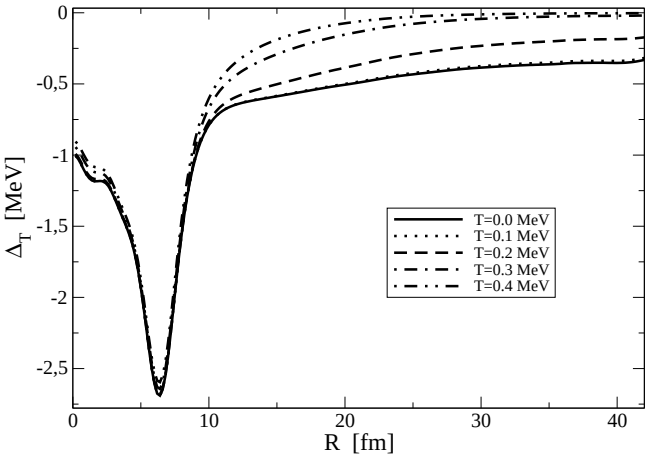

Figure 5.5: Radial distribution of the pairing field for the Wigner-Seitz cell number 6 for various temperatures. The results correspond to the strong pairing force ISS.

et al., 2010) (and communication of X. Vinas in 2011). A complete understanding of this peculiarity of FTHFB is not yet well understood and will be studied in the next future, but it is known that FTHFB is better designed to describe non-uniform matter than FTBHBCS. In section 5.3.3 it will be shown that the non-uniform superfluid transition induced by the temperature leads to two critical temperatures in WS cells, and therefore to two jumps in the specific heat.

5.3.2 Structure of the inner crust with pairing

The effect of pairing correlations on the structure of Wigner-Seitz cells was first investigated in Refs. (Baldo et al., 2005a; Baldo et al., 2006; Baldo et al., 2007) within the Hartree-Fock BCS (HFBCS) approach. In the most recent version of these calculations the authors solved the HFBCS equations with a mixture between the phenomenological functional of Fayans et al (Fayans et al., 2000), employed in the nuclear cluster region, and a microscopical functional derived from Bruckner-Hartree-Fock calculations in infinite neutron matter. The latter was used to describe the neutron gas in the Wigner-Seitz cells. In this framework it was found that the cells have not a magic number of protons, at variance with the original calculation of Negele and Vautherin (Negele and Vautherin, 1973) also reported in table 5.1. It was also found that pairing can change significantly the structure of the cells compared to HF calculations. These findings show that in order to determine the most probable structure of the inner crust one needs more investigations based on various effective interactions and many-body approximations.

The properties of the Wigner-Seitz cells are obtained from the energy minimization at beta equilibrium. To obtain the binding energy of cold baryonic matter we performed HFB calculations with the Skyrme SLy4 interaction and zero-range density-dependent pairing forces of various intensities (ISS, ISW, IVS) (Grill et al., 2011). The proton mean field requires however to be completed by the average mean field created by the uniform distribution of electrons $\rho_e = 3N_e/(4\pi R_{WS}^3)$,

$$u^{\mathrm{Coul}}(r) = -\frac{N_e e^2}{2R_{WS}} \left(3 - (r/R_{WS})^2\right) \delta_{q,p}. \tag{5.21}$$

It can be seen that inside the WS cell the contribution of the proton-electron interaction to the mean field is negative, of the order of 1-2 MeV, and quadratic in the radial coordinate. The HFB energy of the WS cell is the sum of the mean-field nuclear energy (kinetic and mean field) (Bender et al., 2003), the proton-proton

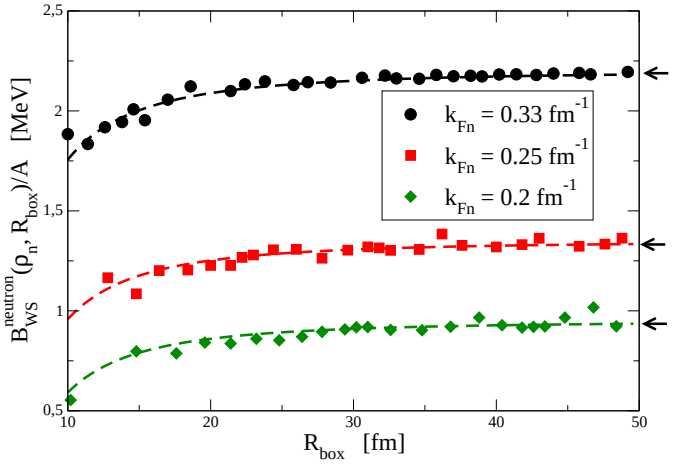

Figure 5.6: Energy of the WS cell filled with only neutrons. The dependence of the energy versus the radius of the cell is represented for various neutron Fermi momenta which correspond to that of the unbound neutron gas in cells 6, 7 and 8. The correction (5.27) is also shown (dashed lines).

Coulomb energy where the exchange term is treated at the Slater approximation, and the pairing energy,

$$E_{\rm Pair,q} = \frac{1}{2}\int d^3\mathbf{r}\; V_0\; g_{{\rm Pair},q}[\rho_n(r),\rho_p(r)]\;|\kappa_{T,q}(r)|^2. \tag{5.22}$$

The energy of the WS cell E_{WS} is the sum of the HFB energy, the kinetic energy of the electrons (Landau and Lifchitz, 1967),

$$T_e = Zm_ec^2\left\{\frac{3}{8x^3}\left[x\left(1+2x^2\right)\sqrt{1+x^2}-\ln\left(x+\sqrt{1+x^2}\right)\right]-1\right\}, \tag{5.23}$$

where x is the relativistic parameter defined as $x = \hbar k_{Fe}/(m_ec^2)$, and the lattice energy induced by the electron-electron and eletron-proton interaction inside the WS cell,

$$E_{\rm Latt.} = \int d^3\mathbf{r}d^3\mathbf{r}'\left(\frac{1}{2}\rho_e(r)-\rho_p(r)\right)\frac{e^2}{|\mathbf{r}-\mathbf{r}'|}\rho_e(r') - \frac{3}{4}\left(\frac{3}{\pi}\right)^{1/3}e^2\int d^3\mathbf{r}\,\rho_e^{4/3}(r), \tag{5.24}$$

with $\hbar c/e^2 = 137$. For constant electron density one gets,

$$E_{\rm Latt.} = \frac{N_ee^2}{R_{WS}}\left(\frac{3}{5}N_e - \frac{3}{2}Z + \frac{2\pi}{R_{WS}^2}\int dr\, r^4\rho_p(r) - \frac{3}{4}\left(\frac{3}{2\pi}\right)^{2/3}N_e^{1/3}\right)\;, \tag{5.25}$$

where the real proton density distribution $\rho_p(r)$ is used to calculate the proton-electron energy.

Before going further, we shall discuss the approximation for the unbound neutrons which are represented by the discrete states of the boxes. This representation introduce an artificial shell effects instead of a continuum distribution of neutrons energies (Chamel et al., 2007). The effect of these spurious neutron shell are shown in Fig. 5.6 where the HF energy of the WS cell are evaluated for different radii (Margueron et al., 2007c). For these calculation, protons have been removed and therefore, neutrons fill the space uniformly. The energy of a uniform distribution of neutrons is independent of the considered volume. In the WS cells,, the energy of the neutrons is however changing with the radius of the cell. When the radius of the cell becomes too small the boundary conditions imposed at the cell border through the WS approximation generate an artificial large distance between the energy levels of the nonlocalized neutrons. Consequently, the binding energy of the neutron gas is significantly underestimated. In Fig. 5.6, this effect

is illustrated for a set of 3 densities ρ_n. The arrows on the right of the figure represent the value of the energy $E_{unif}^{neutron}(\rho_n)/A$ in uniform neutron matter for the density ρ_n. We introduce the function f,

$$f(\rho_n, R_{WS}) \equiv \frac{E_{WS}^{neutron}(\rho_n, R_{WS})}{A} - \frac{E_{unif}^{neutron}(\rho_n)}{A} \ , \tag{5.26}$$

which represent the deviation of the energy in the WS cell from the uniform case. The smooth part of the function f is fitted with the following function (Margueron et al., 2007c),

$$f(\rho_n, R_{WS}) \approx 89.05(\rho_n/\rho_0)^{0.1425} R_{WS}^{-2} \ , \tag{5.27}$$

and is represented in Fig. 5.6. The total energy of the non-uniform system E_{TOT} is decomposed into that of the cluster and that of the unbound neutrons with the density ρ_{n_g}, and the latter is corrected from the smooth dependence on the WS cell radius using the fitted function $f(\rho_{n_g}, R_{WS})$. With this approximation, we obtain

$$E_{TOT}(\rho_B, \rho_{n_g}, R_{WS}) = E_{WS}(\rho_B, R_{WS}) + A f(\rho_{n_g}, R_{WS}). \tag{5.28}$$

From Eq. (5.27), the spurious shell effect induce important correction if: 1- the unbound neutron density ρ_{n_g} is large, and/or 2- the size of the WS cell is small. In the inner crust of neutron stars, these two conditions are satisfied together in the high density region for the configurations with small Z and small cells radii. A comparison of the WS energy E_{WS} and the total energy of the WS cell including the spurious shell effect correction E_{TOT} is shown in Fig. 5.7 (left panel). As expected, the influence of the corrections is more important for the cells 1-5, in which the neutron gas has a higher density, and for those configurations corresponding to small cell radii. For the cell 1 the binding energy after the correction is still decreasing for the smallest Z values, which means that the structure of this cell remains uncertain.

Within the framework presented in the previous sections we have determined the structure of the Wigner-Seitz cells. The calculations have been done for the set of baryonic densities shown in Table 5.1. To find the structure of the cell at a given density we have considered all the configurations with the even number of protons between 12 and 60. For each number of protons we modified the radius of the cell with a step of 0.2 fm, keeping the same total density, until the number of neutrons included in the cell satisfies with the best accuracy the beta equilibrium condition. The most probable configuration at a given density is finally taken as the one with the lowest binding energy. This is illustrated in Fig. 5.7 (right panel) where are shown the energies per baryons at beta equilibrium that are obtained for the different densities (cell 1 to 10, see table 5.1) and the different models (HF, HFB with ISS, ISW and IVS pairing force) as function of the proton number Z. Comparing the HF result (solid line) to the HFB one's (ISW dotted, ISS dashed and IVS dashed-dotted lines) it is first remarked that the pairing correlations reduces the energy of the cell, as expected, and also that the large fluctuations in the energies are smoothed out by the pairing correlations. From Fig. 5.7 we observe that in the cell 1 the binding energy does not converge to a minimum before Z=12. For the cells 2-4 a minimum can be found for the ISW and/or IVS forces but this minimum is very close to the value of binding energy at $Z = 12$. Therefore the structure of the cells 2-4 is ambiguous. The situation is different in the cells 5-10 where the binding energies converge to absolute minima located at a proton number Z larger than the minimum $Z = 12$. Thus for these cells the structure can be well-defined by the present HFB calculations. Moreover in low density cells 6 to 10, different local minima are well pronounced for different values of Z. This behavior could be related to the effect of the unbound neutrons which smooth out the shell effects of the nuclear clusters for the cells 1 to 5.

It is also clear from Fig. 5.7 that the difference between the absolute minimum energy and the energy of other local minima is very small, of the order of 10 keV. The weak dependence of the binding energy on Z observed in Fig. 5.7 is caused by the almost exact compensation between the nuclear energy and the electron kinetic energy. The competition between the nuclear and Coulomb interaction, specific to the so-

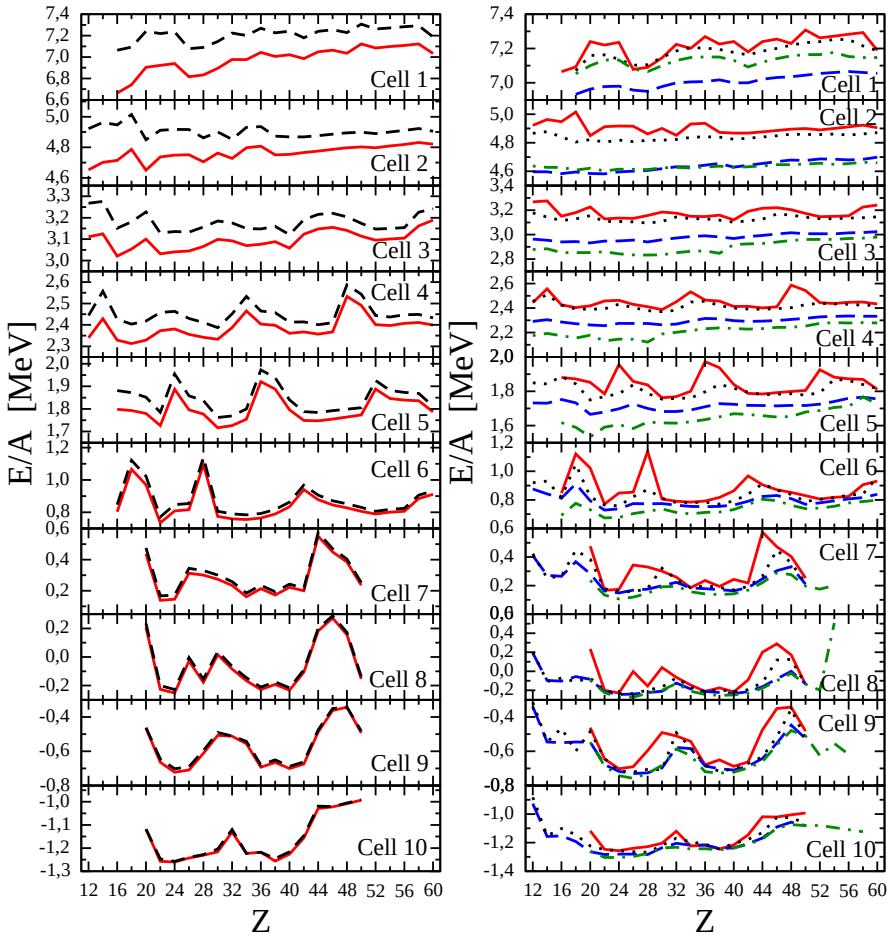

Figure 5.7: The HFB energies per particle as function of proton number for the pairing forces IS W (dotted line), IS S (dashed line) and IS-IV S (dashed-dotted line). The solid lines represent the HF results. In the left panel are shown the results with correction of the supirous shell effect.

called frustrated systems, it is the reason why the structure of the WS cells it is not necessarily determined by the nuclear interaction and the associated nuclear shell effects.

The structure of the WS cells obtained in the HF and HFB approaches is given in Table 5.2. Comparing HF and HFB calculations it can be observed that for the cells 6-9 the numbers of protons in the HF and HFB calculations differ by about 2 units. The largest difference, of 10 units, appears for the cell 5. However, as seen in Fig. 5.7, the HF minimum at Z=30 is in fact very close to the local minimum at Z=22. A similar situation can be noticed in cell 10 for the HF minima at Z=24 and Z=28. In conclusion, these calculations indicate that the pairing does not change much the structure of the low density cells 5-10, but helps in reducing the energy fluctuations in neighbor cells. This could be also observed from the fact that in these cells the intensity of pairing force has only marginal effects on the proton and neutron numbers.

5.3.3 Specific heat of the inner crust baryonic matter

The specific heat calculated from the WS approximation is comparable to that deduced from band theory (Chamel et al., 2009b). With the setting discussed above the FTHFB equations are solved for given Wigner-Seitz cells. For historical reason, the crust structure obtained by Negele and Vautherin and reported in table 5.1 are considered in this section. From the solution of the FTHFB model, the entropy is evaluated

N_{cell}	N				Z				R_{WS} [fm]			
	HF	ISW	ISS	IVS	HF	ISW	ISS	IVS	HF	ISW	ISS	IVS
2		656	676	656		22	22	22		20.0	20.2	20.0
3	980	718	454	734	40	28	20	28	30.2	27.2	23.4	27.4
4	726	712	460	594	30	30	22	28	31.6	31.4	27.2	29.6
5	538	320	336	344	30	20	20	20	33.2	28.0	28.4	28.6
6	252	300	242	238	22	24	22	22	34.6	36.6	34.2	34.0
7	158	202	170	174	22	26	24	24	36.6	39.6	37.6	37.8
8	120	120	118	120	24	24	24	24	38.6	38.6	38.4	38.6
9	80	92	90	94	24	26	26	26	39.8	41.4	41.2	41.6
10	58	84	72	64	24	28	28	26	41.4	46.0	44.2	42.6

Table 5.2: The structure of Wigner-Seitz cells obtained in the HFB approximation including the correction of the spurious shell effects. The results corresponds to the isoscalar weak (ISW), isoscalar strong (ISS) and isovector-isoscalar (IVS) pairing forces. In the table are shown only the structures of the cells which could be well-defined by the HFB calculations.

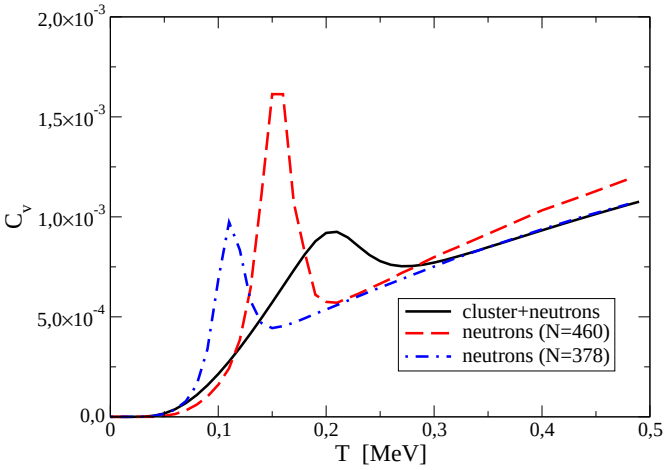

Figure 5.8: Neutron-specific heat in the the Wigner-Seitz cell number 6 for strong pairing ISS. The results corresponds to various approximations discussed in the text. The specific heat is given in units of Boltzman constant k_B.

as,

$$S = -k_B \sum_{i,q} (2j_{i,q}+1)(f_{i,q} \ln f_{i,q} + (1-f_{i,q}) \ln(1-f_{i,q})) \ , \tag{5.29}$$

where k_B is the Boltzmann constant. The specific heat is therefore obtained from the numerical derivation of the entropy as,

$$C_V = \frac{T}{V} \frac{\partial S}{\partial T}, \tag{5.30}$$

where V is the volume of the Wigner-Seitz cell. Due to the energy gap in the excitation spectrum, the specific heat of a superfluid system is dramatically reduced compared to its value in the normal phase. Since the specific heat depends exponentially on the energy gap, its value for a Wigner-Seitz cell is very sensitive to the local variations of the pairing field induced by the nuclear clusters (Sandulescu, 2004).

To illustrate the particular behavior of the specific heat in non uniform matter and the validity of various approximations, in what follows we shall discuss in more detail the results for the cell number 6, which contains N=460 neutrons and Z=40 protons (see table 5.1). In this cell the HFB calculations predict 378

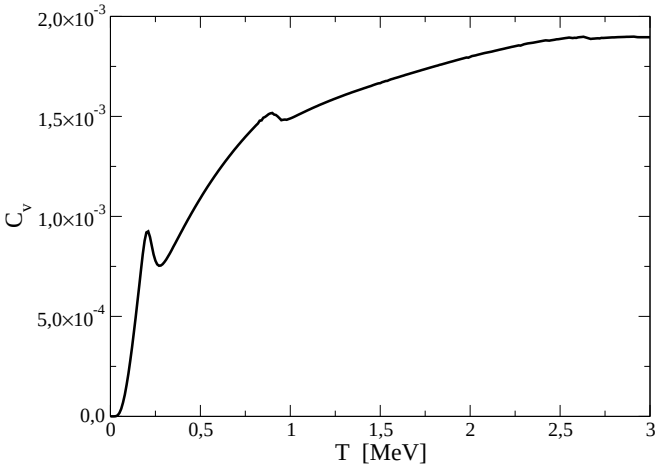

Figure 5.9: Neutron-specific heat in the Wigner-Seitz cell number 6 for strong pairing ISS. Here the results are shown up to high temperatures in order to illustrate the second transition region around T= 900 keV. The specific heat is given in units of k_B.

unbound neutrons. It is interesting that in spite of many neutrons in the cell the number of the bound neutrons in the cluster with Z=40 protons is equal to the magic number 82, as for the dripline nucleus ^{122}Zr (see, e.g., Ref. (Sandulescu et al., 2003)). The specific heat given by the HFB spectrum, in which the contribution of the cluster is included, is shown in Fig. 5.8 by full line. In the same figure are shown also the specific heats corresponding to two approximations employed in some studies (Lattimer et al., 1994; Pizzochero et al., 2002). In these approximations the non uniform distribution of the neutrons is replaced with a uniform gas formed by the total number of neutrons in the cell (dashed line) or by taking only the number of the unbound neutrons (dash-dotted line). The specific heat is deduced from a fit of the BCS calculation in uniform matter (Levenfish and Yakovlev, 1994). The latter case is considered as an effective way of taking into account the influence of the cluster (Pizzochero et al., 2002). How these approximations work is seen in Fig. 5.8. To make the comparison meaningful, the calculations for the uniform neutron gas are done solving the HFB equations with the same boundary conditions as for the non uniform system, i.e., neutrons+cluster. As seen in Fig. 5.8, the transition from the superfluid to the normal phase is taking place at a lower temperature in the case of uniform neutron gas, especially when are considered only the unbound neutrons. We can also notice that, at variance with the uniform system, in the non uniform system the transition from the superfluid to the normal phase is smooth.

In Fig. 5.9, the FTHFB specific heat in cell number 6 is shown up to T=3 MeV. In non uniform system are observed two transition regions which where already observed from the pairing field profile represented in Fig. 5.5 for various temperatures: one around T=200 keV, corresponding mainly to the superfluid transition of the unbound neutrons, and another one, much less pronounced, around T=900 keV, which corresponds to the neutrons localized at the surface region of the cluster.

5.4 Application to the thermalization time of the inner crust

The thermalization time of the crust depends essentially on the crust thickness (Lattimer et al., 1994). However, several studies have shown that the thermalization time depends also significantly on the superfluid properties of the inner crust baryonic matter (Lattimer et al., 1994; Gnedin et al., 2001; Pizzochero et al., 2002; Monrozeau et al., 2007; Sandulescu, 2008). This dependence is induced through the specific

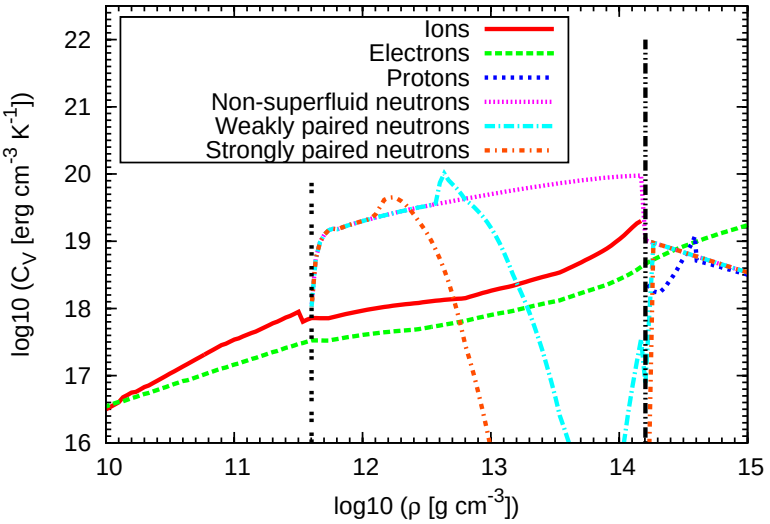

Figure 5.10: Specific heat in the crust of the neutron star for the different components of the star matter and for a temperature of 10^9 K (see the text for more details).

heat of unbound neutrons, strongly affected by the pairing energy gap. At $T = 10^9$ K, the contribution to the total specific heat of the unbound neutrons, of the electrons and of the ions is shown in Fig. 5.10 where the two vertical lines delimitate the inner crust density region. In the absence of superfluidity, the unbound neutrons dominate the other contributions from the electrons and from the ions. However, since the pairing correlations open a gap in the thermal excitations around the Fermi energy, the specific heat is much reduced in the presence of superfluid neutrons (see section 5.3.3). Therefore, for the density region where the critical temperature is larger than $T = 10^9$ K, the neutron specific heat is strongly suppressed. The density region where this suppression occurs is larger with a strong pairing than with a weak pairing since the critical temperature is larger with strong pairing. It is therefore expected that the effect of superfluidity has a large impact on the crust thermalisation (Lattimer et al., 1994).

Moreover, since the neutron pairing gap is influenced by the presence of the nuclear clusters (Barranco et al., 1998; Pizzochero et al., 2002; Sandulescu et al., 2004), a reliable calculation of neutron specific heat should take the clusters into account. How the intensity of pairing correlations affects the specific heat of the neutrons in the presence of nuclear clusters was analysed in section 5.3.3.

The crust thermalization is described here in the rapid cooling scenario in which the core arrives quickly to a much smaller temperature than the crust due to the direct URCA reactions. In this case the interior of the star cools much faster than the crust. Due to this temperature inversion the heat stored in the crust diffuses into the core where it is dissipated by the neutrinos. The thermalization time is defined as the time needed for the cooling wave to traverse the crust and to arrive at the surface of the star. The heat diffusion can be described by the relativistic heat equation (Thorne, 1977):

$$\frac{\partial}{\partial r}\left[\frac{Kr^2}{\Gamma(r)}e^{\phi}\frac{\partial}{\partial r}(e^{\phi}T)\right] = r^2\Gamma(r)e^{\phi}\left(C_V\frac{\partial T}{\partial t} + e^{\phi}Q_{\nu}\right), \tag{5.31}$$

where t is the time, K is the thermal conductivity, C_V is the specific heat and Q_ν is the neutrino emissivity. The effect of the gravity is given through the gravitational potential ϕ, which enters in the definition of the redshifted temperature $\tilde{T} = Te^{\phi}$, and the quantity $\Gamma(r) = \left(1 - 2Gm(r)/rc^2\right)^{-1/2}$, where G is the gravitational constant and $m(r)$ is the gravitational mass included in a sphere of radius r. The latter is obtained from the Tolman-Oppenheimer-Volkoff (TOV) equations (Haensel et al., 2007) based on an equation of

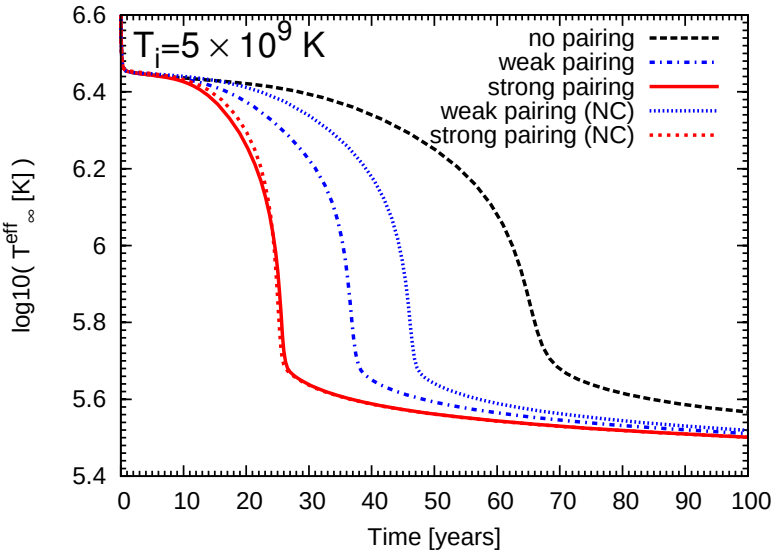

Figure 5.11: Time evolution of the apparent surface temperature for the initial temperatures $T_i = 500$ keV. NC indicates the results of the calculations obtained by neglecting the effect of the clusters.

state obtained from SLy4 Skyrme interaction (Douchin and Haensel, 2001). For the 1.6 $M_\odot$ neuron star considered here, the inner crust extends from R_c=10.72 km, which is the radius at the core-crust interface, to 11.19 km.

The time evolution of the effective surface temperature $T_\infty^{\rm eff}$ is displayed in Fig. 5.11 for the initial temperatures of the crust $T_i = 500$ keV and employing the code of Dany Page (Page et al., 2006). The effective surface temperature shown in Fig. 5.11 is obtained from the temperature at the bottom of the crust, $T_{\rm b} = T(\rho_{\rm b})$, where $\rho_{\rm b} = 10^{10}$ g.cm^{-3} assuming a non-accreted envelope. As expected the pairing enhances significantly the cooling at the surface of the star. In Fig. 5.11 are also shown the apparent surface temperatures obtained neglecting the effect of the clusters, i.e., supposing that the neutron specific heat is given solely by that of the neutron gas. In this case the specific heat of the neutrons is calculated from the quasiparticle spectrum of BCS equations solved for infinite neutron matter at a density corresponding to that of the external neutrons in the WS cell (Levenfish and Yakovlev, 1994). In the case of weakly pairing scenario, the apparent surface temperature is dropping faster for superfluid non uniform matter than for superfluid uniform matter. For the strong pairing scenario, since the pairing correlations suppress the role of the neutron in almost the entire inner crust, the effect of the clusters is largely screened (Fortin et al., 2010).

A simple random walk model for the cooling is sometimes used for estimation of the thermalization time (Brown et al., 1988; Pizzochero et al., 2002; Monrozeau et al., 2007). For pedagogical reasons we briefly present this model here. In this model the diffusion of the cooling wave towards the core is calculated without taking into account the dynamical change of the temperature through the whole crust. The crust is divided into shells of thickness R_i for which the thermal diffusively $D_i = K_i/C_{V,i}$ is considered as constant. The relaxation time of each of these shells is defined as,

$$\tau_i = \Gamma(R)^3 R_i^2/(\gamma D_i), \tag{5.32}$$

where γ is a geometrical factor and R is the radius of the neutron star. The total relaxation through the crust

is given by,

$$\tau_{th} = \left(\sum_i \sqrt{\tau_i} \right)^2 . \tag{5.33}$$

The thermalization time defined as (5.33) satisfy the condition that in a uniform density case, τ_{th} is independent of the shell discretization. Using this model, the effect of the neutron superfluidity has also been estimated to be large (Pizzochero et al., 2002; Monrozeau et al., 2007), and is qualitatively similar to the result deduced from the solving of the heat diffusion equation (5.31).

From the simple random walk model, it can be inferred a scaling relation for the thermal relaxation, $t_{th} = t_1 \alpha^\beta$ where the scaling parameter

$$\alpha = \left(\frac{\Delta R_{\text{crust}}}{1 \text{ km}} \right)^2 \left(1 - 2GM/Rc^2 \right)^{-3/2} \tag{5.34}$$

depends solely on the global properties of the neutron star, i.e., the crust thickness ΔR_{crust}, the star radius R and the mass of the star M. Considering the simpler linear fit, i.e., $t_w \approx \alpha t_1$, as done in (Lattimer et al., 1994; Gnedin et al., 2001), we get for the normalized time t_1 the values $t_1 = \{68.9, 39.3, 22.3\}$ corresponding, respectively, to the normal neutrons, neutrons with weak pairing and neutrons with strong pairing.

For a 1.5 $M_\odot$ neutron star with $\alpha = 1.15$, we obtain $t_1 = \{66.4, 37.4, 26.6\}$. Compared to the results given in Table 2 of the Ref. (Gnedin et al., 2001), our values for t_1 are larger by a factor 2.3 in the non-superfluid case, and 3.4 (3.0) for the weak (strong) pairing scenario. These differences could be explained by the effects of the nuclear clusters on the neutron specific heat, disregarded in Ref. (Gnedin et al., 2001), and by different neutrinos processes and thermal conductivities in the core matter used in the two calculations.

5.5 Conclusions and outlooks

In this chapter we have discussed the influence of pairing correlations on the structure of inner crust of neutron stars. The study was done for the region of the inner crust which is supposed to be formed by a lattice of spherical clusters embedded in a gas of neutrons. The lattice was treated as a set of independent cells described in the Wigner-Seitz approximation. To determine the structure of a cell we have used the nuclear binding energy given by the Skyrme-HFB approach. For the cells with high density and small radii the binding energies do not converge to a minimum when the proton number has small values. We believe that it is related to the discretization of the continuum. For a small radius of the cell the average distance between the energy levels of the non-localised neutrons becomes artificially large which cause an underestimation of the binding energy. To correct this drawback we have used an empirical expression based on the comparison between the binding energy of neutrons calculated in infinite matter and in a finite-size spherical cell. We found that the finite size corrections to the binding energies are significant for the high density cells with small proton numbers. This conclusion indicates the need of a more accurate evaluation of the errors induced by the finite size of the WS cells on nuclear binding energy, which requires to go beyond the empirical expression used here.

Then we have discussed how thermalization of neutron stars crust depends on pairing properties and on cluster structure of the inner crust matter. The thermal evolution was obtained by solving the relativistic heat equation with initial conditions specific to a rapid cooling process. The specific heat of neutrons was calculated from the HFB spectrum. The results show that the crust thermalization is strongly influenced by the intensity of pairing correlation. It is also shown that the cluster structure of the inner crust affects significantly the time evolution of the surface temperature.

Finally, we have also noticed that in non-uniform systems there is a qualitative difference between HFBCS and HFB models that deserve further analysis. A deeper analysis of the relations between BCS and

HFB approach is indeed being performed within an HFB approach expressed in the HF basis with Karim Bennaceur and Alessandro Pastore. The BCS approximation is obtained as a limit of this model and a continuous description from BCS to HFB can be performed by controling a amount of off-diagonal bands included in the HFB model. The origin of the qualitative differences between BCS and HFB is now being unveiled.

Chapter 6

From exotic nuclei towards neutron stars

Through this entier manuscript we illustrate the relation between microscopic modeling and the astrophysics of compact stars and supernovae. In this chapter, we further show that in some cases, direct connexions can be established between measurements of nuclei and properties of neutron stars.

6.1 Introduction

The link between neutron stars and bulk nuclei properties is made tradiationally via the *nuclear matter* concept. For instance, the central density of heavy nuclei is very close to the equilibrium density of nuclear matter, called the saturation density ρ_0. In this chapter, close relations between nuclear physics experiments and neutron stars are shown. The continuum coupling in superfluid nuclear systems close to the drip-line is analyzed and is shown to be very important for the superfluid properties of overflowing Wigner-Seitz cells in the crust of neutron stars. In a second part of this chapter, the relation between the symmetry energy and neutron stars is illustrated in some cases. The correlations between the pressure at the edge of neutrons stars and empirical quantities of the liquid drop model are analyzed. The effect of the symmetry energy on the stiffness of the EoS and on neutron stars properties are also analyzed.

6.2 Pairing and continuum coupling in overflowing systems

Overflowing many-body fermionic systems exist in various situations going from the crust of neutron stars (Haensel et al., 2007) to ultra-cold atoms (Stamper-Kurn et al., 1998; Viverit et al., 2001). Interestingly, these systems offer the possibility to study the coupling between two fluids with very different pairing properties (Grasso et al., 2008; Schuck and Viñas, 2011). In such systems, one fluid is localized inside an initial container, such as for instance a nuclear potential, and a second fluid is overflowing towards a larger container. Being in different environments, these two fluids can acquire different pairing gaps. In this chapter, we address the question of the coupling between the two superfluids and their finite temperature properties.

At the transition between its outer and inner crust, neutron stars provide an example of such microscopic overflowing systems, commonly called neutron dripping (Haensel et al., 2007). In the outer crust, nuclei form a Coulomb lattice which gets more and more neutron rich as the density increases. When the maximum number of neutrons that a nucleus can sustain is reached, the overproduced neutrons drip out of

nuclei. These neutrons populate the continuum states and shall be described within the band theory (see Refs. (Ashcroft and Mermin, 1976; Chamel et al., 2007) and references therein). It should be noted that nuclei surrounded by an infinite neutron gas could exist as a stable configuration in neutron stars where they are bounded by gravitation, while isolated nuclei that exist for instance on earth are limited to the drip lines.

The first prediction of the suppression of pairing in overflowing $Z = 50$ nuclear systems was performed in Ref. (Grasso et al., 2008) and we briefly report these results in section 6.2.1. It was proposed to attribute this suppression to the large coherence length of the weakly-superfluid neutrons gas: the neutron gas can penetrate the dense nuclear system and could impose its weak pairing field. It was however also noted in the same work that neutrons are dripping out of the double-magic nucleus ^{176}Sn. In a recent work, the pairing gap of the last occupied state was also predicted to be quenched in overflowing nuclear systems, metallic grains and cold-atoms (Schuck and Viñas, 2011). It was concluded that the suppression of superfluidity is a generic fact of a fermionic superfluid overflowing from a narrow container into a much wider one. It shall be noted that in this work the nuclear model was mainly limited to ℓ=0 single particle states (s-states). The description of nuclear systems requires however the inclusion of $\ell > 0$ single particle states for the bound and the mean-field resonance states. It is indeed well known that, close to the drip lines, resonance states play an important role for pairing properties and it is referred generally as continuum coupling (Bulgac, 1980; Grasso et al., 2001). It has recently regained some attention in nuclei close to the drip-line (see for instance Refs. (Zhang et al., 2011; Hagino and Sagawa, 2011) and references therein). The general question of continuum coupling in overflowing superfluid systems and various phenomenons such as persistence, suppression and reentrance of pairing remains to be studied. Pairing correlations in the ground state of weakly-bound nuclei are commonly described by the Hartree-Fock-Bogoliubov (HFB) theory (De Gennes, 1989; Ring and Schuck, 1980), see chapter 5 for more details.

The expected nuclei in neutron stars located at the transition between the outer crust and the inner crust have a proton number Z around 30 to 50, depending on the models (Rüster et al., 2006). In the following, we consider various studies: First, fixing the proton number to $Z = 50$, we vary the number of neutrons and analyze the properties of the WS cells for both the ground state and the excited states. Then, we explore more systematically the pairing evolution for 8 isotopes located around Z=28, 40 and 50.

6.2.1 Ground and excited states in $Z = 50$ nuclear systems

We analyze the systematic evolution of the low-lying 2^+ mode in $Z = 50$ nuclear systems. We start with neutron-rich Sn isotopes such as ^{120}Sn, ^{140}Sn and ^{160}Sn. When the drip line (^{176}Sn in our model) is crossed we progressively increase the neutron number up to $N = 1750$, which represents the innermost $Z = 50$ configuration predicted in the crust by Negele and Vautherin (Negele and Vautherin, 1973). For all the systems located beyond the drip line we use a radius of 27.4 fm, that is the WS radius associated to the denser configuration with $Z = 50$ and $N = 1750$ (Negele and Vautherin, 1973). This means that, by increasing the neutron number, the baryonic density of the system grows up and reaches the value of ~ 0.02 fm^{-3} for ^{1800}Sn.

We plot in Fig. 6.1 the normal (dashed line) and anomalous (full line) densities, Eqs. (5.16) and (5.17), for the nuclei ^{120}Sn, ^{140}Sn and ^{160}Sn (first row) and for the unbound systems from ^{180}Sn up to ^{550}Sn. As expected, one observes the development of a neutron gas when the neutron number is increased.

Furthermore, in ^{180}Sn and ^{200}Sn, the anomalous density is practically negligible both inside and outside the cluster. It starts increasing only for ^{250}Sn which is 74 neutrons above the drip-density. Pairing correlations are actually expected to be small in ^{180}Sn because this system is located close to the magic nucleus ^{176}Sn. For the other nuclear systems from ^{176}Sn up to ^{250}Sn, the weakness of pairing is due to the density dependence of the pairing gap in nuclear matter. The pairing gap obtained from the BCS equations goes to zero (Bertsch and Esbensen, 1991; Garrido et al., 1999) when the density goes to zero. This explains why

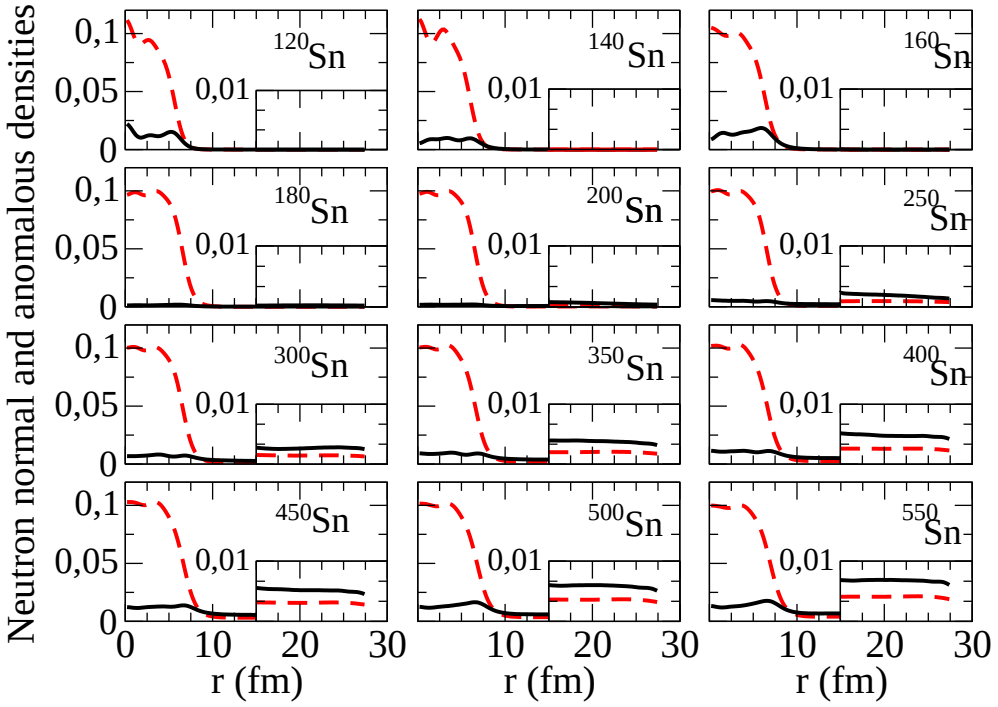

Figure 6.1: Normal (dashed line) and anomalous (full line) neutron densities in units of fm^{-3}.

pairing correlations are so weak in the low-density neutron gas present for instance in ^{200}Sn. Moreover, the Pippard's coherence length, $\xi_P = \hbar^2 k_{Fn}/m_n^* \pi \Delta_n$, is very large for a low-density neutron gas (see section 3.3 for more details). As a consequence, the pairing features of the gas might affect the whole nuclear system and might modify also the pairing inside the nuclear cluster (pairing correlations are weak also inside the cluster). By increasing the density, the pairing gap becomes larger and the coherence length is reduced. The bell-shape dependence of the pairing gap on the density indicates that pairing correlations in the neutron gas are expected to be the strongest approximately at the density of the crust where the system ^{1800}Sn is predicted.

The evolution of the quadrupole response can be observed in Fig. 6.2, from the nucleus ^{140}Sn up to ^{1800}Sn. A low-lying 2^+ mode as well as a giant resonance are found in all the systems. The giant resonance is clearly visible in ^{140}Sn and ^{180}Sn. For the other systems the giant resonance has a much lower strength with respect to the low-energy supergiant mode and is located in the 5-7 MeV region as expected by the 65 $A^{-1/3}$ MeV systematics (Bohr and Mottelson, 1998). We concentrate on the low-lying mode because only low-energy excitations strongly contribute to the specific heat in the crust. We perform a first analysis of the evolution of the low-lying mode with respect to the neutron excess by checking which are the most important configurations that contribute to the excitation. For this, we consider the unperturbed spectrum and compare the nucleus ^{176}Sn and the unbound system ^{180}Sn that is located just beyond the drip line. Pairing correlations are not present in the nucleus ^{176}Sn because it is closed-shell; it has been shown that pairing correlations are practically negligible also in ^{180}Sn. We can thus ignore pairing and consider just particle-hole configurations constructed with the Hartree-Fock spectrum. In ^{176}Sn, that is the last bound nucleus in our model, all the occupied states are bound; 2^+ particle-hole configurations are thus constructed with bound negative energy hole states. Passing to ^{180}Sn four neutrons are added giving an unbound system. The four additional neutrons are placed in the unbound states $4p1/2$ and $4p3/2$, with an occupation of 54% and 73%, respectively. We have checked that the low-lying mode is mainly composed of a few single

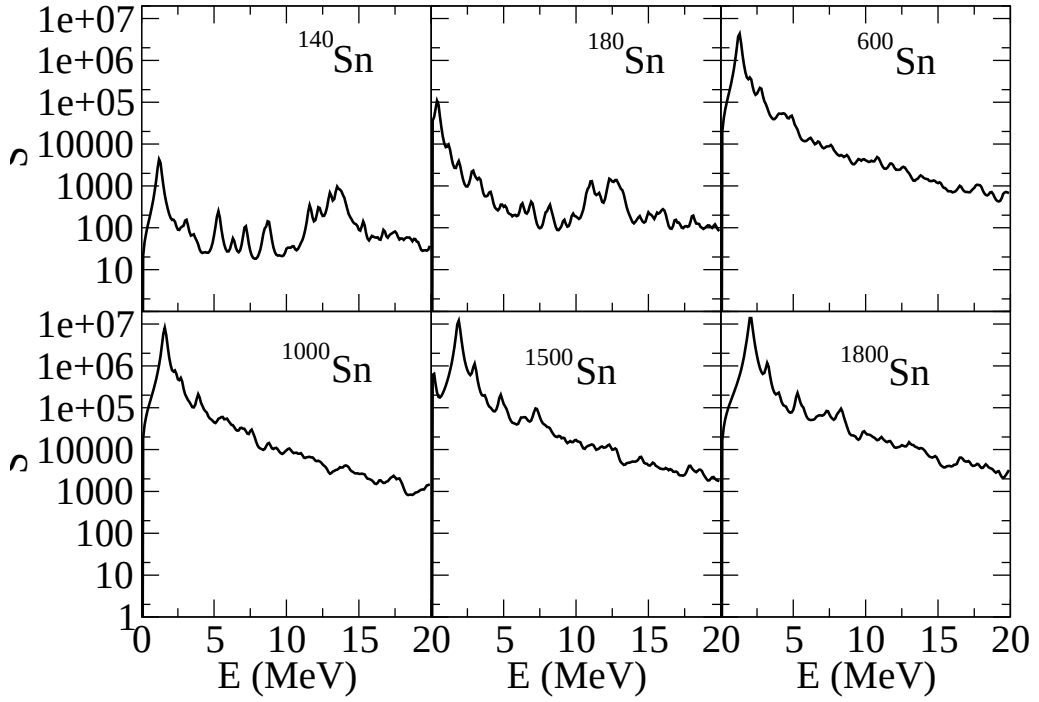

Figure 6.2: QRPA strength distributions for the quadrupole mode in units of fm^4 MeV^{-1}.

particle configurations where the hole states are $4p1/2$ and $4p3/2$ (both single particle energies are ~ 0.2 MeV) and the particle states are the empty states $3f5/2$ and $3f7/2$ (both single particle energies are ~ 0.65 MeV). In the latter case, in particular, both particle and hole states of the most important configurations are unbound. This difference is even accentuated when the baryonic density increases and unbound states of higher energy are populated.

Let us analyze now what is the nature of the excitation mode found in the unbound systems. We perform first a qualitative test. We calculate the denominator of the RPA response function in asymmetric nuclear matter at the hydrodynamical limit (zero transfered energy and momentum) which is related to the determinant of the polarization in the 2×2 isospin space (Garcia-Recio et al., 1992),

$$D = \mathrm{Det} \begin{pmatrix} 1 + N_0^n f_0^{nn} & N_0^n f_0^{np} \\ N_0^p f_0^{pn} & 1 + N_0^p f_0^{pp} \end{pmatrix} , \tag{6.1}$$

where $N_0^\tau = m_\tau^* k_{F\tau}/\pi^2\hbar^2$ is the density of states of the Fermi gas and $f_0^{\tau\tau'}$ is the monopolar Landau parameter in the density-density channel (see, for instance, Ref (Hernandez et al., 1997)). The zeros of the determinant correspond to the poles of the strength and are induced by an attractive residual interaction. We represent in Fig. 6.3 the determinant D, Eq (6.1), calculated within the local density approximation for the systems ^{120}Sn, ^{180}Sn, ^{600}Sn, ^{1000}Sn and ^{1750}Sn. The determinant is represented as a function of the radius. One observes that for all the systems, situated before and after the drip line, the determinant goes to zero at the surface of the nucleus or the cluster. Moreover, for the systems situated beyond the neutron drip, the determinant is close to zero, on the positive side, in the region of the neutron gas located out of the cluster. When the neutron number increases, the determinant progressively approaches zero. This is related to the fact that the residual interaction is getting more and more attractive. One can thus conclude that the nature of the low-lying mode is strongly modified when the drip line is crossed. It is constructed with nucleons located at the surface in nuclei. On the other side, in the unbound systems, it is built with both nucleons located at the surface and neutrons belonging to the low-density free gas region.

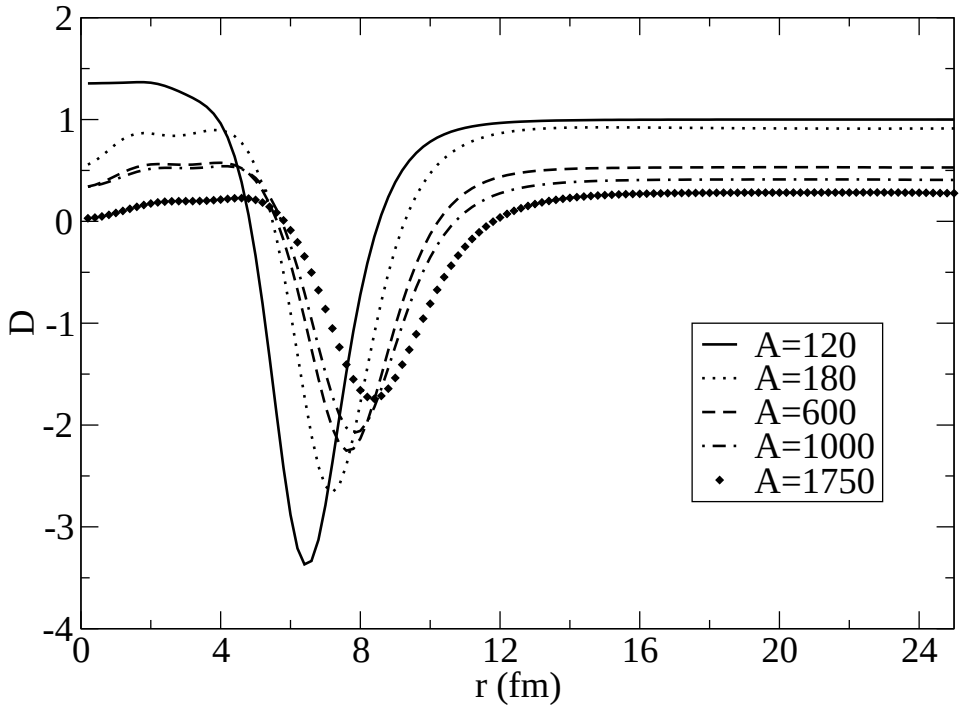

Figure 6.3: Determinant D calculated for the systems ^{120}Sn, ^{180}Sn, ^{600}Sn, ^{1000}Sn and ^{1750}Sn.

In Ref. (Grasso et al., 2008), the system ^{1500}Zr is also studied and exhibit similar feature as the one that we have described here.

6.2.2 Pairing properties at overflow

We selecte 8 isotopes given in Table 6.1 which are located around Z=28, 40 and 50. It is well adapted to perform a spherical HFB calculation since these nuclei are predicted spherical near the neutron drip-line (Hilaire and Girod, 2007).

For these selected isotopes, the neutron-drip number N_{drip}, defined as the neutron number of the last nucleus before the two-neutrons separation energy $S_{2n}(N) = E(N) - E(N-1)$ changes its sign (Ring and Schuck, 1980), is given in table 6.1. The total neutron occupation number of resonance states N_{res} for the drip-line nuclei is also given. The calculation of N_{res} requires the identification of resonance states which, in our case, are defined as positive energy states with rms radii lower than 10 fm. It is interesting to remark from Table 6.1 that the drip-line nuclei with a number of neutrons that coincides with the well-known magic numbers (82 and 126) have no states in the continuum. The shell occupation in this case is 0 or 1, as in magic nuclei. We therefore group Kr, Sr, Sn and Te isotopes in the same group $\mathcal{A}_2$. The persistence of magicity with the same magic numbers as in stable nuclei might be due to the sphericity of these nuclei. In the case of Ni, Zr, Mo and Ru, the drip-line occurs in more complicated shell structure partially involving resonance states and these isotopes are grouped in $\mathcal{A}_1$.

The drip-line isotopes identified in Table 6.1 can be considered as the seed nuclei from which the overflow occurs. The dripping of neutrons shall therefore be influenced by the microscopic structure of these seed nuclei. Nuclei belonging to the group $\mathcal{A}_1$ have a resonance occupation number N_{res} which goes from 2 to 8 particles. This number reveals the large continuum coupling. The number of particles in the resonance states is zero for nuclei belonging to the group $\mathcal{A}_2$, since in the magic nuclei located at the drip-line, pairing correlations are quenched and continuum coupling therefore largely suppressed. From

Isotope	Z	N_{drip}	group	N_{res}
Ni	28	60	$\mathcal{A}_1$	3.0
Kr	36	82	$\mathcal{A}_2$	0.0
Sr	38	82	$\mathcal{A}_2$	0.0
Zr	40	84	$\mathcal{A}_1$	2.2
Mo	42	90	$\mathcal{A}_1$	8.0
Ru	44	92	$\mathcal{A}_1$	3.0
Sn	50	126	$\mathcal{A}_2$	0.0
Te	52	126	$\mathcal{A}_2$	0.0

Table 6.1: Isotope acronym, number of protons Z, number of neutrons of the last nucleus before the drip line N_{drip}, for the selected set. Isotopes for which the drip-line nucleus is non-magic (magic) belongs to the group $\mathcal{A}_1$ ($\mathcal{A}_2$, respectively). The total occupation number of resonance states for the drip-line nuclei N_{res} is shown in the last column (see the text for more details).

a microscopic analysis, the structure of drip-line nuclei is qualitatively different between the group $\mathcal{A}_1$ and $\mathcal{A}_2$. In the following, we show how these differences impact the quenching of pairing correlations at overflowing.

Figs. 6.4 display the average neutron pairing gaps versus the neutron number (top panel) and the difference between the neutron number and the neutron drip $N - N_{drip}$ (bottom panels). The average neutron pairing gap is obtained from the neutron pairing field given by the HFB solution. In Fig. 6.4 the neutron pairing gaps for the $\mathcal{A}_1$ isotopes is shown on the left while the neutron pairing gaps for the $\mathcal{A}_2$ isotopes is shown on the right. In the case of nuclei from the $\mathcal{A}_1$ group, the neutron pairing gap persists beyond the drip line (see bottom left panel of Fig. 6.4). The continuum coupling preserves the pairing diffusivity around the Fermi energy: the occupancy of the scattering states beyond the drip-line does not suppress superfuidity. The presence of an overflowing neutron gas has therefore a limited effect on the pairing gap for the $\mathcal{A}_1$ isotopes, showing the persistence of superfluidity. In the case of the $\mathcal{A}_2$ isotopes, a suppression of the average pairing gap just beyond the drip line is observed in Fig. 6.4 (right panel). The presence of a magic nucleus at the drip-line have therefore a strong influence on the pairing gap at and beyond the drip line: the large spacing between the last occupied state and the first excited state (resonance state) suppresses superfluidity. Fig. 6.4 provides a clear illustration that the shell structure of the drip-line nucleus determines the suppression or the persistence of superfluidity, even in overflowing nuclear systems.

In Ref. (Schuck and Viñas, 2011), the quenching of pairing in overflowing systems has been predicted upon overflow of trapped fermions. It should be underlined that in the present work, the mean-field in nuclear systems have a centrifugal term which gives rise to the mean-field resonance states and continuum coupling, whereas the conclusions obtained in Ref. (Schuck and Viñas, 2011) are applicable only to overflowing systems involving $\ell = 0$ single particle states. In more general systems, like in the crust of neutron stars, a more sophisticated theoretical model such as the present HFB one predicts a suppression of superfluidity only if the continuum coupling is quenched, by the shell structure for instance.

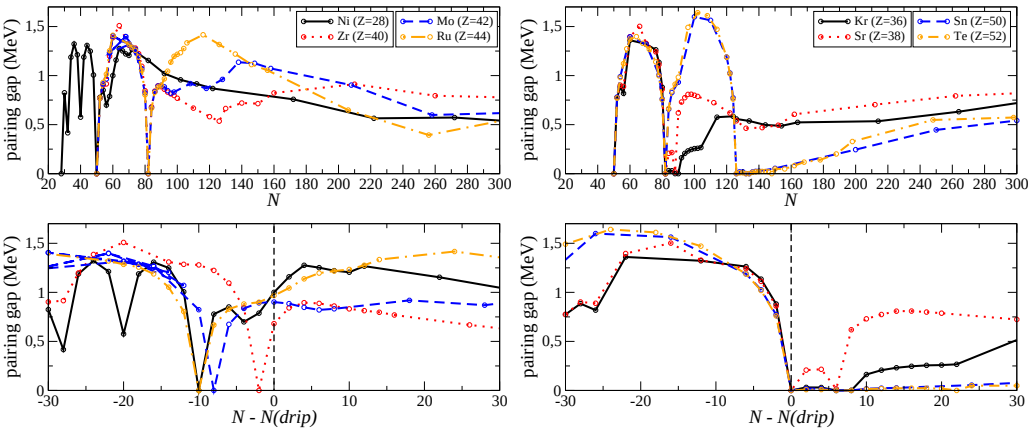

Figure 6.4: Neutron pairing gaps versus neutron density N (top panel) and versus $N - N(drip)$ (bottom panel) for the isotopes in the group $\mathcal{A}_1$ (left panel) and in the group $\mathcal{A}_2$ (right panel).

6.2.3 Pairing reentrance phenomenon

The persistence of superfluidity upon overflow of bound neutrons might not be the only consequence of continuum coupling: in the case where pairing is suppressed, the increase of temperature may generate the reentrance of superfluidity. The finite-temperature HFB model (Sandulescu, 2004), is employed to study the reentrance of pairing in the thermal state of overflowing even-even nuclear systems.

The temperature-averaged pairing gap for ^{160,176,180,200}Sn is shown in Fig. 6.5. In ^{160}Sn and ^{200}Sn it behaves as expected from HFB theory: the pairing gap vanishes at the critical temperature $T_c = 0.57\Delta(T \approx 0)$ (see Ref. (Khan et al., 2007) and references therein). In the case of ^{176}Sn and ^{180}Sn, the reentrance of superfluidity is observed with increasing temperature. This reentrance is induced by the presence of resonances states in the spectrum of these nuclear systems: Being slightly too high in energy, these states are not occupied at zero temperature (see Table 6.1), while at finite temperature, they can be partially occupied from the Fermi-Dirac distribution. At low temperature, the pairing correlations can therefore be switched on allowing the reapparition of the superfluid state. The reentrance critical temperature depends on the step in energy between the last occupied bound state and the first resonance one, which changes from one system to another, as observed in Fig. 6.5 for ^{176}Sn and ^{180}Sn. In the case of ^{200}Sn, this energy step is too large to give rise to the reentrance of superfluidity before the highest critical temperature is reached. The ^{180}Sn overflowing system has an interesting phase diagram including three critical temperatures: with increasing temperature, two of them correspond to the vanishing of superfluidity ($T_{c1} \sim 11$ keV and $T_{c3} \sim 1$ MeV) and one to its reappearance ($T_{c2} \sim 300$ keV). The lowest critical temperature T_{c1} is associated to the transition from the superfluid to the normal state in the overflowing neutron gas. The highest critical temperature T_{c3} is similar for ^{160,176,180}Sn, indicating that superfluidity has been restored in the seed nucleus of ^{176,180}Sn. More generally, pairing reentrance in hot systems is observed for isotopes belonging to the group $\mathcal{A}_2$ where resonances are too high in energy to participate to pairing at zero temperature. For the isotopes belonging to the group $\mathcal{A}_1$, no reentrance is observed since pairing is not quenched at overflow.

Reentrance of superfluidity at finite temperature have been predicted in nuclear systems such as in odd-nuclei (Balian et al., 1999), rotational motion of nuclei (Dean et al., 2010), and the deuteron pairing channel in asymmetric infinite matter (Sedrakian et al., 1997). It was aslo predicted in polarised ^{3,4}He (Frossati et al., 1986; Crowell and Reppy, 1993; Csáthy et al., 2002) and in spin asymmetric cold atom gas (Castorina et al., 2005; Levin and Chen, 2006). In all these systems, pairing at zero temperature is generated by an attraction among Fermions of different spin or isospin. Superfluidity is therefore maximum in spin or

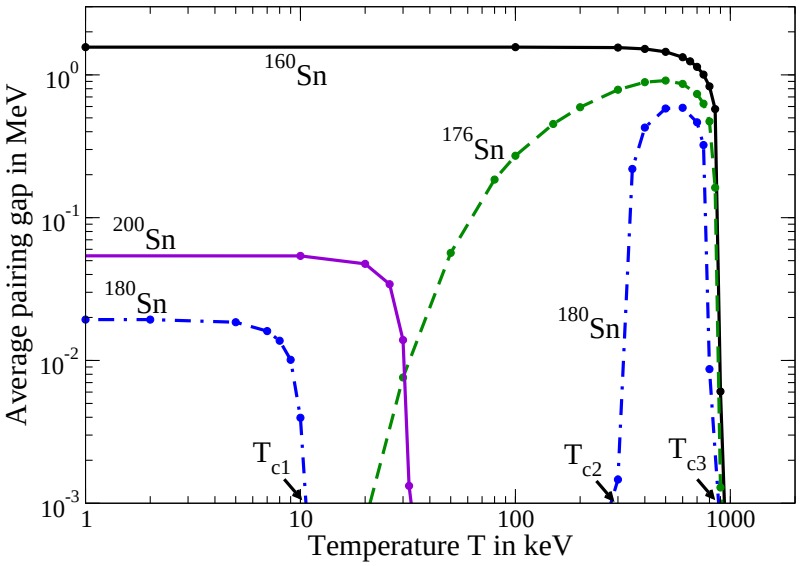

Figure 6.5: Temperature averaged neutron pairing gap versus temperature for ^{160,176,180,200}Sn. A superfluid re-entrant effect is observed for ^{176}Sn and ^{180}Sn.

isospin symmetric systems for which there is a matching of the Fermi levels of the constituent Cooper-pairs. Breaking the spin or isospin symmetry disfavor pairing while temperature in asymmetric systems acts in favor of restoring the broken symmetry and can eventually induce a reentrance of pairing. At variance with this mechanism the pairing reentrance phenomenon discussed in this section is based on a novel mechanism in finite systems where resonance states play a major role.

6.2.4 Final remarks

In summary, we have investigated the pairing properties and discussed the evolution of low-lying 2^+ modes of nuclear systems upon overflowing superfluid neutrons. Low-lying 2^+ modes are found in the same energy region both in nuclei and in the unbound nuclear systems. They are characterized by a huge strength in the unbound systems and for this reason they are called supergiant modes (Khan et al., 2004). We have also discussed suppression, persistence and reentrance of superfluidity in these finite systems. From a systematic HFB calculations on 8 isotopic chains, the pairing properties is shown to be strongly correlated to the continuum coupling, both at zero and finite temperature. At zero temperature, the coupling between the seed nucleus and the gas is weak, and a formal separation of their properties into a nucleus plus a gas provides a qualitative understanding of the suppression and the persistence of superfluidity. With increasing temperature in the normal state, the Fermi-Dirac distribution can populate the resonance states giving rise to the reentrance of superfluidity. The pairing correlations in the nuclear system are switched on again and consecutive critical temperatures are predicted.

The understanding of the suppression, persistence and reentrance of superfluidity in nuclear systems, deeply related to the continuum coupling, opens wide perspectives for discoveries in weakly bound nuclei, as well as it sheds new light on the transition between the inner and outer crusts in neutron stars. The role of resonances around the neutron drip changes the microscopic understanding of the neutron drip-out mechanism. Since these resonances are populated by pairing, the strength of pairing interaction in the crust of neutron stars could have an influence on the seeds nuclei at neutron dripping. The temperatures at work during cooling are typically of the order of 10 to 500 keV (Haensel et al., 2007) and coincide with

the critical temperatures of the reentrance phenomenon. As a consequence, the novel pairing reentrance phenomenon analyzed in this section can also modify the thermodynamical and cooling properties in the crust of neutron stars. Exploratory work in this direction have already started (Fortin et al., 2010).

Eventually, relations with other superfluid Fermi-systems shall also be investigated. For instance in cold Fermionic atoms overflowing from an inner trap to a larger one (Stamper-Kurn et al., 1998; Viverit et al., 2001), the resonance states still exist in the form of stable classical paths above the inner trap. It will therefore be interesting to investigate the role of these stable paths on the superfluid properties of overflowing cold Fermionic atoms.

6.3 Symmetry energy and neutron stars physics

Stimulated by the development of exotic nuclear physics, the efforts to determine the nuclear equation of state (EOS) have focused in the last few years on the density dependence of the symmetry energy $S(\rho)$ (Li et al., 2008a). In particular, the symmetry-energy slope at saturation density, represented by the quantity L, has raised a great deal of interest (Brown, 2000; Typel and Baur, 2001; Steiner et al., 2005; Sagawa et al., 2007b; Xu et al., 2009; Warda et al., 2009; Centelles et al., 2009; Vidaña et al., 2009): while the different nuclear models widely disagree on the value of this basic quantity, increasing experimental data (Li and Chen, 2005; Famiano et al., 2006; Shetty et al., 2007a; Shetty et al., 2007b; Tsang et al., 2009; Danielewicz, 2003; Danielewicz and Lee, 2009) are expected to bring more and more stringent constraints, leading to a radical progress in our knowledge of the EOS of neutron-rich matter. This impacts strongly the properties of compact stars such as the radius (Li and Steiner, 2006), the proton fraction, or the inner edge, which is defined as the transition from the liquid core to the solid crust (Xu et al., 2009).

The most direct impact of the symmetry energy on neutron-star structure concerns the proton fraction $Y_p(\rho)$ in stellar matter, which is fixed by β-equilibrium. For a given density, a lower symmetry energy corresponds to a lower proton fraction at saturation. Since the proton fraction is an important quantity beyond saturation density, for its relation to the quenching of the URCA neutrino emission process for instance, a lower L corresponds also to the lower proton fraction beyond saturation density (Li et al., 2008a). Considering different choices of the in-medium nucleon-nucleon interaction, that show different behavior of the symmetry energy at high density (soft/stiff), the relation between the symmetry energy and the properties of neutron stars is analyzed in this section.

In this section, we also discuss the link between the liquid-drop parameter L, the slope of the symmetry energy, and the inner edge properties. It has indeed been claimed that a precise determination of L would give a tight indication of the density ρ_t and pressure P_t at the transition point (Xu et al., 2009), and consequently on the mass and extension of the crust which play a crucial role in the interpretation of pulsar observations (Pethick and Ravenhall, 1995). The pressure at the inner edge, P_t, is indeed an important quantity that might be measurable indirectly from observations of pulsar glitches since it is related to the crustal fraction of the total moment of inertia (Link, 1999; Steiner et al., 2005; Lattimer and Prakash, 2007). From the experimentally constrained value of L, the pressure P_t has been deduced to be limited between 0.01 and 0.26 MeV/fm^3 for a given model (Xu et al., 2009). Using a different model, the correlation between P_t and L can be largely modified (Moustakidis et al., 2010). However, the role of L in the determination of the core-crust transition needs to be checked against model dependence and clarified, as mentioned in Ref. (Avancini et al., 2008; Avancini et al., 2009). In this section, we use a variety of nuclear models to address this issue.

In Fig. 6.6 is shown the relation between L and the pressure of pure neutron matter, $P_{\rm NM}$, at ρ=0.08 fm^{-3} (left) and the pressure P_{tt} calculated at the crust-core transition defined as the crossing between the line of β equilibrium and the thermodynamic spinodal contour (Pethick and Ravenhall, 1995). Each

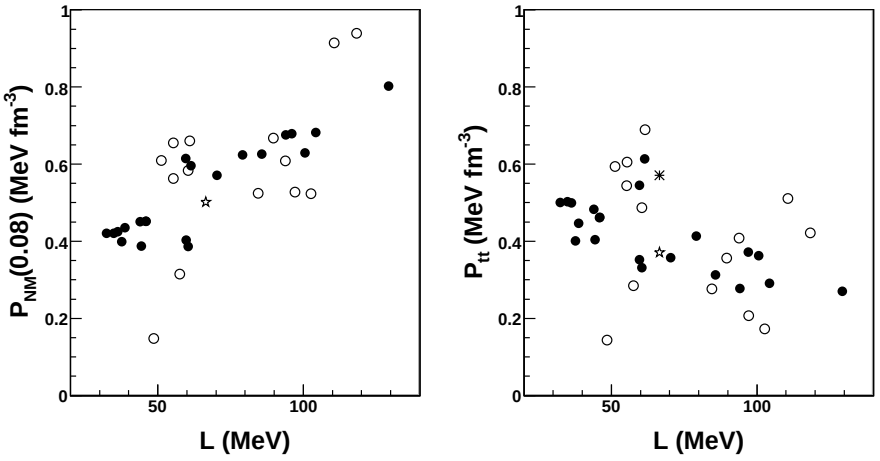

Figure 6.6: Impact of L on the pressure of neutron-rich matter at sub-saturation density, for different nuclear models: Skyrme (full symbols), relativistic (empty symbols), BHF-2 (star) and BHF-$2_{\rm para}$ (asterisk). Both BHF-2 results are identical for neutron matter. Left: pressure of pure neutron matter, for a fixed density typical of the transition: ρ=0.08 fm^{-3}. Right: thermodynamic transition pressure.

dot correspond to a different model among the 30th that we considered. See Refs. (Ducoin et al., 2010; Ducoin et al., 2011) for more details on the models. It is hard to identify a clear correlation partern from Fig. 6.6. In the following, we propose a Generalized Liquid Drop Model (GLDM) to characterize the EoS and the analyze the correlations between the properties at the edge of neutron stars and the parameters of the GLDM.

6.3.1 A Generalized Liquid-Drop Model (GLDM)

The GLDM corresponds to a series expansion of the EOS around a given reference density, $\rho_{\rm ref}$ and for an order of development $\mathcal{N}$, and the energy per particle reads as,

$$E_{\rm GLDM}(\rho,y) \;=\; \sum_{n=0}^{\mathcal{N}} \left(c_{{\rm IS},n} + c_{{\rm IV},n}\, y^2\right) \frac{x^n}{n!} + (E_{\rm kin} - E_{\rm kin}^{\rm para})\,, \;\; \text{with} \;\; x = \frac{\rho-\rho_{\rm ref}}{3\rho_{\rm ref}}\,. \qquad (6.2)$$

The first term on the r.h.s. of Eq. (6.2) contains both the kinetic and the potential contributions to the energy in the parabolic approximation with respect to the asymmetry y. The second term gives the contribution of the kinetic term beyond the parabolic approximation, as it will be explained below. We have introduced in this expression the GLDM coefficients $c_{{\rm IS},n}$ and $c_{{\rm IV},n}$, respectively associated with the derivatives of the energy $E(\rho, y=0)$ and of the symmetry energy $S(\rho)$: the index 'IS' ('IV') stands for isoscalar (isovector). They are expressed as:

$$c_{{\rm IS},n}(\rho_{\rm ref}) \;=\; (3\rho_{\rm ref})^n \frac{\partial^n E}{\partial \rho^n}(\rho_{\rm ref},0) \qquad (6.3)$$

$$c_{{\rm IV},n}(\rho_{\rm ref}) \;=\; (3\rho_{\rm ref})^n \frac{\partial^n S}{\partial \rho^n}(\rho_{\rm ref}) \;\; \text{with} \;\; S(\rho) = \frac{1}{2}\frac{\partial^2 E}{\partial y^2}(\rho,0) \qquad (6.4)$$

In the case $\rho_{\rm ref} = \rho_0$, the lower-order coefficients are usual nuclear matter properties: $c_{{\rm IS},0} = E_0$ (saturation energy), $c_{{\rm IS},2} = K_0$ (incompressibility), $c_{{\rm IS},3} = Q_0$, $c_{{\rm IV},0} = J$ (symmetry energy), $c_{{\rm IV},1} = L$ (symmetry-energy slope), $c_{{\rm IV},2} = K_{\rm sym}$ (symmetry incompressibility), $c_{{\rm IV},3} = Q_{\rm sym}$. The GLDM coefficients $c_{{\rm IS},n}(\rho_{\rm ref})$ and $c_{{\rm IV},n}(\rho_{\rm ref})$ could be nuclear properties determined experimentally at $\rho_{\rm ref}$, from

which we would extrapolate the nuclear EOS at lower or higher densities, or in our work, we obtained it from various nuclear models (non-relativistic Skyrme model, relativistic mean field, Brueckner approach).

To obtain the non-quadratic terms in the kinetic term, we have introduced in Eq. (6.2) a model-independent correction based on the non-relativistic, free Fermi gas kinetic term:

$$E_{\rm kin} = \frac{1}{\rho}\left[\frac{\hbar^2}{2m}(\tau_n+\tau_p)\right], \tag{6.5}$$

where $\tau_q = (3\pi^2\rho_q)^{5/3}/(5\pi^2)$ is the kinetic density of the nucleon species $q = n, p$ and m is the nucleon mass. As a function of density and asymmetry, we have:

$$E_{\rm kin} = \frac{(3\pi^2/2)^{5/3}}{10m\pi^2}\rho^{2/3}\left[(1+y)^{5/3}+(1-y)^{5/3}\right] \tag{6.6}$$

$$E_{\rm kin}^{\rm para} = \frac{(3\pi^2/2)^{5/3}}{10m\pi^2}\rho^{2/3}\left[2+\frac{10}{9}y^2\right], \tag{6.7}$$

where $E_{\rm kin}^{\rm para}$ is the parabolic part of $E_{\rm kin}$. In the GLDM defined by Eq. (6.2), the extra-parabolic behavior of the functional is sketched by the extra-parabolic behavior of $E_{\rm kin}$, which brings the model-independent correction $E_{\rm kin} - E_{\rm kin}^{\rm para}$ (second term on the r.h.s. of Eq. (6.2)).

6.3.2 Application to the transition between the crust and the core

We consider in this section the specific role of the symmetry energy slope L in the determination of the core-crust transition, defined here as the crossing between the line of β equilibrium and the thermodynamic spinodal contour (Ducoin et al., 2010; Ducoin et al., 2011).

Let us write the pressure in the GLDM framework:

$$P(\rho,y) = \frac{\rho^2}{3\rho_0}\left[Ly^2+\sum_{n\geq 2}\left(c_{{\rm IS},n}+c_{{\rm IV},n}y^2\right)\frac{x^{n-1}}{(n-1)!}\right]+\rho^2\frac{\partial(E_{\rm kin}-E_{\rm kin}^{\rm para})}{\partial\rho}. \tag{6.8}$$

From this expression, we expect that for a given density the pressure of neutron-rich matter should increase with L, which is the leading coefficient.

This trend appears on the left panel of Fig. 6.6, representing the relation between L and the pressure of pure neutron matter, $P_{\rm NM}$, at ρ=0.08 fm^{-3}. Thus, a positive correlation between L and P_{tt} should be obtained if we could neglect other contribution of higher-order coefficients in Eq. (6.8). However, as it can be seen on the right panel of Fig. 6.6, the results for $P_{tt}(L)$ present an important dispersion and we cannot extract a clear correlation, although a decreasing trend can be observed among Skyrme models. Four eccentric points close to L=60 MeV weaken this correlation between Skyrme models: they correspond to atypic relations between L and $K_{\rm sym}$, which also affect the plot $P_{\rm NM}(0.08\,{\rm fm}^{-3})$. The lack of correlation between L and P_{tt} when independent models are considered results from a delicate balance between opposite effects, that we have discussed in details in Refs. (Ducoin et al., 2010; Ducoin et al., 2011).

A systematic analysis of the effect of the isovector coefficients J, L and $K_{\rm sym}$ on the transition properties is presented in Tab. 6.2. Our previous study has shown that the relation $X_{tt}(L)$ is affected by atypical values of J and $K_{\rm sym}$ associated with the various models. In order to explore this effect, we have performed two-dimensional fits of the transition data:

$$X_{ti}(M_1,M_2) = a_1M_1+a_2M_2+b\,, \tag{6.9}$$

where $X_{ti} = \{\rho_{tt}, Y_{p,tt}, P_{tt}; \rho_{td}, Y_{p,td}, P_{td}\}$ (dynamic or thermodynamic transition), and M_i are two of the isovector GLDM coefficients: $J_{\rm ref} = S(\rho_{\rm ref})$, $L_{\rm ref} = 3\rho_{\rm ref}[\partial S/\partial\rho](\rho_{\rm ref})$ and $K_{\rm sym,ref} = (3\rho_{\rm ref})^2[\partial^2 S/\partial\rho^2](\rho_{\rm ref})$.

X_{tt}	M_1	M_2	rms	X_{td}	M_1	M_2	rms
ρ_{tt}	L		0.0038 fm^{-3}	ρ_{td}	L		0.0037 fm^{-3}
ρ_{tt}	J	L	0.0028 fm^{-3}	ρ_{td}	J	L	0.0035 fm^{-3}
ρ_{tt}	L	$K_{\rm sym}$	0.0038 fm^{-3}	ρ_{td}	L	$K_{\rm sym}$	0.0037 fm^{-3}
ρ_{tt}	L_{01}		0.0062 fm^{-3}	ρ_{td}	L_{01}		0.0054 fm^{-3}
ρ_{tt}	J_{01}	L_{01}	0.0037 fm^{-3}	ρ_{td}	J_{01}	L_{01}	0.0038 fm^{-3}
ρ_{tt}	L_{01}	$K_{\rm sym,01}$	0.0032 fm^{-3}	ρ_{td}	L_{01}	$K_{\rm sym,01}$	0.0037 fm^{-3}
$Y_{p,tt}$	L		0.0063	$Y_{p,td}$	L		0.0057
$Y_{p,tt}$	J	L	0.0022	$Y_{p,td}$	J	L	0.0024
$Y_{p,tt}$	L	$K_{\rm sym}$	0.0063	$Y_{p,td}$	L	$K_{\rm sym}$	0.0058
$Y_{p,tt}$	L_{01}		0.0081	$Y_{p,td}$	L_{01}		0.0074
$Y_{p,tt}$	J_{01}	L_{01}	0.0016	$Y_{p,td}$	J_{01}	L_{01}	0.0014
$Y_{p,tt}$	L_{01}	$K_{\rm sym,01}$	0.0040	$Y_{p,td}$	L_{01}	$K_{\rm sym,01}$	0.0040
P_{tt}	L		0.117 MeV.fm^{-3}	P_{td}	L		0.085 MeV.fm^{-3}
P_{tt}	J	L	0.076 MeV.fm^{-3}	P_{td}	J	L	0.055 MeV.fm^{-3}
P_{tt}	L	$K_{\rm sym}$	0.092 MeV.fm^{-3}	P_{td}	L	$K_{\rm sym}$	0.067 MeV.fm^{-3}
P_{tt}	L_{01}		0.129 MeV.fm^{-3}	P_{td}	L_{01}		0.101 MeV.fm^{-3}
P_{tt}	J_{01}	L_{01}	0.088 MeV.fm^{-3}	P_{td}	J_{01}	L_{01}	0.069 MeV.fm^{-3}
P_{tt}	L_{01}	$K_{\rm sym,01}$	0.036 MeV.fm^{-3}	P_{td}	L_{01}	$K_{\rm sym,01}$	0.033 MeV.fm^{-3}

Table 6.2: Root mean square of residuals associated with two-variable linear fits $\mathrm{X_{ti}} = \mathrm{a_1} \times \mathrm{M_1} + \mathrm{a_2} \times \mathrm{M_2} + \mathrm{b}$, where $X_{ti} = \{\rho_{tt}, Y_{p,tt}, P_{tt}; \rho_{td}, Y_{p,td}, P_{td}\}$ and M_i are two of the isovector GLDM coefficients: $J_{\rm ref} = S(\rho_{\rm ref})$, $L_{\rm ref} = 3\rho_{\rm ref}[\partial S/\partial\rho](\rho_{\rm ref})$ and $K_{\rm sym,ref} = (3\rho_{\rm ref})^2[\partial^2 S/\partial\rho^2](\rho_{\rm ref})$. J, L and $K_{\rm sym}$ are taken at $\rho_{\rm ref} = \rho_0$; J_{01}, L_{01} and $K_{\rm sym,01}$ are taken at $\rho_{\rm ref} = 0.1$ fm^{-3}. The results for single-variable linear fits in function of L and L_{01} are also shown.

We have considered the saturation coefficients J, L and $K_{\rm sym}$, as well as coefficients at the reference density $\rho_{\rm ref} = 0.1$ fm^{-3}, denoted J_{01}, L_{01} and $K_{\rm sym,01}$. Table 6.2 gives the root mean square (rms) of residuals associated with the different fits, indicating the relevance of the respective combinations of coefficients in the determination of X_{ti}.

It appears that ρ_{ti} is well correlated with L; no significative improvement can be obtained by considering pairs of coefficients. In the cases of Y_{ti} and P_{ti} however, the predictions can be considerably improved by using combinations of coefficients. As expected, Y_{ti} is very well correlated with a combination of J and L, and this result is still improved using a combination of J_{01} and L_{01}. On the other hand, the values of Tab. 6.2 indicate that combinations of L and $K_{\rm sym}$ are not relevant to determine $Y_{p,ti}$. The transition pressure, instead, presents improved correlations with two kinds of parameter combinations: either J and L at saturation density, or L_{01} and $K_{\rm sym,01}$; the latter leads to the smallest rms of residuals.

We show on Fig. 6.7 the most significant correlations obtained between the dynamic transition properties and different combinations of the GLDM coefficients. The quantities ρ_{td}, $Y_{p,td}$ and P_{td} are shown as a function of L and as a function of selected coefficient combinations. For the transition density, we verify the good $L - \rho_{td}$ correlation; we also consider two coefficient combinations, $[J - 0.558 \times L]$ and $[L_{01} + 0.426 \times K_{\rm sym,01}]$, which lead to a similar dispersion, lower than ± 0.004 fm^{-3}. The situation is different for the proton fraction $Y_{p,td}$ and the pressure P_{td}, for which the correlation with L is not so good. The selected coefficient combinations lead to clearly improved correlations. Concerning the proton fraction, the combinations $[J - 0.172 \times L]$ and especially $[J_{01} - 0.160 \times L_{01}]$ present excellent correlations with $Y_{p,td}$. As for the transition pressure, the combinations $[J - 0.127 \times L]$ and $[L_{01} - 0.343 \times K_{\rm sym,01}]$ allow to

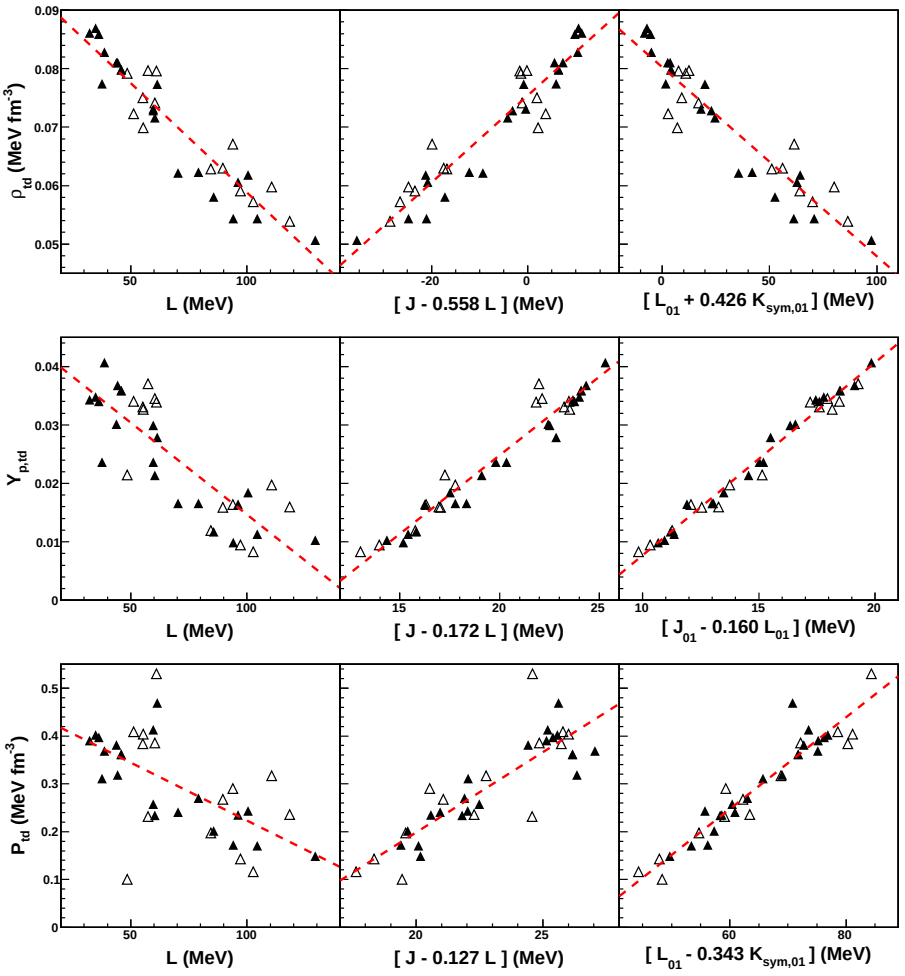

Figure 6.7: Correlations between the dynamic core-crust transition properties and GLDM coefficients (see text).

considerably reduce the data dispersion, and show unambiguous correlations with P_{td}; this is especially true for the second combination (coefficients extracted at 0.1 fm^{-3}), for which the typical model dispersion for P_{td} becomes $\pm$ 0.033 MeV.fm^3 instead of $\pm$ 0.085 MeV.fm^3 in the case of $P_{td}(L)$. The linear fits represented in Fig. 6.7 are:

$$\rho_{td}(L) = -3.75 \times 10^{-4} \times L + 0.0963 \text{ fm}^{-3} \tag{6.10}$$

$$\rho_{td}(J, L) = 7.46 \times 10^{-4} \times [J - 0.558 \times L] + 0.0754 \text{ fm}^{-3} \tag{6.11}$$

$$\rho_{td}(L_{01}, K_{\text{sym},01}) = 3.23 \times 10^{-4} \times [L_{01} + 0.426 \times K_{\text{sym},01}] + 0.0802 \text{ fm}^{-3} \tag{6.12}$$

$$Y_{p,td}(L) = -3.15 \times 10^{-4} \times L + 0.0461 \tag{6.13}$$

$$Y_{p,td}(J, L) = 2.69 \times 10^{-3} \times [J - 0.172 \times L] - 0.0290 \tag{6.14}$$

$$Y_{p,td}(J_{01}, L_{01}) = 3.30 \times 10^{-3} \times [J_{01} - 0.160 \times L_{01}] - 0.0253 \tag{6.15}$$

$$P_{td}(L) = -2.42 \times 10^{-3} \times L + 0.465 \text{ MeV fm}^{-3} \tag{6.16}$$

$$P_{td}(J, L) = 3.36 \times 10^{-2} \times [J - 0.127 \times L] - 0.474 \text{ MeV fm}^{-3} \tag{6.17}$$

$$P_{td}(L_{01}, K_{\text{sym},01}) = 9.59 \times 10^{-3} \times [L_{01} - 0.343 \times K_{\text{sym},01}] - 0.328 \text{ MeV fm}^{-3} \tag{6.18}$$

The relations involving GLDM coefficients at ρ=0.1 fm^{-3} allow to predict the core-crust transition density,

asymmetry and pressure within a reasonable model uncertainty. This indicates that exploring the sub-saturation properties of nuclei in order to constrain directly these low-density coefficients could allow to modelize core-crust transition properties that do not depend strongly on the type of nuclear functional that is used.

6.3.3 Neutron stars properties and the stiffness of the equation of state

The determination of the equation of state (EOS) of asymmetric nuclear matter (NM) has been the main object of numerous nuclear structure and reaction studies involving unstable nuclei lying close to the neutron or proton driplines recently (Li et al., 2008a). The knowledge about the EOS of asymmetric NM is vital for any model of the neutron star formation (Bethe, 1990; Sumiyoshi and Toki, 1994; Douchin and Haensel, 2001; Lattimer and Prakash, 2004), and the nuclear mean-field potential is the most important input for the determination of the nuclear EOS. Many microscopic studies of EOS have been done based on the nuclear mean field given by both nonrelativistic and relativistic nuclear many-body approaches, using realistic two-body and three-body nucleon-nucleon (NN) forces or interaction Lagrangians (see recent reviews (Li et al., 2008a; Baldo and Maieron, 2007)). These many-body studies have shown the important role played by the Pauli blocking effects as well as higher-order NN correlations at different NM densities. These medium effects are normally considered as the physics origin of the density dependence that has been introduced into various versions of the effective NN interactions used in the modern mean-field approaches. Among them, very popular is the so-called M3Y interaction which was originally constructed to reproduce the G-matrix elements of the Reid (Bertsch et al., 1977) and Paris (Anantaraman et al., 1983) NN potentials in an oscillator basis. Several realistic density dependences have been added later on to the M3Y interactions (see Ref. (Loan et al., 2011) and refs. therein) to properly account for the NM saturation properties as well as the ground-state structure of finite nuclei. These density dependent versions of the M3Y interaction have been used in the nonrelativistic Hartree-Fock (HF) studies of symmetric and asymmetric NM. Some of them have been successfully used in the folding model studies of the nucleon-nucleus and nucleus-nucleus scattering.

While these effective NN interactions give more or less the same description of the saturation properties of the symmetric NM, the HF results for the asymmetric NM (Than et al., 2009) show that they are divided into two families, which are associated with two different (*soft* and *stiff*) behaviors of the NM symmetry energy at high nucleon densities. As a result, these two families predict very different behaviors of the proton-to-neutron ratio in the β-equilibrium that can imply two drastically different mechanisms for the neutron star cooling (with or without the direct Urca process) (Lattimer and Swesty, 1991; Lattimer et al., 1994; Page et al., 2004). Here we try to find out how such a difference in the NM symmetry energy can affect the EOS of the β-stable neutron star (NS) matter as well as the main NS properties like the maximum mass, radius, central density and moment of inertia.

The behavior of the density dependence of the proton fraction $x_{\rm p}(n_{\rm b})$ plays a very important role in the determination of the NS cooling rate. In particular, the powerful direct Urca (DU) process of neutrino emission is allowed only if the Fermi momenta of the constituent particles in the npeμ matter satisfy the triangle conditions (Lattimer and Swesty, 1991) that lead to the existence of a DU threshold $x_{\rm DU}$ for the proton fraction that can be estimated as (Klähn et al., 2006)

$$x_{\rm DU} = \frac{1}{1+\left(1+r_e^{1/3}\right)^3}, \tag{6.19}$$

where $r_e = n_e/(n_e+n_\mu)$ is the leptonic electron fraction. $x_{\rm DU}$ has its lowest value of 11.1% at $r_e = 1$ that corresponds to the muon-free threshold for DU process (Lattimer et al., 1994). It can be concluded immediately that the DU process is *not* possible for the NS matter generated with the soft-type interactions

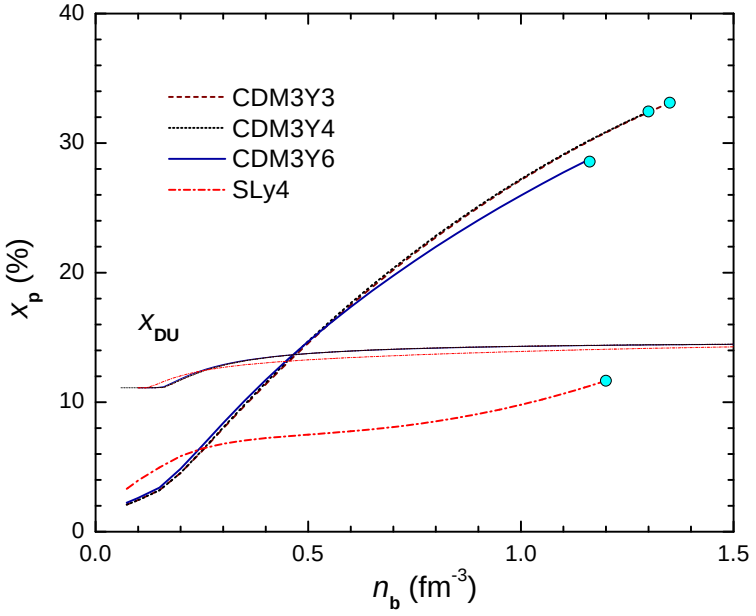

Figure 6.8: Proton fraction $x_{\rm p}$ of the β-stable NS matter using the mean-field potentials given by the stiff-type CDM3Yn and Sly4 interactions. Circles are $n_{\rm p}$ values calculated at the maximum central densities $n_{\rm c}$ given by the solution of the TOV equations. Thin lines are the corresponding DU thresholds (6.19).

when $x_{\rm p}$ can reach at most 4% and then decreases quickly to zero at $n_{\rm b} > 0.6$ fm^{-3}. Fig. 6.3.3 shows that for the stiff-type CDM3Yn interactions, the proton fraction becomes larger than the DU threshold at a rather modest threshold density of $n_{\rm b} \approx 0.45$ fm^{-3} that is far below the corresponding maximum central densities of $1.2 - 1.3$ fm^{-3}. Therefore, the DU process should be a realistic scenario for the NS cooling if the mean-field potential is generated with the CDM3Yn interactions. For the Sly4 interaction, the $x_{\rm p}$ value remains well below the DU threshold up to the maximum central density determined by the TOV equations and the DU process is thus not likely for the NS matter generated with the Sly4 interaction (Douchin and Haensel, 2001).

6.4 Conclusions and outlooks

In this chapter, we have illustrated in some cases how the measurement of nuclear properties such as the strength of the continuum coupling and the symmetry energy impact the properties of neutron stars. This illustration is of course very much incomplete and is mainly focussed on my work on this topic. The physics of compact stars is however complex and most of the conditions that prevails in astrophysics cannot be reproduced on earth. It is certainly only in some few cases that direct constraints from experimental studies can be clearly shown and it is interesting to investigate more on this topic in the future.

Chapter 7

Conclusions and outlooks

Over the last decade, compact stars have shown to be excellent tools to test matter under extreme conditions. Through this manuscript, several illustrations of the links that exist between nuclear physics and compact stars properties have been studied. Most of these links are performed within theoretical modeling that are used to describe both nuclei and nuclear systems in astrophysics. In few cases, the link can be more direct (some illustrations are given in chapter 6).

On the observational side, the new generation of space X-ray and gamma-ray observatories are enabling new observations and breakthrough discoveries (kHz quasi- periodic oscillations, bursting millisecond pulsars, half-day long X-ray superbursts). The thermal emission from isolated neutron stars has provided important information on their radii and cooling history. At the same time, improvements in radio telescopes and interferometric techniques have increased the number of known binary pulsars, allowing for extremely precise neutron star mass measurements. Finally, a large multinational effort has taken place in the last decade to build detectors, offering the exciting prospect of the detection of gravitational waves.

On the experimental side, the next generation of Radioactive Nuclear Beam facilities will allow to explore more systematically regions closer to the nuclear drip lines. In this context nuclei with diffuse neutron skins, i.e. low-density diffuse surfaces, shall be more easily accessible. The impact of strong neutron excess on low-lying excitations will also be investigated in some cases. These new experimental data will certainly permit to better constrain the effective interactions and, consequently, to improve the theoretical models that are applied to neutron stars. However, it is worthwhile to perform some systematic analysis with the presently available models to understand at least qualitatively which phenomena should be expected by increasing the isospin asymmetry.

On the microscopic modeling side, the implementation of microscopic models in astrophysics is a challenge. First, effective interactions have not yet been validated in very asymmetric systems and the isospin dependence of the interaction is of crucial importance to properly describe neutron star properties. Ferromagnetic instabilities, surface-peaked effective masses, low-density two-body correlations, closer link with ab-initio approaches are typical features that shall be included in modern energy density functionals for nuclei and astrophysics. The pairing interaction, which in principle should be derived from the bare potential, is also under debate and the role played by the isospin asymmetry is better understood. Furthermore, a proper theoretical description of the lattice present in the crust should rely on an extension of the Wigner-Seitz approximation and shall go towards a modeling closer to band theory, as well as to include in a better way the statistical distribution of clusters at finite temperature. Effects of finite range interactions, and of relativistic microscopic models, shall be investigated in the future. As a consequence, an extensive work both theoretical and experimental is demanded to better set a suitable theoretical model and to constrain a density functional that could reliably describe both types of nuclear systems.

On the astrophysical side, core-collapse supernovae is impacted by nuclear phenomenons such as the temperature dependence of the effective mass, see chapter 4. The role of pairing, and the interplay with electron capture is still under-debate and shall be investigated in the near future. In the crust of neutron stars, the properties of pairing have revealed interesting features in the models employed such as BCS and HFB. It offers a better understanding of the application of these theories in non-uniform matter and give qualitative differences in the microscopic inputs for global astrophysical modeling. More than one critical temperature for instance can appear, and phenomenons such as persistence, disappearance and reentrance of pairing have been predicted to be strongly related to continuum coupling. The EoS of dense matter is also largely impacted by the density dependence of the symmetry energy, see chapter 6, as well as phase transitions to hyperonic matter, or strange quark matter.

In conclusion, there are a lot of studies for the near future that are interesting for both improving the understanding of the many-body approach in nuclei, and applying the new models, correctly adapted, for dense matter in compact stars and supernovae. Among these studies, I plan to concentrate my efforts in the following subjects.

A simple and unified energy density functional

In the near future, I plan to further investigate the different extensions proposed for the Skyrme interaction in the spin channel and including a surface-peaked effective mass, as well as non-empirical isovector and isoscalar density-dependent pairing interactions. A modification of the isospin degree of freedom in the same approach as the one performed in the spin channel shall also be included. Unifying these extensions and including the tensor force, all fitted in uniformed matter and in finite nuclei, a new mean field model, stable at high density and isospin asymmetry, will be available for wide applications in astrophysics, going from electron capture towards neutrinos propagation in dense matter, including of course EoS and superfluid properties. This model will have the advantage i) to be easily implemented in most of the present codes, ii) to propose a coherent set of microscopic inputs necessary for neutron stars and supernovae derived uniquely from the same model. The model shall also be extended beyond saturation density to include new degrees of freedom such as the onset of hyperons.

A statistical description of dilute nuclear matter

It has recently been understood that the statistical ensembles for describing dilute nuclear matter could not be equivalent (Gulminelli and Raduta, 2012). In stellar matter, nuclear clustering is predicted at almost all values of temperature, density, and proton fraction and thermodynamical quantities continuously change at the phase transition. This specific situation of stellar matter with respect to ordinary nuclear matter has been shown to be due to Coulomb frustration which quenches the first-order phase transition. Dilute nuclear matter is indeed not forming separate phases which are either made of dense nuclei on one side, and a gas at very low density on another side as expected in a first-order phase transition. It is instead made of nuclear clusters of various masses cohabiting together with neutrons and protons. The thermodynamic consequences of this specific thermodynamics with long-range interactions have been addressed to the first time only very recently (Gulminelli and Raduta, 2012). A marked difference between the usual description of phase transition based on the idea of phase coexistence (1st-order) and phase mixing exists from both the theoretical view and the physical properties of the system undergoing these phase transitions.

In order to have analytical results, the first statistical model were based on a schematic nuclear energy functional and the EoS obtained was already qualitatively very promising (Gulminelli and Raduta, 2012). It is clear that more sophisticated energy functionals will have to be implemented in order to have quantitative predictions for the supernova simulations. This project is supported by the ANR SN2NS that have started in 2011, providing a two year post-doctoral position that was attributed to Panagiota Papakonstantinou. An

active collaboration with Francesca Gulminelli has started and we are first improving the simple density functional model for nuclei in a dense medium, guided by a microscopic HFB model for non-uniform matter (see section 5 for instance). The statistical distribution of nuclei in core-collapse supernova will also be convoluted with the microscopic calculation of electron capture for each cluster performed by Elias Khan.

Phase transitions in dense matter, such as the onset of hyperons, or more academically, of a ferromagnetic phase, shall also be reexamined within the idea of phase mixing rather than phase coexistence. The phase transitions in dense matter will also be studied in a second step of this project.

An effective field model combined with a relativistic mean field model

The relativistic models have also recently reached a new step, including the Fock terms within density-dependent coupling constant. In these models, the pion is included and the tensor interaction is mediated by both the pion and the rho mesons. The spin-orbit interaction is also naturally given by the relativistic framework. The advantage of the relativistic approach is that used in an ab-initio approach, such as the DBHF, it can almost give the correct saturation point. The relativistic framework treats naturally processes including antiparticles that are simulated by the three-body interaction in non-relativistic approaches. A link between the relativistic nucleon-nucleon bare potential and the in-medium nuclear interaction based on a relativistic meson exchange model might be realized in the future, and it would provide a unified description of the nuclear interaction.

The relativistic approach, by describing the different channels of the nuclear interaction in terms of mesons exchange, offers moreover a natural framework to include the strange-quark sector, which includes new hadrons like Hyperons (Y) in the baryonic sector as well as new mesons (such as the ϕ). The number of experimental constraints in the strange-quark sector is however quite limited. The phase shift analysis in the YN channel suffers from the number of data points that is 10 times less than in the NN sector, and the YY interaction is yet unconstrained by scattering datas. The limiting number of experimental constraints in the strange sector can be compensated by an universal approach which could be applied to describe the scatterings datas, as well as hypernuclei, where some nucleons in nuclei are replaced by some hyperons, but also relativistic heavy-ion collisions and neutron stars.

During the recent years, much efforts went also into the fundamental understanding of the bare nuclear interaction, either through the development of effective field theories derived from QCD symmetries (Machleidt and Entem, 2011), or through renormalisation group arguments applied to the Lippmann-Schwinger equation which generate a phase-equivalent low energy bare interaction named $v_{\mathrm{low}-k}$ (Bogner et al., 2003). These theories aim at a separation of the long-range component of the nuclear forces dominated by the pion exchange, which is well under control, from the intermediate and short range components, which are dominated by correlated pion and heavy meson exchanges that are poorly known.

From a general point of view, the recent advances in Effective Fields Theories, partially based on mesons exchange theory, and introducing the concept of energy scales from a theoretical side, offer a new avenue for modeling nuclear interaction. Due to all the advantages that the relativistic approach offers, there is a timely opportunity to associate EFT and relativistic mean field approach that could establish a bridge between low-energy QCD and nuclei, encompassing scattering datas, few-body physics, and phase transition in neutron stars.

Appendix A

Thermodynamic properties of bulk nuclear matter

In this chapter, we define the quantities that are used in nuclei and in nuclear matter.

The density matrix could indeed be decomposed as,

$$\begin{aligned}\rho(ij) &= \frac{1}{4}\rho_0(ij)\delta_{\sigma_i\sigma_j}\delta_{\tau_i\tau_j} + \frac{1}{4}\rho_1(ij)\delta_{\sigma_i\sigma_j}\langle\tau_i|\tau|\tau_j\rangle + \frac{1}{4}s_0(ij)\langle\sigma_i|\sigma|\sigma_j\rangle\delta_{\tau_i\tau_j} \\ &\quad + \frac{1}{4}s_1(ij)\langle\sigma_i|\sigma|\sigma_j\rangle\langle\tau_i|\tau|\tau_j\rangle, \end{aligned} \tag{A.1}$$

where σ and τ are the Pauli matrices for the spin and isospin.

The even-density, even kinetic density and even spin-orbit current are defined as ($q = n, p$),

$$\rho_q(\mathbf{r}) = \sum_{\alpha,s} n_{\alpha,q}|\phi_{\alpha,q}(\mathbf{r},s)|^2, \tag{A.2}$$

$$\tau_q(\mathbf{r}) = \sum_{\alpha,s} n_{\alpha,q}|\nabla\phi_{\alpha,q}(\mathbf{r},s)|^2, \tag{A.3}$$

$$\mathbf{J}_q(\mathbf{r}) = \sum_{\alpha,s,s'} n_{\alpha,q}\phi^*_{\alpha,q}(\mathbf{r},s)\nabla\phi_{\alpha,q}(\mathbf{r},s)\langle s'|\sigma|s\rangle, \tag{A.4}$$

where $n_{\alpha,q}$ represent the occupation number of the state (α, q). We have $\rho = \rho_n + \rho_p$, $\tau = \tau_n + \tau_p$ and $\mathbf{J} = \mathbf{J}_n + \mathbf{J}_p$.

For odd systems, the odd-density, the odd kinetic density and the odd spin-orbit current are defined as,

$$s_q(\mathbf{r}) = \sum_{s,s'} \rho_q(\mathbf{r},s;\mathbf{r},s')\langle s|\sigma|s'\rangle, \tag{A.5}$$

$$T_q(\mathbf{r}) = \sum_{s,s'} \nabla\nabla'\rho_q(\mathbf{r},s;\mathbf{r}',s')\langle s|\sigma|s'\rangle|_{\mathbf{r}=\mathbf{r}'}, \tag{A.6}$$

$$j_q(\mathbf{r}) = -\frac{i}{2}\sum_{s}(\nabla-\nabla')\rho_q(\mathbf{r},s;\mathbf{r}',s')|_{\mathbf{r}=\mathbf{r}'}. \tag{A.7}$$

In the uniform-density case, it becomes,

$$n_q = \frac{g}{2\pi^2}\int_0^\infty dk\ k^2 f_q(k), \tag{A.8}$$

$$\tau_q = \frac{g}{2\pi^2}\int_0^\infty dk\ k^4 f_q(k). \tag{A.9}$$

Introducing the density of states $\rho(e) = de(k)/dk^3$, these quantities become

$$n_q = \int \frac{de}{(2\pi)^3}\, \rho_t(e) f(x, e/T), \tag{A.10}$$

$$\tau_q = \int \frac{de}{(2\pi)^3}\, \rho_t(e) k^2 f(x, e/T). \tag{A.11}$$

A.1 Non-relativistic Fermi gas

For a non-relativistic Fermi gas, we have $e(k) = \hbar^2 k^2/(2m) + u$, where u is the mean field. Therefore, the density of state $\rho_{NR}(e)$ is defined as

$$\rho_{NR}(e) = g4\pi\sqrt{2}\frac{m^{3/2}}{\hbar^3}\sqrt{e-u}, \tag{A.12}$$

where g is the degeneracy of a state with momentum k. For an electron gas, it represent the spin degeneracy and $g = 2$.

The non-relativistic and the relativistic densities are defined as

$$n_t^{NR} = \frac{g}{4\pi^2}\lambda_{th,t}^{-3} F_{1/2}(\eta_t), \tag{A.13}$$

$$\tau_t^{NR} = \frac{g}{4\pi^2}\lambda_{th,t}^{-5} F_{3/2}(\eta_t), \tag{A.14}$$

where $\eta_t = (u_t - \mu_t)/T$. The Fermi integrals $F_{1/2}$ and $F_{3/2}$ are defined in Appendix B and the thermal de Broglie wavelength $\lambda_{th,t}$ is defined for a non-relativistic free ideal gas of massive particle in equilibrium as

$$\lambda_{th,t} = \frac{\hbar}{\sqrt{2m_t T}}. \tag{A.15}$$

The thermal de Broglie wavelength is roughly the average de Broglie wavelength, $\lambda = h/p$ where p is the impulsion of the particle, of a classical and non-relativistic free ideal gas with average energy $E \sim \pi T$.

The thermal wave-length defines the transition from the classical limit to the quantum one's. When the thermal de Broglie wavelength is much smaller than the inter-particle distance, the gas can be considered to be a classical or Maxwell-Boltzmann gas. One the other hand, when the thermal de Broglie wavelength is on the order or larger than the inter-particle distance, quantum effects will dominate and the gas must be treated as a Fermi gas. Notice that the same criterium applies also for the Bose gas. The Fermi temperature $T_F = \epsilon_F$ is also used as a order parameter, and it can be shown that the ratio $T_F/T \sim 3(\lambda_{th,t}/d)^2$, where $d = n^{-1/3}$ is the average inter-particle distance.

At zero temperature, we obtain

$$n_t = \frac{g_t}{6\pi^2}k_{Ft}^3, \tag{A.16}$$

$$\tau_t = \frac{3}{5}n_t k_{Ft}^2 = \frac{3}{5}\left(\frac{6\pi^2}{g_t}\right)^{2/3} n_t^{5/3}. \tag{A.17}$$

The development at low temperature gives

$$n_t = \frac{g}{4\pi^2}\lambda_{th,t}^{-3}\beta^{3/2}\mu^{3/2}\big(1 + \frac{(\pi T)^2}{8\mu^2} + ...\big). \tag{A.18}$$

If the density is fixed independently of the temperature, this equation is used to extract the T-dependence of the chemical potential,

$$\mu(T) = \mu(0)\big(1 - \frac{1}{12}\left(\frac{\pi T}{\mu(0)}\right)^2 + ...\big). \tag{A.19}$$

and we get

$$\tau(T) = \tau(0)\big(1 + \frac{5}{12}\left(\frac{\pi T}{\mu(0)}\right)^2 + ...\big). \tag{A.20}$$

In bulk nuclear matter, the entropy density s_t is given by

$$s_t = -\sum_\alpha [n_{\alpha,t} \ln n_{\alpha,t} + (1 - n_{\alpha,t}) \ln(1 - n_{\alpha,t})], \tag{A.21}$$

which for uniform matter can be manipulated upon integration by parts into the particularly simple form

$$s_t = \frac{5}{3}\lambda_{th,t}^2 \tau_t + \beta n_t (u_t - \mu_t). \tag{A.22}$$

The pressure P of the matter is found from the thermodynamical relationship

$$P = -e_{nucl} + \sum_{t=n,p} (T s_t + \mu_t n_t). \tag{A.23}$$

A.2 Relativistic Fermi gas

For a relativistic gas, we have $e(k) = \sqrt{m^2 + k^2} + \Sigma_0$

$$N_R(e) = g 4\pi e \sqrt{(e - \Sigma_0)^2 - m^2}, \tag{A.24}$$

A.3 Incompressibility and symmetry energy

The compressibility χ is usually defined by

$$\chi = -\frac{1}{V}\frac{\partial V}{\partial P} = \frac{1}{\rho}\left(\frac{\partial P}{\partial \rho}\right)^{-1}, \tag{A.25}$$

and the pressure is related to the energy density ϵ by

$$P = -\frac{\partial E}{\partial V} = \rho^2 \frac{\partial E/A}{\partial \rho} = \rho \frac{\partial \epsilon}{\partial \rho} - \epsilon = \rho\mu - \epsilon. \tag{A.26}$$

The chemical potential is defined by

$$\mu = \frac{\partial E}{\partial A} = \frac{\partial \epsilon}{\partial \rho}. \tag{A.27}$$

From Eqs. (A.25) and (A.26), we obtain

$$\frac{1}{\chi} = \rho^2 \frac{\partial^2 \epsilon}{\partial \rho^2}. \tag{A.28}$$

The compressibility $\chi(\rho)$ is a function of the density ρ and the asymmetry parameter δ. Furthermore one defines the incompressibility at the saturation density in symmetric nuclear matter by

$$K_\infty = k_F^2 \frac{\partial^2 E/A}{\partial k_F^2}\bigg|_{k_{F\infty}} = 9\rho_0^2 \frac{\partial^2 E/A}{\partial \rho^2}\bigg|_{\rho_0}. \tag{A.29}$$

The relation between K_∞ and χ is given by

$$K_\infty = \frac{9}{\rho_0 \chi(\rho_0)}. \tag{A.30}$$

It is worth keeping in mind that the incompressibility K_∞ is defined only at the saturation density ρ_0, and in particular the relation (A.30) is valid only for $\rho = \rho_0$. Indeed, more generally, we can define the density-dependent incompressibility (or bulk modulus) as (Fetter and Walecka, 1971)

$$K(\rho) = \frac{9}{\rho\chi} = 9\rho^2 \frac{\partial^2 E/A}{\partial \rho^2} + \frac{18}{\rho} P \tag{A.31}$$

which coincides with the incompressibility K_∞ at the saturation density.

The symmetry energy $S(\rho)$ is defined by

$$S(\rho) = \frac{1}{2}\frac{\partial^2 \epsilon/\rho}{\partial \delta^2}\bigg|_{\delta=0}. \tag{A.32}$$

The symmetry energy can be expanded, around the saturation density, as

$$S(\rho) = J + L\left(\frac{\rho-\rho_0}{3\rho_0}\right) + \frac{1}{2}K_{\rm sym}\delta^2\left(\frac{\rho-\rho_0}{3\rho_0}\right)^2, \tag{A.33}$$

where J is defined by $J = S(\rho_0)$, $L = \frac{3}{\rho_0}\frac{\partial S}{\partial \rho}|_{\rho_0}$, and $K_{\rm sym} = \frac{9}{\rho_0^2}\frac{\partial^2 S}{\partial \rho^2}|_{\rho_0}$.

Appendix B

Fermi functions and integrals

In this chapter, we give detailed expressions for the Fermi function and the Fermi integrals that are used in thermal Fermi systems.

B.1 Fermi function

The Fermi function is defined as,

$$f_t(k) = \frac{1}{1+\exp[\beta(\epsilon_{k,t}-\mu_t)]}, \tag{B.1}$$

$$f_t(x,y) = \frac{1}{1+\exp[y-x]}, \tag{B.2}$$

where $y=\epsilon_{k,t}/T$, $x=\mu_t/T$ with the energy of the quasi-particle $\epsilon_{k,t}$, the chemical potential μ_t and the temperature $T=1/\beta$. We have the following limits, for constant x:

$$\lim_{y\to-\infty} f(x,y) = 1, \tag{B.3}$$

$$\lim_{y\to+\infty} f(x,y) = 0. \tag{B.4}$$

B.2 Complete and incomplete Fermi integrals

The complete and incomplete Fermi integrals $F_n(x)$ and $I_n(x,a)$ of order n (integer or half integer) are defined as,

$$F_n(x) = \int_0^\infty du\ u^n/[1+\exp(u-x)], \tag{B.5}$$

$$I_n(x,a) = \int_a^\infty du\ u^n/[1+\exp(u-x)]. \tag{B.6}$$

We have the following properties:

$$F_0(x) = \ln(1+\exp x), \tag{B.7}$$

$$I_n(x,0) = F_n(x), \tag{B.8}$$

$$I_0(x,a) = F_0(x-a), \tag{B.9}$$

$$I_1(x,a) = F_1(x-a) - aF_0(x-a), \tag{B.10}$$

$$I_n(x,a) = \sum_{k=0}^{n} c_n^k a^{n-k} F_k(x-a). \tag{B.11}$$

where the binomial formula have been used, $(x+y)^n = \sum_{k=0}^{n} c_n^k x^{n-k} y^k$ with the binomial coefficients $c_n^k = n!/(k!(n-k)!)$.

The Fermi functions $F_n(x)$ have been fitted over the whole range of argument x and given in Buchler and Coon ApJ 212 807 (1977).

A numerical calculation can also be performed once for all and stored in the data file and in practice, read this data file and use an interpolation routine.

B.3 Low temperature expansion of the Fermi integral

We explore the low temperature expansion of the Fermi integral. In practice, this limit is defined if $x > 30$.

The low temperature Fermi integral is developed around the zero temperature limit,

$$\delta F_n(x) = F_n(x) - \int_0^{u_0} du\ u^n = \int_0^{\infty} du\ u^n g(u,x), \tag{B.12}$$

where $u_0 = \mu/T$ and the function g is defined as $g(u,x) = f(u,x) - 1$ if $u < u_0$ and $g(u,x) = f(u,x)$ otherwise. The function $g(u,x)$ is symmetric in u with respect to u_0. setting $y = u - x$, and after some work on the integrals, it is shown that

$$\delta F_n(x) = \int_0^{\infty} dy\ \frac{1}{1+\exp y}\big((x+y)^n - (x-y)^n\big). \tag{B.13}$$

and developing $(x \pm y)^n$ around x, we obtain

$$\delta F_n(x) = 2nx \int_0^{\infty} dy\ \frac{y^{n-1}}{1+\exp y} + \frac{n(n-1)(n-2)}{3} x^2 \int_0^{\infty} dy\ \frac{y^{n-3}}{1+\exp y} + ... \tag{B.14}$$

Bibliography

Abadie, J., Abbott, B. P., Abbott, R., Abbott, T. D., Abernathy, M., Accadia, T., Acernese, F., and Others: 2012, *Physical Review D* **022001**, 022001

Abadie, J., Abbott, B. P., Abbott, R., Abernathy, M., Accadia, T., Acernese, F., and Others: 2010, *Physical Review D* **82**, 102001

Agrawal, B. K., Shlomo, S., and Kim Au, V.: 2003, *Physical Review C* **68**, 031304(R)

Akmal, A., Pandharipande, V. R., and Ravenhall, D. G.: 1998, *Physical Review C* **58**, 1804

Ambartsumyan, V. A.: 1966, *Transactions of the International Astronomical Union* **12B**, 578

Ambartsumyan, V. A. and Saakyan, G. S.: 1961, *Astronomicheskii Zhurnal* **38**, 1016

Anantaraman, N., Toki, H., and Bertsch, G. F.: 1983, *Nuclear Physics A* **398**, 269

Anderson, P. W. and Itoh, N.: 1975, *Nature* **256**, 25

Arnett: 1968a, *Nature* **219**, 1344

Arnett, W. D.: 1968b, *The Astrophysical Journal* **153**, 341

Ashcroft, N. W. and Mermin, N. D.: 1976, *Solid State Physics*, Saunders College Publishing

Avancini, S., Brito, L., Marinelli, J., Menezes, D., de Moraes, M., Providência, C., and Santos, A.: 2009, *Physical Review C* **79**, 035804

Avancini, S., Menezes, D., Alloy, M., Marinelli, J., Moraes, M., and Providência, C.: 2008, *Physical Review C* **78**, 015802

Avez, B. and Simenel, C.: 2008, *Physical Review C* **044318**, 1

Baade, W. and Zwicky, F.: 1934, *Physical Review* **45**, 76

Baldo, M.: 1999, in M. Baldo (ed.), *Nuclear Methods and the Nuclear Equation of State, International Review of Nuclear Physics - Vol. 8*, World Scientific, Singapore

Baldo, M. and Ferreira, L. S.: 1988, *Nuclear Physics A* **480**, 271

Baldo, M., Lombardo, U., Pankratov, S. S., and Saperstein, E. E.: 2010, *Journal of Physics G: Nuclear and Particle Physics* **37**, 064016

Baldo, M., Lombardo, U., Saperstein, E. E., and Tolokonnikov, S. V.: 2004a, *JETP letters* **80(8)**, 523

Baldo, M., Lombardo, U., Saperstein, E. E., and Tolokonnikov, S. V.: 2005a, *Nuclear Physics A* **750**, 409

Baldo, M., Lombardo, U., and Schuck, P.: 1995, *Physical Review C* **52**, 975

Baldo, M. and Maieron, C.: 2007, *Journal of Physics G: Nuclear and Particle Physics* **34**, R243

Baldo, M., Maieron, C., Schuck, P., and Viñas, X.: 2004b, *Nuclear Physics A* **736**, 241

Baldo, M., Saperstein, E. E., and Tolokonnikov, S. V.: 2005b, *Nuclear Physics A* **749**, 42c

Baldo, M., Saperstein, E. E., and Tolokonnikov, S. V.: 2006, *Nuclear Physics A* **775**, 235

Baldo, M., Saperstein, E. E., and Tolokonnikov, S. V.: 2007, *European Physical Journal A* **32(1)**, 97

Baldo, M., Schuck, P., and Viñas, X.: 2008, *Physics Letters B* **663**, 390

Balian, R., Flocard, H., and Veneroni, M.: 1999, *Physics Reports* **317**, 251

Baran, V., Colonna, M., Di Toro, M., and Greco, V.: 2001, *Physical Review Letters* **86**, 4492

Baran, V. and Margueron, J.: 2006, *The European Physical Journal A* **30**, 317

Bardeen, J., Cooper, L. N., and Schrieffer, J. R.: 1957, *Physical Review* **108**, 1175

Baron, E., Bethe, H. A., Brown, G. E., Cooperstein, J., and Kahana, S.: 1987, *Physical Review Letters* **59**, 736

Baron, E. and Cooperstein, J.: 1990, *The Astrophysical Journal* **353**, 597

Barranco, F., Broglia, R. A., Esbensen, H., and Vigezzi, E.: 1998, *Physical Review C* **58**, 1257

Baym, G., Bethe, H. A., and Pethick, C. J.: 1971, *Nuclear Physics A* **175**, 225

Becker, W. and Pavlov, G.: 2001, in *The century of space science*, No. January, Kluwer Academic Publishers

Bejger, M., Gondek-Rosiska, D., Gourgoulhon, E., Haensel, P., Taniguchi, K., and Zdunik, J. L.: 2005, *Astronomy & Astrophysics* **431**, 297

Bell Burnell, S. J.: 2004, *Science (New York, N.Y.)* **304(5670)**, 489

Bender, M., Heenen, P.-H., and Reinhard, P.-G.: 2003, *Reviews of Modern Physics* **75**, 121

Benhar, O. and Farina, N.: 2009, *Physics Letters B* **680**, 305

Bernard, V. and Van Giai, N.: 1979, *Nuclear Physics A* **327**, 397

Bertsch, G. F., Bertulani, C. A., Nazarewicz, W., Schunck, N., and Stoitsov, M. V.: 2009, *Physical Review C* **79**, 034306

Bertsch, G. F., Borysowicz, J., McManus, H., and Love, W. G.: 1977, *Nuclear Physics A* **284**, 399

Bertsch, G. F. and Esbensen, H.: 1991, *Annals of Physics* **209**, 327

Bertsch, G. F. and Kuo, T. T. S.: 1968, *Nuclear Physics A* **112**, 204

Bertulani, C. A., Liu, H., and Sagawa, H.: 2012, *Physical Review C* **85**, 014321

Bertulani, C. A., Lü, H. F., and Sagawa, H.: 2009, *Physical Review C* **80**, 027303

Bethe, H. A.: 1990, *Reviews of Modern Physics* **62**, 801

Bethe, H. A., Brown, G. E., Applegate, J., and Lattimer, J. M.: 1979, *Nuclear Physics A* **324**, 487

Bethe, H. A., Brown, G. E., Cooperstein, J., and Wilson, J. R.: 1983, *Nuclear Physics A* **403**, 625

Beyer, M., Sofianos, S. A., Kuhrts, C., Röpke, G., and Schuck, P.: 2000, *Physics Letters B* **488**, 247

Bhattacharya, D. and Soni, V.: 2007, *A Natural Explanation for Magnetars*, Technical report

Blaizot, J.-P.: 1980, *Physics Reports* **64(4)**, 171

Blondin, J. M., Mezzacappa, A., and DeMarino, C.: 2003, *The Astrophysical Journal* **584**, 971

Blottiau, P.: 1989, *Ph.D. thesis*, Université Paris VII, Paris, France

Bogner, S. K., Furnstahl, R. J., Ramanan, S., and Schwenk, A.: 2006, *Nuclear Physics A* **773**, 203

Bogner, S. K., Furnstahl, R. J., Ramanan, S., and Schwenk, A.: 2007, *Nuclear Physics A* **784**, 79

Bogner, S. K., Kuo, T. T. S., and Coraggio, L.: 2001, *Nuclear Physics A* **684**, 432c

Bogner, S. K., Kuo, T. T. S., and Schwenk, A.: 2003, *Physics Reports* **386**, 1

Bohigas, O., Lane, A. M., and Mortorell, J.: 1979, *Physics Reports* **51**, 267

Bohr, A. and Mottelson, B. R.: 1998, *Nuclear Structure vol. II*, World Scientific

Bombaci, I., Polls, A., Ramos, A., Rios, A., and Vidaña, I.: 2006, *Physics Letters B* **632**, 638

Bonazzola, S. and Gourgoulhon, E.: 1999, in *Experimental Physics of Gravitational waves*, World Scientific

Bonche, P. and Vautherin, D.: 1981, *Nuclear Physics A* **372**, 496

Bortignon, P. F. and Dasso, C. H.: 1987, *Physics Letters B* **189**, 381

Borzov, I. N.: 2006, *Nuclear Physics A* **777**, 645

Boek, P., Dean, D. J., and Müther, H.: 2006, *Physical Review C* **74**, 014303

Boek, P., Margueron, J., and Müther, H.: 2005, *Annals of Physics* **318**, 245

Brockmann, R. and Machleidt, R.: 1990, *Physical Review C* **42**, 1965

Broglia, R. A., De Blasio F., Lazzari, G., Lazzari, M., and Pizzochero, P. A. M.: 1994, *Physical Review D* **50**, 4781

Broglia, R. A., Hansen, O., and Riedel, C.: 1973, *Advances in Nuclear Physics* **6**, 287

Brown, B. A.: 2000, *Physical Review Letters* **85**, 5296
Brown, E. F. and Cumming, A.: 2009, *The Astrophysical Journal* **698(2)**, 1020
Brown, G. E., Dehesa, J. S., and Speth, J.: 1979, *Nuclear Physics A* **330**, 290
Brown, G. E. and Gunn, J. H.: 1963, *Nuclear Physics* **46**, 598
Brown, G. E., Kubodera, K., Page, D., and Pizzochero, P. A. M.: 1988, *Physical Review D* **37**, 2042
Bruenn, S. W.: 1985, *The Astrophysical Journal* **58**, 771
Bruenn, S. W., De Nisco, K. R., and Mezzacappa, A.: 2001, *The Astrophysical Journal* **560**, 326
Bulgac, A.: 1980, *preprint No. FT-194-1980, Institute of Atomic Physics, Bucharest* pp 1–11
Buras, R., Janka, H.-T., and Rampp, M.: 2006a, *Astronomy & Astrophysics* **457**, 281
Buras, R., Rampp, M., Janka, H.-T., and Kifonidis, K.: 2003, *Physical Review Letters* **90**, 241101
Buras, R., Rampp, M., Janka, H.-T., and Kifonidis, K.: 2006b, *Astronomy & Astrophysics* **447**, 1049
Burrows, A.: 1988, *The Astrophysical Journal* **334**, 891
Burrows, A., Dessart, L., Livne, E., Ott, C. D., and Murphy, J.: 2007, *The Astrophysical Journal* **664**, 416
Burrows, A., Hayes, J., and Fryxell, B. A.: 1995, *The Astrophysical Journal* **450**, 830
Burrows, A. and Lattimer, J. M.: 1986, *The Astrophysical Journal* **307**, 178
Burrows, A., Livne, E., Dessart, L., Ott, C. D., and Murphy, J.: 2006, *New Astronomy Reviews* **50**, 487
Cackett, E. M., Wijnands, R., Linares, M., Miller, J. M., Homan, J., and Lewin, W. H. G.: 2006, *Monthly Notices of the Royal Astronomical Society* **372**, 479
Cao, L.-G., Lombardo, U., and Schuck, P.: 2006a, *Physical Review C* **74**, 64301
Cao, L.-G., Lombardo, U., Shen, C. W., and Van Giai, N.: 2006b, *Physical Review C* **73(1)**, 14313
Carlson, J., Chang, S.-Y., Pandharipande, V. R., and Schmidt, K. E.: 2003, *Physical review letters* **91**, 50401
Carter, B., Chamel, N., and Haensel, P.: 2005, *Nuclear Physics A* **748**, 675
Castorina, P., Grasso, M., Oertel, M., Urban, M., and Zappalà, D.: 2005, *Physical Review A* **72**, 025601
Centelles, M., Roca-Maza, X., Viñas, X., and Warda, M.: 2009, *Physical Review Letters* **102**, 122502
Chabanat, E., Bonche, P., Haensel, P., Meyer, J., and Schaeffer, R.: 1997, *Nuclear Physics A* **627**, 710
Chabanat, E., Bonche, P., Haensel, P., Meyer, J., and Schaeffer, R.: 1998a, *Nuclear Physics A* **635**, 231
Chabanat, E., Bonche, P., Haensel, P., Meyer, J., and Schaeffer, R.: 1998b, *Nuclear Physics A* **643**, 441
Chamel, N.: 2005, *Nuclear Physics A* **747**, 109
Chamel, N.: 2006, *Nuclear Physics A* **773**, 263
Chamel, N.: 2010, *Physical Review C* **82**, 014313
Chamel, N. and Goriely, S.: 2010, *Physical Review C* **82**, 045804
Chamel, N., Goriely, S., and Pearson, J. M.: 2008, *Nuclear Physics A* **812**, 72
Chamel, N., Goriely, S., and Pearson, J. M.: 2009a, *Physical Review C* **80**, 065804
Chamel, N., Goriely, S., Pearson, J. M., and Onsi, M.: 2010, *Physical Review C* **81**, 045804
Chamel, N., Margueron, J., and Khan, E.: 2009b, *Physical Review C* **79**, 012801(R)
Chamel, N., Naimi, S., Khan, E., and Margueron, J.: 2007, *Physical Review C* **75**, 55806
Chen, L.-w., Ko, C. M., and Li, B.-a.: 2007, *Physical Review C* **76**, 054316
Chiu, H.-y. and Salpeter, E. E.: 1964, *Physical Review Letters* **12**, 413
Chomaz, P.: 2003, *Comptes Rendus Physique* **4**, 419
Chomaz, P., Colonna, M., and Randrup, J.: 2004, *Physics Reports* **389**, 263
Civitarese, O., Dumrauf, A. G., Reboiro, M., Ring, P., and Sharma, M. M.: 1991, *Physical Review C* **43**, 2622
Colgate, S. A. and White, R. H.: 1966, *The Astrophysical Journal* **143**, 626
Colò, G., Van Giai, N., Meyer, J., Bennaceur, K., and Bonche, P.: 2004, *Physical Review C* **70**, 024307
Corradi, L., Pollarolo, G., and Szilner, S.: 2009, *Journal of Physics G: Nuclear and Particle Physics* **36**, 1

Crowell, P. A. and Reppy, J. D.: 1993, *Physical Review Letters* **70**, 3291

Csáthy, G. A., Kim, E., and Chan, M. H. W.: 2002, *Physical Review Letters* **88**, 045301

Danielewicz, P.: 2003, *Nuclear Physics A* **727**, 233

Danielewicz, P. and Lee, J.: 2009, *Nuclear Physics A* **818**, 36

De Gennes, P. G.: 1989, *Superconductivity of metals and alloys*, Addison-Wesley

De Jong, F. and Lenske, H.: 1998, *Physical Review C* **57(6)**, 3099

Dean, D. J. and Hjorth-Jensen, M.: 2003, *Reviews of Modern Physics* **75**, 607

Dean, D. J., Langanke, K., Nam, H., and Nazarewicz, W.: 2010, *Physical Review Letters* **105**, 212504

Dean, D. J., Langanke, K., and Sampaio, J.: 2002, *Physical Review C* **66(4)**, 1

Demorest, P. B., Pennucci, T., Ransom, S. M., Roberts, M. S. E., and Hessels, J. W. T.: 2010, *Nature* **467(7319)**, 1081

Di Gallo, L., Oertel, M., and Urban, M.: 2011, *Physical Review C* **84**, 045801

Dickhoff, W. H. and Barbieri, C.: 2004, *Progress in Particle and Nuclear Physics* **52**, 377

Dickhoff, W. H. and Van Neck, D.: 2005, *Many-Body Theory Exposed!*, World Scientific, Singapore

Dobaczewski, J. and Dudek, J.: 1995, *Physical Review C* **52**, 1827

Dobaczewski, J., Flocard, H., and Treiner, J.: 1984, *Nuclear Physics A* **422**, 103

Dobaczewski, J., Nazarewicz, W., and Reinhard, P.-G.: 2001, *Nuclear Physics A* **693**, 361

Donati, P. and Pizzochero, P. A. M.: 2004, *Nuclear Physics A* **742**, 363

Donati, P. and Pizzochero, P. A. M.: 2006, *Physics Letters B* **640**, 74

Donati, P., Pizzochero, P. A. M., Bortignon, P. F., and Broglia, R. A.: 1994, *Physical Review Letters* **72**, 2835

Douchin, F. and Haensel, P.: 2001, *Astronomy and Astrophysics* **380**, 151

Dover, C. B. and Van Giai, N.: 1972, *Nuclear Physics* **190**, 373

Ducoin, C., Margueron, J., and Chomaz, P.: 2008, *Nuclear Physics A* **809**, 30

Ducoin, C., Margueron, J., and Providência, C.: 2010, *Europhysics Letters* **91(3)**, 32001

Ducoin, C., Margueron, J., Providência, C., and Vidaña, I.: 2011, *Physical Review C* **83(4)**, 045810

Duguet, T.: 2004, *Physical Review C* **69**, 054317

Duguet, T., Bonche, P., Heenen, P.-H., and Meyer, J.: 2001a, *Physical Review C* **65**, 014310

Duguet, T., Bonche, P., Heenen, P.-H., and Meyer, J.: 2001b, *Physical Review C* **65**, 014311

Engelbrecht, J. R., Randeria, M., and Sa de Melo, C. A. R.: 1997, *Physical Review B* **55**, 15153

Entem, D. R. and Machleidt, R.: 2003, *Physical Review C* **68**, 041001(R)

Esbensen, H., Bertsch, G. F., and Hencken, K.: 1997, *Physical Review C* **56**, 3054

Fabrocini, A., Fantoni, S., Illarionov, A. Y., and Schmidt, K. E.: 2005, *Physical Review Letters* **95**, 192501

Fabrocini, A., Fantoni, S., Illarionov, A. Y., and Schmidt, K. E.: 2008, *Nuclear Physics A* **803**, 137

Famiano, M. A., Liu, T., Lynch, W. G., Mocko, M., Rogers, A. M., Tsang, M. B., Wallace, M. S., Charity, R. J., Komarov, S., Sarantites, D. G., Sobotka, L. G., and Verde, G.: 2006, *Physical Review Letters* **97**, 052701

Fantina, A. F.: 2010, *Ph.D. thesis*, Paris-Sud XI

Fantina, A. F., Blottiau, P., Margueron, J., Mellor, P., and Pizzochero, P. A. M.: 2012, *Astronomy & Astrophysics* **541**, A30

Fantina, A. F., Donati, P., and Pizzochero, P. A. M.: 2009, *Physics Letters B* **676**, 140

Fantina, A. F., Margueron, J., Donati, P., and Pizzochero, P. A. M.: 2011, *Journal of Physics G: Nuclear and Particle Physics* **38(2)**, 025101

Fantoni, S., Sarsa, A., and Schmidt, K. E.: 2001, *Physical Review Letters* **87**, 181101

Farine, M., Pearson, J. M., and Tondeur, F.: 2001, *Nuclear Physics A* **696**, 396

Farine, M. and Schuck, P.: 1999, *Physics Letters B* **459**, 444

Fayans, S. A., Tolokonnikov, S. V., Trykov, E. L., and Zawischa, D.: 2000, *Nuclear Physics A* **676**, 49

Feenberg, E.: 1969, *Theory of Quantum Fluids*, Academic Press, New-York

Fetter, A. L. and Walecka, J. D.: 1971, *Quantum Theory of Many-Particle Systems*, Dover Publications, New-York

Finelli, P., Kaiser, N., Vretenar, D., and Weise, W.: 2003, *The European Physical Journal A - Hadrons and Nuclei* **17**, 573

Finelli, P., Kaiser, N., Vretenar, D., and Weise, W.: 2004, *Nuclear Physics A* **735**, 449

Foglizzo, T.: 2002, *Astronomy & Astrophysics* **368**, 353

Foglizzo, T., Galletti, P., Scheck, L., and Janka, H.-T.: 2007, *The Astrophysical Journal* **654**, 1006

Fortin, M., Grill, F., Margueron, J., Page, D., and Sandulescu, N.: 2010, *Physical Review C* **82**, 065804

Fracasso, S. and Colò, G.: 2007, *Physical Review C* **76**, 044307

Franey, M. A., Bayman, B. F., Lilley, J. S., and Phillips, W. R.: 1978, *Physical Review Letters* **41**, 837

Frossati, G., Bedell, K. S., Wiegers, S. A. J., and Vermeulen, G. A.: 1986, *Physical Review Letters* **57**, 1032

Fuchs, C.: 2004, in *Lectures Notes in Physics "Extended Density Functionals in Nuclear Structure Physics"*, Vol. 146, pp 119–146, Springer

Fuchs, C., Faessler, A., Zabrodin, E., and Zheng, Y.-M.: 2001, *Physical Review Letters* **86(10)**, 1974

Fuchs, C., Wolter, H. H., and Lenske, H.: 1995, *Physical Review C* **52**, 3043

Fuller, G. M.: 1982, *The Astrophysical Journal* **252**, 741

Fuller, G. M., Fowler, W. A., and Newman, M. J.: 1980, *The Astrophysical Journal Supplement Series* **42**, 447

Fuller, G. M., Fowler, W. A., and Newman, M. J.: 1982, *The Astrophysical Journal Supplement Series* **48**, 279

Fuller, G. M., Fowler, W. A., and Newman, M. J.: 1985, *The Astrophysical Journal* **293**, 1

Furnstahl, R. J.: 2004, in G. A. Lalazissis, P. Ring, and D. Vretenar (eds.), *Lectures Notes in Physics "Extended Density Functionals in Nuclear Structure Physics"*, Vol. 29, pp 1–29, Springer

Garcia-Recio, C., Navarro, J. F., Van Giai, N., and Salcedo, L. L.: 1992, *Annals of Physics* **214**, 293

Garrido, E., Sarriguren, P., Moya De Guerra, E., and Schuck, P.: 1999, *Physical Review C* **60**, 064312

Giovanardi, N., Bortignon, P. F., Broglia, R. A., and Huang, W.: 1996, *Physical Review Letters* **77**, 24

Glendenning, N. K.: 2000, *Compact Stars: Nuclear Physics, Particle Physics and General Relativity*, Springer

Gnedin, O. Y., Yakovlev, D. G., and Potekhin, A. Y.: 2001, *Monthly Notices of the Royal Astronomical Society* **324**, 725

Gögelein, P. and Müther, H.: 2007, *Physical Review C* **76**, 024312

Gögelein, P., Van Dalen, E. N. E., Gad, K., Hassaneen, K. S. A., and Müther, H.: 2009, *Physical Review C* **79**, 24308

Gogny, D.: 1975, in G. Ripka and M. Porneuf (eds.), *Proceedings of the international conference on nuclear self-consistent fields*, North Holland, Amsterdam, Triestre

Gold, T.: 1968, *Nature* **218**, 731

Gold, T.: 1969, *Nature* **221**, 25

Goldreich, P. and Weber, S. V.: 1980, *The Astrophysical Journal* **238**, 991

Goodman, A. L.: 1981, *Nuclear Physics A* **352**, 30

Goriely, S., Chamel, N., and Pearson, J. M.: 2009, *Physical Review Letters* **102**, 152503

Goriely, S., Samyn, M., and Pearson, J. M.: 2007, *Physical Review C* **75**, 064312

Goriely, S., Samyn, M., Pearson, J. M., and Onsi, M.: 2005, *Nuclear Physics A* **750**, 425

Gourgoulhon, E.: 2010, in *Lectures at the CompStar 2010 School, GANIL, Caen*, No. September

Gourgoulhon, E. and Haensel, P.: 2003, *Astronomy & Astrophysics* **412**, 777

Grasso, M., Khan, E., Margueron, J., and Van Giai, N.: 2008, *Nuclear Physics A* **807**, 1

Grasso, M., Sandulescu, N., Van Giai, N., and Liotta, R. J.: 2001, *Physical Review C* **64**, 064321

Grill, F., Margueron, J., and Sandulescu, N.: 2011, *Physical Review C* **84**, 065801

Gross-Boelting, T., Fuchs, C., and Faessler, A.: 1999, *Nuclear Physics A* **648(1-2)**, 105

Grygorov, P., Van Dalen, E. N. E., Müther, H., and Margueron, J.: 2010, *Physical Review C* **82**, 014315

Gulminelli, F. and Raduta, A.: 2012, *Physical Review C* **85**, 025803

Haensel, P. and Bonazzola, S.: 1996, *Astronomy and Astrophysics* **314**, 1017

Haensel, P., Potekhin, A. Y., and Yakovlev, D. G.: 2007, *Neutron Stars I*, Vol. 3, Springer

Hagino, K. and Sagawa, H.: 2011, *Physical Review C* **84**, 011303(R)

Hagino, K., Sagawa, H., Carbonell, J., and Schuck, P.: 2007, *Physical Review Letters* **99**, 022506

Hagino, K., Sagawa, H., and Schuck, P.: 2010, *Journal of Physics G: Nuclear and Particle Physics* **37**, 064040

Haidenbauer, J. and Plessas, W.: 1984, *Physical Review C* **30**, 1822

Hanke, F., Marek, A., Müller, B., and Janka, H.-T.: 2011, *The Astrophysical Journal, arXiv:1108.4355v1(astro-ph)*

Harakeh, M. N. and Van der Woude, A.: 2001, *Giant Resonances: Fundamental High-Frequency Modes of Nuclear Excitation*, Oxford Studies in NUclear Physics (New-York: Oxford University Press)

Hasse, R. W. and Schuck, P.: 1986, *Physics Letters B* **179**, 313

Hebeler, K., Duguet, T., Lesinski, T., and Schwenk, A.: 2009, *Physical Review C* **80**, 044321

Heger, A., Langanke, K., Martínez-Pinedo, G., and Woosley, S. E.: 2001, *Physical Review Letters* **86**, 1678

Hernandez, E. S., Navarro, J. F., and Polls, A.: 1997, *Nuclear Physics A* **627**, 460

Hernandez, E. S., Navarro, J. F., and Polls, A.: 1999, *Nuclear Physics A* **658**, 327

Hilaire, S. and Girod, M.: 2007, *The European Physical Journal A* **33**, 237

Hix, W., Messer, O. E. B., Mezzacappa, A., Liebendörfer, M., Sampaio, J., Langanke, K., Dean, D. J., and Martínez-Pinedo, G.: 2003, *Physical Review Letters* **91**, 201102

Hix, W. R., Messer, O. E. B., Mezzacappa, A., Sampaio, J., Langanke, K., Martínez-Pinedo, G., Liebendörfer, M., and Dean, D. J.: 2005, *Nuclear Physics A* **758**, 31

Horowitz, C. J. and Schwenk, A.: 2006a, *Nuclear Physics A* **776**, 55

Horowitz, C. J. and Schwenk, A.: 2006b, *Physics Letters B* **638**, 153

Igarashi, M., Kubo, K.-i., and Yagi, K.: 1991, *Physics Reports* **199**, 1

Iwamoto, N. and Pethick, C. J.: 1982, *Physical Review D* **25**, 313

Jaminon, M. and Mahaux, C.: 1989, *Physical Review C* **40**, 354

Janka, H.-T., Buras, R., Joyanes, F. S. K., Marek, A., Rampp, M., and Scheck, L.: 2005, *Nuclear Physics A* **758**, 19

Janka, H.-T., Langanke, K., Marek, A., Martínez-Pinedo, G., and Müller, B.: 2007, *Physics Reports* **442**, 38

Janka, H.-T. and Müller, E.: 1995, *The Astrophysical Journal* **448**, L109

Janka, H.-T. and Müller, E.: 1996, *Astronomy & Astrophysics* **306**, 167

Jin, M., Urban, M., and Schuck, P.: 2010, *Physical Review C* **82**, 024911

Kamada: 2006, *Prog. Theor. Phys.* **115**, 839

Khan, E.: 2009, *Physical Review C* **80**, 011307(R)

Khan, E., Grasso, M., and Margueron, J.: 2009, *Physical Review C* **80(4)**, 044328

Khan, E., Margueron, J., Colò, G., Hagino, K., and Sagawa, H.: 2010, *Physical Review C* **82**, 024322

Khan, E., Sandulescu, N., Grasso, M., and Van Giai, N.: 2002, *Physical Review C* **66**, 024309

Khan, E., Sandulescu, N., and Van Giai, N.: 2005, *Physical Review C* **71**, 042801(R)

Khan, E., Van Giai, N., and Grasso, M.: 2004, *Nuclear Physics A* **731**, 311

Khan, E., Van Giai, N., and Sandulescu, N.: 2007, *Nuclear Physics A* **789**, 94

Kittel, C.: 1996, *Introduction to Solid State Physics, 7th ed.*, Wiley, New-York

Klähn, T., Blaschke, D., Typel, S., Van Dalen, E. N. E., Faessler, A., Fuchs, C., Gaitanos, T., Grigorian, H., Ho, A., Kolomeitsev, E. E., Miller, M. C., Röpke, G., Trümper, J., Voskresensky, D. N., Weber, F., and Wolter, H. H.: 2006, *Physical Review C* **74**, 035802

Klimkiewicz, A., Paar, N., Adrich, P., Fallot, M., Boretzky, K., Aumann, T., Cortina-Gil, D., Pramanik, U. D., Elze, T. W., Emling, H., Geissel, H., and Others: 2007, *Physical Review C* **76**, 051603

Koster, G. F.: 1957, *Solid State Physics 5*, Academic Press

Kuckei, J., Montani, F., Müther, H., and Sedrakian, A. D.: 2003, *Nuclear Physics A* **723**, 32

Kutschera, M. and Wójcik, W.: 1994, *Physics Letters B* **325**, 271

Lalazissis, G. A., König, J., and Ring, P.: 1997, *Physical Review C* **55**, 540

Landau, L.: 1932, *Physikalische Zeitschrift der Sowjetunion* **1**, 285

Landau, L. and Lifchitz, E.: 1967, *Statistical Physics*, Mir

Langanke, K. and Martinez-Pinedo, G.: 2000, *Nuclear Physics A* **673**, 481

Langanke, K., Martínez-Pinedo, G., Sampaio, J., Dean, D. J., Hix, W. R., Messer, O., Mezzacappa, A., Liebendörfer, M., Janka, H.-T., and Rampp, M.: 2003, *Physical Review Letters* **90**, 10

Lassaut, M., Flocard, H., Bonche, P., Heenen, P.-H., and Suraud, E.: 1987, *Astronomy and Astrophysics* **183**, L3

Lattimer, J. M., Pethick, C. J., Prakash, M., and Haensel, P.: 1991, *Physical Review Letters* **66**, 2701

Lattimer, J. M. and Prakash, M.: 2001, *The Astrophysical Journal* **550**, 426

Lattimer, J. M. and Prakash, M.: 2004, *Science (New York, N.Y.)* **304(5670)**, 536

Lattimer, J. M. and Prakash, M.: 2007, *Physics Reports* **442**, 109

Lattimer, J. M. and Prakash, M.: 2010, in *Gerry Brown's Festschrift*, World Scientific

Lattimer, J. M. and Swesty, F. D.: 1991, *Nuclear Physics A* **535**, 331

Lattimer, J. M., Van Riper, K. A., Prakash, M., and Prakash, M.: 1994, *The Astrophysical Journal* **425**, 802

Lazzati, D.: 2005, *Nature* **434**, 1075

Lee, S. Y. and Suzuki, K.: 1980, *Physics Letters B* **91**, 173

Lesinski, T., Bennaceur, K., Duguet, T., and Meyer, J.: 2006, *Physical Review C* **74**, 044315

Levenfish, K. P. and Yakovlev, D. G.: 1994, *Astronomy Reports* **38**, 247

Levin, K. and Chen, Q.: 2006, in *Lecture given at the International School of Physics "Enrico Fermi" – the 2006 Varenna Summer School on "Ultracold Fermi Gases",*, pp 1–27

Li, B.-A. and Chen, L.-w.: 2005, *Physical Review C* **72**, 064611

Li, B.-A., Chen, L.-w., and Ming, C.: 2008a, *Physics Reports* **464**, 113

Li, B.-A. and Steiner, A. W.: 2006, *Physics Letters B* **642**, 436

Li, J., Colò, G., and Meng, J.: 2008b, *Physical Review C* **78**, 064304

Li, T., Garg, U., Liu, Y., Marks, R., Nayak, B. K., Madhusudhana Rao, P. V., Fujiwara, M., Hashimoto, H., Kawase, K., Nakanishi, K., Okumura, S., Yosoi, M., Itoh, M., Ichikawa, M., Matsuo, R., Terazono, T., Uchida, M., Kawabata, T., Akimune, H., Iwao, Y., Murakami, T., Sakaguchi, H., Terashima, S., Yasuda, Y., Zenihiro, J., and Harakeh, M. N.: 2007, *Physical Review Letters* **99**, 162503

Li, T., Garg, U., Liu, Y., Marks, R., Nayak, B. K., Madhusudhana Rao, P. V., Ichikawa, M., Itoh, M., Matsuo, R., Terazono, T., Uchida, M., Iwao, Y., Kawabata, T., Murakami, T., Sakaguchi, H., Terashima, S., Yasuda, Y., Zenihiro, J., Akimune, H., Kawase, K., and Harakeh, M. N.: 2010, *Physical Review C* **81**, 034309

Liebendörfer, M., Messer, O. E. B., Mezzacappa, A., Bruenn, S. W., Cardall, C. Y., and Thielemann, F.-K.: 2004, *The Astrophysical Journal Supplement Series* **150**, 263

Liebendörfer, M., Mezzacappa, A., Thielemann, F.-k., Messer, O. E. B., Hix, W. R., and Bruenn, S. W.:

2001, *Physical Review D* **63**, 103004

Liebendörfer, M., Rampp, M., Janka, H.-T., and Mezzacappa, A.: 2005, *The Astrophysical Journal* **620**, 840

Link, B.: 1999, *Physical Review Letters* **83**, 3362

Liu, B., Guo, H., Di Toro, M., and Greco, V.: 2005, *European Physical Journal A* **25**, 293

Liu, K.-F., Luo, H., Ma, Z. Y., and Shen, Q.: 1991a, *Nuclear Physics A* **534**, 25

Liu, K.-F., Luo, H., Ma, Z. Y., Shen, Q., and Moszkowski, S. A.: 1991b, *Nuclear Physics A* **534**, 1

Loan, D. T., Tan, N. H., Khoa, D. T., and Margueron, J.: 2011, *Physical Review C* **83**, 065809

Lombardo, U.: 1999, in M. Baldo (ed.), *Nuclear Methods and the Nuclear Equation of State, International Review of Nuclear Physics - Vol. 8*, Vol. 9, pp 458–510, World Scientific

Lombardo, U. and Schuck, P.: 2001, *Physical Review C* **63**, 038201

Long, W.-H., Meng, J., Van Giai, N., and Zhou, S.-G.: 2004, *Physical Review C* **69**, 034319

Long, W.-H., Sagawa, H., Van Giai, N., and Meng, J.: 2007, *Physical Review C* **76**, 034314

Long, W.-H., Van Giai, N., and Meng, J.: 2006, *Physics Letters B* **640**, 150

Lutz, M., Friman, B. L., and Appel, C.: 2000, *Physics Letters B* **474**, 7

Ma, Z. Y. and Wambach, J.: 1983, *Nuclear Physics A* **402**, 275

Machleidt, R. and Entem, D. R.: 2011, *Physics Reports* **503**, 1

Machleidt, R., Sammarruca, F., and Song, Y.: 1996, *Physical review C* **53(4)**, R1483

Magierski, P. and Heenen, P.-H.: 2002, *Physical Review C* **65**, 045804

Mahaux, C., Bortignon, P. F., Broglia, R. A., and Dasso, C. H.: 1985, *Physics Reports* **120**, 1

Mahaux, C. and Sartor, R.: 1992, *Physical Report* **211**, 53

Marek, A. and Janka, H.-T.: 2009, *The Astrophysical Journal* **694**, 664

Marek, A., Janka, H.-T., and Müller, E.: 2009, *Astronomy and Astrophysics* **496**, 475

Margueron, J.: 2001, *Ph.D. thesis*, Université Paris-Sud XI

Margueron, J., Bonaccorso, A., and Brink, D. M.: 2002a, *Nuclear Physics A* **703**, 105

Margueron, J., Bonaccorso, A., and Brink, D. M.: 2003a, *Nuclear Physics A* **720**, 337

Margueron, J., Bonaccorso, A., and Brink, D. M.: 2004a, *Nuclear Physics A* **741**, 381

Margueron, J. and Chomaz, P.: 2003, *Physical Review C* **67**, 041602(R)

Margueron, J. and Chomaz, P.: 2005, *Physical Review C* **71**, 024318

Margueron, J., Goriely, S., Grasso, M., Colò, G., and Sagawa, H.: 2009, *Journal of Physics G: Nuclear and Particle Physics* **36**, 125103

Margueron, J., Navarro, J. F., and Blottiau, P.: 2004b, *Physical Review C* **70**, 028801

Margueron, J., Navarro, J. F., and Van Giai, N.: 2002b, *Physical Review C* **66**, 014303

Margueron, J., Navarro, J. F., and Van Giai, N.: 2003b, *Nuclear Physics A* **719**, 169c

Margueron, J. and Sagawa, H.: 2009, *Journal of Physics G: Nuclear and Particle Physics* **36**, 125102

Margueron, J., Sagawa, H., and Hagino, K.: 2007a, *Physical Review C* **76**, 064316

Margueron, J., Sagawa, H., and Hagino, K.: 2008, *Physical Review C* **77**, 054309

Margueron, J. and Sandulescu, N.: 2012, in C. A. Bertulani and J. Piekarewicz (eds.), *Neutron Star crust*, pp 68–86, World Scientific

Margueron, J., Van Dalen, E. N. E., and Fuchs, C.: 2007b, *Physical Review C* **76**, 034309

Margueron, J., Van Giai, N., and Navarro, J. F.: 2005, *Physical Review C* **72**, 034311

Margueron, J., Van Giai, N., and Navarro, J. F.: 2006, *Physical Review C* **74**, 015805

Margueron, J., Van Giai, N., and Sandulescu, N.: 2007c, in U. Lombardo, M. Baldo, F. Burgio, and H.-J. Schulze (eds.), *Exotic States of Nuclear Matter*, p. 362, World Scientific

Margueron, J., Vidaña, I., and Bombaci, I.: 2003c, *Physical Review C* **68**, 055806

Matsuo, M.: 2006, *Physical Review C* **73**, 044309

Matsuo, M., Mizuyama, K., and Serizawa, Y.: 2005, *Physical Review C* **71**, 064326

Mezzacappa, A., Liebendörfer, M., Messer, O. E. B., Hix, W. R., Thielemann, F.-k., and Bruenn, S. W.: 2001, *Physical Review Letters* **86**, 1935

Migdal, A. B.: 1959, *Nuclear Physics* **13**, 655

Migdal, A. B.: 1967, *Theory of finite Fermi systems and applications to atomic nuclei*, Interscience Publishers, New-York

Mihalas, D.: 1999, *Foundation of radiation hydrodynamics*, Dover Publications, New-York

Monrozeau, C., Margueron, J., and Sandulescu, N.: 2007, *Physical Review C* **75**, 65807

Montani, F., May, C., and Müther, H.: 2004, *Physical Review C* **69**, 065801

Moustakidis, C. C., Nikšić, T., Lalazissis, G., Vretenar, D., and Ring, P.: 2010, *Physical Review C* **81**, 065803

Müller, B., Janka, H.-T., and Dimmelmeier, H.: 2010, *The Astrophysical Journal Supplement Series* **189**, 104

Müller, H. and Serot, B. D.: 1995, *Physical Review C* **52**, 2072

Myra, E. S. and Bludman, S. A.: 1989, *The Astrophysical Journal* **340**, 384

Nakada, H.: 2003, *Physical Review C* **68**, 014316

Negele, J. W.: 1970, *Physical Review C* **1**, 1260

Negele, J. W. and Vautherin, D.: 1972, *Physical Review C* **5**, 1472

Negele, J. W. and Vautherin, D.: 1973, *Nuclear Physics A* **207**, 298

Niembro, R., Bernardos, P., Lopez-Quelle, M., and Marcos, S.: 2001, *Physical Review C* **64**, 055802

Noh, W. F.: 1978, *Journal of Computational Physics* **72**, 78

Nordhaus, J., Burrows, A., Almgren, A., and Bell, J.: 2010, *The Astrophysical Journal* **720**, 694

Nozières, P. and Schmitt-Rink, J.: 1985, *Journal of Low Temperature Physics* **59**, 195

Okubo, S.: 1954, *Prog. Theor. Phys.* **12**, 603

Onsi, M., Dutta, A. K., Chatri, H., Goriely, S., Chamel, N., and Pearson, J. M.: 2008, *Physical Review C* **77**, 065805

Oppenheimer, J. R. and Volkoff, G. M.: 1939, *Physical Review* **55**, 379

Osterfeld, F.: 1992, *Reviews of Modern Physics* **64**, 491

Özel, F., Baym, G., and Güver, T.: 2010, *Physical Review D* **82**, 101301(R)

Pacini, F.: 1967, *Nature* **216**, 567

Pacini, F.: 1968, *Nature* **219**, 145

Page, D., Geppert, U., and Weber, F.: 2006, *Nuclear Physics A* **777**, 497

Page, D., Lattimer, J. M., Prakash, M., and Steiner, A. W.: 2004, *The Astrophysical Journal Supplement Series* **155**, 623

Page, D. and Reddy, S.: 2006, *Annual Review on Nuclear and Particles Sciences* **56**, 327

Pandharipande, V. R. and Wiringa, R. B.: 1979, *Reviews of Modern Physics* **51**, 821

Papenbrock, T. and Bertsch, G. F.: 1999, *Physical Review C* **59**, 2052

Perey, F. G. and Buck, B.: 1962, *Nuclear Physics* **32**, 353

Pethick, C. J. and Ravenhall, D. G.: 1995, *Nuclear Physics A* **584**, 675

Pieri, P. and Strinati, G. C.: 2003, *Physical Review Letters* **91**, 030401

Pillet, N., Sandulescu, N., and Schuck, P.: 2007, *Physical Review C* **76**, 024310

Pillet, N., Sandulescu, N., Schuck, P., and Berger, J.-F.: 2010, *Physical Review C* **81**, 034307

Pines, D. and Alpar, M. A.: 1985, *Nature* **316**, 27

Pizzochero, P. A. M., Barranco, F., Vigezzi, E., and Broglia, R. A.: 2002, *The Astrophysical Journal* **569**, 381

Pizzochero, P. A. M., Viverit, L., and Broglia, R. A.: 1997, *Physical Review Letters* **79**, 3347

Polls, A., Ramos, A., and Vidaña, I.: 2002, *Physical Review C* **65**, 035804

Potel, G., Barranco, F., Vigezzi, E., and Broglia, R. A.: 2010, *Physical Review Letters* **105**, 172502

Prakash, M., Bombaci, I., Prakash, M., Ellis, P. J., Lattimer, J. M., and Knorren, R.: 1997, *Physics Reports* **280**, 1

Rampp, M. and Janka, H.-T.: 2000, *The Astrophysical Journal* **539**, L33

Rampp, M. and Janka, H.-T.: 2002, *Astronomy & Astrophysics* **396**, 361

Ravenhall, D. G., Pethick, C. J., and Wilson, J. R.: 1983, *Physical Review Letters* **50**, 2066

Reddy, S., Prakash, M., and Lattimer, J. M.: 1998, *Physical Review D* **58**, 013009

Reinhard, P.-G., Bürvenich, T., Cornelius, T., Fleischer, P., Klüpfel, P., and Maruhn, J. A.: 2004, *Nuclear Physics A* **746**, 76c

Rikovska Stone, J., Miller, J. C., Koncewicz, R., Stevenson, P. D., and Strayer, M. R.: 2003, *Physical Review C* **68**, 034324

Ring, P.: 1996, *Progress in Particle and Nuclear Physics* **73**, 193

Ring, P. and Schuck, P.: 1980, *The Nuclear Many-Body Problem*, Springer-Verlag

Rüster, S. B., Hempel, M., and Schaffner-Bielich, J.: 2006, *Physical Review C* **73**, 035804

Rutledge, R. E., Bildsten, L., Brown, E. F., Pavlov, G. G., Zavlin, V. E., Ushomirsky, G., and Al, R. E. T.: 2002, *The Astrophysical Journal* **580**, 413

Sagawa, H., Yoshida, S., Zeng, G.-M., Gu, J.-Z., and Zhang, X.-Z.: 2007a, *Physical Review C* **76**, 034327

Sagawa, H., Yoshida, S., Zeng, G.-M., Gu, J.-Z., and Zhang, X.-Z.: 2008, *Physical Review C* **77**, 049902(E)

Sagawa, H., Yoshida, S., Zhou, X.-R., Yako, K., and Sakai, H.: 2007b, *Physical Review C* **76**, 024301

Sandulescu, N.: 2004, *Physical Review C* **70(2)**, 025801

Sandulescu, N.: 2008, *The European Physical Journal Special Topics* **156**, 265

Sandulescu, N., Geng, L., Toki, H., and Hillhouse, G.: 2003, *Physical Review C* **68**, 054323

Sandulescu, N., Van Giai, N., and Liotta, R. J.: 2004, *Physical Review C* **69**, 045802

Schuck, P. and Viñas, X.: 2011, *Physical Review Letters* **107**, 205301

Sedrakian, A. D., Alm, T., and Lombardo, U.: 1997, *Physical Review C* **55**, 582

Sedrakian, A. D., Kuo, T. T. S., Müther, H., and Schuck, P.: 2003, *Physics Letters B* **576**, 68

Sedrakian, A. D., Müther, H., and Polls, A.: 2006, *Physical Review Letters* **97**, 140404

Serot, B. D.: 1992, *Reports on Progress in Physics* **55**, 1855

Serot, B. D. and Walecka, J. D.: 1986, in *Advances in Nuclear Physics*, p. 1, Plenium, New-York

Serot, B. D. and Walecka, J. D.: 1997a, *Int. J. Mod. Phys. E* **6**, 515

Serot, B. D. and Walecka, J. D.: 1997b, in *International Journal of Modern Physics E*, p. 515, World Scientific

Shapiro, S. L. and Teukolsky, S. A.: 1983, *Black holes, White Dwarfs, and Neutron Stars*, John Wiley & Sons, New-York

Shetty, D. V., Yennello, S. J., and Souliotis, G. A.: 2007a, *Physical Review C* **75**, 034602

Shetty, D. V., Yennello, S. J., and Souliotis, G. A.: 2007b, *Physical Review C* **76**, 024606

Shlomo, S., Kolomietz, V. M., and Colò, G.: 2006, *European Physical Journal A* **30**, 23

Shternin, P. S., Yakovlev, D. G., Haensel, P., and Potekhin, A. Y.: 2007, *Monthly Notices of the Royal Astronomical Society* **382**, L43

Skyrme, T. H. R.: 1956, *Philosophical Magazine* **1(11)**, 1043

Skyrme, T. H. R.: 1959, *Nuclear Physics* **9**, 615

Stamper-Kurn, D., Miesner, H.-J., Chikkatur, A., Inouye, S., Stenger, J., and Ketterle, W.: 1998, *Physical Review Letters* **81**, 2194

Steiner, A. W., Prakash, M., Lattimer, J. M., and Ellis, P. J.: 2005, *Physics Reports* **411**, 325

Strohmayer, T. and Bildsten, L.: 2006, *Compact Stellar X-Ray Sources*, Cambridge Astrophysics Series

Sturm, C., Böttcher, I., Dbowski, M., Förster, a., Grosse, E., Koczo, P., Kohlmeyer, B., Laue, F., Mang, M., Naumann, L., Oeschler, H., Pühlhofer, F., Schwab, E., Senger, P., Shin, Y., Speer, J., Ströbele, H., Surówka, G., Uhlig, F., Wagner, a., and Waluś, W.: 2001, *Physical Review Letters* **86(1)**, 39

Sumiyoshi, K. and Toki, H.: 1994, *The Astrophysical Journal* **422**, 700

Sumiyoshi, K., Yamada, S., Suzuki, H., Shen, H., Chiba, S., and Toki, H.: 2005, *The Astrophysical Journal* **629**, 922

Suraud, E.: 1985, *Astronomy & Astrophysics* **143**, 108

Suzuki, K.: 1982, *Prog. Theor. Phys.* **68**, 246

Suzuki, T. and Sakai, H.: 1999, *Physics Letters B* **455**, 25

Swesty, F. D., Lattimer, J. M., and Myra, E. S.: 1994, *The Astrophysical Journal* **425**, 195

Szilner, S., Ur, C. A., Corradi, L., Pollarolo, G., Stefanini, A. M., Beghini, S., Behera, B. R., Fioretto, E., Gadea, A., Guiot, B., Latina, A., Mason, P., Montagnoli, G., Scarlassara, F., Trotta, M., Angelis, G. D., Vedova, F. D., Farnea, E., Haas, F., Lenzi, S., Lunardi, S., Menegazzo, R., Napoli, D. R., Nespolo, M., and Pokrovsky, I. V.: 2007, *Physical Review C* **76**, 024604

ter Haar, B. and Malfliet, R.: 1987, *Physics Reports* **149**, 207

Than, H. S., Khoa, D. T., and Van Giai, N.: 2009, *Physical Review C* **80**, 064312

Thompson, C. and Duncan, R. C.: 1995, *Monthly Notices of the Royal Astronomical Society* **275**, 255

Thompson, T. A., Burrows, A., and Pinto, P. A.: 2003, *The Astrophysical Journal* **592**, 434

Thorne, K. S.: 1977, *The Astrophysical Journal* **212**, 825

Thouless, D. J.: 1961, *Nuclear Physics* **22**, 78

Tian, Y., Ma, Z. Y., and Ring, P.: 2009, *Physics Letters B* **676**, 44

Tohsaki, A., Horiuchi, H., Schuck, P., and Röpke, G.: 2001, *Physical Review Letters* **87**, 192501

Tolman, R. C.: 1939, *Physical Review* **55**, 364

Trippa, L., Colò, G., and Vigezzi, E.: 2008, *Physical Review C* **77**, 061304(R)

Tsang, M. B., Zhang, Y., Danielewicz, P., Famiano, M., Li, Z., Lynch, W. G., and Steiner, A. W.: 2009, *Physical Review Letters* **102**, 122701

Typel, S. and Baur, G.: 2001, *Physical Review C* **64**, 024601

Typel, S. and Wolter, H. H.: 1999, *Nuclear Physics A* **656**, 331

Van Dalen, E. N. E., Fuchs, C., and Faessler, A.: 2004, *Nuclear Physics A* **744**, 227

Van Dalen, E. N. E., Fuchs, C., and Faessler, A.: 2005, *Physical Review Letters* **95**, 022302

Van Dalen, E. N. E., Gögelein, P., and Müther, H.: 2009, *Physical Review C* **80**, 44312

Van Dalen, E. N. E. and Müther, H.: 2011, *Physical Review C* **84**, 024320

Van Giai, N., Carlson, B. V., Ma, Z. Y., and Wolter, H. H.: 2010, *Journal of Physics G: Nuclear and Particle Physics* **37(6)**, 064043

Van Giai, N. and Van Thieu, P.: 1983, *Physics Letters B* **126**, 421

Vautherin, D. and Brink, D. M.: 1972, *Physical Review C* **5**, 626

Vidaña, I. and Bombaci, I.: 2002, *Physical Review C* **66**, 045801

Vidaña, I., Providência, C., Polls, A., and Rios, A.: 2009, *Physical Review C* **80**, 045806

Vigezzi, E., Barranco, F., Broglia, R. A., Colò, G., Gori, G., and Ramponi, F.: 2005, *Nuclear Physics A* **752**, 600

Vinh Mau, N. and Vautherin, D.: 1985, *Nuclear Physics A* **445**, 245

Viverit, L., Giorgini, S., Pitaevskii, L., and Stringari, S.: 2001, *Physical Review A* **63**, 033603

Vogel, P., Jonson, B., and Hansen, P. G.: 1984, *Physics Letters B* **139**, 227

von Oertzen, W. and Vitturi, A.: 2001, *Reports on Progress in Physics* **64**, 1247

Warda, M., Viñas, X., Roca-Maza, X., and Centelles, M.: 2009, *Physical Review C* **80**, 024316

Waroquier, M., Heyde, K., Isacker, P. V., and Vincx, H.: 1979a, *Physics Letters B* **83**, 9

Waroquier, M., Heyde, K., and Wenes, G.: 1983, *Nuclear Physics A* **404**, 269

Waroquier, M., Sau, J., Heyde, K., Van Isacker, P., and Vincx, H.: 1979b, *Physical Review C* **19**, 1983

Wigner, E. and Seitz, F.: 1933, *Physical Review* **43**, 804

Wigner, E. and Seitz, F.: 1934, *Physical Review* **46**, 509

Wiringa, R. B., Pieper, S. C., Carlson, J., and Pandharipande, V. R.: 2000, *Physical Review Letters* **62**, 014001

Wiringa, R. B., Stoks, V. G. J., and Schiavilla, R.: 1995, *Physical Review C* **51**, 38

Xu, J., Chen, L.-W., Li, B.-A., and Ma, H.-R.: 2009, *Physical Review C* **79**, 035802

Yamagami, M., Margueron, J., Sagawa, H., and Hagino, K.: 2012, *Physical Review C* **86**, 034333

Yamagami, M., Shimizu, Y. R., and Nakatsukasa, T.: 2009, *Physical Review C* **80**, 064301

Yoshida, S. and Sagawa, H.: 2008, *Physical Review C* **77**, 054308

Zalewski, M., Olbratowski, P., and Satua, W.: 2010, *Physical Review C* **81**, 044314

Zdunik, J. L., Bejger, M., Haensel, P., and Gourgoulhon, E.: 2007, *Astronomy & Astrophysics* **465**, 533

Zdunik, J. L., Bejger, M., Haensel, P., and Gourgoulhon, E.: 2008, *Astronomy & Astrophysics* **479**, 515

Zdunik, J. L., Haensel, P., and Gourgoulhon, E.: 2000, *Astronomy & Astrophysics* **356**, 612

Zdunik, J. L., Haensel, P., Gourgoulhon, E., and Bejger, M.: 2004, *Astronomy & Astrophysics* **416**, 1013

Zhang, S. S., Cao, L.-G., Lombardo, U., Zhao, E. G., and Zhou, S. G.: 2010, *Physical Review C* **81**, 044313

Zhang, Y., Matsuo, M., and Meng, J.: 2011, *Physical Review C* **83**, 054301

Zuo, W., Lejeune, A., Lombardo, U., and Mathiot, J.-F.: 2002, *European Physical Journal A* **14**, 469

Zuo, W., Shen, C. W., and Lombardo, U.: 2003, *Physical Review C* **67**, 037301